

LUDWIG-MAXIMILIANS-UNIVERSITY MUNICH

**Theoretical and Experimental
Study of the Electronic Structure
of Graphene-based Systems with
the Quantum Twisting Microscope**

Master Thesis

submitted by

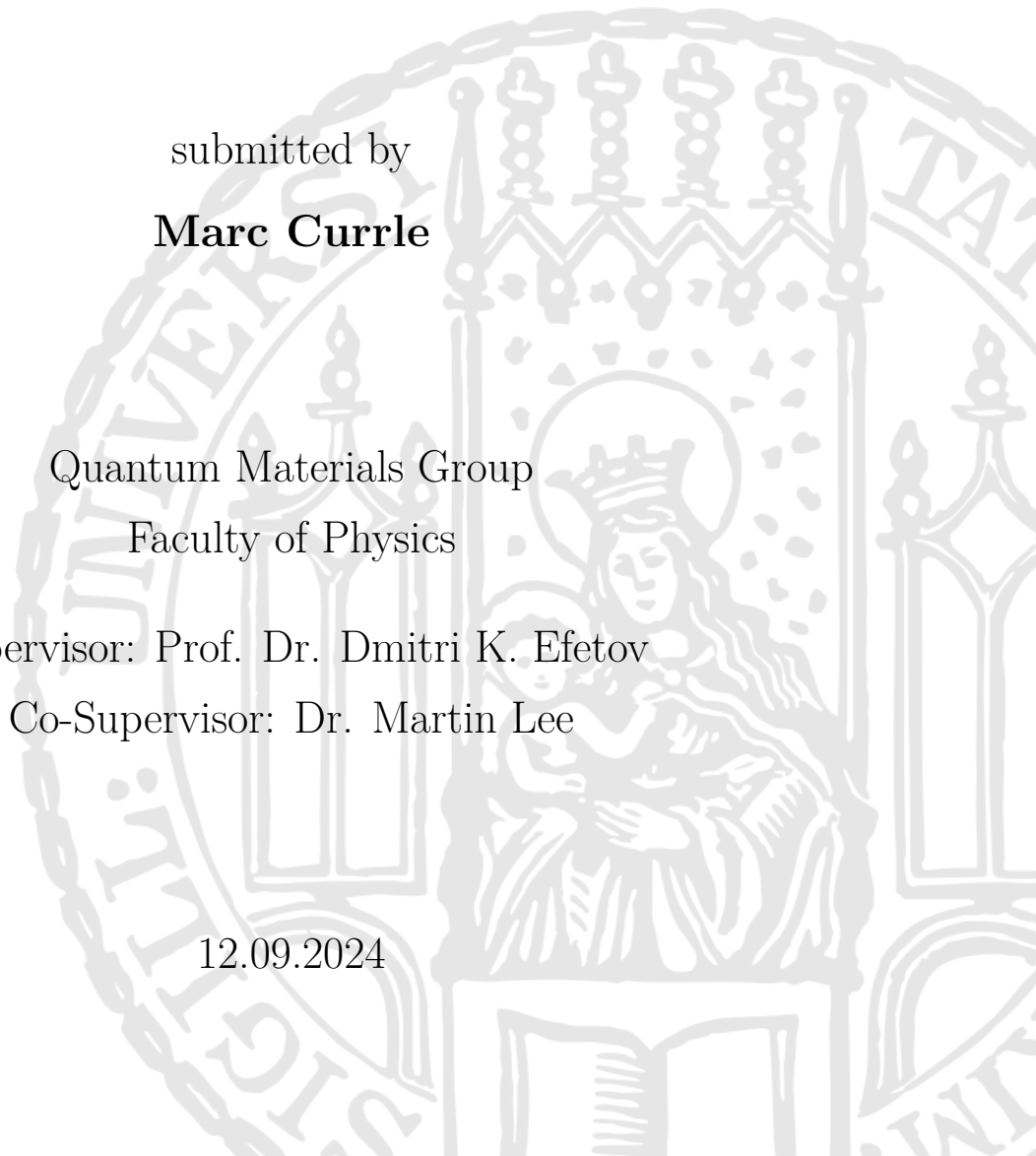
Marc Curre

Quantum Materials Group
Faculty of Physics

Supervisor: Prof. Dr. Dmitri K. Efetov

Co-Supervisor: Dr. Martin Lee

12.09.2024



**Theoretische und experimentelle
Untersuchung der elektronischen
Struktur von graphen-basierten
Systemen mit dem
Quanten-Verdrehungs-Mikroskop**

Masterarbeit

vorgelegt von

Marc Currele

Quantenmaterialien Gruppe

Fakultät für Physik

Betreuer: Prof. Dr. Dmitri K. Efetov

Weiterer Betreuer: Dr. Martin Lee

12.09.2024

Abstract

The discovery of correlated insulating states and superconductivity in magic-angle bilayer graphene has highlighted the twist angle between two-dimensional materials as a new pathway to engineer exotic phases of matter. Since then, the experimental realization and theoretical understanding of these phenomena have become some of the most active research topics in contemporary condensed matter physics. However, precise control of the twist angle and direct probing of the material's electronic structure remain challenging. In this work, we utilize the Quantum Twisting Microscope as a novel approach to create continuously twistable interfaces and for momentum-resolved tunneling measurements. Additionally, we provide a comprehensive theoretical perspective on the electronic properties of layered graphene systems and their characterization through twist angle dependent tunneling spectroscopy.

Contents

	Page
1 Introduction	1
2 Band Structure of Graphene-based Systems	9
2.1 Lattices	10
2.1.1 Bravais Lattices	10
2.1.2 The Reciprocal Lattice	11
2.2 Band Structure	13
2.2.1 Bloch's Theorem	13
2.2.2 Tight Binding Model	14
2.2.3 Density of States and Material Classes	17
2.3 From Carbon to Graphene	20
2.3.1 The Carbon Atom	20
2.3.2 From Atoms to Crystals	21
2.4 Monolayer Graphene	24
2.4.1 Crystal Structure	24
2.4.2 Band Structure	26
2.4.3 Low Energy Physics	33
2.5 Bilayer Graphene	36
2.5.1 Crystal Structure	36
2.5.2 Band Structure	37
2.5.3 Low-Energy Physics	39
2.6 From Graphene to Graphite	42
2.6.1 Crystal Structure	42
2.6.2 Band Structure	43
2.6.3 Low-Energy Physics	44
2.7 Twisted Graphene Layers	45
2.7.1 Moiré Lattice	46
2.7.2 Moiré Reciprocal Lattice	48
2.7.3 Moiré Potential	50
2.7.4 Momentum Space Delocalization	54
2.7.5 Simplifications of the Hopping Term	55

2.7.6	Moiré Band Structure	56
3	Experimental Methods	65
3.1	Exfoliation	66
3.2	Transfer setup	67
3.3	Raman Spectroscopy	67
3.4	Tip Device	69
3.4.1	Scanning Electron Microscope	69
3.4.2	Electron-Substrate Interaction	72
3.4.3	Electron-Precursor Interaction	73
3.4.4	Electron-beam Induced Deposition	75
3.4.5	Polymer Membrane Transfer Technique	86
3.5	Sample Device	90
3.6	Quantum Twisting Microscope	92
4	Tunneling Spectroscopy	95
4.1	QTM's Working Principle - STM and AFM	96
4.2	Transport Between Two-Dimensional Materials with Finite Disorder	101
4.3	Simulation of Interlayer Conductance	102
4.4	Measurement of the Interlayer Conductance	107
4.5	Hexagonal Boron Nitride Tunneling Barrier	109
4.6	Electrostatics of the Tunnel Junction	112
4.7	Fowler-Nordheim Tunneling	116
4.8	Monolayer Graphene	117
4.8.1	Theory	117
4.8.2	Measurement	129
4.9	Bilayer Graphene	132
4.9.1	Theory	132
4.9.2	Measurement	143
4.10	Few-Layer Graphene	147
4.10.1	Theory	147
4.10.2	Trilayer Graphene	150
4.10.3	Pentalayer Graphene	151
5	Conclusion	155
	List of Figures	159
	Bibliography	165

Acknowledgements 175

Chapter 1

Introduction

Richard P. Feynman, in his seminal lecture “There is Plenty of Room at the Bottom,” posed the following question: “What could we do with layered structures with just the right layers? What would the properties of materials be if we could really arrange the atoms the way we want them? They would be very interesting to investigate theoretically. I can’t see exactly what would happen, but I can hardly doubt that when we have some control of the arrangement of things on a small scale, we will get an enormously greater range of possible properties that substances can have, and of different things that we can do...” [1]. In this visionary lecture, Feynman foresaw a future where artificial materials could be engineered with bespoke properties.

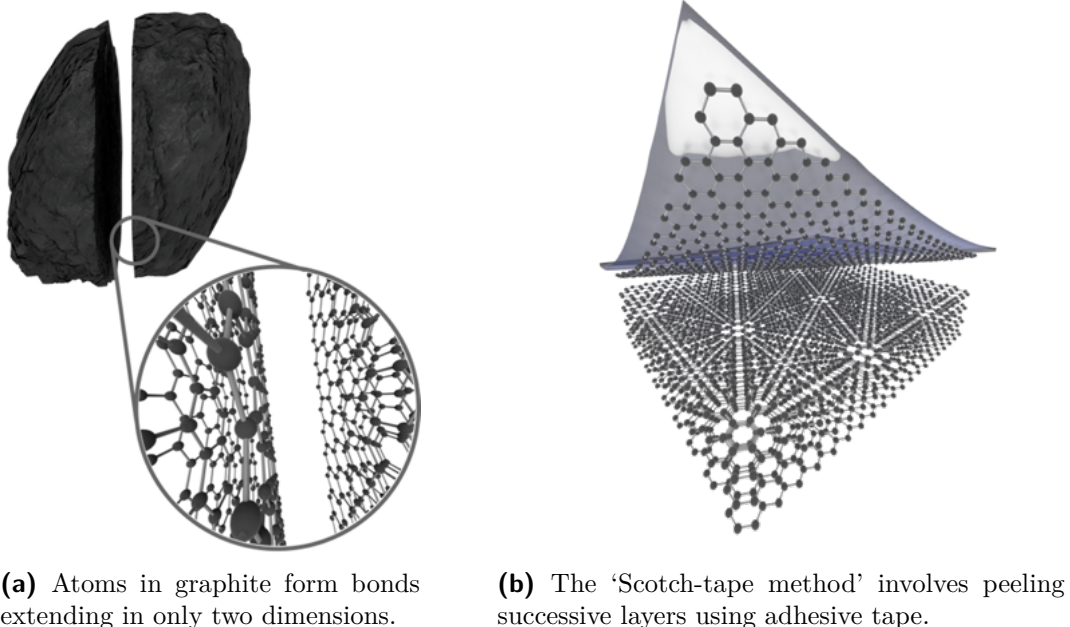


Figure 1.1 Mechanical exfoliation of graphene from bulk graphite. Adapted from [2].

A significant milestone towards realizing Feynman’s vision occurred in 2004 when

Andrei Geim and Konstantin Novoselov successfully isolated a single layer of graphene from bulk graphite using a straightforward technique known as mechanical exfoliation with Scotch tape (Fig. 3.2) [3]. This breakthrough was followed by the successful exfoliation of numerous other two-dimensional (2D) materials, including isolated monolayers of hexagonal boron nitride (hBN), molybdenum disulfide (MoS_2), tungsten diselenide (WSe_2), various dichalcogenides, and layered oxides [4].

Inspired by the graphene revolution, research into 2D materials has burgeoned into a vast field, with thousands of publications on various aspects of graphene appearing annually [4]. Building upon this foundation, the realization of artificial materials has become a reality. By utilizing isolated 2D materials as building blocks, we can engineer and design matter at the macromolecular level by stacking different 2D crystals on top of each other. The fundamental principle is straightforward: take a monolayer, place it on top of another monolayer or a crystal with a few layers, add another 2D crystal, and so on (Fig. 1.2).

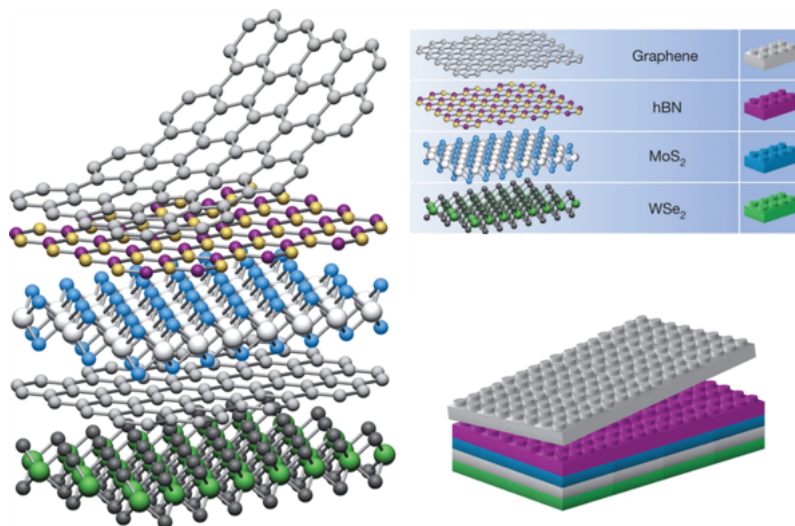


Figure 1.2 An illustration of the assembly of artificial materials through stacking different 2D crystals. Adapted from [4].

The resulting stack constitutes an artificial material assembled in the desired sequence. The emerging interlayer interactions between adjacent layers are highly specific, depending on the atomic constituents of the interacting layers and their relative arrangements at the interface. These parameters allow us to fine-tune the electronic properties of the system.

In recent years, significant efforts have been directed towards engineering flat bands around the Fermi level (E_F), a research area experiencing rapid advancements across various lattice systems. A particularly important example is twisted bilayer graphene, which consists of two graphene layers stacked and rotated relative to each other by an angle θ (Fig. 1.3) [5].

Numerical calculations demonstrate that at specific "magic angles," the electron velocity nearly vanishes along the entire band, resulting in the formation of a flat band [6]. This flat band inherently emphasizes the critical role of many-body effects. The problem of interacting electrons within flat bands is exceedingly complex, yet it is certain that fascinating phenomena occur. Indeed, they do: Cao et al. discovered insulating behavior [7] and superconductivity [8] in twisted bilayer graphene at the magic angle $\theta \approx 1.1^\circ$, attributed to many-body effects, which emerge due to the flat band.

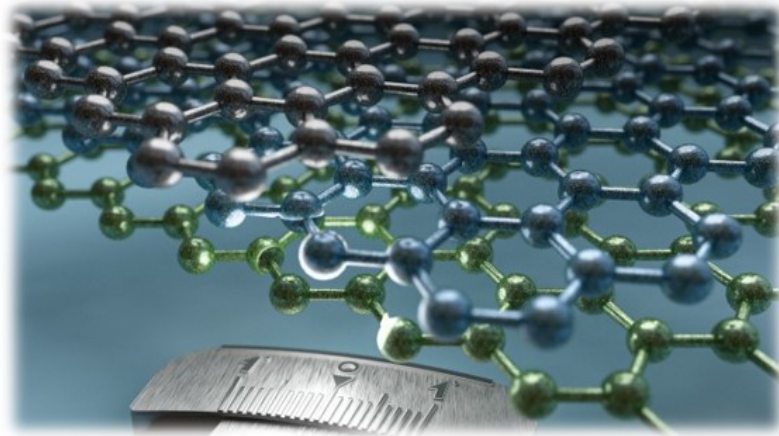


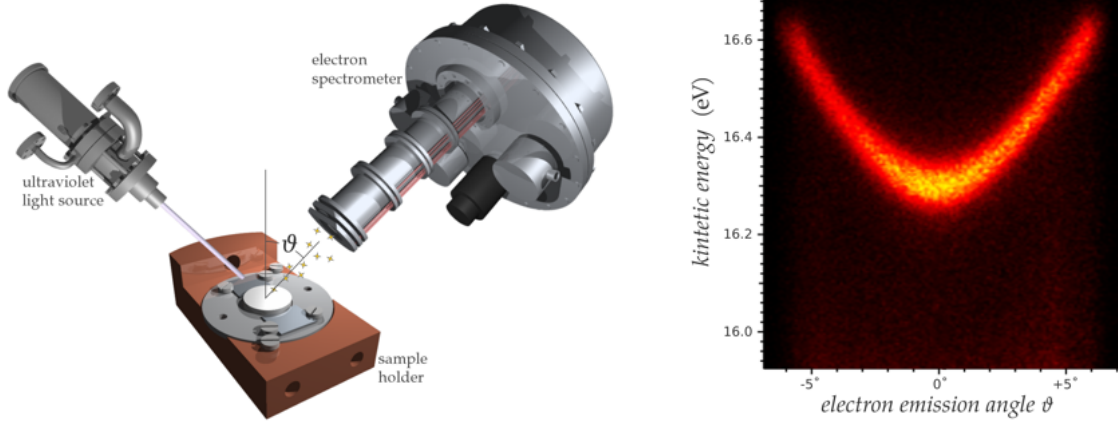
Figure 1.3 Illustration of the rotational misalignment between graphene layers. Adapted from [5].

Six years after this groundbreaking discovery in 2018, researchers continue to explore the intricate and exotic properties of twisted bilayer graphene, striving to fully understand its unique behavior.

However, direct momentum-resolved measurements have proved to be challenging. The most capable method in the experimentalist's arsenal is Angle-Resolved Photoemission Spectroscopy (ARPES). A typical setup, depicted in Fig. 1.4a, consists of a light source, a sample holder attached to a manipulator, and an electron spectrometer. To suppress any interaction with gas molecules and protect the sample surface from adsorbates, ARPES is performed in ultra-high vacuum (UHV) chambers [9].

Through interaction with the light field, electrons in an initial band state with two-dimensional crystal momentum \mathbf{k} and energy $E(\mathbf{k})$ are excited to a free-space final state with three-dimensional momentum \mathbf{p} , kinetic energy E_{kin} , and an angle ϑ relative to the surface normal, by incident photons with energy $\hbar\omega$, provided the photon energy is large enough to overcome the binding energy E_{B} . Energy conservation ensures that $E_{\text{kin}} = \hbar\omega + E(\mathbf{k}) - E_{\text{B}}$.

As the electron crosses the surface barrier, only the component of \mathbf{p} that is parallel



(a) Typical laboratory setup. Helium discharge lamp as an ultraviolet light source, sample holder attached to a vacuum manipulator, and hemispherical electron energy analyzer.

(b) ARPES spectrum of a two-dimensional electronic state. The energy exhibits a free-electron-like momentum dependence $E(\mathbf{k}) \sim \frac{\hbar^2 \mathbf{k}^2}{2m^*}$.

Figure 1.4 Angle-resolved photoemission spectroscopy working principle. Adapted from [10].

to the surface, $\mathbf{p}_{||}$, is preserved. Its magnitude is given by

$$|\mathbf{k}| = \frac{1}{\hbar} |\mathbf{p}_{||}| = \frac{1}{\hbar} |\mathbf{p}| \sin \vartheta, \quad |\mathbf{p}| = \sqrt{2m_e E_{\text{kin}}}, \quad (1.1)$$

where ϑ is measured between the surface and the spectrometer (azimuth angle is neglected in this illustration).

By analyzing the energy and momentum of the outgoing electrons, electron emission intensity maps $I(\vartheta, E_{\text{kin}})$, i.e., electron counts per kinetic energy and emission angle channel, can be obtained. Using the above relationship, this allows reconstruction of the energy dispersion $E(\mathbf{k})$ of the solid. Figure 1.4b depicts the spectrum of a two-dimensional system with parabolic dispersion.

For graphene-like two-dimensional materials, the most limiting factor for ARPES studies is their size. Two-dimensional crystal flakes produced by mechanical exfoliation have the highest quality but typically measure only $1\text{--}50\mu\text{m}$, which is smaller than the typical beam spot size of $25\text{--}100\mu\text{m}$ in conventional ARPES experiments. Further collimation to a size comparable to the samples requires special optical elements, whose critical disadvantage is beam efficiency, often causing a loss of more than 90% of the incident beam [11]. Additionally, identifying flakes with the desired layer number and directing the light for ARPES measurements to the exact same spot is challenging in a UHV environment [9].

Figure 1.5 displays the ARPES spectra collected from a graphene monolayer and twisted bilayer graphene (TBG). The monolayer spectrum shows the typical linear band dispersion characteristic of graphene. In contrast, the spectrum from TBG

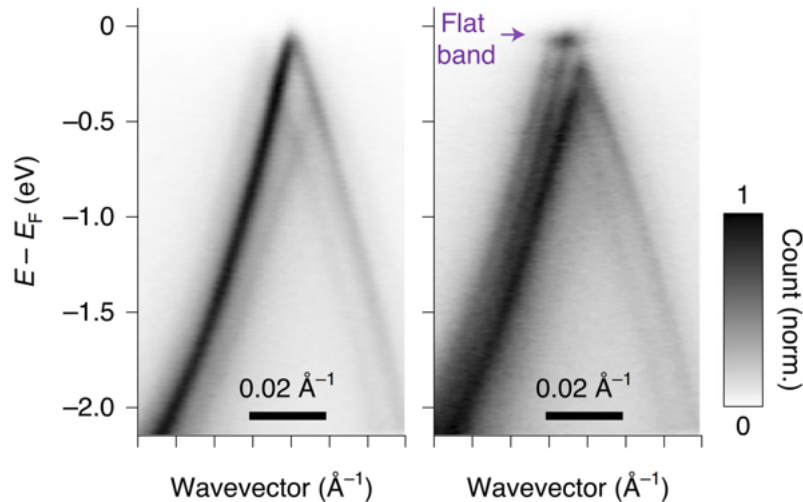


Figure 1.5 ARPES spectrum of graphene (left) and TBG (right). Adapted from [12].

exhibits a sharp feature near the Fermi level, corresponding to the flat electronic band. The presence of such a flat band implies a singularity in the density of states. Accordingly, the system may reduce the total electronic ground state energy via an energy gap opening, thereby triggering the emergence of the observed exotic quantum phase transitions. However, due to the resolution limit of this ARPES measurements, these predicted finer substructures are broadened out.

TBG systems are just one example within the broader family of materials that can host flat electronic bands. The creation and investigation of other moiré superlattice-induced flat bands in related van der Waals heterostructure systems have become one of the most active research topics in current condensed matter physics. This seemingly simple twist has opened up a Pandora’s box of new possibilities for realizing interacting topological phases, superconductivity, magnetism, and other many-body states of matter [5].

In conclusion, there are two major obstacles to advancing this field. The first is the precise control of the twist angle. It is one of the critical parameters that determine the electronic behaviour of materials such as TBG; altering it by merely one-tenth of a degree can transform the material from an exotic superconductor into an unconventional insulator. The second challenge is the experimental characterization of the band structure. Detailed access to the electronic structure of these materials is essential for a more quantitative understanding of moiré physics and the utilization of the extraordinary properties.

A new experimental concept is called for to overcome these challenges. In order to realise these exotic states, the in-situ tuning of the twist angle in the MAGIC state would be desirable. Secondly, a local probe measurement technique is required to circumvent the inherent twist-angle inhomogeneity in a device and also provide an

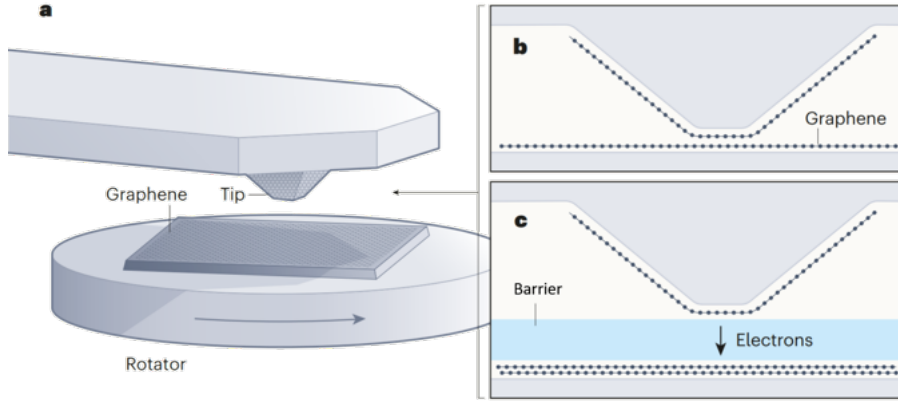


Figure 1.6 **a** The quantum twisting microscope, which can be used to control the angular alignment between one or more sheets comprising single layers of atoms, such as graphene. The microscope consists of a pyramid-shaped tip that is covered in one sheet (of graphene, for example), and brought into contact with a second sample on a rotator. **b** In this way, the microscope can be used to control the angular alignment of such layers in situ. **c** The device can also measure and change the way in which the energy of electrons in the multilayered structure depends on their momentum. In this mode, the electrons move through an added barrier layer of an insulating material. Adapted from [13].

energy resolution that allows correlation effects to be resolved.

A novel scanning probe microscopy technique developed by Inbar et al. [14], the Quantum Twisting Microscope (QTM), promises great potential to meet these challenging requirements. The QTM replaces the conventional sharp tip of an atomic force microscope with a tip composed of a flat layer of a 2D material, such as a monolayer of graphene. This unique configuration allows the QTM to bring the tip layer into controlled contact with the surface of a sample material at a specified twist angle, θ , enabling the on-demand creation of tailored moiré superlattices. Measuring the current flowing between the tip and the sample, allows the characterization of the interlayer interaction at the two-dimensional interface.

Moreover, the QTM offers a powerful new approach to resolving electronic energy bands, presenting significant advantages over traditional ARPES measurements. Unlike ARPES, which relies on inducing transitions between Bloch states and free space states and subsequently measuring the electron current as a function of kinetic energy and angle, the QTM operates by inducing a tunneling current between the tip and sample through a tunneling barrier via an applied bias voltage V_b . This current is governed by the interference of the tip and sample wavefunctions, allowing an electron to tunnel only if its wavefunctions on both sides of the interface match exactly in energy and momentum. The QTM's twisting capability is used to identify the angle at which this alignment occurs: as the tip is continuously twisted relative to the sample, the corresponding wavefunctions also undergo relative rotation.

When these wavefunctions match on both sides of the interface, tunneling occurs, and the QTM can map the position. By analyzing the angles at which electrons cross the interface, as revealed by the current spectrum $I(\theta, V_b)$, the band structure of the material under investigation can be determined.

This thesis provides a comprehensive theoretical examination of the electronic properties of graphene-based systems and the description of bias and twist angle dependent interlayer transport between graphene layers, which is then applied for the interpretation of the QTM measurements conducted. Furthermore, we provide a method of fabricating the QTM tips.

The structure of this thesis is as follows: In Chapter [2](#), we explore the electronic properties of graphene layers in detail. Chapter [3](#) describes the experimental setups, including the fabrication and characterization methods employed. Chapter [4](#) introduces the theoretical framework for interlayer transport between graphene layers and examines the electrostatics of the QTM junction. Based on this theory, we simulate the expected dynamics and compare them with the experimental results. Finally, Chapter [5](#) presents our conclusions.

Chapter 2

Band Structure of Graphene-based Systems

This chapter focuses on the study of the crystal and band structures of the materials of interest. First, we introduce the concept of Bravais lattices and the tight-binding method. Next, we apply these formalisms to analyze the properties of monolayer and bilayer graphene in detail. Finally, we extend our examination to multi-layer graphene systems.

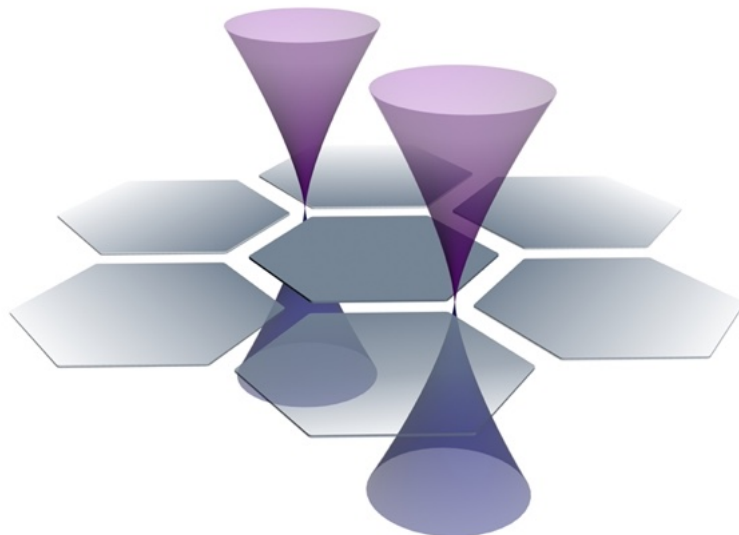


Figure 2.1 Adapted from [15].

2.1 Lattices

In this section, we introduce the terminology required to describe various types of periodic structures in both real and reciprocal space.

2.1.1 Bravais Lattices

A Bravais lattice is a periodic array of points where the environment around any point is identical to that around any other point. This lattice is generated by an infinite set of vectors Λ , where the addition of any two vectors in the set results in another vector within the set. Λ can be defined by an integer sum of linearly independent basis vectors, known as primitive lattice vectors \mathbf{a}_i . In two dimensions, a Bravais lattice Λ can be expressed as:

$$\Lambda = \left\{ \mathbf{r} = n_1 \mathbf{a}_1 + n_2 \mathbf{a}_2 \mid (n_1, n_2)^T \in \mathbb{Z}^2 \right\} \quad (2.1)$$

The choice of basis vectors is not unique, as illustrated in Fig. 2.2, where both sets of vectors generate the same square lattice.

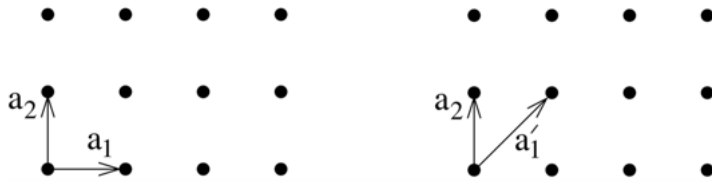


Figure 2.2 Illustration of two different sets of basis vectors generating the same square lattice. Adapted from [16].

A primitive unit cell is a region of space that contains a single lattice point and, when translated by the primitive lattice vectors \mathbf{a}_i , tessellates the space. This means that when many such identical regions are stacked together, they completely fill all of space, reconstructing the lattice. Primitive unit cells are also not unique. As an example, let's look again at the 2-dimensional square lattice in Fig. 2.3.

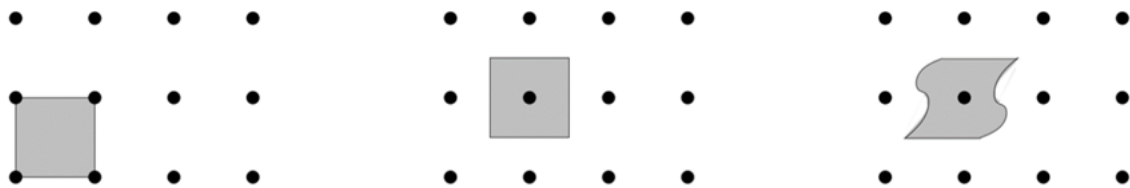


Figure 2.3 Different choices of primitive unit cells. Adapted from [16].

Within a fundamental cell Ω , points relative to a lattice site are referenced by the set of vectors:

$$\Omega = \left\{ \mathbf{d} = m_1 \mathbf{a}_1 + m_2 \mathbf{a}_2 \mid (m_1, m_2)^T \in [0, 1)^2 \right\}. \quad (2.2)$$

Not all atomic lattices of interest are Bravais lattices. However, the framework is applicable by decomposing the lattice into repeating groups of atoms, where each group sits on an underlying Bravais lattice Λ (Fig 2.4). The resulting unit cell consists of several atomic constituents displaced from a vertex by vectors \mathbf{d}_i , defining the so-called basis. The entire lattice is then described by the union of the Bravais lattice and the basis $\cup_i \{\Lambda + \mathbf{d}_i\}$ [16].

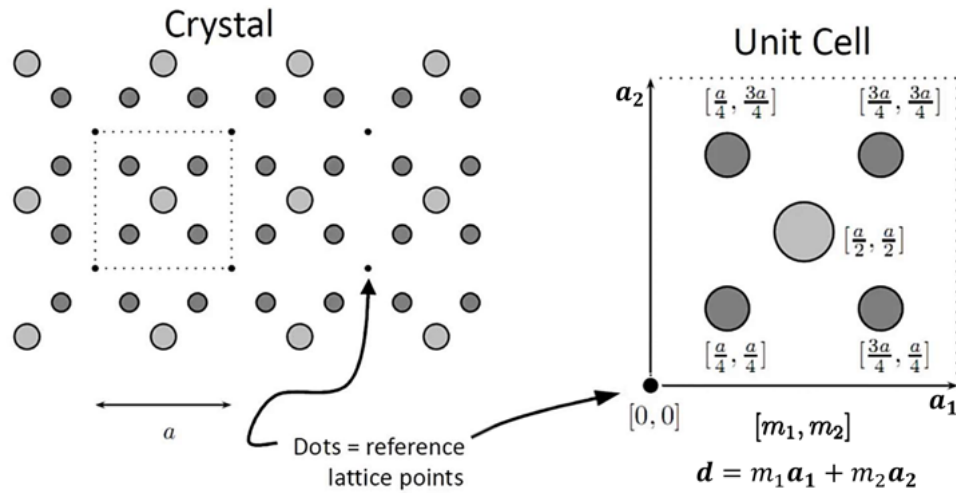


Figure 2.4 Inner structure of a unit cell, where $[m_1, m_2]$ are the relative positions of the atomic constituents in terms of the basis vectors. Adapted from [17].

2.1.2 The Reciprocal Lattice

Given a 2D Bravais lattice Λ , defined by primitive vectors \mathbf{a}_i , the reciprocal lattice Λ^* is defined by the set of points [16]

$$\Lambda^* = \left\{ \mathbf{G} = l_1 \mathbf{b}_1 + l_2 \mathbf{b}_2 \mid (l_1, l_2)^T \in \mathbb{Z}^2 \right\}, \quad (2.3)$$

where the reciprocal lattice vectors \mathbf{b}_i satisfy

$$\mathbf{a}_i \cdot \mathbf{b}_j = 2\pi \delta_{ij}. \quad (2.4)$$

This condition can also be stated as

$$e^{i\mathbf{G}\cdot\mathbf{r}} = 1 \quad \forall \mathbf{r} \in \Lambda, \mathbf{G} \in \Lambda^*. \quad (2.5)$$

Due to the periodic structure in reciprocal space (\mathbf{k} -space), it is possible to define a unit cell known as the Brillouin zone (BZ). The first Brillouin zone Ω^* is the unit cell centered around the point $\mathbf{k} = \mathbf{0}$, defined as

$$\Omega^* = \left\{ \mathbf{k} = h_1 \mathbf{b}_1 + h_2 \mathbf{b}_2 \mid (h_1, h_2)^T \in [0, 1)^2 \right\}. \quad (2.6)$$

States in reciprocal space that are related by reciprocal lattice vectors \mathbf{G} are indistinguishable, meaning all information is contained within Ω^* . Additionally, several points within the BZ are related by symmetry and are thus indistinguishable; these are the high symmetry points, illustrated in Fig. 2.5.

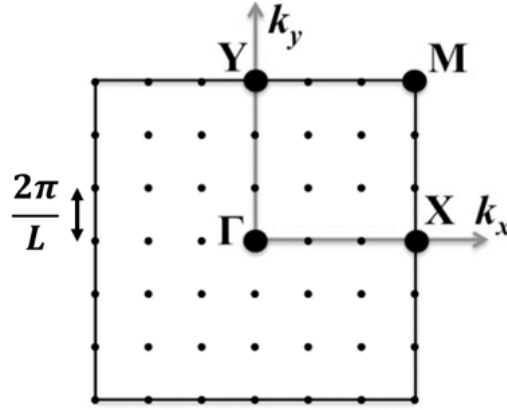


Figure 2.5 Brillouin zone of a square lattice with high symmetry points Γ , M , and X . Adapted from [18].

For a finite two-dimensional sample with length L and applying the Born-von Kármán boundary condition [19], the number of possible \mathbf{k} -components is

$$k_i = \frac{2\pi}{L} m_i, \quad i \in \{x, y\}, m_i \in \mathbb{Z}. \quad (2.7)$$

The local density of \mathbf{k} -states of an $L \times L$ sample per unit area per \mathbf{k} -space element is therefore

$$\rho(\mathbf{k}) = \frac{g}{L^2} \left(\frac{2\pi}{L} \right)^{-2} = \frac{g}{(2\pi)^2}, \quad (2.8)$$

where g accounts for the degeneracy of each state.

2.2 Band Structure

Now that we have established the terminology for describing periodic structures, we can proceed to understand how electrons behave when moving in the presence of a fixed lattice

2.2.1 Bloch's Theorem

“When I started to think about it, I felt that the main problem was to explain how the electrons could sneak by all the ions in a metal.... I found to my delight that the wave differed from a plane wave of free electron only by a periodic modulation. This was so simple that I didn't think it could be much of a discovery, but when I showed it to Heisenberg he said right away, ‘That's it.’”

Felix Bloch

Consider an electron moving in a potential $V(\mathbf{x})$ which has the periodicity of a Bravais lattice Λ ,

$$V(\mathbf{x} + \mathbf{r}) = V(\mathbf{x}) \quad \forall \mathbf{r} \in \Lambda \quad (2.9)$$

Bloch's theorem states that the energy eigenstates (Fig. 2.6) take the form

$$\psi_{\mathbf{k}}(\mathbf{x}) = e^{i\mathbf{k}\cdot\mathbf{x}} u_{\mathbf{k}}(\mathbf{x}) \quad (2.10)$$

where $u_{\mathbf{k}}(\mathbf{x})$ has the same periodicity as the lattice,

$$u_{\mathbf{k}}(\mathbf{x} + \mathbf{r}) = u_{\mathbf{k}}(\mathbf{x}) \quad \forall \mathbf{r} \in \Lambda. \quad (2.11)$$

The energy eigenstates are labeled by the wavevector $\mathbf{k} \in \Omega^*$, called the crystal momentum [16].

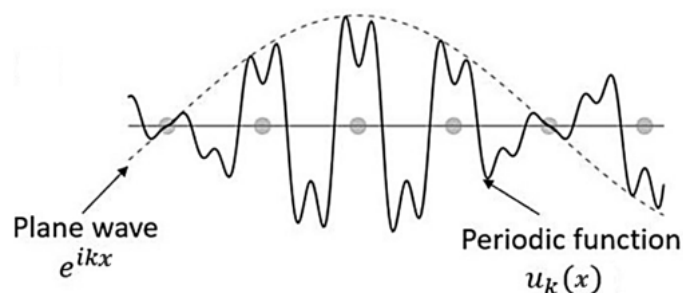


Figure 2.6 Bloch wave, consisting of a periodic function modulated by a plane wave. Adapted from [20].

2.2.2 Tight Binding Model

In this section, we introduce the tight-binding method, a theoretical framework widely employed to compute the electronic band structure of crystalline materials. This approach effectively breaks down the complex quantum dynamics of electrons into a manageable set of localized atomic interactions, known as hopping terms γ , which encapsulate the strength of electron transfers between neighboring atomic sites.

We begin with the Hamiltonian that governs the motion of electrons within a periodic lattice potential:

$$H = \frac{\mathbf{p}^2}{2m} + V_{\text{lattice}}(\mathbf{x}), \quad (2.12)$$

where \mathbf{p} denotes the momentum operator, m is the electron mass, and $V_{\text{lattice}}(\mathbf{x})$ represents the periodic potential generated by the underlying lattice structure [16].

Due to the periodic nature of $V_{\text{lattice}}(\mathbf{x})$, the eigenstates of H exhibit Bloch form. However, the specific functional form of $u_{\mathbf{k}}(\mathbf{x})$ depends intricately on the internal configuration of a unit cell, a detail that varies between different materials and will be elucidated for graphene based systems in subsequent sections.

To proceed, we define an arbitrary basis of electronic states $\{|\mathbf{r}, n\rangle\}$ localized in a unit cell at $\mathbf{r} \in \Lambda$, where $n \in \{1, \dots, N\}$. They span the Hilbert space $\mathcal{H} := \ell^2(\mathbb{Z}^2; \mathbb{C}^N)$, which encompasses all possible electronic configurations within the lattice. We decompose the complete wavefunction at lattice site \mathbf{r} as a linear combination weighted with coefficients c_n :

$$|u(\mathbf{r})\rangle = \sum_n c_n |\mathbf{r}, n\rangle. \quad (2.13)$$

We write wavefunctions in the Bloch domain $L^2(\Omega^*; \mathbb{C}^N)$ as $|\mathbf{k}\rangle$, where $\mathbf{k} \in \Omega^*$. The unitary Bloch transform $\mathcal{H} \rightarrow L^2(\Omega^*; \mathbb{C}^N)$ is given by

$$|\mathbf{k}\rangle = \frac{1}{\sqrt{\tilde{N}}} \sum_{\mathbf{r} \in \Lambda} e^{i\mathbf{k} \cdot \mathbf{r}} |u(\mathbf{r})\rangle = \frac{1}{\sqrt{\tilde{N}}} \sum_{\mathbf{r} \in \Lambda} e^{i\mathbf{k} \cdot \mathbf{r}} \sum_n c_n |\mathbf{r}, n\rangle, \quad (2.14)$$

where \tilde{N} is the number of lattice sites. For convenience, we write the Bloch state as

$$|\mathbf{k}\rangle = \sum_n c_n |\mathbf{k}, n\rangle, \quad |\mathbf{k}, n\rangle = \frac{1}{\sqrt{\tilde{N}}} \sum_{\mathbf{r} \in \Lambda} e^{i\mathbf{k} \cdot \mathbf{r}} |\mathbf{r}, n\rangle. \quad (2.15)$$

We interpret c_n as the contribution from a sublattice consisting only of n -type or-

bitals. The expected energy is then given by

$$E(\mathbf{k}) = \frac{\langle \mathbf{k} | H | \mathbf{k} \rangle}{\langle \mathbf{k} | \mathbf{k} \rangle}. \quad (2.16)$$

First, consider the denominator:

$$\langle \mathbf{k} | \mathbf{k} \rangle = \frac{1}{\tilde{N}} \sum_{\mathbf{r}, \mathbf{r}' \in \Lambda} e^{i\mathbf{k} \cdot (\mathbf{r} - \mathbf{r}')} \sum_{n, n'} c_{n'}^* c_n \langle \mathbf{r}', n' | \mathbf{r}, n \rangle = \frac{1}{\tilde{N}} \sum_{\mathbf{r}, \mathbf{r}' \in \Lambda} e^{-i\mathbf{k} \cdot (\mathbf{r}' - \mathbf{r})} \sum_{n, n'} c_{n'}^* \alpha_{n', n}(\mathbf{r}', \mathbf{r}) c_n, \quad (2.17)$$

where $\alpha_{n', n}(\mathbf{r}', \mathbf{r}) = \langle \mathbf{r}', n' | \mathbf{r}, n \rangle$ measures the overlap of the n -th state localized at lattice site \mathbf{r} and the n' -th state localized at \mathbf{r}' . Assuming that the coupling term to only depend on the relative distance between lattice sites $\Delta \mathbf{r} = \mathbf{r}' - \mathbf{r}$ (two point approximation) and since by definition $\Delta \mathbf{r} \in \Lambda$, we can write

$$\langle \mathbf{k} | \mathbf{k} \rangle = \frac{1}{\tilde{N}} \sum_{\mathbf{r}, \mathbf{r}' \in \Lambda} e^{-i\mathbf{k} \cdot (\mathbf{r}' - \mathbf{r})} \sum_{n, n'} c_{n'}^* \alpha_{n', n}(\mathbf{r}' - \mathbf{r}) c_n = \frac{1}{\tilde{N}} \sum_{\Delta \mathbf{r} \in \Lambda} e^{-i\mathbf{k} \cdot \Delta \mathbf{r}} \sum_{n, n'} c_{n'}^* \alpha_{n', n}(\Delta \mathbf{r}) c_n. \quad (2.18)$$

Applying the same procedure for the numerator results in

$$\langle \mathbf{k} | H | \mathbf{k} \rangle = \frac{1}{\tilde{N}} \sum_{\mathbf{r}, \mathbf{r}' \in \Lambda} e^{i\mathbf{k} \cdot (\mathbf{r} - \mathbf{r}')} \sum_{n, n'} c_{n'}^* c_n \langle \mathbf{r}', n' | H | \mathbf{r}, n \rangle = \frac{1}{\tilde{N}} \sum_{\Delta \mathbf{r} \in \Lambda} e^{-i\mathbf{k} \cdot \Delta \mathbf{r}} \sum_{n, n'} c_{n'}^* \gamma_{n', n}(\Delta \mathbf{r}) c_n, \quad (2.19)$$

where we introduced the hopping parameters $\gamma_{n', n}(\Delta \mathbf{r})$, which characterize the strength of the transition from an n state to an n' state with relative distance $\Delta \mathbf{r}$ of the respective lattice site (Fig. 2.7) [16].

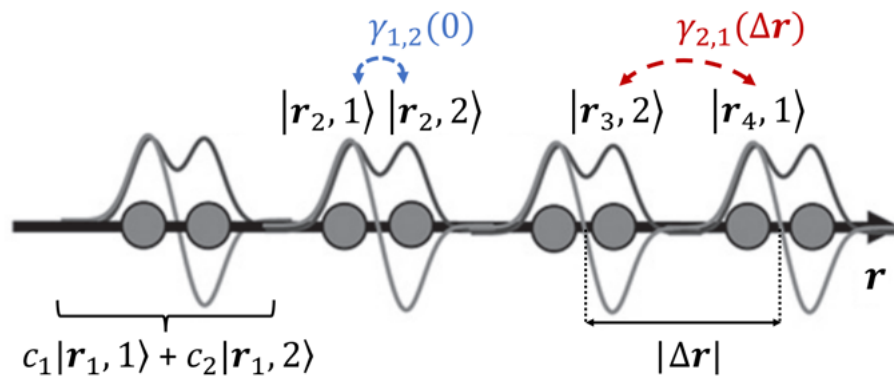


Figure 2.7 Hopping terms in 1D crystal with two-atomic basis. Adapted from [21].

We determine the coefficients $\{c_n\}$ by a variational ansatz. To find the ground state, we minimize $E(\mathbf{k})$ with respect to all c_n . Accordingly, we solve

$$\frac{\partial E(\mathbf{k})}{\partial c_{n'}^*} = \frac{1}{\langle \mathbf{k} | \mathbf{k} \rangle} \frac{\partial}{\partial c_{n'}^*} \langle \mathbf{k} | H | \mathbf{k} \rangle - \frac{\langle \mathbf{k} | H | \mathbf{k} \rangle}{\langle \mathbf{k} | \mathbf{k} \rangle^2} \frac{\partial}{\partial c_{n'}^*} \langle \mathbf{k} | \mathbf{k} \rangle = 0, \quad (2.20)$$

which simplifies to

$$\frac{\partial}{\partial c_{n'}^*} \langle \mathbf{k} | H | \mathbf{k} \rangle - E(\mathbf{k}) \frac{\partial}{\partial c_{n'}^*} \langle \mathbf{k} | \mathbf{k} \rangle = 0. \quad (2.21)$$

Inserting the expressions for $\langle \mathbf{k} | H | \mathbf{k} \rangle$ and $\langle \mathbf{k} | \mathbf{k} \rangle$ leads to the secular equation

$$\sum_{\Delta \mathbf{r} \in \Lambda} e^{-i\mathbf{k} \cdot \Delta \mathbf{r}} \sum_n [\gamma_{n',n}(\Delta \mathbf{r}) - E(\mathbf{k}) \alpha_{n',n}(\Delta \mathbf{r})] c_n = 0. \quad (2.22)$$

In the following, we assume that electrons are "tightly bound" to their orbital centers and neglect the overlap with neighboring states. Thus, $\alpha_{n',n}(\Delta \mathbf{r}) = \delta_{n',n} \delta(\Delta \mathbf{r})$. Moreover $\gamma_{n',n}(\Delta \mathbf{r})$ decays with increasing $\Delta \mathbf{r}$, so only a set of vectors pointing to near sites $\{\boldsymbol{\delta}_i\}$ needs to be considered. This simplifies the equation to

$$\sum_i e^{-i\mathbf{k} \cdot \boldsymbol{\delta}_i} \sum_n \gamma_{n',n}(\boldsymbol{\delta}_i) c_n = E(\mathbf{k}) c_{n'}. \quad (2.23)$$

The resulting expression is an eigenvalue problem with the tight-binding Hamiltonian $H(\mathbf{k})$, defined by [16]

$$H_{n',n}(\mathbf{k}) = \sum_i e^{-i\mathbf{k} \cdot \boldsymbol{\delta}_i} \gamma_{n',n}(\boldsymbol{\delta}_i). \quad (2.24)$$

In matrix form, if we include N localized states at each site, $H(\mathbf{k})$ becomes an $N \times N$ matrix:

$$\begin{bmatrix} H_{1,1} & \cdots & H_{1,N} \\ \vdots & \ddots & \vdots \\ H_{N,1} & \cdots & H_{N,N} \end{bmatrix} = \begin{bmatrix} \sum_i e^{-i\mathbf{k} \cdot \boldsymbol{\delta}_i} \gamma_{1,1}(\boldsymbol{\delta}_i) & \cdots & \sum_i e^{-i\mathbf{k} \cdot \boldsymbol{\delta}_i} \gamma_{1,N}(\boldsymbol{\delta}_i) \\ \vdots & \ddots & \vdots \\ \sum_i e^{-i\mathbf{k} \cdot \boldsymbol{\delta}_i} \gamma_{N,1}(\boldsymbol{\delta}_i) & \cdots & \sum_i e^{-i\mathbf{k} \cdot \boldsymbol{\delta}_i} \gamma_{N,N}(\boldsymbol{\delta}_i) \end{bmatrix}. \quad (2.25)$$

The matrix equation reads as

$$\begin{bmatrix} H_{1,1} & \cdots & H_{1,N} \\ \vdots & \ddots & \vdots \\ H_{N,1} & \cdots & H_{N,N} \end{bmatrix} \begin{bmatrix} c_1 \\ \vdots \\ c_N \end{bmatrix} = E(\mathbf{k}) \begin{bmatrix} c_1 \\ \vdots \\ c_N \end{bmatrix}. \quad (2.26)$$

The resulting functions $E(\mathbf{k}) : \Omega^* \rightarrow \mathbb{R}$ are known as the Bloch band functions, defining the energy of an electron occupying the state $|\mathbf{k}\rangle$ [22].

2.2.3 Density of States and Material Classes

”I first heard of this when Fowler was explaining it to one of Rutherford’s closest collaborators, who said ‘very interesting’ in a tone which implied that he was not interested at all. Neither was I.”

Nevil Mott,

recollecting the glorious moment he first learned
of the difference between metals and insulators.

In the context of 2D-materials, the density of states (DOS) describes the number of states per unit surface per unit energy. It is defined as follows [23]:

$$DOS(E) = \frac{1}{A} \sum_{\mathbf{k}} \delta(E - E(\mathbf{k})), \quad (2.27)$$

where A denotes the surface area, and the summation extends over all \mathbf{k} -states within the BZ.

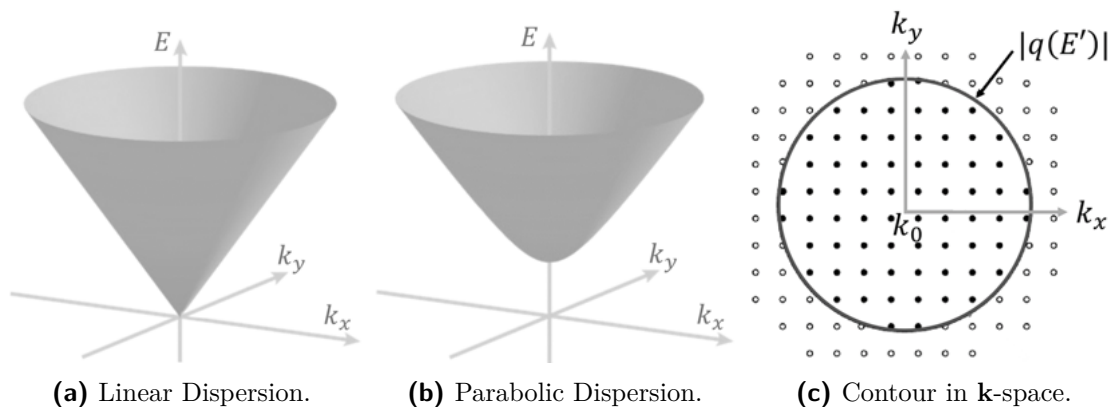


Figure 2.8 Illustrations of typical dispersion relations in E - \mathbf{k} -space. Adapted from [24].

Typically, one is interested in the behavior of the DOS near special points where the bands exhibit a minimum or maximum. Figure 2.8a depicts the case of a linear

dispersion, while Fig. 2.8b illustrates the parabolic case. In both instances, we assume rotational symmetry for the low-energy regime, such that the band structure $E(\mathbf{k})$ can be locally approximated around the extremal point \mathbf{k}_0 by:

$$E(\mathbf{k}) = E_0 + \hbar v_F |\mathbf{k} - \mathbf{k}_0| + \frac{\hbar^2}{2m^*} |\mathbf{k} - \mathbf{k}_0|^2 + \mathcal{O}(|\mathbf{k} - \mathbf{k}_0|^3), \quad (2.28)$$

where $E_0 = E(\mathbf{k}_0)$, $v_F = \frac{1}{\hbar} \partial_{\mathbf{k}} E(\mathbf{k}) \Big|_{\mathbf{k}=\mathbf{k}_0}$, and $m^* = \frac{\hbar^2}{\partial_{\mathbf{k}}^2 E(\mathbf{k}) \Big|_{\mathbf{k}=\mathbf{k}_0}}$.

For subsequent analysis, we neglect the constant term E_0 and define $\mathbf{q} = \mathbf{k} - \mathbf{k}_0$. Consequently, fig. 2.8a can be approximated to first order by $E(\mathbf{q}) = \hbar v_F |\mathbf{q}|$. For fig. 2.8b, the lowest non-vanishing order is quadratic, thus characterized by $E(\mathbf{q}) = \frac{\hbar^2 |\mathbf{q}|^2}{2m^*}$.

These approximations enable the determination of the DOS in the low-energy regime. Notably, due to rotational symmetry, all states with the same energy E' lie on a circle with radius $q' = |\mathbf{q}(E')|$ (fig. 2.8c). The total number of states below an energy E' can be expressed as:

$$\sum_{|\mathbf{q}| < q'} = \int_0^{q'} 2\pi |\mathbf{q}| \rho(\mathbf{q}) d|\mathbf{q}| = \int_0^{E'} 2\pi |\mathbf{q}| \rho(\mathbf{q}) \frac{\partial |\mathbf{q}|}{\partial E} dE = \int_0^{E'} DOS(E) dE, \quad (2.29)$$

where $\rho(\mathbf{q})$ results from the discrete structure of \mathbf{k} -space (eq. 2.8). For a linear dispersion $|\mathbf{q}(E)| = \frac{|E|}{\hbar v_F}$:

$$DOS(E) = 2\pi \frac{E}{\hbar v_F} \frac{g}{(2\pi)^2} \frac{\partial}{\partial E} \left(\frac{E}{\hbar v_F} \right) = \frac{gE}{2\pi \hbar^2 v_F^2}. \quad (2.30)$$

For a parabolic dispersion $|\mathbf{q}(E)| = \frac{\sqrt{2m^*|E|}}{\hbar}$:

$$DOS(E) = 2\pi \frac{\sqrt{2m^*E}}{\hbar} \frac{g}{(2\pi)^2} \frac{\partial}{\partial E} \left(\frac{\sqrt{2m^*E}}{\hbar} \right) = \frac{gm^*}{2\pi \hbar^2}. \quad (2.31)$$

The DOS allows for the classification of solids into four categories: metals, semi-metals, semiconductors, and insulators [19]. The critical factor is the position of the Fermi level E_F , which represents the energy of the highest occupied state at $T = 0$. Figure 2.9 illustrates the different cases.

Metals feature a large $DOS(E_F)$, with E_F lying within a band, which is hence partially filled. In contrast, semi-metals are distinguished from metals by having a negligible density of states at the Fermi level.

If $DOS(E) = 0$ around the Fermi level, no free states are available, implying that

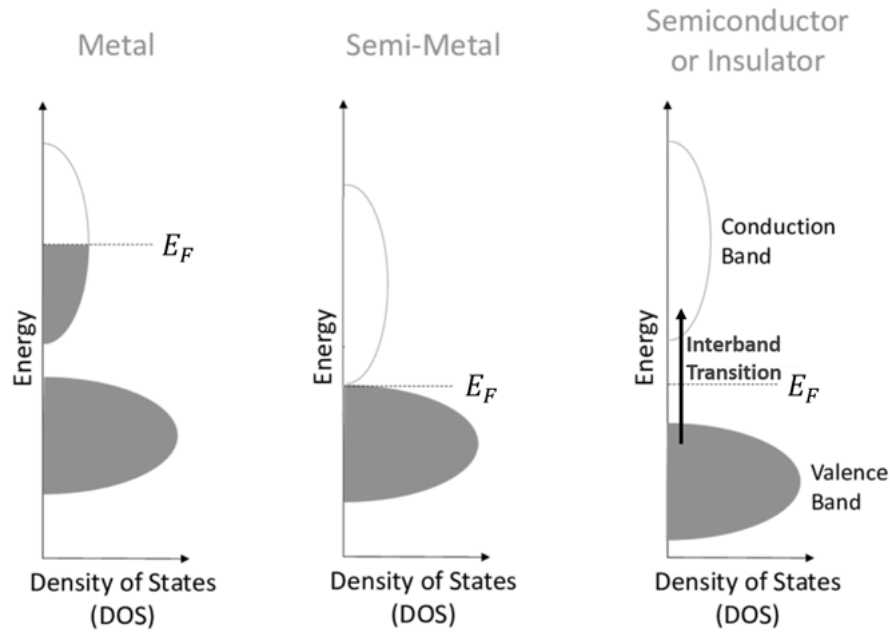


Figure 2.9 Electronic Structure of Solids. Adapted from [25].

E_F lies between two bands, within a so-called band gap of size E_G . At $T = 0K$, all states of the lower band (valence band) are completely occupied with electrons, while the band above (conduction band) is empty. Such materials are classified as insulators ($E_G > 4eV$) or semiconductors ($E_G < 4eV$) [24].

Electrons in a fully filled band cannot carry any current [19]. Thus, excitation of electrons from the valence band to the conduction band is required to enable charge transport. The transition of an electron into an empty conduction band state creates a vacancy in the valence band. This so-called hole can be treated as a positively charged quasi-particle moving through the solid with the opposite wave vector $\mathbf{k}_h = -\mathbf{k}_e$ of the removed electron.

2.3 From Carbon to Graphene

“Graphene consists of a single molecular layer of carbon atoms tightly bonded to form an ultra-thin, ultra-durable sheet. It is almost transparent and weighs practically nothing, yet is the toughest material known to science – two hundred times stronger than steel and stronger even than diamonds. In principle, you could balance an elephant on a pencil and then place the pencil point on a sheet of graphene without breaking or tearing it. As a bonus, graphene also conducts electricity.”

Michio Kaku

2.3.1 The Carbon Atom

Figure 2.10 Carbon in the periodic table. Adapted from [26].

Carbon, with an atomic number of 6, has six electrons. Neglecting electron-electron interaction, the single-particle Hamiltonian H on $\mathcal{H} := \ell^2(\mathbb{C}^N)$ and the corresponding eigenvalue problem of the free carbon atom are defined as follows:

$$H = \frac{\mathbf{p}^2}{2m} + V_{\text{ion}}(\mathbf{x}), \quad H |n\rangle = E_n |n\rangle,$$

where V_{ion} describes the attractive interaction of an electron with the positively charged core, and $\{|n\rangle\}$ with $n \in \{1, \dots, N\}$ is the set of eigenstates, e.g., atomic orbitals.

Due to the spherical symmetry of the atomic potential, the orbital function can be separated into the radial and angular parts. The latter can be represented

by the spherical harmonics $Y_{l,m}(\vartheta, \varphi)$, which are labeled by the angular momentum $l \in \{s, p, d, \dots\} := \{0, 1, 2, \dots\}$ and the magnetic quantum number m . The angular

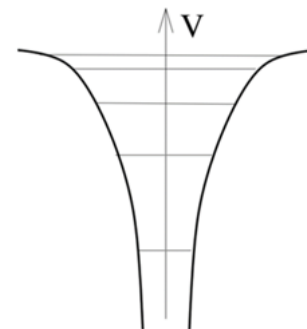


Figure 2.11 Potential V . Adapted from [16].

dependence of the s and p orbitals is given by:

$$Y_{0,0}(\vartheta, \varphi) = \frac{1}{\sqrt{4\pi}}, \quad (2.32)$$

$$Y_{1,0}(\vartheta, \varphi) = i\sqrt{\frac{3}{4\pi}} \cos \vartheta, \quad (2.33)$$

$$Y_{1,\pm 1}(\vartheta, \varphi) = \mp i\sqrt{\frac{3}{8\pi}} \sin \vartheta \exp(\mp i\varphi), \quad (2.34)$$

where ϑ and φ are polar angles. Rather than taking $Y_{l,m}(\vartheta, \varphi)$ as basis functions for the p -orbitals, it is more convenient to choose their orthonormalized linear combinations:

$$\frac{i}{\sqrt{2}} [Y_{1,1}(\vartheta, \varphi) - Y_{1,-1}(\vartheta, \varphi)] = \sqrt{\frac{3}{4\pi}} \sin \vartheta \cos \varphi, \quad (2.35)$$

$$\frac{i}{\sqrt{2}} [Y_{1,1}(\vartheta, \varphi) + Y_{1,-1}(\vartheta, \varphi)] = \sqrt{\frac{3}{4\pi}} \sin \vartheta \sin \varphi, \quad (2.36)$$

$$-iY_{1,0}(\vartheta, \varphi) = \sqrt{\frac{3}{4\pi}} \cos \vartheta, \quad (2.37)$$

which define representations of the states $|p_x\rangle$, $|p_y\rangle$, and $|p_z\rangle$ [23]. The orbitals of the second shell are visualized in fig. 2.12. The $2s$ orbital remains completely spherical symmetric, while the $2p$ orbitals are asymmetrical with respect to the nodal plane and rotationally symmetrical along their corresponding alignment axis. Successive filling of the eigenstates results in the electronic configuration for the ground state shown in fig. 2.15a. The $1s$ and $2s$ orbitals are completely filled, whereas two of the $2p$ orbitals are each occupied by only one electron.

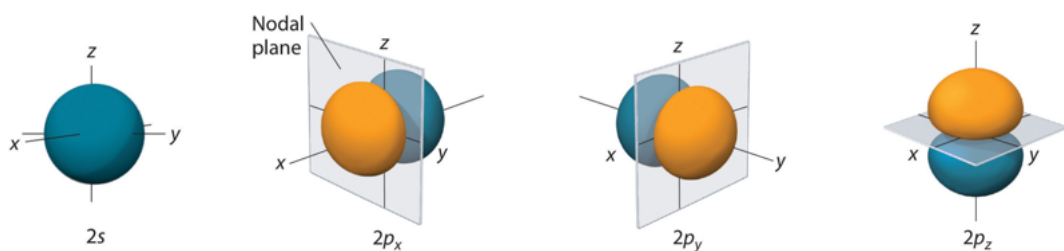


Figure 2.12 Orbital Shapes of the Second Shell. Adapted from [27].

2.3.2 From Atoms to Crystals

When many atoms come together, they can form a crystal lattice, within which each atom is surrounded by other atoms interacting through their respective Coulomb potentials. To account for this emerging crystal field, the potentials of all surround-

ing ion nuclei must be included in the energy term. For a general lattice, we can write:

$$V_{\text{crystal}}(\mathbf{x}) = \sum_{\mathbf{r} \in \Lambda} \sum_m V_{\text{ion}}^m(\mathbf{x} - \mathbf{r}), \quad (2.38)$$

where \mathbf{r} defines the lattice site of a unit cell and m indexes the contribution of all ions within (Fig. 2.13).

To get the new eigenstates, we would have to solve the corresponding new eigenvalue problem. However, with a few assumptions, the rough charge distribution can be surmised without explicitly solving the eigenvalue equation.

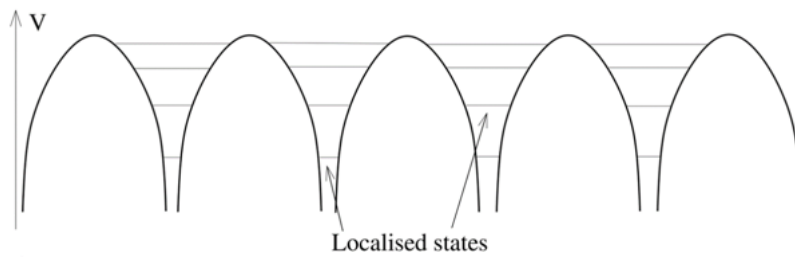


Figure 2.13 Crystal lattice potential composed of several atomic potentials. Adapted from [16].

Hybridization describes this construction of new basis states from the superposition of the eigenstates of the unperturbed Hamiltonian. First, we assume that the crystal field is not so strong that energy states of different shells would be mixed. Consequently, the new base states should be composed of the 2s and 2p orbitals of the second shell. On the other hand, the overlap of neighboring wave functions should be maximized. This allows the formation of molecular orbitals spread over the whole molecule, thereby increasingly delocalizing electrons, which reduces the kinetic energy. This leads to the formation of covalent bonds, which lower the ground state energy compared to a loose group of carbon atoms.

These assumptions motivate the following ansatz for the new set of hybrid orbitals:

$$|sp_1^2\rangle = \frac{1}{\sqrt{3}} |2s\rangle - \sqrt{\frac{2}{3}} |2p_y\rangle, \quad (2.39)$$

$$|sp_2^2\rangle = \frac{1}{\sqrt{3}} |2s\rangle + \sqrt{\frac{2}{3}} \left(\frac{\sqrt{3}}{2} |2p_x\rangle + \frac{1}{2} |2p_y\rangle \right), \quad (2.40)$$

$$|sp_3^2\rangle = -\frac{1}{\sqrt{3}} |2s\rangle + \sqrt{\frac{2}{3}} \left(-\frac{\sqrt{3}}{2} |2p_x\rangle + \frac{1}{2} |2p_y\rangle \right), \quad (2.41)$$

Here, we mixed the 2s-orbital and two 2p-orbitals, a method known as sp^2 -hybridization [23]. The resulting hybrid orbitals are shown in Fig. 2.14.

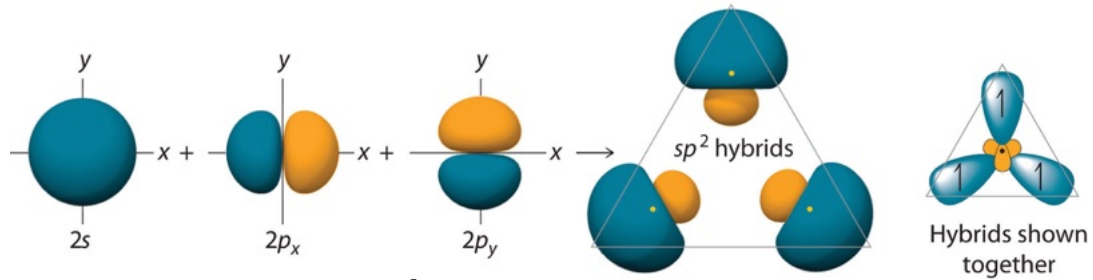


Figure 2.14 sp^2 -hybrid orbitals. Adapted from [27].

The charge density of the sp^2 -hybrids is now concentrated much further away from the nucleus, which maximizes the overlap of the wave functions with those of neighboring atoms. The corresponding maxima lie in the xy -plane and are separated from each other by angles of 120 degrees. This leaves us with the remaining p_z orbitals, which do not participate in the hybridization process and point out of the plane. This results in a new electronic configuration depicted in fig. 2.15b.

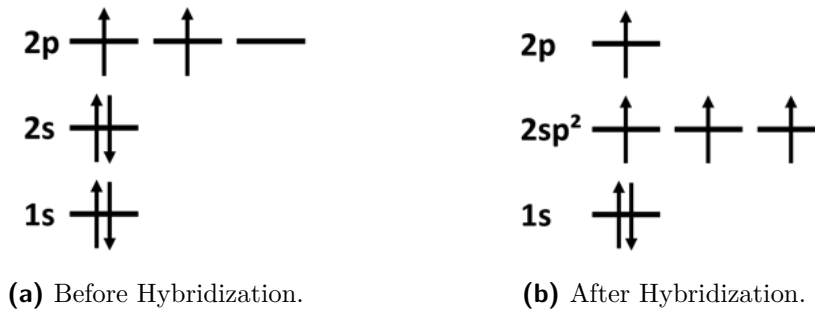


Figure 2.15 Orbital Configuration.

Due to these inter-atomic interactions, carbon atoms can form the energetically favorable lattice configuration shown in Fig. 2.16a. This is the hexagonal crystal structure of graphene, also known as the honeycomb structure. The sp^2 -hybrids substantially overlap and form strong σ -bonds. The resulting large binding energy gained during the formation of a covalent bond gives rise to the ultra-strong mechanical properties of the graphene lattice (Fig. 2.16b).

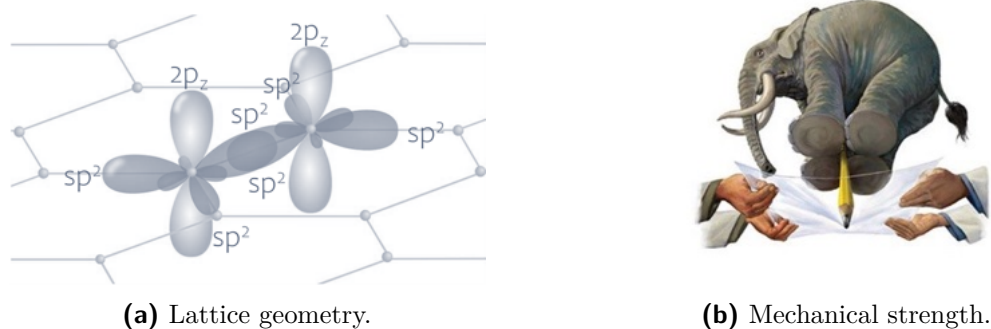


Figure 2.16 Origin of the mechanical properties. Adapted from [28] [29].

2.4 Monolayer Graphene

Our qualitative analysis has led to the conclusion that the pronounced anisotropy of the σ -orbitals is responsible for the formation of the hexagonal lattice structure, whereas the π -orbitals play a pivotal role in determining the electronic properties of graphene. In the subsequent sections, we will employ the methodologies we have developed to provide a quantitative description of both the crystal structure and the electronic properties of graphene.

2.4.1 Crystal Structure

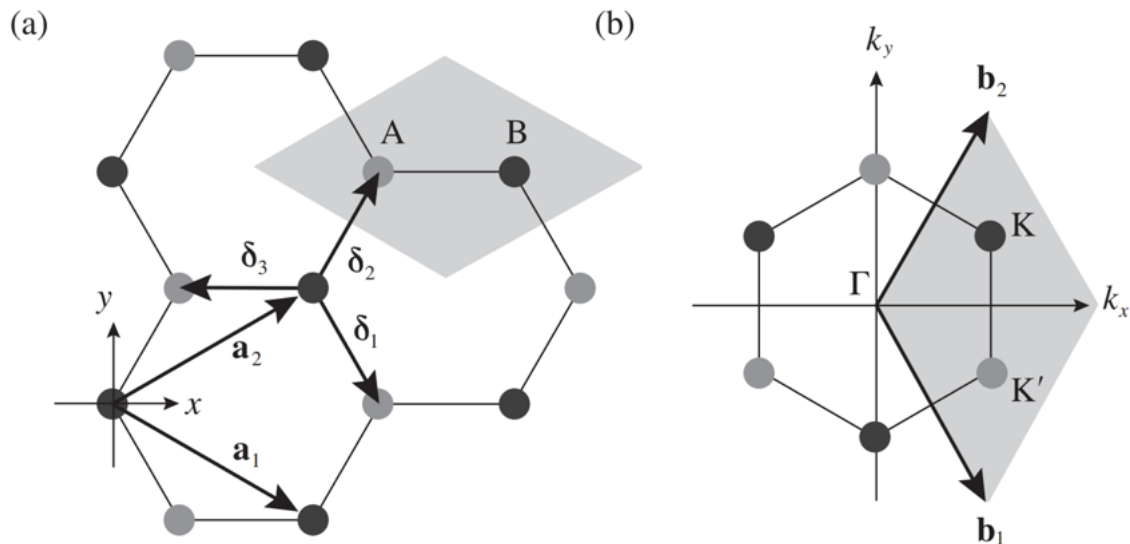


Figure 2.17 (a) Real-space honeycomb graphene lattice. The lattice consists of two overlapping Bravais sublattices, A (gray dots) and B (black dots). The primitive unit cell is drawn as a shaded area. \mathbf{a}_1 and \mathbf{a}_2 are the primitive lattice vectors. δ_1 , δ_2 , and δ_3 are vectors pointing from a B atom to its nearest A atoms. (b) Reciprocal unit cell of graphene drawn as a shaded area. \mathbf{b}_1 and \mathbf{b}_2 are the primitive vectors of the reciprocal lattice. Dirac points \mathbf{K} (black dots) and \mathbf{K}' (gray dots) are marked. Adapted from [30].

Monolayer graphene (MLG) is a two-dimensional crystal of carbon atoms arranged in a hexagonal structure. The typical carbon-carbon spacing between adjacent atoms is approximately $a = 1.42\text{\AA}$. However, the lattice is not a Bravais lattice because not all points share the same surroundings. To illustrate this, consider a single hexagon from the lattice as shown in Fig. 2.17a. Each of the black points has a neighbor directly to the left and two neighbors diagonally to the right. The gray dots, however, have one neighbor directly to the right and two neighbors diagonally to the left. In fact, this is a trigonal lattice with a diatomic basis, characterized by the primitive lattice vectors [30]

$$\mathbf{a}_1 = \frac{\sqrt{3}a}{2} \begin{bmatrix} \sqrt{3} \\ -1 \end{bmatrix}, \quad \mathbf{a}_2 = \frac{\sqrt{3}a}{2} \begin{bmatrix} \sqrt{3} \\ 1 \end{bmatrix} \quad (2.42)$$

and the basis vectors

$$\mathbf{d}_{\text{black}} = \begin{bmatrix} 0 \\ 0 \end{bmatrix}, \quad \mathbf{d}_{\text{grey}} = \begin{bmatrix} -a \\ 0 \end{bmatrix}. \quad (2.43)$$

As depicted in Fig. 2.17, the black vertices form the triangular sublattice B, while the gray vertices form the displaced sublattice A.

Each lattice ion of a specific sublattice has three nearest neighbors from the other sublattice. Their relative positions from a B-atom are defined by the set of vectors $\{\boldsymbol{\delta}_i\}$ given by

$$\boldsymbol{\delta}_1 = \frac{a}{2} \begin{bmatrix} 1 \\ -\sqrt{3} \end{bmatrix}, \quad \boldsymbol{\delta}_2 = \frac{a}{2} \begin{bmatrix} 1 \\ \sqrt{3} \end{bmatrix}, \quad \boldsymbol{\delta}_3 = \begin{bmatrix} -a \\ 0 \end{bmatrix}. \quad (2.44)$$

The vectors to the six next-nearest neighbors $\{\boldsymbol{\delta}'_i\}$, situated on the same sublattice, are defined by

$$\boldsymbol{\delta}'_1 = \mathbf{a}_1, \quad \boldsymbol{\delta}'_2 = -\mathbf{a}_1, \quad \boldsymbol{\delta}'_3 = \mathbf{a}_2 - \mathbf{a}_1, \quad (2.45)$$

$$\boldsymbol{\delta}'_4 = \mathbf{a}_2, \quad \boldsymbol{\delta}'_5 = -\mathbf{a}_2, \quad \boldsymbol{\delta}'_6 = -(\mathbf{a}_2 - \mathbf{a}_1). \quad (2.46)$$

Besides the evident three-fold rotational symmetry around the center (C_3 -symmetry) and the mirror symmetry with respect to the xy -plane (σ_{xy} -symmetry), it is important to note that even though neighboring carbon atoms occupy symmetrically non-equivalent sites, they are still indistinguishable particles. This grants the graphene crystal inversion symmetry (I -symmetry).

The corresponding reciprocal lattice also forms a hexagonal structure with reciprocal basis vectors [30]

$$\mathbf{b}_1 = \frac{2\pi}{3a} \begin{bmatrix} 1 \\ -\sqrt{3} \end{bmatrix}, \quad \mathbf{b}_2 = \frac{2\pi}{3a} \begin{bmatrix} 1 \\ \sqrt{3} \end{bmatrix}. \quad (2.47)$$

In the following chapter, the corner points of the BZ will play a significant role. Some of these corners are linked by translations via reciprocal lattice vectors, allowing them to be divided into two groups of three equivalent reciprocal lattice points each. Representatives of the two inequivalent points in the Brillouin zone are given by \mathbf{K} and \mathbf{K}' , with the positions:

$$\mathbf{K} = \frac{2\pi}{3\sqrt{3}a} \begin{bmatrix} \sqrt{3} \\ 1 \end{bmatrix}, \quad \mathbf{K}' = \frac{2\pi}{3\sqrt{3}a} \begin{bmatrix} \sqrt{3} \\ -1 \end{bmatrix}. \quad (2.48)$$

The points \mathbf{K} and $-\mathbf{K}'$ differ by the reciprocal lattice vector $\mathbf{G} = \mathbf{b}_1 - \mathbf{b}_2$, so the point \mathbf{K}' is equivalent to $-\mathbf{K}$.

Time-reversal symmetry (T -symmetry) inverts the sign of time and consequently has the effect $\mathbf{k} \rightarrow -\mathbf{k}$. In the same way that sublattices A and B are linked by I -symmetry, T -symmetry maps \mathbf{K} to $-\mathbf{K}$ and therefore to \mathbf{K}' .

2.4.2 Band Structure

In this section, we employ the tight-binding method to explicitly calculate the band structure of graphene. Given that graphene has a two-atomic basis, we use the atomic states of the A-atoms $\{|\mathbf{r}, n_A\rangle\}$ and the B-atoms $\{|\mathbf{r}, n_B\rangle\}$ as our basis.

Following the arguments in Sec. [2.2.2](#), we construct the Bloch state as

$$|\mathbf{k}\rangle = \frac{1}{\sqrt{2N}} \sum_{\mathbf{r} \in \Lambda} e^{i\mathbf{k}\cdot\mathbf{r}} \left(c_A \sum_{n_A} c_{n_A} |\mathbf{r}, n_A\rangle + c_B \sum_{n_B} c_{n_B} |\mathbf{r}, n_B\rangle \right). \quad (2.49)$$

To determine the band structure, we consider the set of all hopping terms $\{\gamma_{n',n}(\Delta\mathbf{r})\}$, which represent the coupling strengths between atomic orbitals. Each carbon atom in the unit cell contributes three sp^2 -orbitals and one p_z -orbital, resulting in eight bands upon solving the eigenvalue problem. However, symmetry considerations allow us to identify decoupled orbitals.

The sp^2 -orbitals are mirror-symmetric with respect to the xy -plane, while the p_z -orbitals are asymmetric, changing the sign of phase. Due to the σ_{xy} -symmetry of the crystal potential, overlap integrals involving a p_z - and an sp^2 -orbital vanish.

Accordingly, these two types of orbitals are decoupled and contribute to different bands.

Furthermore, these two band systems occupy different energy regimes. Strong coupling γ_σ arises from the substantial overlap of the sp^2 -orbitals, leading to significant energy splitting into bonding and antibonding configurations. Consequently, the resulting σ -bands are positioned far from the Fermi level. In contrast, the weaker overlap of p_z orbitals ($\gamma_\pi \ll \gamma_\sigma$) results in π -bands that are situated at lower energies [17].

Given that electronic properties are mainly determined by low energy dynamics near the Fermi level, we focus on the low energy bands emerging from the p_z -orbitals (Fig. 2.18).

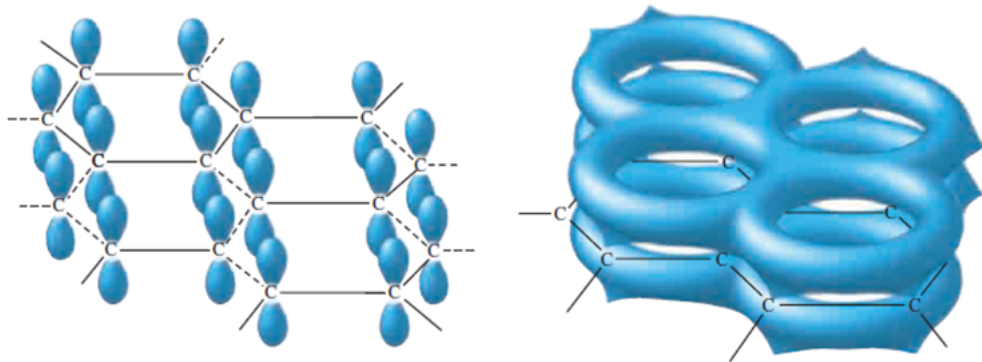


Figure 2.18 Conduction and Valence bands originating from an extensive π -bonding network. Adapted from [31].

We compose the wave functions of electrons in graphene as elements of the Hilbert space $\mathcal{H}_{\text{MLG}} := \ell^2(\mathbb{Z}^2; \mathbb{C}^2)$, comprising the p_z states $\{|\mathbf{r}, A\rangle, |\mathbf{r}, B\rangle\}$ from the A- and B-sublattices at lattice site $\mathbf{r} \in \Lambda$. In the Bloch domain $L^2(\Omega^*; \mathbb{C}^2)$, this is represented as:

$$|\mathbf{k}\rangle = \frac{1}{\sqrt{2}}(|\mathbf{k}, A\rangle + |\mathbf{k}, B\rangle) = \frac{c_A}{\sqrt{2N}} \sum_{\mathbf{r} \in \Lambda} e^{i\mathbf{k} \cdot \mathbf{r}} |\mathbf{r}, A\rangle + \frac{c_B}{\sqrt{2N}} \sum_{\mathbf{r} \in \Lambda} e^{i\mathbf{k} \cdot \mathbf{r}} |\mathbf{r}, B\rangle. \quad (2.50)$$

The tight-binding Hamiltonian matrix elements are given by eq. 2.24, where $n, n' \in \{A, B\}$.

Initially, we consider only the coupling to the three nearest neighbors, resulting in the three non-zero hopping parameters $\gamma_{B,A}(\boldsymbol{\delta}_1)$, $\gamma_{B,A}(\boldsymbol{\delta}_2)$, and $\gamma_{B,A}(\boldsymbol{\delta}_3)$. The Hamiltonian matrix then becomes:

$$H = \begin{bmatrix} \gamma_{A,A}(0) & \sum_i \gamma_{A,B}(-\boldsymbol{\delta}_i) e^{i\mathbf{k}\cdot\boldsymbol{\delta}_i} \\ \sum_i \gamma_{B,A}(\boldsymbol{\delta}_i) e^{-i\mathbf{k}\cdot\boldsymbol{\delta}_i} & \gamma_{B,B}(0) \end{bmatrix} \quad (2.51)$$

Due to graphene's inversion symmetry (I -symmetry), we can set $\gamma_{A,A}(0) = \gamma_{B,B}(0) = 0$. The C_3 -symmetry enforces the equivalence of all three hopping processes, so $\gamma_{B,A}(\boldsymbol{\delta}_i) = \gamma_{A,B}(-\boldsymbol{\delta}_j)$ for $i, j \in \{1, 2, 3\}$. Thus, the eigenvalue problem is:

$$\begin{bmatrix} 0 & -\gamma_0 f(\mathbf{k}) \\ -\gamma_0 f(\mathbf{k})^* & 0 \end{bmatrix} \begin{bmatrix} c_1 \\ c_2 \end{bmatrix} = E(\mathbf{k}) \begin{bmatrix} c_1 \\ c_2 \end{bmatrix}, \quad (2.52)$$

where the tight-binding parameter is defined as [32]:

$$\gamma_0 = -\langle A|H|B \rangle = -\langle B|H|A \rangle \approx 3eV, \quad (2.53)$$

and the function $f(\mathbf{k})$ describing phase accumulation is evaluated as:

$$f(\mathbf{k}) = \sum_i e^{i\mathbf{k}\cdot\boldsymbol{\delta}_i} \quad (2.54)$$

$$= e^{i\mathbf{k}\cdot\boldsymbol{\delta}_1} + e^{i\mathbf{k}\cdot\boldsymbol{\delta}_2} + e^{i\mathbf{k}\cdot\boldsymbol{\delta}_3} \quad (2.55)$$

$$= 1 + e^{i\mathbf{k}\cdot\mathbf{a}_1} + e^{i\mathbf{k}\cdot\mathbf{a}_2}. \quad (2.56)$$

The energy eigenvalues are:

$$E(\mathbf{k}) = \pm |\gamma_0 f(\mathbf{k})|, \quad (2.57)$$

which can be expressed as:

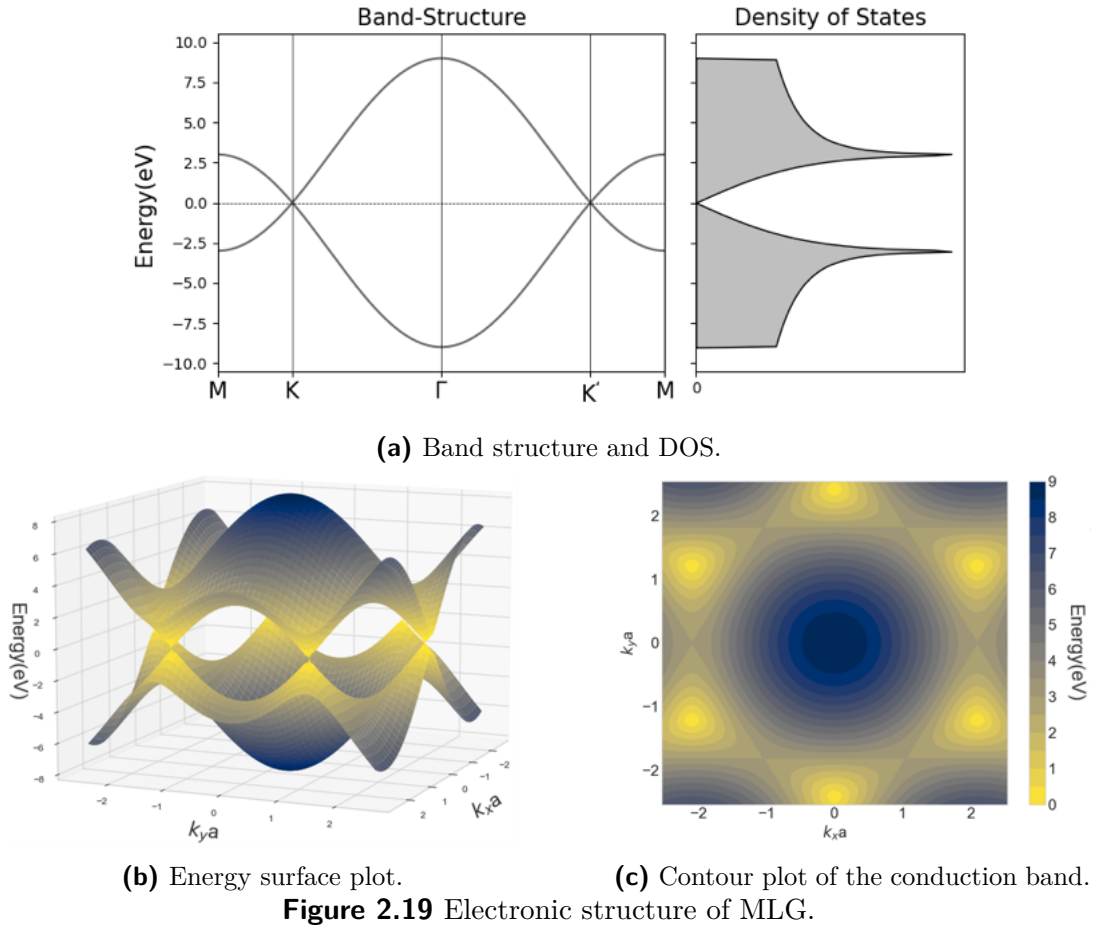
$$E(\mathbf{k})^2 = \gamma_0^2 \left| 1 + e^{i\mathbf{k}\cdot\mathbf{a}_1} + e^{i\mathbf{k}\cdot\mathbf{a}_2} \right|^2 = \gamma_0^2 \left| 1 + 2e^{3ik_x a/2} \cos \frac{\sqrt{3}k_y a}{2} \right|^2. \quad (2.58)$$

Expanding this, we obtain the Bloch Band function [16]:

$$E(\mathbf{k}) = \pm \gamma_0 \sqrt{1 + 4 \cos \frac{3k_x a}{2} \cos \frac{\sqrt{3}k_y a}{2} + 4 \cos^2 \frac{\sqrt{3}k_y a}{2}}. \quad (2.59)$$

In eq. 2.59, the plus sign corresponds to the conduction band (π^* -band), and the minus sign corresponds to the valence band (π -band). The energy band structure and the corresponding DOS are illustrated in Fig. 2.19a. Notably, the energy spectrum

is a double cover of the first Brillouin zone, symmetric about $E = 0$.



First, let us examine the extreme energy cases at the Γ -point ($\mathbf{k} = 0$). Here, the eigenenergies are $E = \pm 3\gamma_0$, corresponding to the eigenstates $[c_A, c_B] = \frac{1}{\sqrt{2}}[1, \mp 1]$, respectively. For the valence band state, the amplitudes c_A and c_B of the wave functions for sublattices A and B share the same sign, resulting in bonding orbitals that are highly delocalized, thus lowering the energy (fig. 2.20). Conversely, the conduction band state at Γ is linked to antibonding orbitals, where c_A and c_B have opposite signs, leading to a high curvature of the wave function and increased kinetic energy (fig. 2.21).

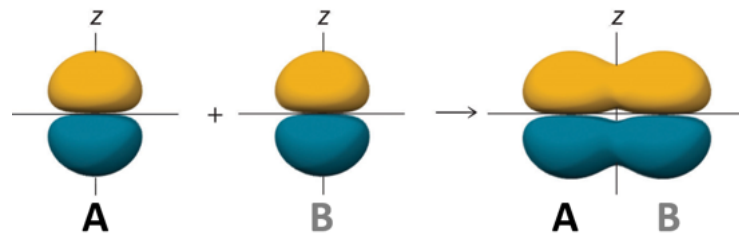


Figure 2.20 Bonding configuration within a diatomic unit cell. Adapted from [27].

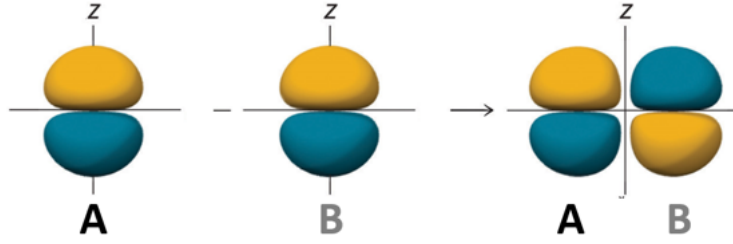
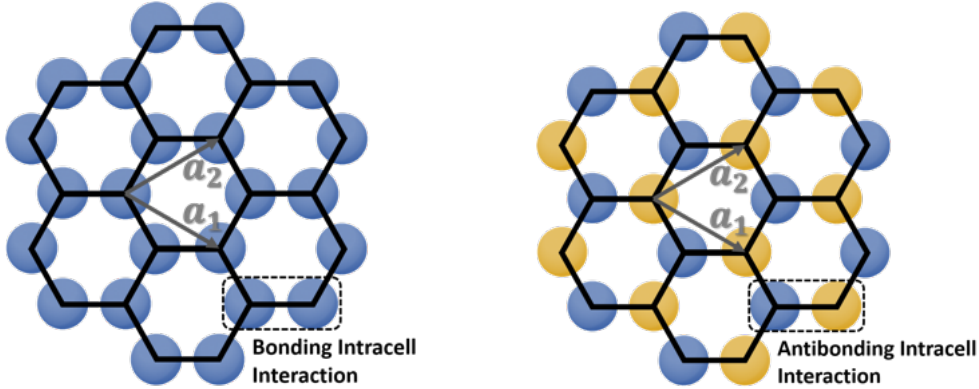


Figure 2.21 Antibonding configuration within a diatomic unit cell. Adapted from [27].

Throughout the lattice, the unit cell orbitals are translated along \mathbf{a}_1 and \mathbf{a}_2 without any phase change (since $\mathbf{k} = \mathbf{0}$), forming the π -orbital network shown in fig. 2.22. Consequently, in the π -band, all interactions are bonding with respect to each neighbor, while in the π^* -band, all interactions are antibonding, resulting in the largest possible energy separation [33].



(a) Bonding network.

(b) Antibonding network.

Figure 2.22 Bonding and antibonding orbital networks at the Γ -point.

When examining energies closer to zero, we encounter saddle points in the electron energy spectrum at the \mathbf{M} -point. These regions feature flat bands and a large DOS, creating distinct peaks in the DOS plot at the \mathbf{M} -point energy. Again, the energy separation at \mathbf{M} is explained by the bonding (π) and antibonding (π^*) states. Given that the \mathbf{M} -point corresponds to $\mathbf{k} = \left(\frac{\pi}{a}, 0\right)$, there is a real-space modulation with a wavelength of $\lambda = \frac{a}{2}$. A translation along \mathbf{a}_1 involves phase reversal, whereas along \mathbf{a}_2 , there is no phase change.

Figure 2.23 shows that in the π -band, each carbon atom bonds with two neighbors and antibonds with the third, with the reverse occurring in the π^* -band. Thus, the energy separation at \mathbf{M} is approximately one-third of that at Γ , given by $E = \pm\gamma_0$ [33].

In the low-energy regime of graphene, a notable phenomenon occurs: the bands meet at the \mathbf{K} and \mathbf{K}' points, where $\cos\left(\frac{3k_x a}{2}\right) = -1$ and $\cos\left(\frac{\sqrt{3}k_y a}{2}\right) = \frac{1}{2}$. Near

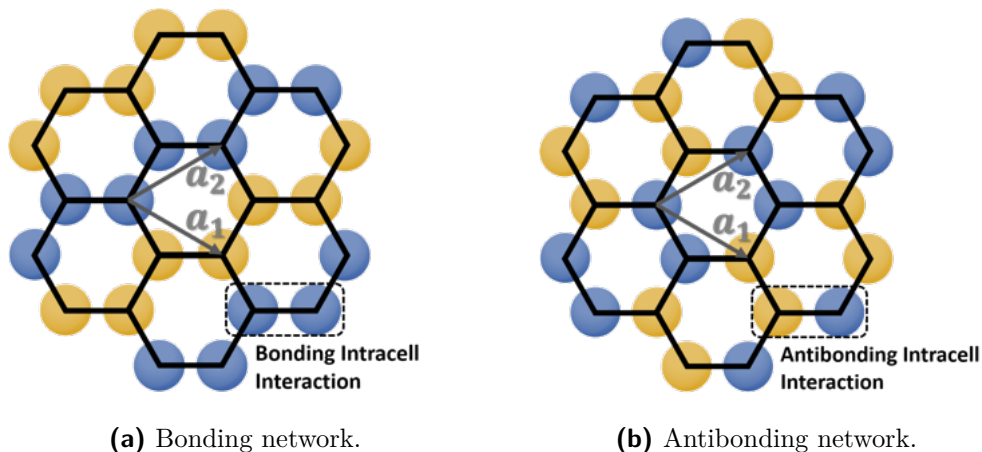


Figure 2.23 Bonding and antibonding orbital networks at the \mathbf{M} -point.

these points, the energy dispersion is linear, forming cone-like surfaces. As discussed in Sec. 2.2.3, this results in a linear decrease in the DOS as we approach zero energy.

At the \mathbf{K} -point, bonding and antibonding configurations are degenerate. Given that $|\mathbf{K}| = \frac{4\pi}{3a}$, the modulation wavelength is $\lambda = \frac{3a}{2}$. This indicates that the wave lacks the crystal's periodicity, preventing the placement of a node at every unit cell, as shown in Fig. 2.24. Inspection reveals that bonding and antibonding interactions around any carbon atom exactly cancel out, resulting in the degeneracy at the \mathbf{K} -point [33].

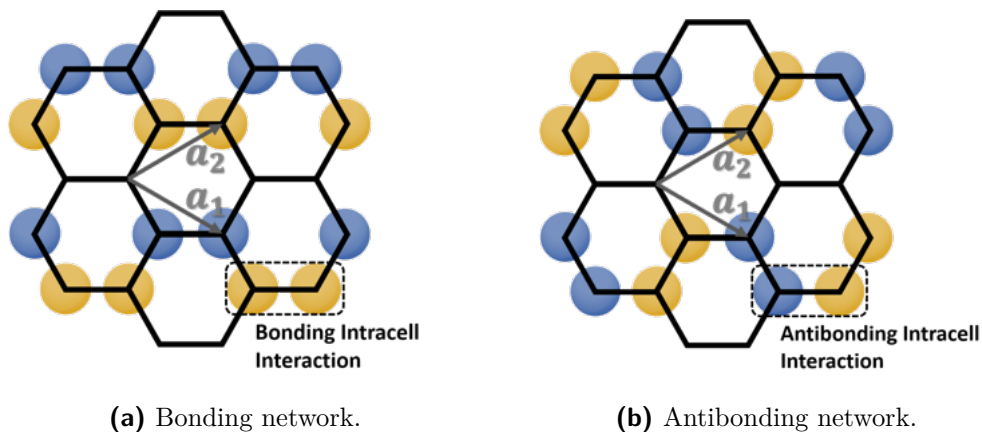


Figure 2.24 Bonding and antibonding orbital networks at the \mathbf{K} -point.

In summary, the bands are widely separated at Γ , less separated at \mathbf{M} , and degenerate at \mathbf{K} . This behavior is explained by the modulation of bonding and antibonding orbitals. However, apart from these special points, a graphene eigenstate is not strictly bonding or antibonding within a unit cell.

Next, let us consider hopping to the six next-nearest neighbors defined by $\{\delta'_i\}$. These neighbors reside on the same sublattice, contributing only to the diagonal terms $H_{A,A}$ and $H_{B,B}$, which characterize intra-sublattice hopping processes. By symmetry, we set $\gamma_{A,A}(\delta'_i) = \gamma_{B,B}(\delta'_i) = -\gamma_n \approx 0.3eV$ [34]:

$$H_{A,A} = H_{B,B} = -\gamma_n \sum_i e^{i\mathbf{k}\delta'_i} \quad (2.60)$$

$$= -\gamma_n \sum_i \left(e^{i\mathbf{k}\mathbf{a}_i} + e^{-i\mathbf{k}\mathbf{a}_i} \right) \quad (2.61)$$

$$= -\gamma_n \sum_i 2 \cos(\mathbf{k}\mathbf{a}_i), \quad (2.62)$$

where the summation is over the lattice vectors $\mathbf{a}_1, \mathbf{a}_2$, and $\mathbf{a}_3 = \mathbf{a}_2 - \mathbf{a}_1$.

Substituting the values of \mathbf{a}_i , we define:

$$g(\mathbf{k}) = \sum_i 2 \cos(\mathbf{k}\mathbf{a}_i) \quad (2.63)$$

$$= 2 \left[\cos\left(\frac{3k_x a}{2} + \frac{\sqrt{3}k_y a}{2}\right) + \cos\left(\frac{3k_x a}{2} - \frac{\sqrt{3}k_y a}{2}\right) + \cos(\sqrt{3}k_y a) \right] \quad (2.64)$$

$$= 2 \left[2 \cos\left(\frac{3k_x a}{2}\right) \cos\left(\frac{\sqrt{3}k_y a}{2}\right) + \cos(\sqrt{3}k_y a) \right]. \quad (2.65)$$

The corresponding eigenvalue equation takes the form:

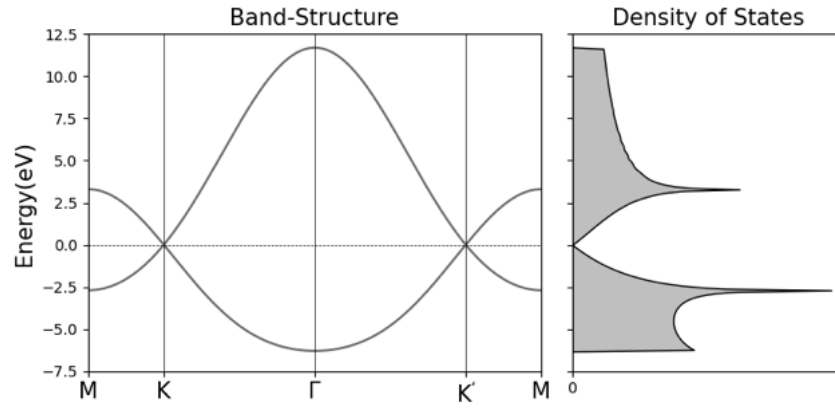
$$\begin{bmatrix} -\gamma_n g(\mathbf{k}) & -\gamma_0 f(\mathbf{k}) \\ -\gamma_0 f^*(\mathbf{k}) & -\gamma_n g(\mathbf{k}) \end{bmatrix} \begin{bmatrix} c_1 \\ c_2 \end{bmatrix} = E(\mathbf{k}) \begin{bmatrix} c_1 \\ c_2 \end{bmatrix}. \quad (2.66)$$

Finally this result in the Bloch band function [35]:

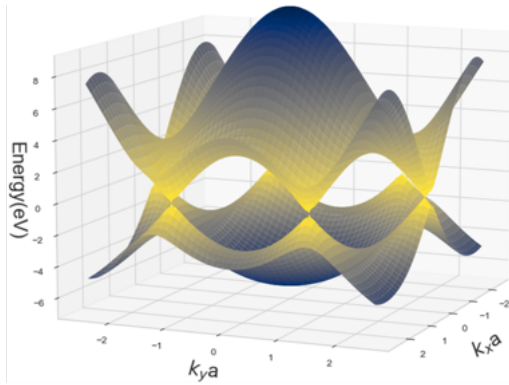
$$E(\mathbf{k}) = \pm \gamma_0 |f(\mathbf{k})| - \gamma_n |f(\mathbf{k})|^2 + 3\gamma_n \quad (2.67)$$

Henceforth we subtract the constant term $3\gamma_n$.

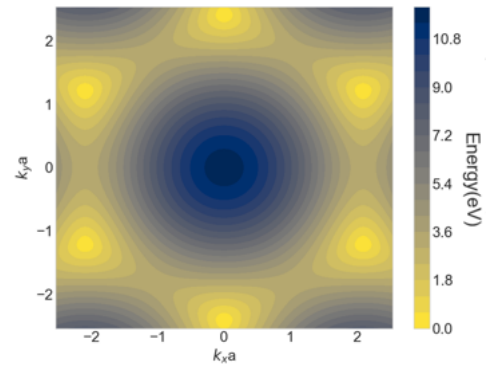
As illustrated in Fig. 2.25a, the next-nearest neighbor contribution breaks electron-hole symmetry without altering the Hamiltonian's behavior near the conical points. This observation is noteworthy because, typically, even slight perturbations eliminate such degeneracies and open a band gap. However, in graphene, the gapless state is protected by a combination of inversion and time-reversal symmetry (*IT*-symmetry) (Sec. 2.4.1). Hence, any perturbation that respects these symmetries cannot induce a gap. This robust degeneracy at the \mathbf{K} points enables graphene to exhibit exotic properties, as discussed in the subsequent section.



(a) Band structure and DOS.



(b) Energy surface plot.



(c) Contour plot of the conduction band.

Figure 2.25 Electronic structure of MLG including next nearest neighbour interaction.

2.4.3 Low Energy Physics

“CERN on the desk.”

Mikhail Katsnelson

Graphene exhibits a linear dispersion relation in the low-energy regime. Given that only one electron per carbon atom contributes, only the lower band with $E(\mathbf{k}) < 0$ is occupied. Consequently, the Fermi surface in graphene consists of just two points, \mathbf{K} and \mathbf{K}' , where the bands intersect. This makes graphene a prime example of a semi-metal.

Most physical phenomena and carrier transitions occur at energy levels around the Fermi level. Thus, we expand the Hamiltonian near the \mathbf{K} point, assuming $|\mathbf{k} - \mathbf{K}| \ll |\mathbf{K}|$. Setting $\mathbf{k} = \mathbf{q} + \mathbf{K}$, we expand:

$$f(\mathbf{k}) = 1 - 2e^{3iq_x a/2} \cos\left(\frac{\pi}{3} + \frac{\sqrt{3}q_y a}{2}\right) \quad (2.68)$$

$$= 1 - 2e^{3iq_x a/2} \left[\frac{1}{2} \cos\left(\frac{\sqrt{3}q_y a}{2}\right) - \frac{\sqrt{3}}{2} \sin\left(\frac{\sqrt{3}q_y a}{2}\right) \right] \quad (2.69)$$

$$\approx 1 - 2 \left(1 + \frac{3iq_x a}{2} + \dots\right) \left(\frac{1}{2} - \frac{3q_y a}{4} + \dots\right) \quad (2.70)$$

$$\approx \frac{3a}{2}(iq_x - q_y) \quad (2.71)$$

Introducing the Fermi velocity $v_F = \frac{3\gamma_0 a}{2\hbar}$, the low-energy Hamiltonian can be expressed as:

$$H'_{\mathbf{K}} = \hbar v_F \begin{bmatrix} 0 & iq_x - q_y \\ -iq_x - q_y & 0 \end{bmatrix} = -\hbar v_F (q_x \sigma^y + q_y \sigma^x), \quad (2.72)$$

where σ^x and σ^y are Pauli matrices. The chosen orientation of the honeycomb lattice has resulted in a slightly inconvenient form for the Hamiltonian. To simplify, we rotate the system by 90° . The corresponding $SU(2)$ -transformation $U \in SU(2)$ is given by $U = e^{i\theta\sigma^z/2}$:

$$H_{\mathbf{K}} = U^{-1} H'_{\mathbf{K}} U \quad (2.73)$$

$$= \begin{bmatrix} e^{-i\pi/4} & 0 \\ 0 & e^{i\pi/4} \end{bmatrix} \begin{bmatrix} 0 & \hbar v_F (iq_x - q_y) \\ -\hbar v_F (iq_x + q_y) & 0 \end{bmatrix} \begin{bmatrix} e^{i\pi/4} & 0 \\ 0 & e^{-i\pi/4} \end{bmatrix} \quad (2.74)$$

$$= \begin{bmatrix} 0 & \hbar v_F (q_x - iq_y) \\ \hbar v_F (q_x + iq_y) & 0 \end{bmatrix} \quad (2.75)$$

$$= \hbar v_F (q_x \sigma^x + q_y \sigma^y) \quad (2.76)$$

$$= \hbar v_F \mathbf{q} \cdot \boldsymbol{\sigma}, \quad (2.77)$$

where $\boldsymbol{\sigma} = [\sigma^x, \sigma^y]$. A similar equation is obtained near the \mathbf{K}' point:

$$H_{\mathbf{K}'} = \hbar v_F \mathbf{q} \cdot \boldsymbol{\sigma}^*. \quad (2.78)$$

This formulation represents the Dirac equation for a massless particle in two dimensions. However, instead of the speed of light c , the particles move with the Fermi

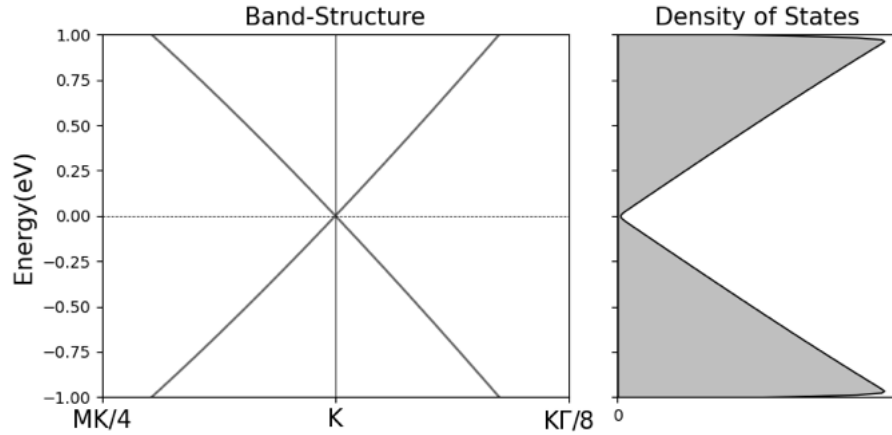


Figure 2.26 Low energy band structure and DOS calculated using the tight-binding method.

velocity v_F . The corresponding Bloch band function is:

$$E(\mathbf{k}) = \pm \hbar v_F |\mathbf{q}|, \quad (2.79)$$

and the eigenstates are [30]:

$$\langle \mathbf{r} | \mathbf{K} + \mathbf{q} \rangle = \psi_{\pm, \mathbf{K}}(\mathbf{r}) = \frac{e^{i\mathbf{q}\mathbf{r}}}{\sqrt{2}} \begin{bmatrix} 1 \\ \pm e^{i\theta_{\mathbf{q}}} \end{bmatrix}, \quad \langle \mathbf{r} | \mathbf{K}' + \mathbf{q} \rangle = \psi_{\pm, \mathbf{K}'}(\mathbf{r}) = \frac{e^{i\mathbf{q}\mathbf{r}}}{\sqrt{2}} \begin{bmatrix} \pm e^{i\theta_{\mathbf{q}}} \\ 1 \end{bmatrix}, \quad (2.80)$$

for \mathbf{K} and \mathbf{K}' , respectively, where $\theta_{\mathbf{q}} = \arctan\left(\frac{q_y}{q_x}\right)$. These conical points are thus known as Dirac points, while the cones are referred to as Dirac cones.

There are, however, important distinctions to be made. In the original Dirac equation, the 2×2 matrix structure arises due to the electron's spin. In this context, the upper component defines the probability amplitude for the spin-up state, while the lower component corresponds to the spin-down state. In graphene, the emergent "spin" degree of freedom stems from the presence of two sublattices, A and B. Therefore, the spinor represents the quantum mechanical amplitudes for different sublattices rather than spin projections. This is why it is referred to as pseudospin [16].

The formal similarity between ultrarelativistic particles and electrons in graphene renders graphene an ideal platform for studying various quantum relativistic effects.

This linear approximation holds only as long as $|\mathbf{q}|a \ll 1$, as illustrated in the contour plot in Fig. 2.27. In this regime, graphene exhibits circular iso-energetic lines. At higher energy and momentum \mathbf{q} , a triangular perturbation of these circular lines,

known as trigonal warping, arises. This effect occurs because the band structure follows the symmetry of the crystal lattice inherent in the full momentum dependence of the function $f(\mathbf{k})$.

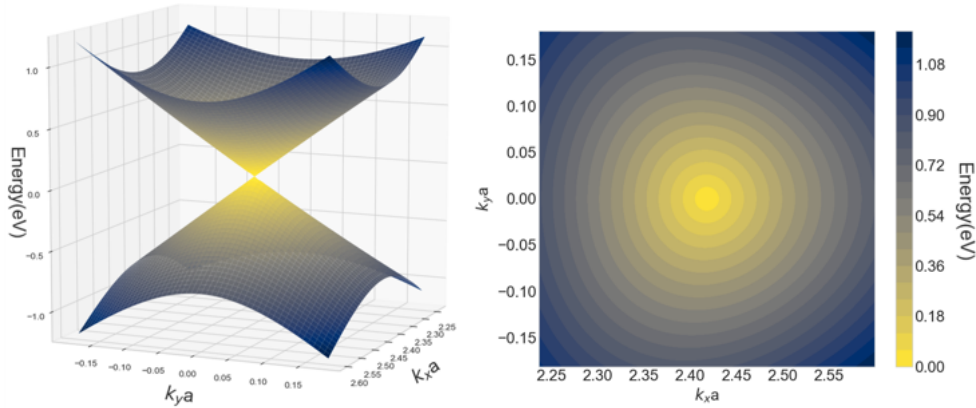


Figure 2.27 Low energy surface plot and contour plot of the conduction band.

2.5 Bilayer Graphene

Due to the attractive van der Waals force, two monolayers of graphene can form a stable coupled system known as bilayer graphene (BLG). The emergent interlayer interaction alters the structural and electronic properties of the material, which is the focus of this chapter.

2.5.1 Crystal Structure

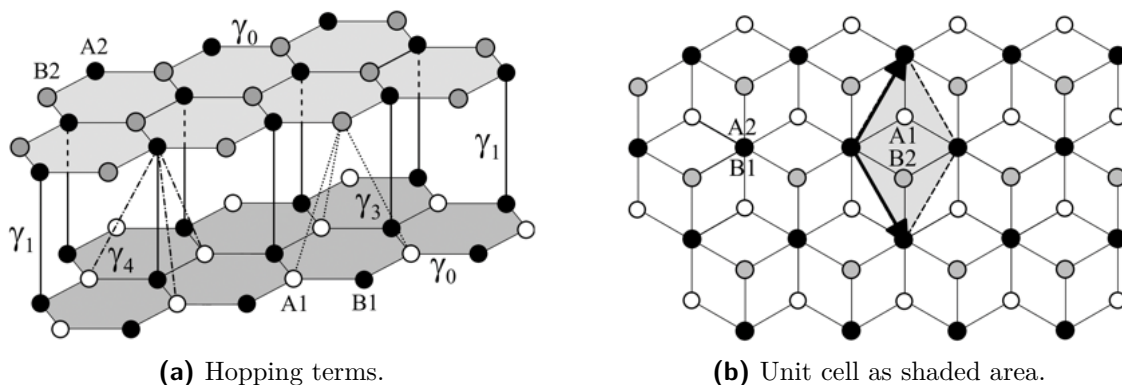


Figure 2.28 BLG lattice, consisting of four overlapping trigonal Bravais sublattices A_1, B_1, A_2 and B_2 . Adapted from [36].

The crystal structure of the most stable configuration of BLG is illustrated in Fig. 2.28a. The second carbon layer is rotated by 60° relative to the first layer (arbitrary twist angles will be explored in Sec. 2.7.6). The layers are separated by a distance of $L = 3.35 \text{ \AA}$ [34].

Consequently, the system acquires a three-dimensional character due to the finite extent in the z -direction. However, the crystal can still be effectively described as a two-dimensional system, by projecting the relative positions of the atoms onto the xy -plane.

The projected positions of the atoms are depicted in Fig. 2.28b. The crystal lattice and the corresponding reciprocal lattice can be generated using the same choice of primitive vectors as in MLG, but now with a four-atomic basis, since each graphene layer contributes two atoms per unit cell. The respective sublattices are labeled A_1 , B_1 for the lower layer and A_2 , B_2 for the upper layer. Due to the 60° rotation, one of the atoms from the lower layer (B_1) is directly below an atom (A_2) from the upper layer. These two atomic sites are referred to as 'dimer' sites because their electronic orbitals are coupled together by a relatively strong interlayer interaction. The other two atoms, A_1 and B_2 , do not have a counterpart directly above or below them; they sit in the center of the other layer's hexagon and are referred to as 'monomer' sites [36].

2.5.2 Band Structure

In the tight-binding description of BLG, we consider the four $2p_z$ orbitals of the four atomic sites in the unit cell, allowing us to write the wavefunctions as elements of $\mathcal{H}_{BLG} := \ell^2(\mathbb{Z}^2; \mathbb{C}^2) \oplus \ell^2(\mathbb{Z}^2; \mathbb{C}^2)$, derived from the p_z states $\{|\mathbf{r}, A_1\rangle, |\mathbf{r}, B_1\rangle, |\mathbf{r}, A_2\rangle, |\mathbf{r}, B_2\rangle\}$ associated with atoms at lattice site $\mathbf{r} \in \Lambda$. In the Bloch domain, $L^2(\Omega^*; \mathbb{C}^2) \oplus L^2(\Omega^*; \mathbb{C}^2)$, we decompose the wavefunction in the basis $\{|\mathbf{k}, 1, A\rangle, |\mathbf{k}, 1, B\rangle, |\mathbf{k}, 2, A\rangle, |\mathbf{k}, 2, B\rangle\}$. Following eq. 2.24, the Hamiltonian can be represented as a 4×4 matrix:

$$H = \begin{bmatrix} 0 & -\gamma_0 f(\mathbf{k}) & \gamma_4 f(\mathbf{k}) & -\gamma_3 f^*(\mathbf{k}) \\ -\gamma_0 f^*(\mathbf{k}) & 0 & \gamma_1 & \gamma_4 f(\mathbf{k}) \\ \gamma_4 f^*(\mathbf{k}) & \gamma_1 & 0 & -\gamma_0 f(\mathbf{k}) \\ -\gamma_3 f(\mathbf{k}) & \gamma_4 f^*(\mathbf{k}) & -\gamma_0 f^*(\mathbf{k}) & 0 \end{bmatrix}, \quad (2.81)$$

where the tight-binding parameters are defined as [32]:

$$\gamma_0 = -\langle A_1 | H | B_1 \rangle = -\langle A_2 | H | B_2 \rangle \approx 3.0 \text{ eV}, \quad (2.82)$$

$$\gamma_1 = \langle A_2 | H | B_1 \rangle \approx 0.4 \text{ eV}, \quad (2.83)$$

$$\gamma_3 = -\langle A_1 | H | B_2 \rangle \approx 0.3 \text{ eV}, \quad (2.84)$$

$$\gamma_4 = \langle A_1 | H | A_2 \rangle = \langle B_1 | H | B_2 \rangle \approx 0.1 \text{ eV}. \quad (2.85)$$

The upper-left and lower-right 2×2 blocks of H describe intralayer interactions and are straightforward generalizations of the MLG Hamiltonian.

The upper-right and lower-left 2×2 blocks of H describe interlayer coupling. The parameter γ_1 characterizes coupling between dimer sites B_1 and A_2 . Since this is a vertical coupling, the corresponding terms in H do not include $f(\mathbf{k})$, which accounts for the finite in-plane hopping. The parameter γ_3 describes interlayer coupling between non-dimer sites A_1 and B_2 , while γ_4 accounts for coupling between dimer and non-dimer sites A_1 and A_2 or B_1 and B_2 . Both γ_3 and γ_4 involve a component of in-plane hopping. Each atom on one layer has three equidistant nearest neighbors on the other layer, and the corresponding in-plane components are analogous to nearest-neighbor hopping within a single layer. Thus, these "skew" interlayer hoppings (e.g., $\langle A_1|H|B_2\rangle$, $\langle A_1|H|A_2\rangle$, and $\langle B_1|H|B_2\rangle$) contain the phase factor $f(\mathbf{k})$ [36].

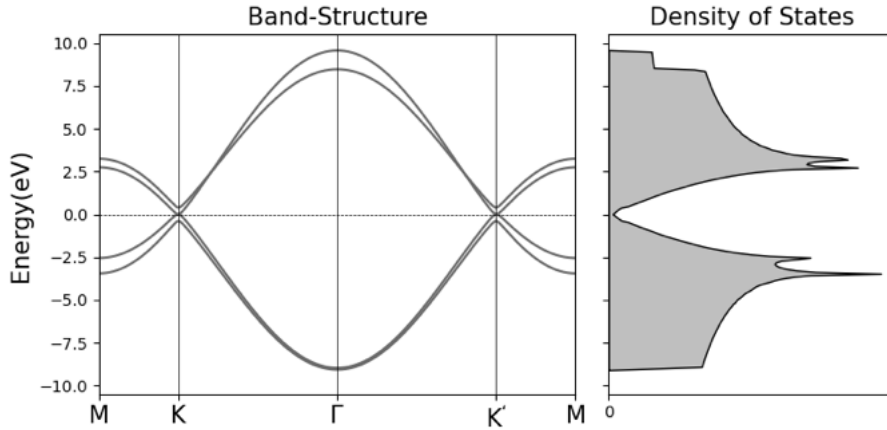


Figure 2.29 Band structure and DOS calculated using the tight-binding method.

The resulting four energy bands are illustrated in Fig. 2.29. These bands consist of two conduction bands and two valence bands. Given that $\gamma_0 \gg \gamma_1$, across most of the Brillouin zone where $\gamma_0|f(\mathbf{k})| \gg \gamma_1/2$, the energy can be approximated as $E_{\pm}^{\alpha} \approx \pm(\gamma_0|f(\mathbf{k})| + \alpha\gamma_1/2)$. This approximation suggests that the $\alpha = \pm 1$ bands resemble the MLG bands but are split by the interlayer coupling term γ_1 . As discussed in Sec. 2.4.2, the intralayer interaction is most pronounced at the Γ -point, resulting in a significant energy gap of the order of γ_0 , while it vanishes at the \mathbf{K} -point [36].

Since BLG contributes four electrons per unit cell, only the two lower bands are occupied, positioning the Fermi level at the intersection of the two low-energy bands, thus exhibiting a semi-metallic characteristic [33].

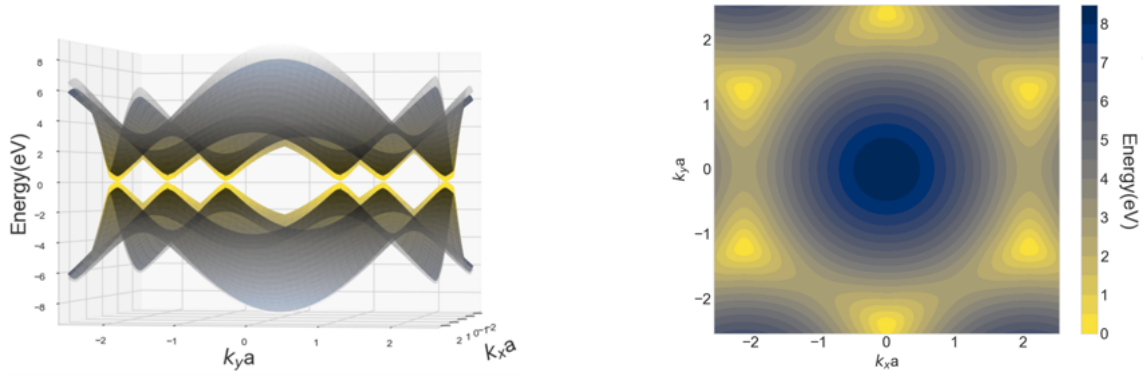


Figure 2.30 Energy surface plot and contour plot of the conduction band in BLG.

2.5.3 Low-Energy Physics

At the \mathbf{K} -point, two bands touch at zero energy, forming what are referred to as 'low-energy' bands, while the other conduction and valence bands (termed 'high-energy' bands) remain separated by approximately $2\gamma_1$. The Hamiltonian describing this scenario is depicted in Fig. 2.31.

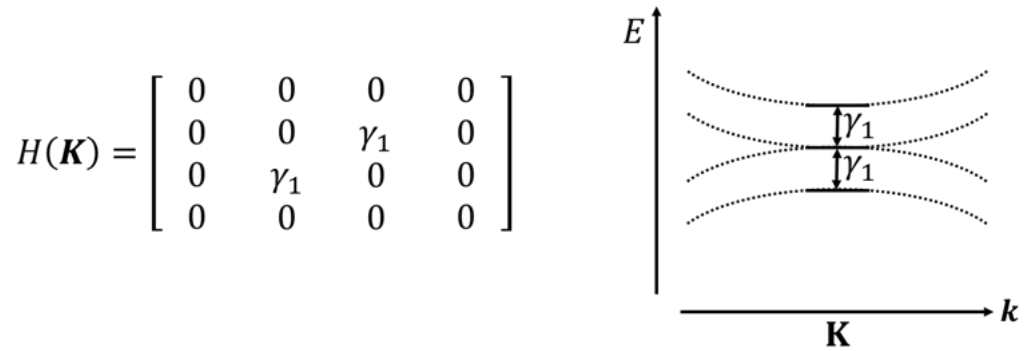


Figure 2.31 Energy bands at the \mathbf{K} -point.

The energy of the Bloch states at the \mathbf{K} -point arises solely from vertical interlayer interactions. For the high-energy states, the amplitudes associated with the monomer sites c_{A1} and c_{B2} diminish as \mathbf{k} approaches \mathbf{K} . Consequently, electrons in these states are primarily localized on the dimer sites. The energy splitting originates from the formation of bonding or antibonding orbital configurations, as shown in Fig. 2.32 [33].

Conversely, for electrons in the touching bands, the dimer site amplitudes c_{B1} and c_{A2} vanish as \mathbf{k} approaches \mathbf{K} . Hence, the 'low-energy' bands are generated from hopping between the monomer sites. Due to the absence of vertical interaction, these states remain at zero energy (Fig. 2.33).

To further extend our analysis to band states in the vicinity of the \mathbf{K} -points, we apply a similar approach to that in Sec. 2.4.3, expanding $f(\mathbf{q} + \mathbf{K})$ for small $|\mathbf{q}|$, where $\mathbf{q} = \mathbf{k} - \mathbf{K}$. In the intermediate energy range $(\gamma_3/\gamma_0)^2\gamma_1 < E < \gamma_1$, it is

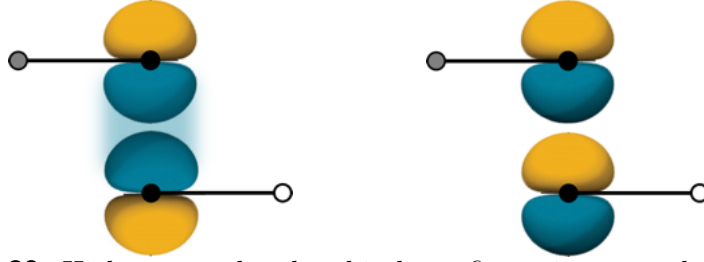


Figure 2.32 High-energy band orbital configurations at the \mathbf{K} -point. Adapted from [27].

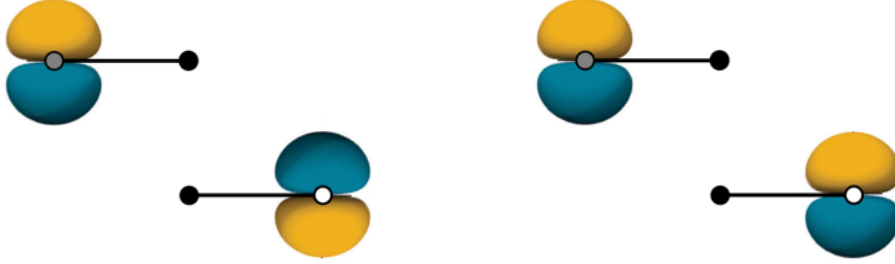


Figure 2.33 Low-energy band orbital configurations at the \mathbf{K} -point. Adapted from [27].

justifiable to neglect terms proportional to γ_3 and γ_4 . The Hamiltonian can then be approximated as:

$$H = \begin{bmatrix} 0 & \hbar v_F(q_x - iq_y) & 0 & 0 \\ \hbar v_F(q_x + iq_y) & 0 & \gamma_1 & 0 \\ 0 & \gamma_1 & 0 & \hbar v_F(q_x - iq_y) \\ 0 & 0 & \hbar v_F(q_x + iq_y) & 0 \end{bmatrix},$$

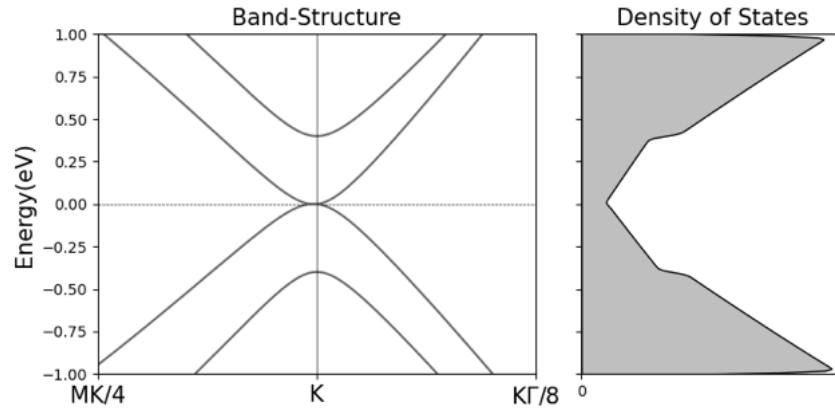
leading to the Bloch band functions:

$$E_{\pm}^{\alpha}(\mathbf{q}) = \pm \frac{\gamma_1}{2} \left[\sqrt{1 + \left(\frac{2\hbar v_F}{\gamma_1} \right)^2 |\mathbf{q}|^2} + \alpha \right], \quad (2.86)$$

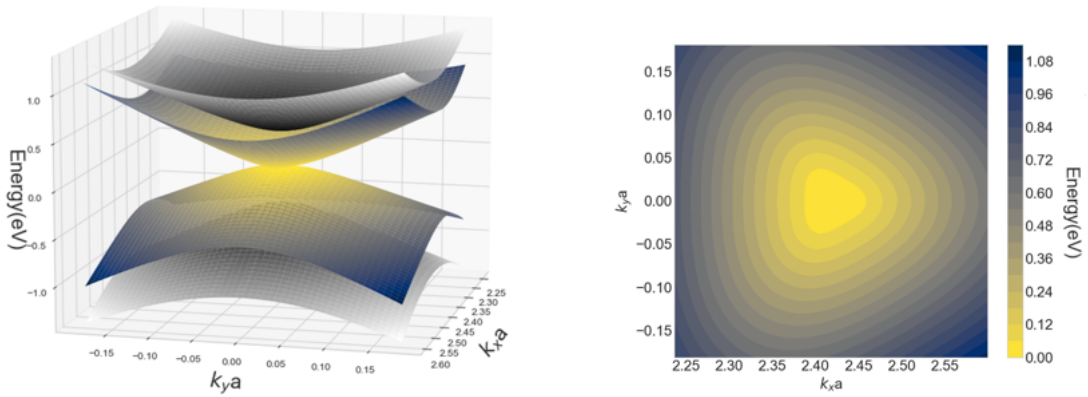
where the \pm signs correspond to the conduction and valence bands, respectively, and $\alpha = \pm 1$ denotes the higher and lower energy bands [36].

The function $E_{\pm}^{\alpha}(\mathbf{q})$ transitions from an approximately linear dispersion $E_{\pm}^{-1}(\mathbf{q}) \approx \pm \hbar v_F |\mathbf{q}|$ at large momentum to a quadratic one $E_{\pm}^{-1}(\mathbf{q}) \approx \pm \frac{\mathbf{p}^2}{2m^*}$ with an effective mass $m^* = \frac{\gamma_1}{2v_F}$. This behavior is reflected in the DOS. At zero energy, there is a notable onset, transitioning to linear behavior, followed by a second onset due to the parabolic high-energy band edge (Sec. 2.2.3).

In addition to the vertical interlayer hopping that imparts a ‘mass’ $\propto \gamma_1$ to the elec-



(a) Band structure and DOS.



(b) Energy surface plot.

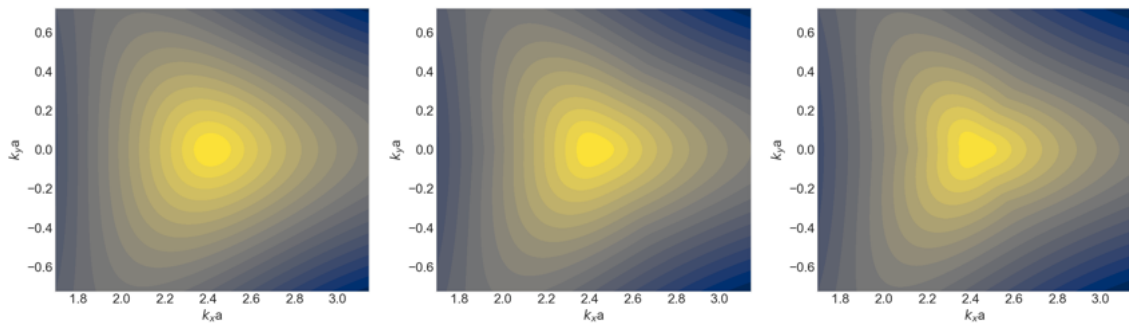
(c) Contour plot of the conduction band.

Figure 2.34 Low-energy electronic structure of BLG

trons, additional "skew" interlayer couplings γ_3 and γ_4 are present. It is convenient to introduce the effective velocities $v_3 = \frac{3\gamma_3 a}{2\hbar}$ and $v_4 = \frac{3\gamma_4 a}{2\hbar}$.

The v_3 term is particularly relevant at low energies because it directly couples the A_1 and B_2 orbitals, which constitute the two low-energy bands. For energies $|E| \ll \gamma_1$, the low-energy bands can be described by [36]:

$$E_{\pm}^{-}(\mathbf{q}) = \sqrt{(\hbar v_3 |\mathbf{q}|)^2 - \frac{v_3 \hbar^3 |\mathbf{q}|^3}{m^*} \cos(3\theta_{\mathbf{q}}) + \left(\frac{\hbar^2 |\mathbf{q}|^2}{2m^*}\right)^2}, \quad (2.87)$$

(a) $\gamma_3 = 0.005\gamma_0$.(b) $\gamma_3 = 0.1\gamma_0$.(c) $\gamma_3 = 0.2\gamma_0$.**Figure 2.35** Contour plots showing the effects of varying γ_3 .

Compared to MLG, the term with $\cos(3\theta_{\mathbf{q}})$ introduces a second source of trigonal warping, manifesting along the directions $\theta_{\mathbf{q}} = 0, \frac{2}{3}\pi, \frac{4}{3}\pi$. In Fig. 2.35, we illustrate the impact of increasing γ_3 in the intermediate energy regime, further distorting the circular isoenergetic lines around the \mathbf{K} point.

Lastly, interlayer hopping γ_4 between a non-dimer and a dimer site introduces electron-hole asymmetry. This effect is also shown in the intermediate energy regime in Fig. 2.36. For energies $|E| \ll \gamma_1$, the low-energy dispersion can be approximated as:

$$E_{\pm}^{\pm}(\mathbf{q}) = \pm \frac{\hbar^2 |\mathbf{q}|^2}{2m^*} \left(1 \pm 2 \frac{v_4}{v_F} \right), \quad (2.88)$$

where the effect of trigonal warping has been neglected [36].

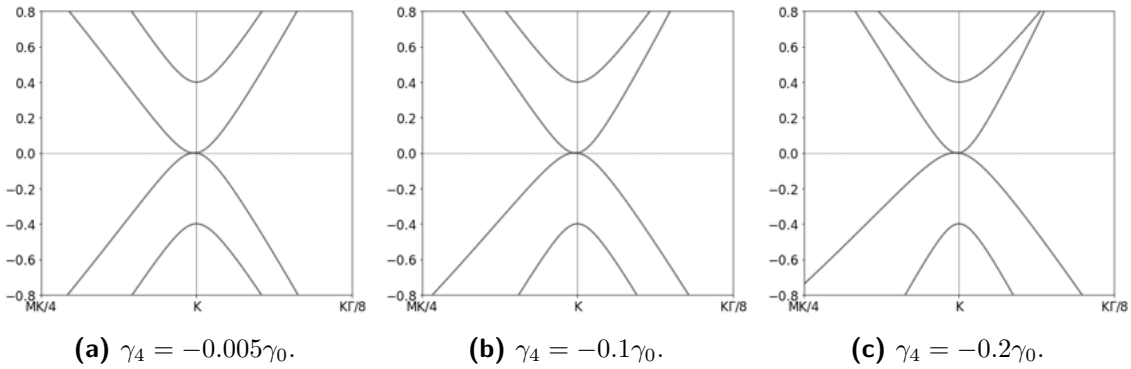


Figure 2.36 Band structure plots showing the effects of varying γ_4 .

2.6 From Graphene to Graphite

As we transition from MLG to BLG, we can extend this to few-layer graphene (FLG) systems by vertically stacking N layers. The energetically most stable configuration is the Bernal stacking order, which is predominant in naturally occurring few-layer graphene systems. When $N \rightarrow \infty$, the material is referred to as graphite.

2.6.1 Crystal Structure

Bernal stacking occurs when successive layers are alternately rotated by $+60^\circ$ and -60° . For instance, consider the transition from bilayer to trilayer graphene. While the second layer is rotated by 60° relative to the first layer to create bilayer graphene, the third layer is rotated by -60° relative to the second layer, aligning it directly above the first layer. This stacking configuration results in the crystal structure depicted in Fig. 2.37a. The unit cell is defined by the previous lattice vectors but now

contains $2N$ atoms. The dimer of BLG transforms into an N -component multimer, while the remaining N atoms can be treated as monomer states.

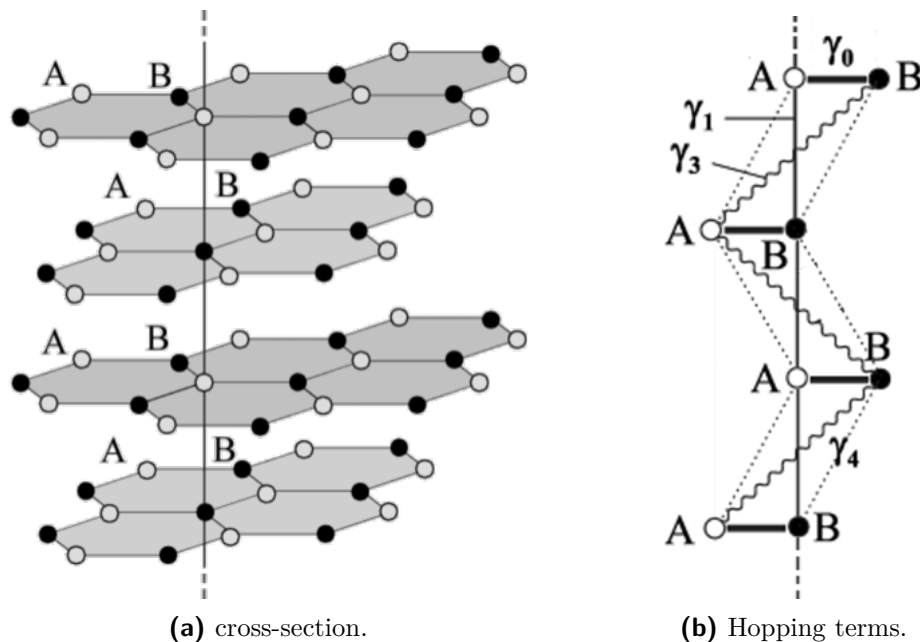


Figure 2.37 Crystal structure of FLG. Adapted from [37].

2.6.2 Band Structure

The band structure of few-layer graphene systems can be analyzed similarly to MLG and BLG by projecting the interatomic distances onto a 2D plane. For N -layer graphene, we work in the Hilbert space $\mathcal{H}_{FLG} := L^2(\Omega^*; \mathbb{C}^2)^{\oplus N}$ with the basis $\{|\mathbf{k}, 1, \alpha\rangle, |\mathbf{k}, 2, \alpha\rangle, \dots, |\mathbf{k}, N, \alpha\rangle\}$ and the eigenvector $[c_{\alpha_1}, c_{\alpha_2}, \dots, c_{\alpha_N}]$, where $\alpha \in \{A, B\}$. The Hamiltonian is block diagonal and can be constructed as [38]:

$$H = \begin{bmatrix} H_0 & V & 0 & \dots & 0 \\ V^\dagger & H_0 & V^\dagger & \dots & 0 \\ 0 & V & H_0 & \ddots & \vdots \\ \vdots & \vdots & \ddots & \ddots & V \\ 0 & 0 & \dots & V^\dagger & H_0 \end{bmatrix}$$

where the interlayer terms are given by:

$$H_0 = \begin{bmatrix} 0 & -\gamma_0 f(\mathbf{k}) \\ -\gamma_0 f^*(\mathbf{k}) & 0 \end{bmatrix}, \quad V = \begin{bmatrix} \gamma_4 f(\mathbf{k}) & -\gamma_3 f^*(\mathbf{k}) \\ \gamma_1 & \gamma_4 f(\mathbf{k}) \end{bmatrix}$$

The coupling terms describe the same hopping processes as in bilayer graphene, with next-nearest layer interactions (γ_2 and γ_5) being neglected. The band structures and DOS for trilayer, tetralayer, pentalayer, and decalayer graphene are illustrated in

fig.2.38. Variations are particularly notable in the DOS plots. With an increasing number of layers, the DOS shows additional peaks at the \mathbf{M} -point energy and several new onsets at the $\mathbf{\Gamma}$ -point energy, corresponding to flat bands and band edges, respectively.

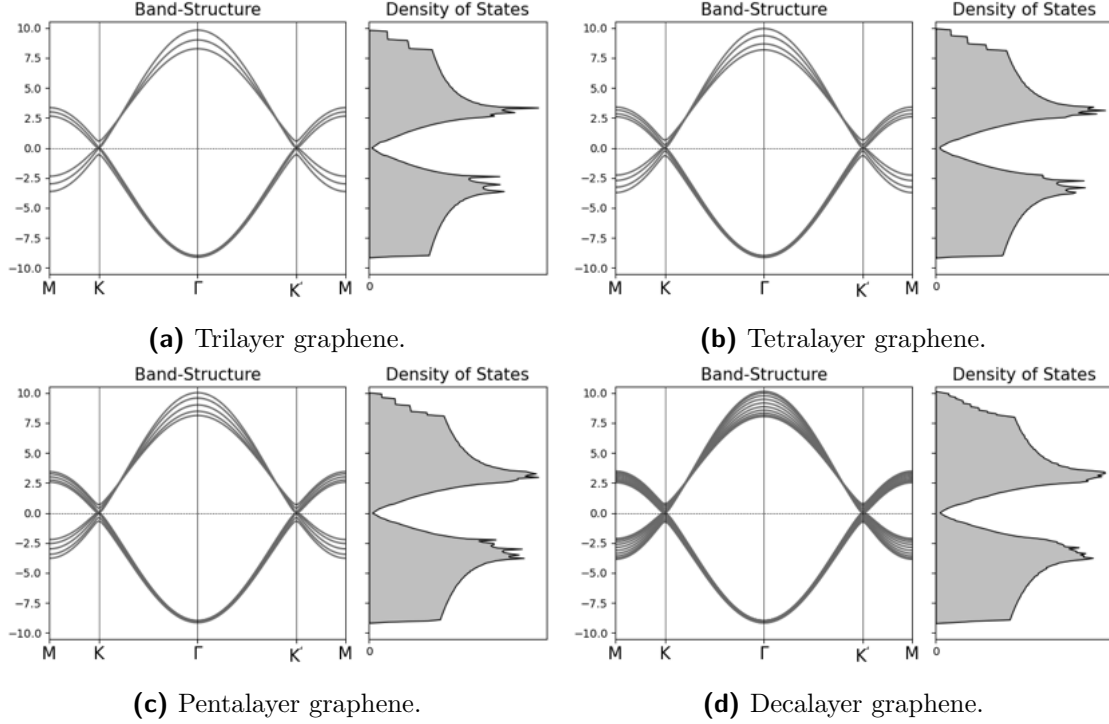


Figure 2.38 Band structures and DOS of FLG systems.

2.6.3 Low-Energy Physics

The low-energy Hamiltonian for N -layer graphene can be approximated by [39]:

$$H_{FLG} = \begin{bmatrix} H_0 & V & 0 & \cdots & 0 \\ V^\dagger & H_0 & V^\dagger & \cdots & 0 \\ 0 & V & H_0 & \ddots & \vdots \\ \vdots & \vdots & \ddots & \ddots & V \\ 0 & 0 & \cdots & V^\dagger & H_0 \end{bmatrix}$$

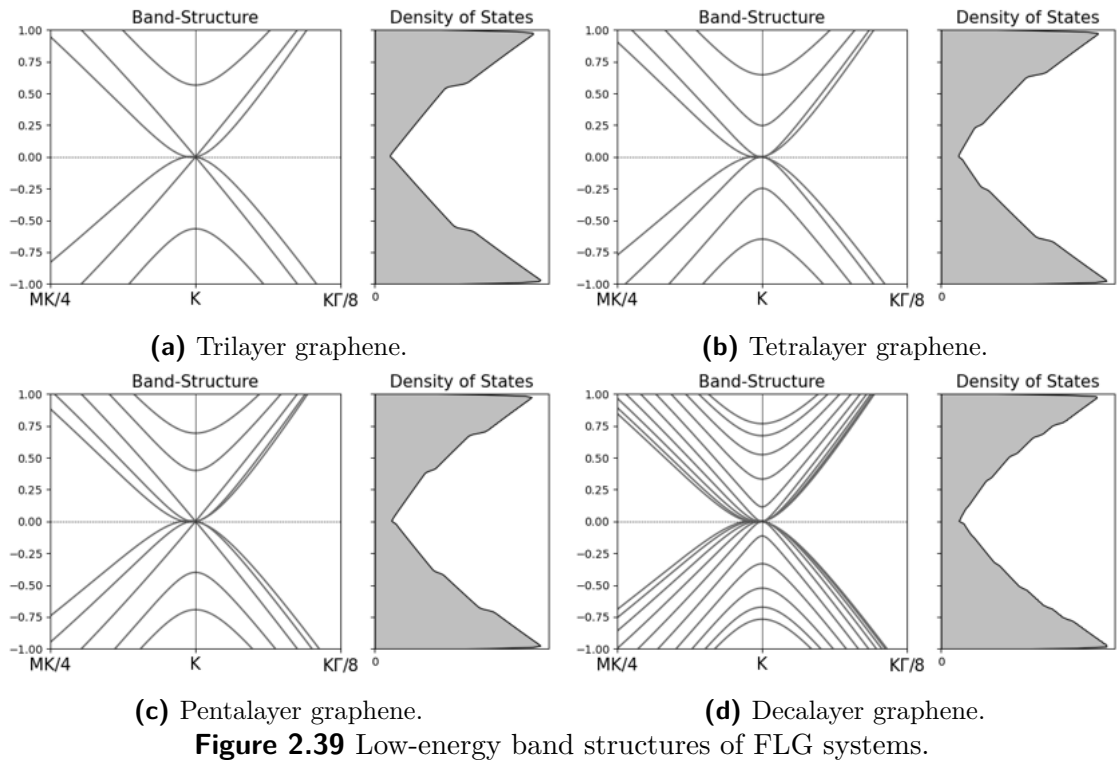
where

$$H_0 = \begin{bmatrix} 0 & \hbar v_F(q_x - iq_y) \\ \hbar v_F(q_x + iq_y) & 0 \end{bmatrix}, \quad V = \begin{bmatrix} 0 & 0 \\ \gamma_1 & 0 \end{bmatrix}$$

The resulting energy spectrum of N -layer graphene is given by [39]:

$$E(\mathbf{q}) = \gamma_1 \cos\left(\frac{r\pi}{N+1}\right) \pm \sqrt{\hbar v_F |\mathbf{q}|^2 + \gamma_1^2 \cos^2\left(\frac{r\pi}{N+1}\right)} \quad (2.89)$$

The bands of trilayer, tetralayer, pentalayer, and decalayer graphene in the low-energy regime are shown in Fig. 2.39. An even-odd layer number effect is observed. Near \mathbf{K} , the band structure of odd N and even N layer graphene resembles N parabolic bilayer-like bands. For odd N , the mode with $r = \frac{N+1}{2}$ resembles a monolayer-like band with linear dispersion. For $\mathbf{q} \rightarrow 0$, the system can be modeled by the multimer consisting of N atoms and N decoupled monomers. Analogous to bilayer graphene, the lowest energy bands result from the non-bonding monomers, creating N zero-energy states at \mathbf{K} . The multimer features N different orthogonal configuration states. For even N , there are full bonding and anti-bonding states, forming the highest energy bands, while semi-bonding and anti-bonding states form bands at lower energy. For odd N , the multimer additionally features a non-bonding configuration forming the $(N + 1)$ -fold degenerate zero-energy level with the monomers. The DOS plots feature additional onsets, corresponding to the increased number of band edges in the low energy regime.



2.7 Twisted Graphene Layers

The QTM's working principle relies on the interlayer transport between the tip and the sample. In this chapter, we develop a quantitative description of the dynamics at the interface of two twisted graphene layers. The following analysis is essentially built upon the work of Bistritzer et al. [40] [6].

2.7.1 Moiré Lattice

Instead of a rotation of 60° , we consider now arbitrary relative rotations between two stacked layers of graphene, which generates a moiré pattern. This pattern manifests as alternating bright and dark fringes, corresponding to localized 'AA'- and 'AB'-rich regions, as illustrated in Fig. 2.40. The AA-regions represent areas where each sublattice site in the top layer coincides with the lower layer. In contrast, the AB-regions resemble Bernal-stacked layers where the layers are arranged so that one of the atoms from the lower layer, B_1 , is directly below an atom, A_2 [41].

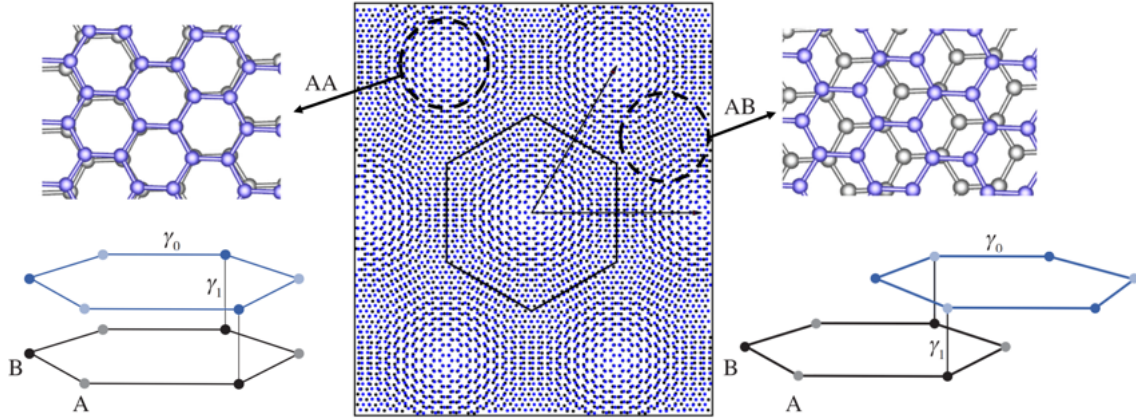


Figure 2.40 Moiré pattern resulting from alternating regions of AA and AB stacking. Adapted from [30] [42] [43].

A unit cell of the moiré pattern is defined by connecting these local 'AA'- or 'AB'-regions. The moiré periodicity a_M is the distance between two nearest 'AA'- or 'AB'-regions. Assuming that the top layer is rotated anticlockwise by $\theta/2$ and the bottom layer is rotated clockwise by the same amount, such that the relative twist angle between them is θ , we can define the new lattice from the primitive lattice vectors of the unrotated lattice $\{\mathbf{a}_i\}$ and the two-atomic basis $\{\mathbf{d}_i\}$ as follows:

$$\Lambda_1 = \bigcup_i \left\{ \mathbf{r}^{(1)} = R_{+\theta/2}(n_1\mathbf{a}_1 + n_2\mathbf{a}_2 + \mathbf{d}_i) \mid (n_1, n_2)^T \in \mathbb{Z}^2 \right\} \quad (2.90)$$

$$\Lambda_2 = \bigcup_i \left\{ \mathbf{r}^{(2)} = R_{-\theta/2}(n'_1\mathbf{a}_1 + n'_2\mathbf{a}_2 + \mathbf{d}_i) \mid (n'_1, n'_2)^T \in \mathbb{Z}^2 \right\} \quad (2.91)$$

where R_θ is the rotation matrix describing rotation by θ about the origin of a 2D coordinate system:

$$R_\theta = \begin{bmatrix} \cos \theta & -\sin \theta \\ \sin \theta & \cos \theta \end{bmatrix} \quad (2.92)$$

For smaller twist angles, the moiré periodicity a_M is much larger than the lattice constant of graphene a , resulting in a moiré-cell containing a significantly large number of atoms. Note that this apparent moiré periodicity is an approximate periodicity in a sense that the corners of the moiré unit cell may not align with the same atomic configuration, as depicted in Fig. 2.41. Consequently, the number of atoms in one hexagon may differ from another [41].

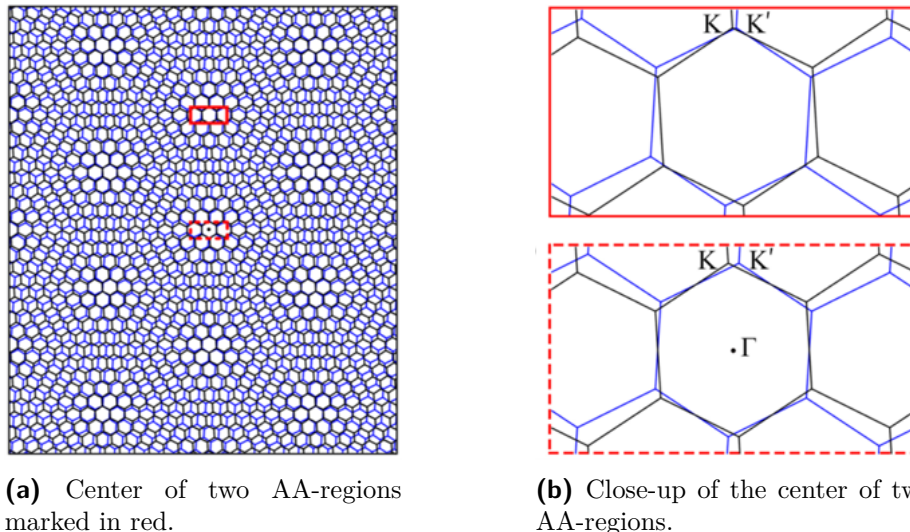
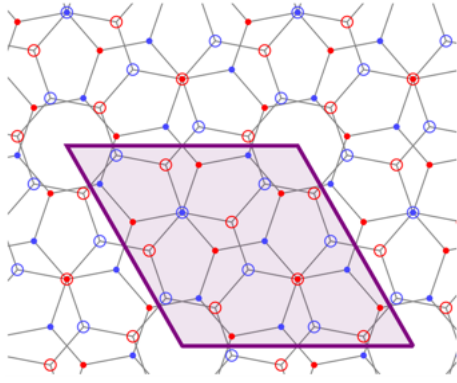


Figure 2.41 Primitive translations in the moiré lattice may not reproduce the same atomic configuration. Adapted from [43].

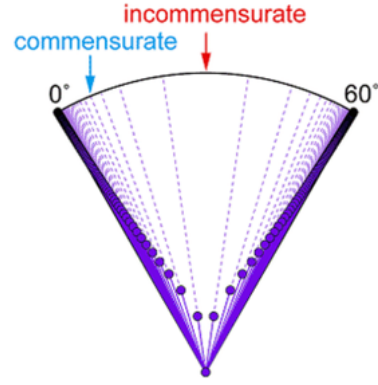
In twisted bilayer graphene (TBG), the underlying structure is exactly periodic only at certain twist angles. At these angles, the exact stacking repeats in any direction, and a chosen unit cell contains precisely the same number of carbon atoms as in any other throughout the crystal. These are commensurate structures. Every vector \mathbf{r}^M within the resulting Moiré Lattice Λ_M can be represented by vectors of the MLG-systems [41]:

$$\mathbf{r}^M = n_1 \mathbf{a}_1^{(1)} + n_2 \mathbf{a}_2^{(1)} = n'_1 \mathbf{a}_1^{(2)} + n'_2 \mathbf{a}_2^{(2)} \quad (2.93)$$

Commensurability is defined by the condition $\Lambda^1 \cap \Lambda^2 \neq \{\mathbf{0}\}$, which is fulfilled for a set of angles θ_0 . For instance, the moiré unit cell for the commensurate angle $\theta_0 \approx 38.2^\circ$ is illustrated in Fig. 2.42a. All corner positions of the purple rhombus feature the same atomic configuration, making this unit cell a periodic repeating unit. In Fig. 2.42b, we illustrate the entire spectrum of these commensurate angles. The range of interest is narrowed down by considering that TBG with $\theta + 120^\circ$ is identical to TBG with θ due to C_3 -symmetry. Furthermore, TBG with $-\theta$ is a mirror image of TBG with θ . Hence, we confine ourselves to the range of $0^\circ < \theta < 60^\circ$. It is evident that commensuration easily forms around 0° , whereas for larger twist angles, especially around 30° , incommensurate superlattices are more common [44].



(a) Unit cell (purple rhombus) at commensurate angle $\theta_0 \approx 38.2^\circ$. The top (bottom) atoms are represented by dots (circles) and the A (B) sublattices in each layer are colored blue (red).



(b) θ -distribution for forming commensurate TBG. The corresponding Moiré period is represented by the length of solid line (with logarithmic scale).

Figure 2.42 Commensurate and incommensurate angles. Adapted from [45] [44].

2.7.2 Moiré Reciprocal Lattice

In the previous section, we observed the emergence of AA and AB stacking regions upon twisting. This results in a modulation of the interlayer coupling strength with the periodicity of the moiré lattice. Here, we aim to develop the corresponding momentum space representation in detail.

We start by decomposing the Hamiltonian of the TBG system, H_{TBG} , into contributions from the two rotated monolayers, H_1 and H_2 , and the interlayer interaction, V [41]:

$$H_{\text{TBG}} = H_1 + H_2 + V. \quad (2.94)$$

To describe the emerging dynamics in the Bloch domain $L^2(\Omega^*; \mathbb{C}^2) \oplus L^2(\Omega^*; \mathbb{C}^2)$, we use the Bloch basis $\{|k, l, \alpha\rangle\}$, representing electrons in layer $l \in \{1, 2\}$ and sublattice $\alpha \in \{A, B\}$, with the real-space representation:

$$|k, l, \alpha\rangle = \frac{1}{\sqrt{N}} \sum_{\mathbf{r}^{(l)}} e^{i\mathbf{k} \cdot (\mathbf{r}^{(l)} + \mathbf{d}_\alpha^{(l)})} |\mathbf{r}^{(l)}, \alpha\rangle, \quad (2.95)$$

where $\{\mathbf{r}^{(l)}\}$ are the lattice vectors pointing to unit cells in layer l and $\{\mathbf{d}_\alpha^{(l)}\}$ defines the two-atomic basis within a unit cell (eq. 2.43).

Consider the interlayer matrix element:

$$T_{\mathbf{k}, \mathbf{k}'}^{\alpha, \alpha'} = \langle \mathbf{k}, 1, \alpha | V | \mathbf{k}', 2, \alpha' \rangle, \quad (2.96)$$

which corresponds to an electron hopping from sublattice α' in the bottom layer

with momentum \mathbf{k}' to sublattice α in the top layer with momentum \mathbf{k} . Inserting eq. 2.95 results in:

$$T_{\mathbf{k},\mathbf{k}'}^{\alpha,\alpha'} = \frac{1}{N} \sum_{\mathbf{r}^{(1)},\mathbf{r}^{(2)}} e^{-i\mathbf{k}\cdot(\mathbf{r}^{(1)}+\mathbf{d}_\alpha^{(1)})+i\mathbf{k}'\cdot(\mathbf{r}^{(2)}+\mathbf{d}_{\alpha'}^{(2)})} \langle \mathbf{r}^{(1)}, \alpha | V | \mathbf{r}^{(2)}, \alpha' \rangle \quad (2.97)$$

$$= \frac{1}{N} \sum_{\mathbf{r}^{(1)},\mathbf{r}^{(2)}} e^{-i\mathbf{k}\cdot(\mathbf{r}^{(1)}+\mathbf{d}_\alpha^{(1)})+i\mathbf{k}'\cdot(\mathbf{r}^{(2)}+\mathbf{d}_{\alpha'}^{(2)})} \gamma(\mathbf{r}^{(1)} - \mathbf{r}^{(2)} + \mathbf{d}_\alpha^{(1)} - \mathbf{d}_{\alpha'}^{(2)}) \quad (2.98)$$

$$= \frac{1}{N^2|\Omega|} \sum_{\mathbf{r}^{(1)},\mathbf{r}^{(2)}} \sum_{\mathbf{p}} e^{i(\mathbf{p}-\mathbf{k})\cdot\mathbf{r}^{(1)}} e^{i(\mathbf{k}'-\mathbf{p})\cdot\mathbf{r}^{(2)}} e^{i(\mathbf{p}-\mathbf{k})\cdot\mathbf{d}_\alpha^{(1)}-i(\mathbf{p}-\mathbf{k}')\cdot\mathbf{d}_{\alpha'}^{(2)}} \gamma_\perp(\mathbf{p}) \quad (2.99)$$

$$= \sum_{\mathbf{G}^{(1)},\mathbf{G}^{(2)}} \frac{\gamma_\perp(\mathbf{k} + \mathbf{G}^{(1)})}{|\Omega|} e^{i(\mathbf{G}^{(1)}\cdot\mathbf{d}_\alpha^{(1)}-\mathbf{G}^{(2)}\cdot\mathbf{d}_{\alpha'}^{(2)})} \delta_{\mathbf{k}+\mathbf{G}^{(1)},\mathbf{k}'+\mathbf{G}^{(2)}} \quad (2.100)$$

In the second line, we introduced the interlayer hopping matrix element γ_\perp defined by:

$$\langle \mathbf{r}^{(1)}, \alpha | V | \mathbf{r}^{(2)}, \alpha' \rangle = \gamma_\perp(\mathbf{r}^{(1)} - \mathbf{r}^{(2)} + \mathbf{d}_\alpha^{(1)} - \mathbf{d}_{\alpha'}^{(2)}). \quad (2.101)$$

In the third line, we inserted the Fourier transform of the hopping element:

$$\gamma_\perp(\mathbf{r}^{(1)} - \mathbf{r}^{(2)} + \mathbf{d}_\alpha^{(1)} - \mathbf{d}_{\alpha'}^{(2)}) = \frac{1}{|\Omega|N} \sum_{\mathbf{p}} \gamma(\mathbf{p}) e^{i\mathbf{p}\cdot(\mathbf{r}^{(1)}-\mathbf{r}^{(2)}+\mathbf{d}_\alpha^{(1)}-\mathbf{d}_{\alpha'}^{(2)})}, \quad (2.102)$$

where $|\Omega|$ is the area of the unit cell Ω . In the fourth line, we evaluated the sum using the orthogonality relation:

$$\frac{1}{N} \sum_{\mathbf{r}} e^{i(\mathbf{p}-\mathbf{k})\cdot\mathbf{r}} = \delta_{\mathbf{p},\mathbf{k}}. \quad (2.103)$$

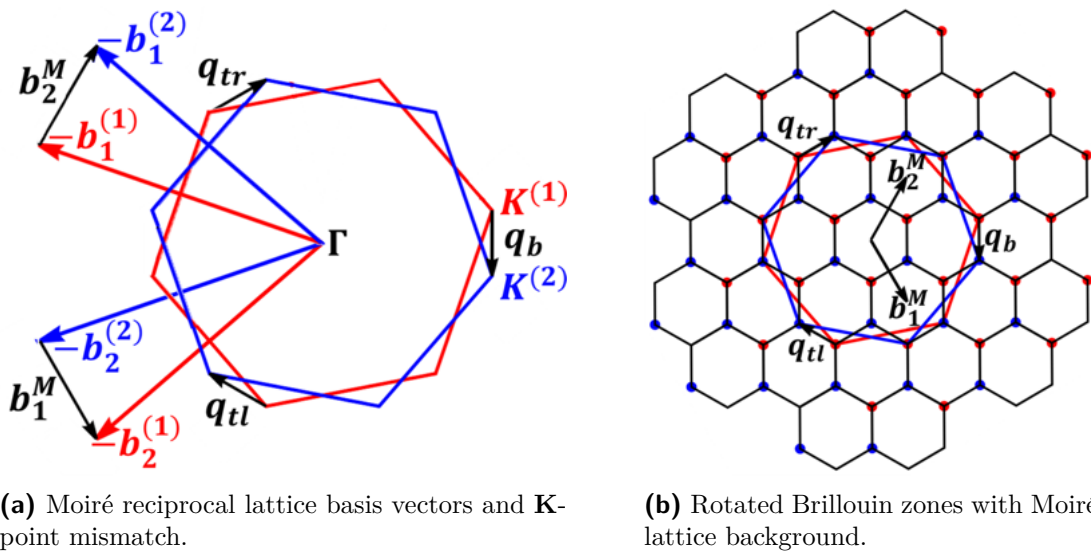


Figure 2.43 Moiré reciprocal lattice. Adapted from [41].

The moiré pattern manifests itself in the Kronecker delta, enforcing $\mathbf{p} = \mathbf{k} + \mathbf{G}^{(1)} =$

$\mathbf{k}' + \mathbf{G}^{(2)}$, and consequently $\Delta\mathbf{k} = \mathbf{k} - \mathbf{k}' = \mathbf{G}^{(2)} - \mathbf{G}^{(1)}$. Therefore, the momentum difference in the interlayer hopping $\Delta\mathbf{k}$ must be a vector from the union of all vectors $\{\mathbf{G}^{(1)}\} \cup \{\mathbf{G}^{(2)}\}$, which generate the reciprocal lattice $\Lambda_M^* := \Lambda_1^* \cup \Lambda_2^*$ [34]. We choose the following moiré reciprocal lattice vectors (Fig. 2.43a):

$$\mathbf{b}_1^M = \mathbf{b}_2^{(2)} - \mathbf{b}_2^{(1)} = \frac{4\pi \sin(\theta/2)}{3a} \begin{bmatrix} 1 \\ -\sqrt{3} \end{bmatrix}, \quad (2.104)$$

$$\mathbf{b}_2^M = \mathbf{b}_1^{(1)} - \mathbf{b}_1^{(2)} = \frac{4\pi \sin(\theta/2)}{3a} \begin{bmatrix} 1 \\ \sqrt{3} \end{bmatrix}. \quad (2.105)$$

We define the moiré reciprocal lattice as:

$$\Lambda_M^* = \left\{ \mathbf{G}^M = l_1 \mathbf{b}_1^M + l_2 \mathbf{b}_2^M \mid (l_1, l_2)^T \in \mathbb{Z}^2 \right\}, \quad (2.106)$$

which is plotted in the background of the two rotated Brillouin zones in Fig. 2.43b.

This hexagonal moiré lattice features lattice points with three nearest neighbors defined by the relative vectors:

$$\begin{aligned} \mathbf{q}_b &= \frac{4\pi \sin(\theta/2)}{3\sqrt{3}a} \begin{bmatrix} 0 \\ -1/2 \end{bmatrix}, \\ \mathbf{q}_{\text{tr}} &= \frac{4\pi \sin(\theta/2)}{3\sqrt{3}a} \begin{bmatrix} \sqrt{3} \\ 1 \end{bmatrix}, \\ \mathbf{q}_{\text{tl}} &= \frac{4\pi \sin(\theta/2)}{3\sqrt{3}a} \begin{bmatrix} -\sqrt{3} \\ 1 \end{bmatrix}. \end{aligned} \quad (2.107)$$

These vectors provide a nice geometrical interpretation (Fig. 2.43b), characterizing the momentum mismatch between the corners of the two rotated layers \mathbf{K} , with magnitudes $|\mathbf{q}_b|, |\mathbf{q}_{\text{tr}}|, |\mathbf{q}_{\text{tl}}| = 2|\mathbf{K}| \sin(\theta/2) (\approx |\mathbf{K}|\theta \text{ for small angles})$.

2.7.3 Moiré Potential

To advance our discussion, we must specify the function γ_\perp . We anticipate that its behavior will closely resemble that depicted in Fig. 2.44, showing a smooth oscillation of the local interaction strength on the scale of a_M , which emerges from the corresponding variation in the local configuration of the p -orbitals of the respective layers. Up to this point, we have examined two configurations of p -orbital pairs: the π -bond, which characterizes the intralayer interaction, and the σ -bond, which describes the vertical interlayer interaction in bilayers on dimer sites. However, in contrast to our considerations in Sec. 2.5, the relative positions of the p -orbitals vary

in space, forcing us to account for the spatial dependence of the overlap integrals.

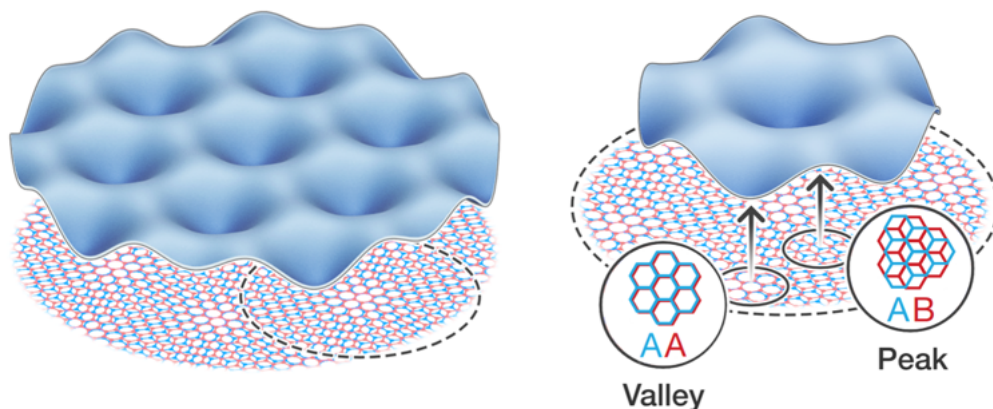
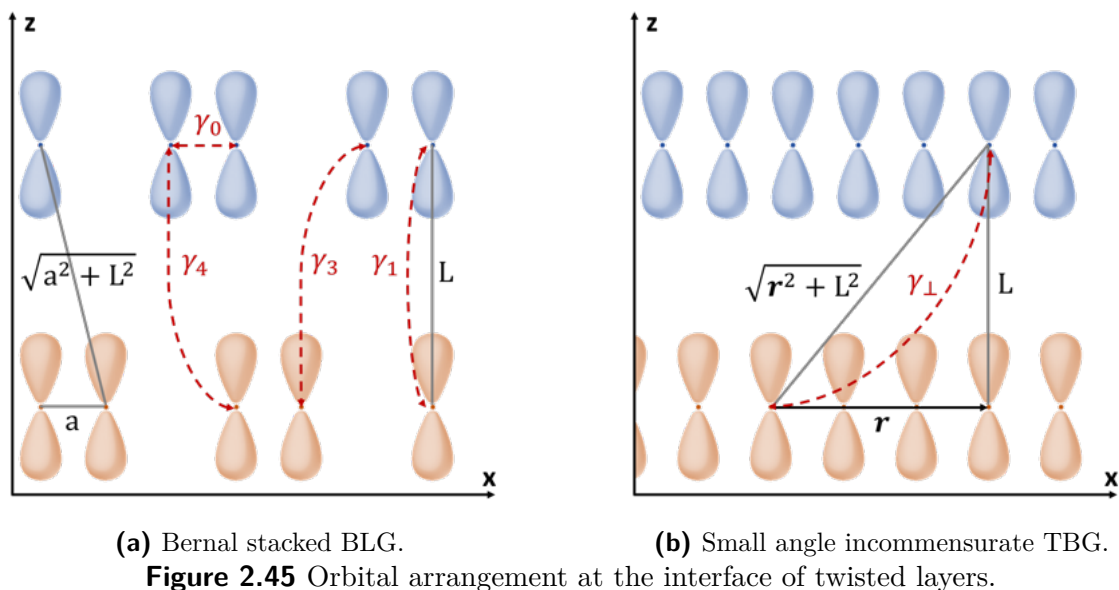


Figure 2.44 Moiré potential in real space. Adapted from [46].

Within the two-center approximation (Sec. 2.2.2), these overlap matrix elements can generally be well approximated by an exponential decay with a material- and orbital-specific pre-exponential factor λ , so that we can make the ansatz $\gamma(R) \propto \exp(-\lambda R)$, where R is the three-dimensional distance $R = \sqrt{|\mathbf{r}|^2 + L^2}$ between sites [47]. Accordingly, we write

$$\gamma(\mathbf{r}) \rightarrow \gamma(R) = \gamma(\sqrt{|\mathbf{r}|^2 + L^2}), \quad (2.108)$$

where L is the graphene layer separation and \mathbf{r} is the planar projection of the three-dimensional distance.



We can determine λ by ensuring that our expression reproduces γ_0 and γ_1 . Consequently, the transfer integrals γ_π (π -bond) and γ_σ (σ -bond) of the p -orbitals in

carbon can be written as [48]:

$$\gamma_\pi(R) = -\gamma_0 \exp\left(\lambda_\pi\left(1 - \frac{R}{a}\right)\right) \quad (2.109)$$

$$\gamma_\sigma(R) = \gamma_1 \exp\left(\lambda_\sigma\left(1 - \frac{R}{L}\right)\right) \quad (2.110)$$

Since $\gamma_\pi(a) = \gamma_0$ and $\gamma_\sigma(L) = \gamma_1$, these expressions are consistent with our previous results for MLG and BLG. To determine λ_π , we consider the second nearest neighbor hopping amplitude γ_n (Sec 2.4.2), so that

$$\frac{\gamma_\pi(a)}{\gamma_\pi(\sqrt{3}a)} = \frac{\gamma_0}{\gamma_n} = \frac{1}{\exp(\lambda_\pi(1 - \sqrt{3}))} = \exp(\lambda_\pi(\sqrt{3} - 1)) \quad (2.111)$$

and we obtain [34]

$$\lambda_\pi = \frac{\ln(\gamma_0/\gamma_n)}{\sqrt{3} - 1} \approx 3.15. \quad (2.112)$$

The remaining parameter, λ_σ , can be fixed by assuming equal spatial exponential-decreasing coefficients [34], i.e.,

$$\frac{\lambda_\pi}{a} = \frac{\lambda_\sigma}{L} \Rightarrow \lambda_\sigma = \lambda_\pi \frac{L}{a} \approx 7.42. \quad (2.113)$$

Both overlap terms are plotted in Fig 2.47a. To model $\gamma_\perp(\mathbf{r})$, we assume that the coupled p_z -orbitals lie in the xz -plane. We rotate the coordinate system passively clockwise, such that \mathbf{R} aligns with the z -axis in the new coordinate system (Fig 2.46). Now we can describe both orbitals as linear combinations of p_x and p_z orbitals, $|p_z\rangle \rightarrow \sin(\alpha)|p_x\rangle + \cos(\alpha)|p_z\rangle$.

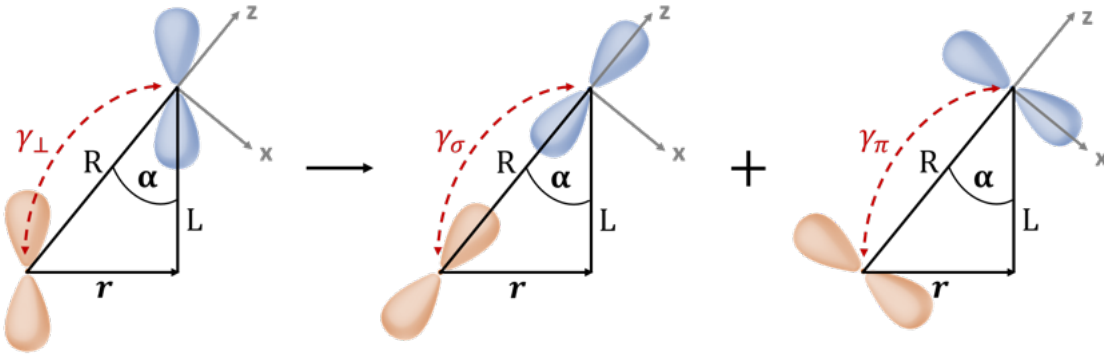


Figure 2.46 Illustration of the overlap integral calculation: One p_z -orbital is initially located at the origin, while another p_z -orbital is at the separation vector \mathbf{R} . The coordinate system is rotated so that the second orbital shifts to $R\hat{z}$, resulting in the orbitals becoming linear combinations of p_x and p_z .

Our overlap integral then takes the form [49]

$$\gamma_{\perp}(\mathbf{r}) = \cos^2(\alpha)\gamma_{\sigma}(R) + \sin^2(\alpha)\gamma_{\pi}(R), \quad (2.114)$$

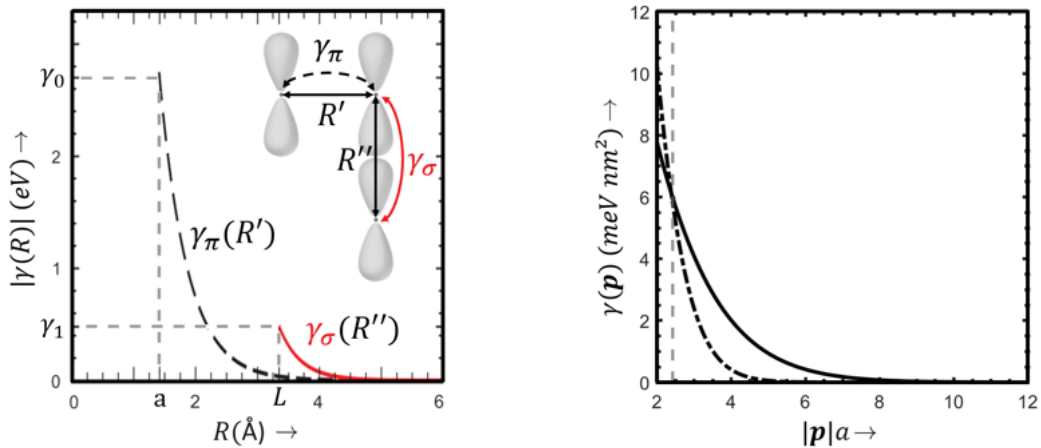
where α is the angle between the z -axis and \mathbf{r} , defined by

$$\cos^2(\alpha) = \frac{L^2}{L^2 + |\mathbf{r}|^2}. \quad (2.115)$$

Inserting equations [2.109], [2.110], and [2.115] into eq [2.114] gives us

$$\gamma_{\perp}(\mathbf{r}) = \frac{1}{L^2 + |\mathbf{r}|^2} \left(-\gamma_0 L^2 \exp\left(3.15\left(1 - \frac{\sqrt{L^2 + |\mathbf{r}|^2}}{a}\right)\right) + \gamma_1 |\mathbf{r}|^2 \exp\left(7.42\left(1 - \frac{\sqrt{L^2 + |\mathbf{r}|^2}}{L}\right)\right) \right),$$

again as a function of the projected two-dimensional distance \mathbf{r} .



(a) Decay of the real space amplitude of [2.109] (black dashed line) and [2.110] (red solid line)

(b) Decay of the Fourier amplitude of eq. [2.114] (solid) and eq. [2.116] (dashed-dot). Dashed gray line at $\mathbf{K}a$.

Figure 2.47 Functional form of the interlayer coupling amplitude. Adapted from [41].

The corresponding 2D in-plane Fourier transform of $\gamma_{\perp}(\mathbf{r})$ is obtained numerically and is plotted in Fig. [2.47b] along with an exponential ansatz fitted directly in Fourier space, given as

$$\gamma_{\perp}(\mathbf{p}) = t_0 e^{-\lambda_{\perp}(|\mathbf{p}|L)^{\eta}}, \quad (2.116)$$

where $t_0 = 20 \text{ meV nm}^2$, $\lambda_{\perp} = 0.13$, $\eta = 1.25$, and $L = 0.335 \text{ nm}$ [40].

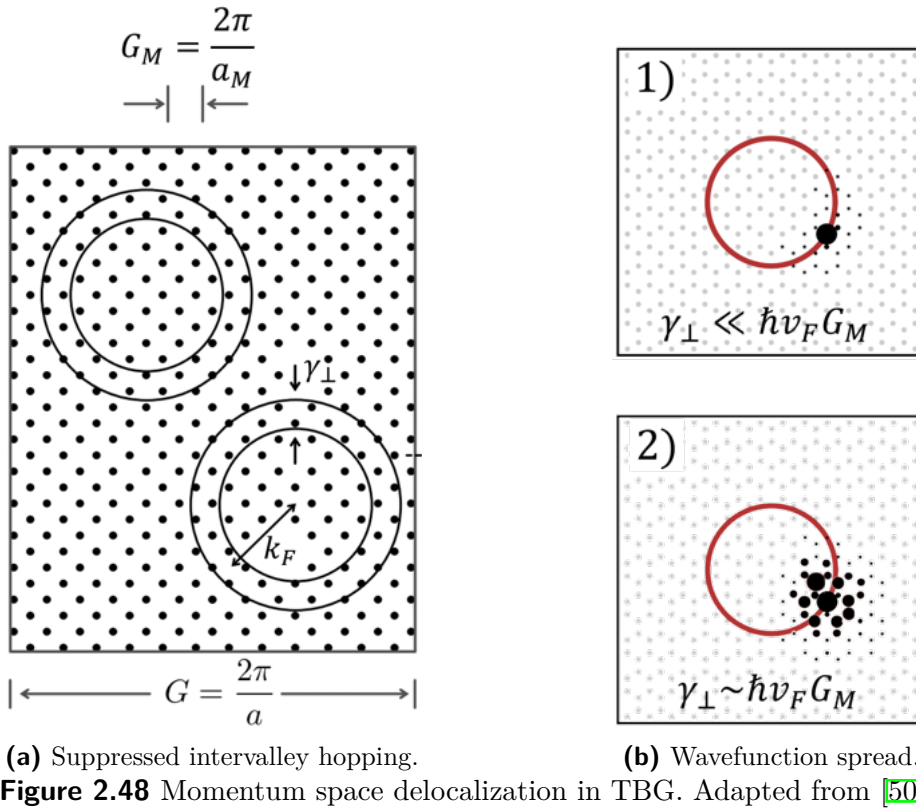
Note that the two-dimensional Fourier transform of $\gamma(\mathbf{p})$ exhibits a rapid decay as a function of $|\mathbf{p}|$, indicative of the short-ranged nature of $\gamma_{\perp}(\mathbf{p})$ in momentum space.

Qualitatively, this behavior can be understood by considering that the layer separation

ration L exceeds the separation between carbon atoms a within the layers by more than a factor of two. Given that the coupling strength between orbitals decays on the scale of the inter-orbital distance a , hopping processes with a large in-plane component are strongly suppressed. Consequently, the predominant contribution arises from the small \mathbf{r} -regime, where $|\mathbf{r}| \ll L$. We can conclude that γ_{\perp} varies with R on the scale of L , leading to a broadened distribution in terms of a . Thus, its two-dimensional Fourier transform is sharply peaked and declines rapidly for $|\mathbf{p}|L > 1$.

In the following, the exponential ansatz eq. 2.116 as proposed by Bistritzer et al. [40], is adopted, since the numerical result tends to underestimate hopping amplitudes near the Dirac points.

2.7.4 Momentum Space Delocalization



The interlayer coupling term γ_{\perp} effectively begins to delocalize states in momentum space by coupling to neighboring sites connected by $\mathbf{G}^M \in \Lambda_M^*$. As a result, instead of having eigenvectors $|\mathbf{k}, l, \alpha\rangle$ with well-defined momentum \mathbf{k} , the interlayer coupling term causes the wave functions to spread in momentum space.

This effect can be visualized as broadened quasi-one-dimensional Fermi surfaces centered around the Fermi lines of the unperturbed system. More precisely, typical

wave functions probe a region of width proportional to γ_{\perp} around these contours, as depicted in Fig. 2.48a for two different valleys. For small twist angles where $\gamma_{\perp}(\mathbf{p})/|\Omega| \ll \hbar v_F |\mathbf{G}|$, intervalley hopping processes are negligible, allowing us to focus on the vicinity of a \mathbf{K} point's Fermi surface.

In the regime of small γ_{\perp} , the spread remains relatively localized. We can quantify this hybridization criterion by the ratio α between the interlayer hopping amplitude γ_{\perp} , which describes the coupling strength, and the energy shift between nearest sites in the moiré momentum lattice ($\hbar v_F |\mathbf{q}_b|, \hbar v_F |\mathbf{q}_{tr}|, \hbar v_F |\mathbf{q}_d| = \hbar v_F |\mathbf{K}(\theta)$), given by:

$$\alpha = \frac{\gamma_{\perp}(\mathbf{p})/|\Omega|}{\hbar v_F |\mathbf{K}(\theta)} \quad (2.117)$$

Qualitatively, this characterizes the competition between the kinetic energy and the interlayer hybridization energy. Figure 2.48b illustrates the resulting momentum space delocalization for TBG in the regimes of large α and small α . In the former case ($\theta > 10^\circ$), γ_{\perp} is small compared to the typical Moiré Brillouin zone dimensions. Consequently, all interlayer hopping processes are strongly suppressed, implying the absence of correlations between distinct eigenfunctions and their eigenvalues. This limit corresponds to complete momentum space localization, where the system can essentially be treated as two decoupled monolayers with individual eigenfunctions centered around specific momenta \mathbf{k} in the MLG Brillouin zone. This regime is directly relevant for bilayer graphene at large incommensurate twist angles [50].

Conversely, for $\theta < 10^\circ$, many sites fall within the probed energy regime, so the moiré potential begins to delocalize the wavefunction through efficient coupling of sites in the momentum space moiré lattice over scales $\sim \frac{2\pi}{a_M}$. Consequently, the wavefunctions become correlated.

2.7.5 Simplifications of the Hopping Term

“Wissen Sie, wenn man zu rechnen anfängt, b'scheisst man unwillkürlich.”

Albert Einstein

From our discussion, we derived two important insights. First, $T_{\mathbf{k},\mathbf{k}'}^{\alpha,\alpha'}$ causes the wave function to hybridize over neighbors of the momentum lattice connected by $\Delta\mathbf{k} = \mathbf{G}^{(2)} - \mathbf{G}^{(1)}$, provided the energy difference is of the order $\approx \hbar v_F \Delta\mathbf{k} < \gamma_{\perp}$. Accordingly, in leading order and for small angles, this condition constrains hopping governed by the smallest moiré reciprocal vectors [34]:

$$\Delta\mathbf{k} \in \{\mathbf{0}, \mathbf{b}_1^{(1)} - \mathbf{b}_1^{(2)}, \mathbf{b}_2^{(1)} - \mathbf{b}_2^{(2)}\} = \{\mathbf{0}, \mathbf{b}_2^M, -\mathbf{b}_1^M\}. \quad (2.118)$$

The second insight is that the contributions from the Fourier components $\gamma(\mathbf{k} + \mathbf{G}^{(1)})$ and $\gamma(\mathbf{k}' + \mathbf{G}^{(2)})$ are strongly suppressed with increasing distance from the Γ -point. This implies that we need to consider only the valley closest to the Γ -point. We take the Dirac point $\mathbf{K}_D = \frac{4\pi}{3\sqrt{3}a}[1, 0]^T$ as a reference, so that the other two equivalent counterparts are connected by $-\mathbf{b}_1$ and $-\mathbf{b}_2$. Since these feature the same distance from the Γ -point, we fix the coupling strength $\omega_0 = \frac{\gamma_{\perp}(\mathbf{K}_D^{(l)} + \mathbf{G}_i^{(l)})}{|\Gamma|} = 110\text{meV}$ for all processes near the valleys, where $\mathbf{G}_1 = \mathbf{0}$, $\mathbf{G}_2 = -\mathbf{b}_1$, and $\mathbf{G}_3 = -\mathbf{b}_2$. We redefine eq. 2.117 as [6]:

$$\alpha = \frac{\omega_0}{\hbar v_F |\mathbf{K}| \theta}, \quad (2.119)$$

while the interlayer hopping is then governed by:

$$\begin{aligned} T_{\mathbf{k}, \mathbf{k}'}^{\alpha, \alpha'} &= \sum_{i \in \{1, 2, 3\}} \omega_0 e^{i(\mathbf{G}_i^{(1)} \cdot \mathbf{d}_{\alpha}^{(1)} - \mathbf{G}_i^{(2)} \cdot \mathbf{d}_{\alpha'}^{(2)})} \delta_{\mathbf{k} - \mathbf{k}', \mathbf{G}^{(2)} - \mathbf{G}^{(1)}} \\ &= T_1^{\alpha, \alpha'} \delta_{\mathbf{k} - \mathbf{k}', \mathbf{0}} + T_2^{\alpha, \alpha'} \delta_{\mathbf{k} - \mathbf{k}', \mathbf{b}_2^M} + T_3^{\alpha, \alpha'} \delta_{\mathbf{k} - \mathbf{k}', -\mathbf{b}_1^M}, \end{aligned} \quad (2.120)$$

where the sublattice-dependent interlayer hopping is governed by the matrices [6]:

$$T_1 = \omega_0 \begin{bmatrix} 1 & 1 \\ 1 & 1 \end{bmatrix}, \quad (2.121)$$

$$T_2 = \omega_0 \begin{bmatrix} e^{i\phi} & 1 \\ e^{-i\phi} & e^{i\phi} \end{bmatrix}, \quad (2.122)$$

$$T_3 = \omega_0 \begin{bmatrix} e^{-i\phi} & 1 \\ e^{i\phi} & e^{-i\phi} \end{bmatrix}, \quad (2.123)$$

where $\phi = \frac{2\pi}{3}$.

2.7.6 Moiré Band Structure

For commensurate twist angles, electrons move within a periodic potential, exhibiting the periodicity of the moiré lattice Λ_M . Consequently, Bloch's Theorem applies, and we anticipate coherent electronic motion across the layers. The electronic properties of this hybridized interface can be determined using our tight-binding method, which now involves n -component eigenvectors to account for the contributions of all n atoms within the new supercell.

In contrast, generic twist angles are incommensurate, resulting in a loss of period-

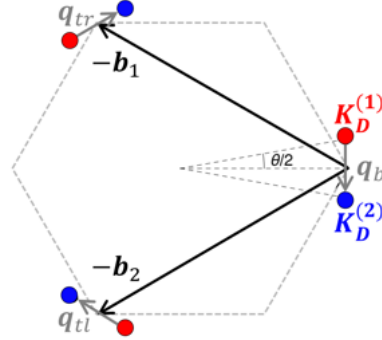


Figure 2.49 k-space geometry.

icity. As a result, Bloch's theorem is no longer applicable, and it becomes inappropriate to refer to energy bands. However, due to the strong suppression of large hopping processes not included in eq.2.118 at small angles ($\theta < 10^\circ$), the low-energy dynamics can still be well approximated by a periodic Hamiltonian [6].

Low-Energy Physics

In the low-energy regime, the Hamiltonian H_{MLG} is described by the Dirac Hamiltonian. Incorporating the relative twist yields:

$$H_1 = \hbar v_F |\mathbf{q}| \begin{bmatrix} 0 & e^{-i(\theta_q + \theta/2)} \\ e^{i(\theta_q + \theta/2)} & 0 \end{bmatrix} = \hbar v_F \boldsymbol{\sigma}^{\theta/2} \cdot \mathbf{q}, \quad (2.124)$$

$$H_2 = \hbar v_F |\mathbf{q}| \begin{bmatrix} 0 & e^{-i(\theta_q - \theta/2)} \\ e^{i(\theta_q - \theta/2)} & 0 \end{bmatrix} = \hbar v_F \boldsymbol{\sigma}^{-\theta/2} \cdot \mathbf{q}, \quad (2.125)$$

where we have defined the 'rotated' Pauli matrices: $\boldsymbol{\sigma}^\theta = e^{-i\theta\sigma^z/2}[\sigma^x, \sigma^y]^T e^{i\theta\sigma^z/2}$.

In the low-energy approximation, eq.2.120 takes the form:

$$\begin{aligned} T_{\mathbf{q}, \mathbf{q}'}^{\alpha, \alpha'} &= \sum_{i \in \{1, 2, 3\}} T_i^{\alpha, \alpha'} \delta_{(\mathbf{q} + \mathbf{K}_D^{(1)}) - (\mathbf{q}' + \mathbf{K}_D^{(2)}), \mathbf{G}_i^{(2)} - \mathbf{G}_i^{(1)}} \\ &= T_1^{\alpha, \alpha'} \delta_{\mathbf{q} - \mathbf{q}', \mathbf{K}_D^{(2)} - \mathbf{K}_D^{(1)}} + T_2^{\alpha, \alpha'} \delta_{\mathbf{q} - \mathbf{q}', \mathbf{K}_D^{(2)} - \mathbf{K}_D^{(1)} + \mathbf{b}_2^M} + T_3^{\alpha, \alpha'} \delta_{\mathbf{q} - \mathbf{q}', \mathbf{K}_D^{(2)} - \mathbf{K}_D^{(1)} - \mathbf{b}_1^M} \\ &= T_1^{\alpha, \alpha'} \delta_{\mathbf{q} - \mathbf{q}', \mathbf{q}_b} + T_2^{\alpha, \alpha'} \delta_{\mathbf{q} - \mathbf{q}', \mathbf{q}_{tr}} + T_3^{\alpha, \alpha'} \delta_{\mathbf{q} - \mathbf{q}', \mathbf{q}_{tl}}, \end{aligned} \quad (2.126)$$

where

$$\mathbf{q}_b = \mathbf{K}_D^{(2)} - \mathbf{K}_D^{(1)}, \quad (2.127)$$

$$\mathbf{q}_{tr} = \mathbf{K}_D^{(2)} - \mathbf{K}_D^{(1)} + \mathbf{b}_2^M = \mathbf{q}_b + \mathbf{b}_2^M, \quad (2.128)$$

$$\mathbf{q}_{tl} = \mathbf{K}_D^{(2)} - \mathbf{K}_D^{(1)} - \mathbf{b}_1^M = \mathbf{q}_b - \mathbf{b}_1^M. \quad (2.129)$$

These vectors correspond to the nearest neighbors in momentum space as previously introduced in eq.2.107. Thus, our results critically depend on the assumption that "nearest-neighbor" momentum space hopping predominates.

By folding out the first moiré Brillouin zone to the extended zone scheme, a lattice emerges that is spanned by the reciprocal moiré lattice vectors, as depicted in Fig.2.50.

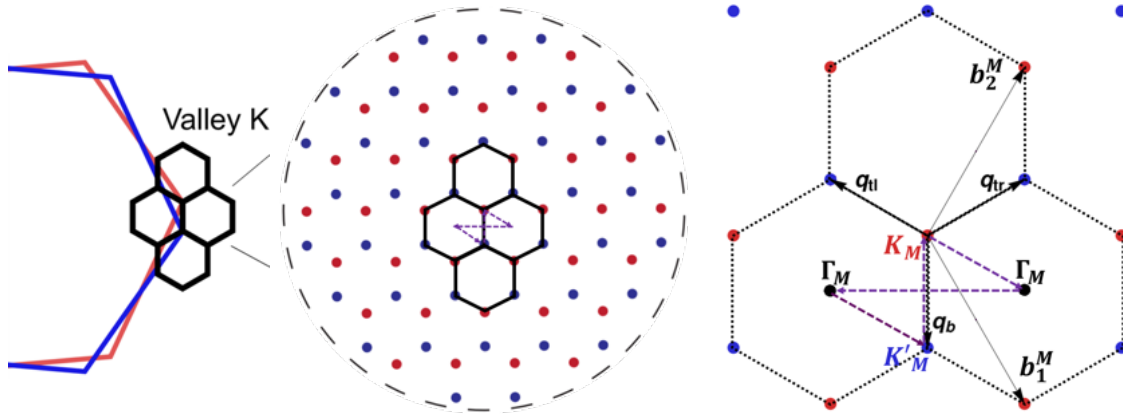


Figure 2.50 Emergence of the moiré Brillouin zone in the extended zone scheme from the momentum mismatch in the \mathbf{K} -valley. The purple dashed path marks the trajectory in \mathbf{k} -space for Fig. 2.55, Fig. 2.57, and Fig. 2.58. Adapted from [34] [51].

Shell Numbering of the Momentum Lattice

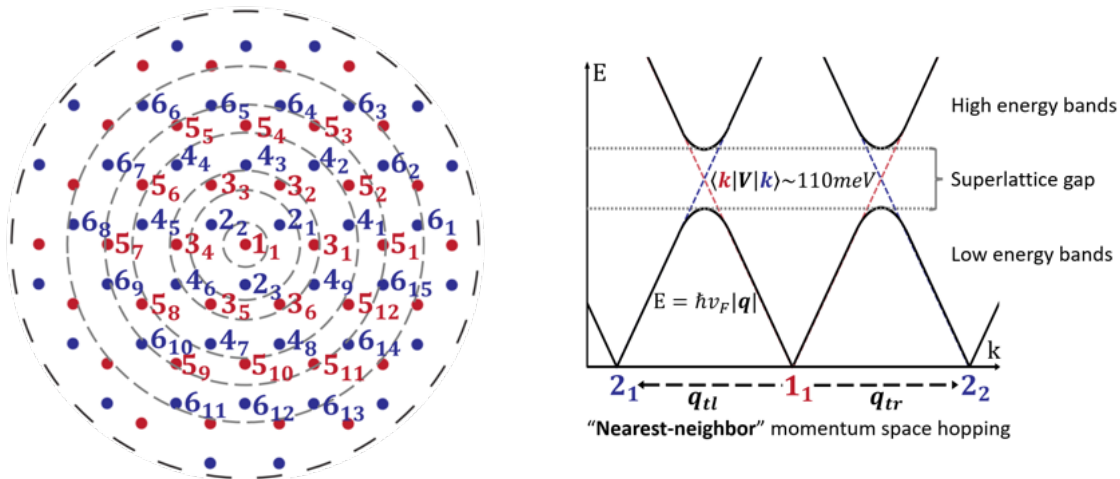


Figure 2.51 Shell numbering and next-nearest-neighbor interaction in the momentum lattice.

In this section, we develop the eigenstates of H_{TBG} in the Bloch basis $\{|\mathbf{k}, l, \alpha\rangle\} = \{|\mathbf{q} + \mathbf{K}_D, l, \alpha\rangle\}$. Due to the successive coupling of each site with its surrounding neighbors across the momentum lattice, the eigenvalue equation cannot be brought into a closed form. However, given the finite spread in momentum space $\sim \frac{\omega_0}{\hbar v_F |\mathbf{K}_D|}$, we expect diminishing contributions from larger \mathbf{G}^M vectors. Therefore, it is essential to establish an appropriate cutoff to ensure the convergence of the Hamiltonian. To this end, we introduce a shell numbering system in momentum space, centered around the \mathbf{K}_M -point 1_1 of the moiré lattice (Fig. 2.51). The sites within shell n are denoted as n_i , where $n - 1$ represents the minimal graph distance (i.e., the minimal number of bonds traversed on the honeycomb lattice) from the center 1_1 , and i indexes the number of sites with the same graph distance $n - 1$. Assuming that only nearest-neighbor coupling is relevant, the momentum hopping T_i occurs exclusively

between sites in different shells $n \leftrightarrow n + 1$, and not between sites within the same shell [52].

$$H(\mathbf{q}) \begin{bmatrix} c_{A_1}^{\mathbf{q}} \\ c_{B_1}^{\mathbf{q}} \\ c_{A_2}^{\mathbf{q}+\mathbf{q}_b} \\ c_{B_2}^{\mathbf{q}+\mathbf{q}_b} \\ c_{A_2}^{\mathbf{q}+\mathbf{q}_{tr}} \\ c_{B_2}^{\mathbf{q}+\mathbf{q}_{tr}} \\ c_{A_1}^{\mathbf{q}+\mathbf{q}_{tl}} \\ c_{B_2}^{\mathbf{q}+\mathbf{q}_{tl}} \end{bmatrix} = H(\mathbf{q}) \begin{bmatrix} c_{A_1}^{\mathbf{q}} \\ c_{B_1}^{\mathbf{q}} \\ c_{A_2}^{\mathbf{q}+\mathbf{q}_b} \\ c_{B_2}^{\mathbf{q}+\mathbf{q}_b} \\ c_{A_2}^{\mathbf{q}+\mathbf{q}_b+b_2^M} \\ c_{B_2}^{\mathbf{q}+\mathbf{q}_b+b_2^M} \\ c_{A_1}^{\mathbf{q}+\mathbf{q}_b-b_1^M} \\ c_{B_2}^{\mathbf{q}+\mathbf{q}_b-b_1^M} \end{bmatrix} = E(\mathbf{q}) \begin{bmatrix} c_{A_1}^{\mathbf{q}} \\ c_{B_1}^{\mathbf{q}} \\ c_{A_2}^{\mathbf{q}+\mathbf{q}_b} \\ c_{B_2}^{\mathbf{q}+\mathbf{q}_b} \\ c_{A_2}^{\mathbf{q}+\mathbf{q}_b+b_2^M} \\ c_{B_2}^{\mathbf{q}+\mathbf{q}_b+b_2^M} \\ c_{A_1}^{\mathbf{q}+\mathbf{q}_b-b_1^M} \\ c_{B_2}^{\mathbf{q}+\mathbf{q}_b-b_1^M} \end{bmatrix}$$

Figure 2.52 Eigenvalue equation with truncation at $n = 2$.

The eigenvalue equation of the simplest version of this model, truncated at $n = 2$, with sites 1_1 and $2_1, 2_2, 2_3$, is illustrated in Fig. 2.52, where \mathbf{q} lies within the moiré reciprocal space (Fig. 2.51).

$ (0, 0), 1\rangle$	$ (0, 0), 2\rangle$	$ (0, 1), 2\rangle$	$ (-1, 0), 2\rangle$	
$H_1(\mathbf{q} + \mathbf{0})$	T_1	T_2	T_3	$\langle(0, 0), 1 $
T_1^\dagger	$H_2(\mathbf{q} + \mathbf{q}_b)$	0	0	$\langle(0, 0), 2 $
T_2^\dagger	0	$H_2(\mathbf{q} + \mathbf{q}_{tr})$	0	$\langle(0, 1), 2 $
T_3^\dagger	0	0	$H_2(\mathbf{q} + \mathbf{q}_{tl})$	$\langle(-1, 0), 2 $

Figure 2.53 Hamiltonian matrix elements of the 8-band model ($n = 2$).

The minimum matrix Hamiltonian for the TBG system is 8×8 , which gives rise to 8 bands. Instead of writing out the entire system of equations, we can compress and interpret it using the following convenient notation:

$$|(m_1, m_2), 1\rangle = |\mathbf{q} + m_1 b_1^M + m_2 b_2^M, 1\rangle, \quad (2.130)$$

$$|(m_1, m_2), 2\rangle = |\mathbf{q} + \mathbf{q}_b + m_1 b_1^M + m_2 b_2^M, 2\rangle, \quad (2.131)$$

such that the Hamiltonian matrix elements $\langle(m_1, m_2), l|H_{TBG}|(m'_1, m'_2), l'\rangle$ are represented as shown in Fig. 2.53.

$ (0, 0), 1\rangle$	$ (0, 0), 2\rangle$	$ (0, 1), 2\rangle$	$ (-1, 0), 2\rangle$	$ (0, -1), 1\rangle$	$ (1, 0), 1\rangle$	$ (0, 1), 1\rangle$	$ (1, 1), 1\rangle$	$ (-1, 0), 1\rangle$	$ (-1, -1), 1\rangle$	
-	T_1	T_2	T_3	0	0	0	0	0	0	$\langle(0, 0), 1 $
T_1^\dagger	-	0	0	T_2^\dagger	T_3^\dagger	0	0	0	0	$\langle(0, 0), 2 $
T_2^\dagger	0	-	0	0	0	T_1^\dagger	T_3^\dagger	0	0	$\langle(0, 1), 2 $
T_3^\dagger	0	0	-	0	0	0	0	T_1^\dagger	T_2^\dagger	$\langle(-1, 0), 2 $
0	T_2	0	0	-	0	0	0	0	0	$\langle(0, -1), 1 $
0	T_3	0	0	0	-	0	0	0	0	$\langle(1, 0), 1 $
0	0	T_1	0	0	0	-	0	0	0	$\langle(0, 1), 1 $
0	0	T_3	0	0	0	0	-	0	0	$\langle(1, 1), 1 $
0	0	0	T_1	0	0	0	0	-	0	$\langle(-1, 0), 1 $
0	0	0	T_2	0	0	0	0	0	-	$\langle(-1, -1), 1 $

Figure 2.54 Hamiltonian matrix elements of the 20-band model ($n = 3$).

Similarly, if we consider a truncation at $n = 3$, the model expands to a 20-band system, defined by the non-diagonal matrix elements (the diagonal ones are trivial and are omitted for brevity) shown in Fig. 2.54

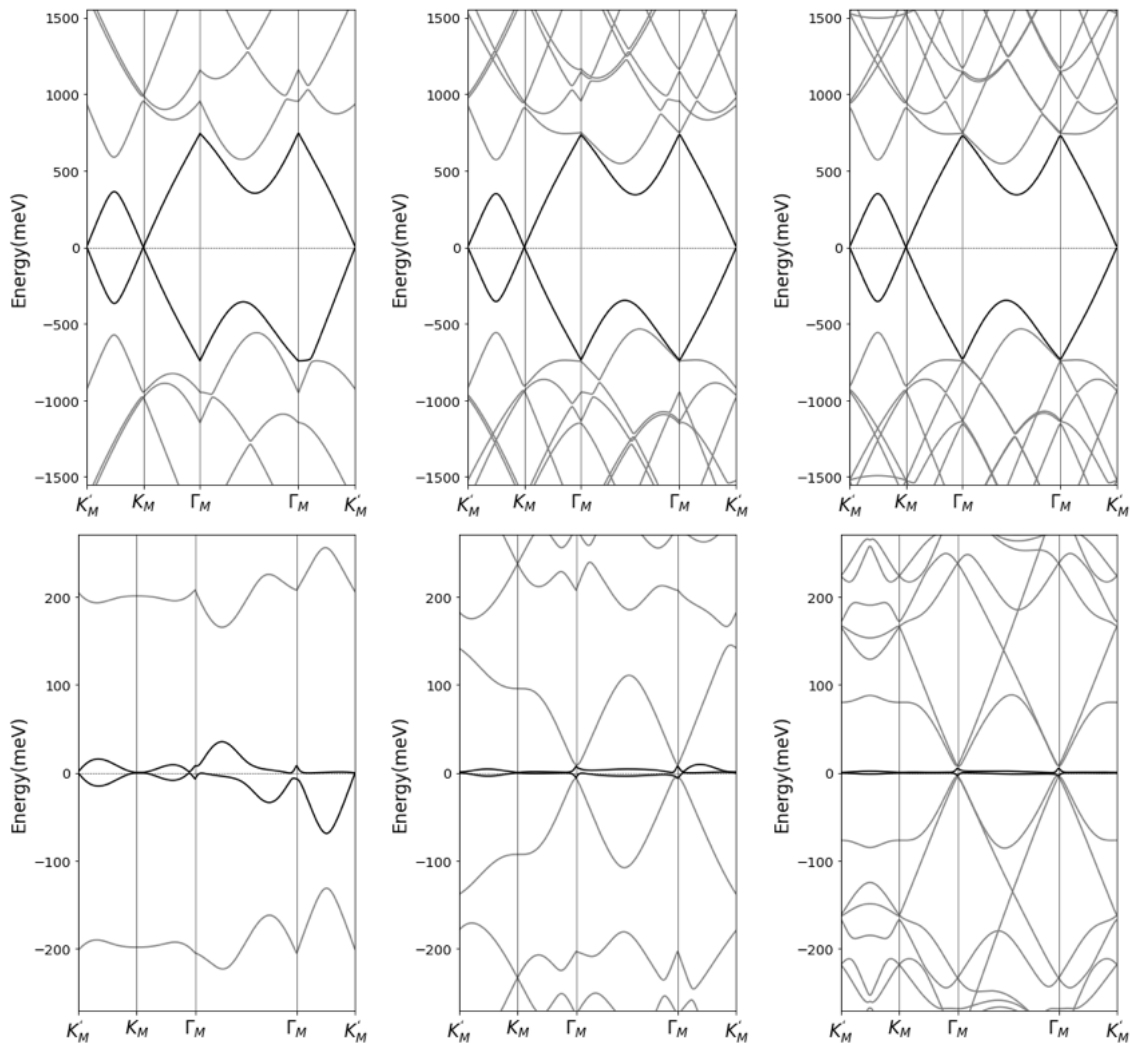


Figure 2.55 The band structure of TBG resulting for different truncations (from left to right: $n = 2, 3, 4$) plotted along the path in Fig. 2.50 for twist angles $\theta = 5.00^\circ$ (top) and 1.05° (bottom).

In Fig. 2.55, we plot the band structures for TBG at twist angles of 5° and 1.05° for cutoff shells $n = 2, 3, 4$ along the purple dashed path in Fig. 2.50. The different convergence behaviors are evident: while the band structure for 5° exhibits minimal changes between the third and fourth shells, indicating good convergence at the third shell, the 1.05° case requires the inclusion of the fourth shell. This behavior is expected, as decreasing the twist angle corresponds to increasing α , which forces us to consider the wavefunction spread over larger areas in momentum space.

Lattice Relaxation

In the models discussed thus far, we have assumed that the carbon atoms within the lattice are rigid, maintaining a fixed carbon-carbon bond length of 0.142nm and an interlayer distance of 0.33nm. However, in reality, these atoms are not static; they can move to positions that minimize their potential energy.

In TBG, the local stacking order smoothly transitions between AA and AB stacking. In the absence of lattice relaxation, these regions would occupy the same amount of area. However, from an energetic perspective, the AA stacking configuration exhibits higher potential energy due to the increased overlap of electron clouds in adjacent layers, as more atoms are directly aligned on top of each other. This increased overlap enhances Pauli repulsion, leading to a distortion or stretching of the AA regions in order to reduce the system's energy [53].

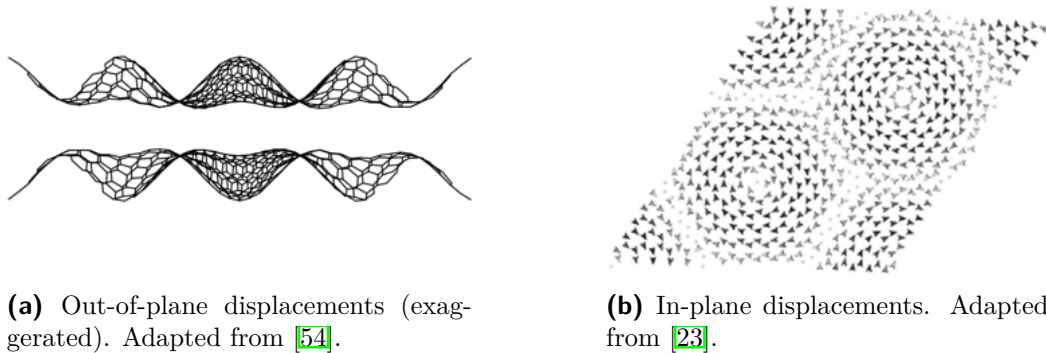


Figure 2.56 Effects of lattice relaxation on the crystal structure.

The equilibrium configuration represents a compromise between stacking energy and strain energy, as excessive distortion, stretching, or sliding is also energetically unfavorable. There are two major relaxation effects in TBG. First, the interlayer distance increases in AA regions relative to AB regions, suppressing interlayer hybridization, as illustrated in Fig. 2.56a. Second, the AA regions tend to shrink in size relative to the AB regions, resulting in an in-plane displacement of carbon atoms. This effect is achieved by a slight rotation of each moiré pattern around the AA center, as depicted in Fig. 2.56b, which shows the displacements from positions prior to relaxation.

These local relaxation effects can significantly influence the electronic band structure of TBG, especially at small twist angles, where the material consists of larger, well-defined AA and AB regions. The interlayer hopping amplitudes between AA (BB) and AB (BA) regions are altered due to these relaxation effects.

To account for the increased interlayer separation at AA-stacking sites and the shrinkage of their areas, we introduce a ratio, ω , that modifies the AA and AB interlayer hopping terms. Consequently, the hopping matrices have different diagonal

and off-diagonal elements when relaxation is considered. They are expressed as:

$$T_1 = \omega_0 \begin{bmatrix} \omega & 1 \\ 1 & \omega \end{bmatrix}, \quad (2.132)$$

$$T_2 = \omega_0 \begin{bmatrix} \omega e^{i\phi} & 1 \\ e^{-i\phi} & \omega e^{i\phi} \end{bmatrix}, \quad (2.133)$$

$$T_3 = \omega_0 \begin{bmatrix} \omega e^{-i\phi} & 1 \\ e^{i\phi} & \omega e^{-i\phi} \end{bmatrix}, \quad (2.134)$$

where $\phi = \frac{2\pi}{3}$ [53].

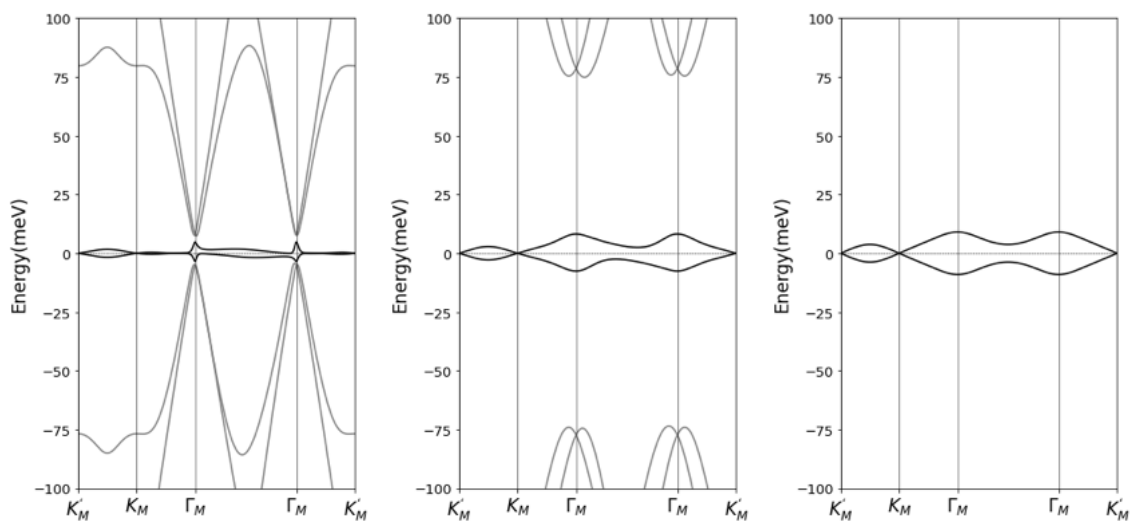


Figure 2.57 Effect of lattice relaxation (from left to right: $\omega = 1.0, 0.5, 0.0$) on the band structure of TBG plotted along the path in Fig.2.50 for $\theta = 1.05^\circ$.

In Fig.2.57, we present the band structure resulting from relaxed lattices at $\theta = 1.05^\circ$ for $\omega = 1.0, 0.5, 0.0$, revealing certain quantitative differences. Notably, the gaps separating the low-energy bands from the high-energy bands get enhanced, and the bands themselves become somewhat more dispersive. For realistic small-angle TBG, $\omega \approx 0.8$ [14]. The corresponding band structure is shown in Fig.2.58

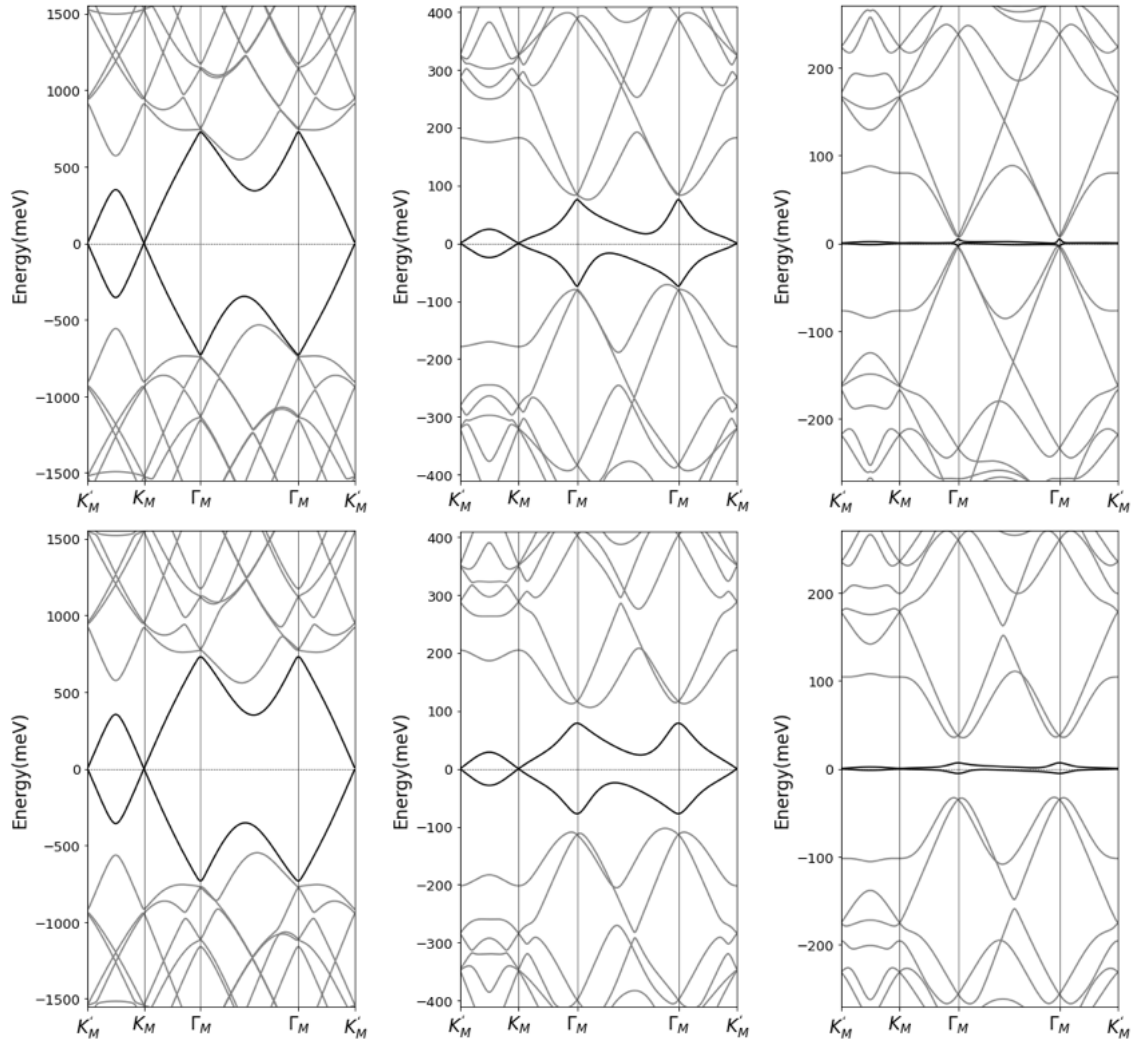


Figure 2.58 The band structure of TBG plotted along the path in Fig. 2.50, with (bottom) and without (top) lattice relaxation ($\omega = 0.8$) at different angles (from left to right: $\theta = 5.0^\circ, 1.5^\circ, 1.05^\circ$).

Flat Bands

The avoided crossings at the intersection of the Dirac cones lead to the flattening of the energy bands. As illustrated in Fig. 2.51, the resulting hybridization gap separates a branch of dispersive high-energy bands from the low-energy states, which, on the other hand, are pushed towards zero energy. Quantitatively, this flattening can be characterized by the renormalized band velocity v_F^* at the \mathbf{K} -point, plotted as a function of the twist angle θ in Fig. 2.59.

As the twist angle decreases, v_F^* also diminishes, resulting in the entire low-energy band being compressed into a narrow energy win-

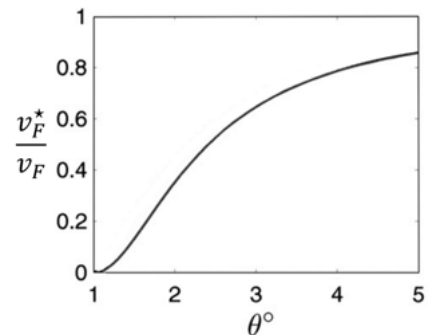


Figure 2.59 Renormalized Dirac-point band velocity. Adapted from [6].

dow of only a few meV (Fig. 2.60). This effect becomes particularly pronounced at $\theta = 1.05^\circ$, the largest of the so-called magic angles. Numerical analysis further indicates the existence of other magic angles at $\theta = 0.5^\circ, 0.35^\circ, 0.24^\circ, 0.2^\circ$, etc., where v_F^* approaches zero [6].

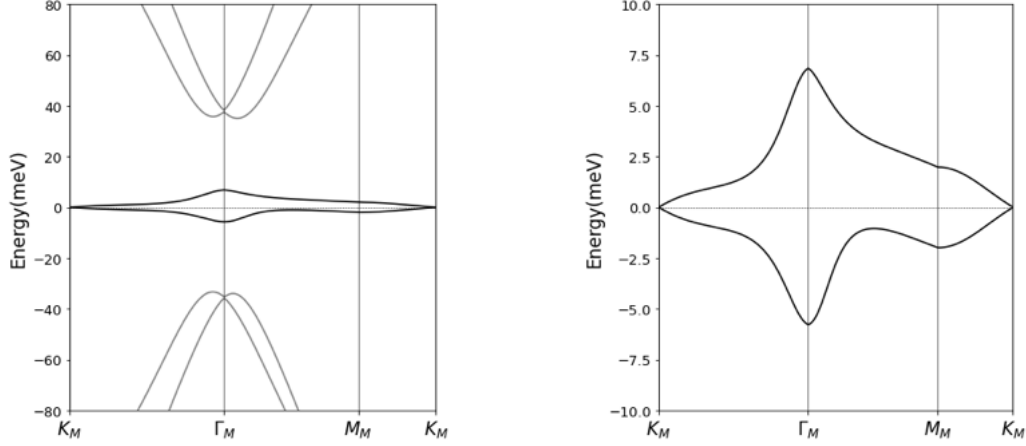
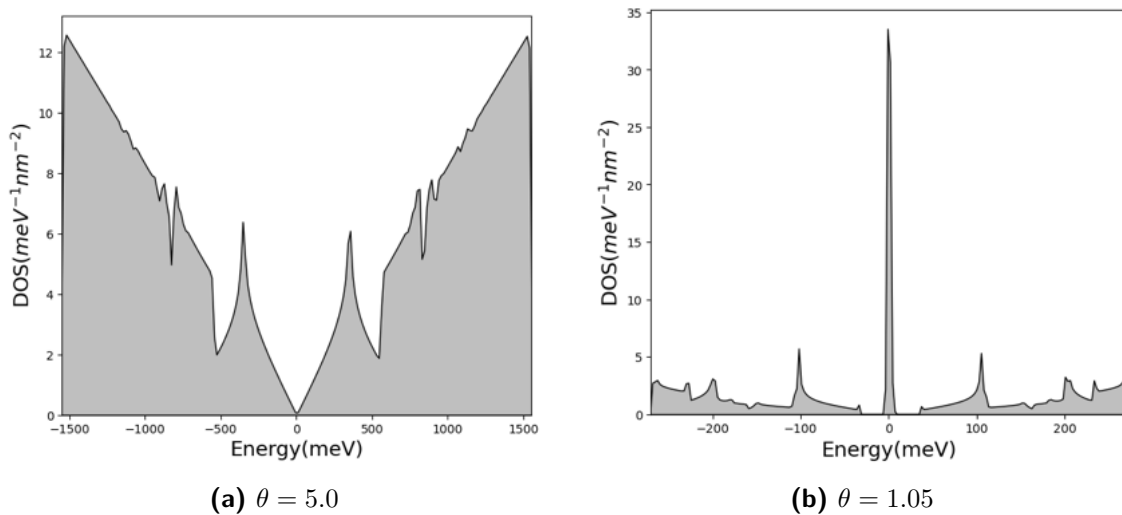


Figure 2.60 Band structure of magic angle TBG.

The strong confinement of electronic states within these narrow energy intervals significantly impacts the DOS, as shown in Fig. 2.61. Unlike the linear relationship observed in decoupled monolayers, the DOS in this context exhibits a complex energy dependence. The avoided crossings induce gaps and saddle points in the band structure, which manifest as the emerging dips and peaks in the DOS. The most notable difference between the two plots is observed at the Dirac point energy. At $\theta = 5.00^\circ$, the Dirac cones remain relatively well-separated, leading to a DOS that behaves similarly to MLG, decreasing linearly to zero. In contrast, at $\theta = 1.05^\circ$, the flat moiré bands contribute a pronounced peak in the DOS.



(a) $\theta = 5.0$

(b) $\theta = 1.05$

Figure 2.61 DOS of TBG.

Chapter 3

Experimental Methods

In this chapter, we provide an overview of the experimental methods employed in our research. We briefly introduce the concepts of mechanical exfoliation and Raman spectroscopy for the fabrication of 2D devices. As mentioned in the introduction, two of the QTM's main components are the sample and the tip. Here, we offer a more in-depth discussion of their fabrication processes before describing the general QTM setup and how it can be realized from a modified Atomic Force Microscope.

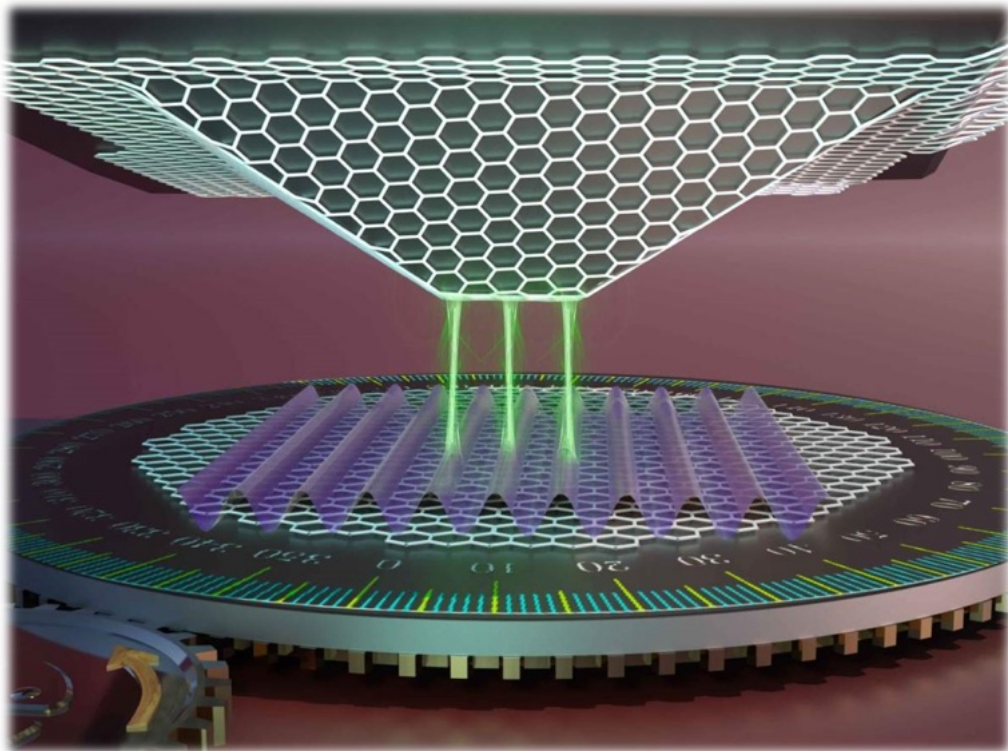


Figure 3.1 Adapted from [55].

3.1 Exfoliation

Van der Waals materials feature strong covalent bonds within a single layer, while interlayer interactions are mediated by much weaker van der Waals forces. Thus, each layer can be easily peeled off from the bulk using Scotch tape. This method, known as mechanical exfoliation, has produced the highest quality flakes to date [56]. We provide a brief introduction to this method for exfoliating graphene and hexagonal boron nitride (hBN) flakes.

First, we use a diamond scribe and cleaver to cleave the Si/SiO₂ chips into dimensions of 5cm × 5cm. These chips are then cleaned with O₂ plasma and act as carrier substrates.

We begin the exfoliation by attaching a small amount of bulk crystal to a piece of Scotch tape. The tape is then folded 5-6 times to thin the material, ensuring a uniform layer of material on the tape. The number of folds is limited to prevent the crystal from becoming too small. Next, the tape is brought close to the clean substrates, and gently pressed to increase adhesion between the flakes and the substrates. For graphene and graphite (and hBN tunnel barrier flakes; see Sec.3.5), the substrates and tape are placed on a hot plate at 110°C for 5-7 minutes. Finally, the tape is slowly peeled off, leaving freshly cleaved material on the substrates. This procedure creates flakes of various sizes and thicknesses on the substrate [57].

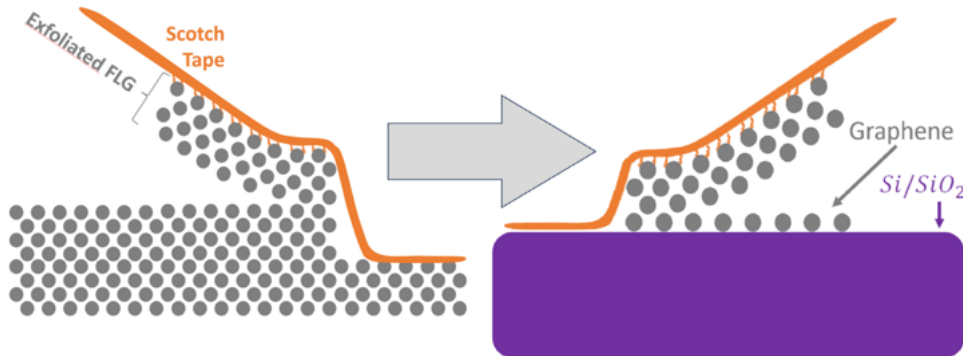


Figure 3.2 Scheme of two representative steps of mechanical exfoliation. On the left, Scotch tape is used to exfoliate FLG from bulk graphite, and on the right, the same Scotch tape is pressed against a silicon chip (in purple), resulting in a layer of graphene being deposited. Adapted from [58].

3.2 Transfer setup

Fabrication of sample and tip device relies on distinct transfer methods, that we discuss in Sec. 3.4.5 and Sec. 3.5. Despite the differences between these methods they all rely on very similar experimental tools: namely a long working distance optical inspection system in combination with micropositioning systems. Fig. 3.3 shows an image of our deterministic placement setup based on a modified optical microscope equipped with long working distance objectives and two manually actuated micropositioners: one to move the sample holder and another to position the flake for transfer.

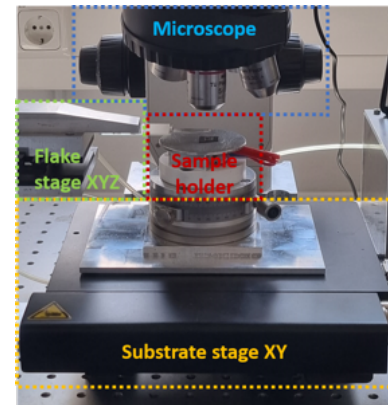
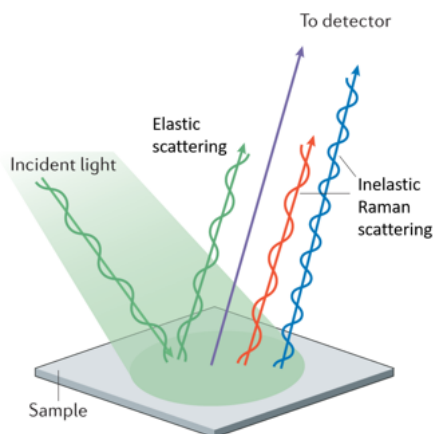


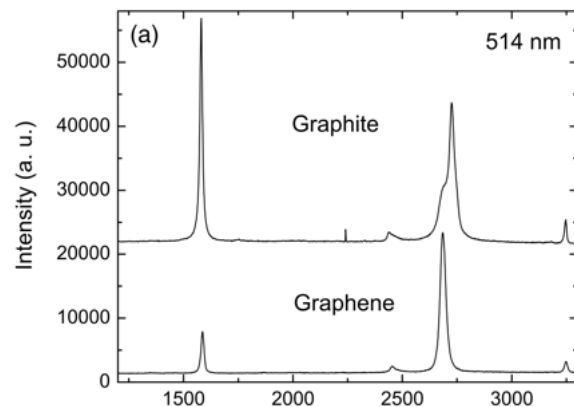
Figure 3.3 Transfer setup.

3.3 Raman Spectroscopy

Raman spectroscopy is a powerful characterization technique based on the inelastic scattering of photons by phonons within a material. By exposing a sample material to an appropriate light field and collecting the scattered light (Fig. 3.4a), a Raman spectrum is obtained, which is highly sensitive to the material's vibrational and electronic properties.



(a) Illustration of Raman scattering.



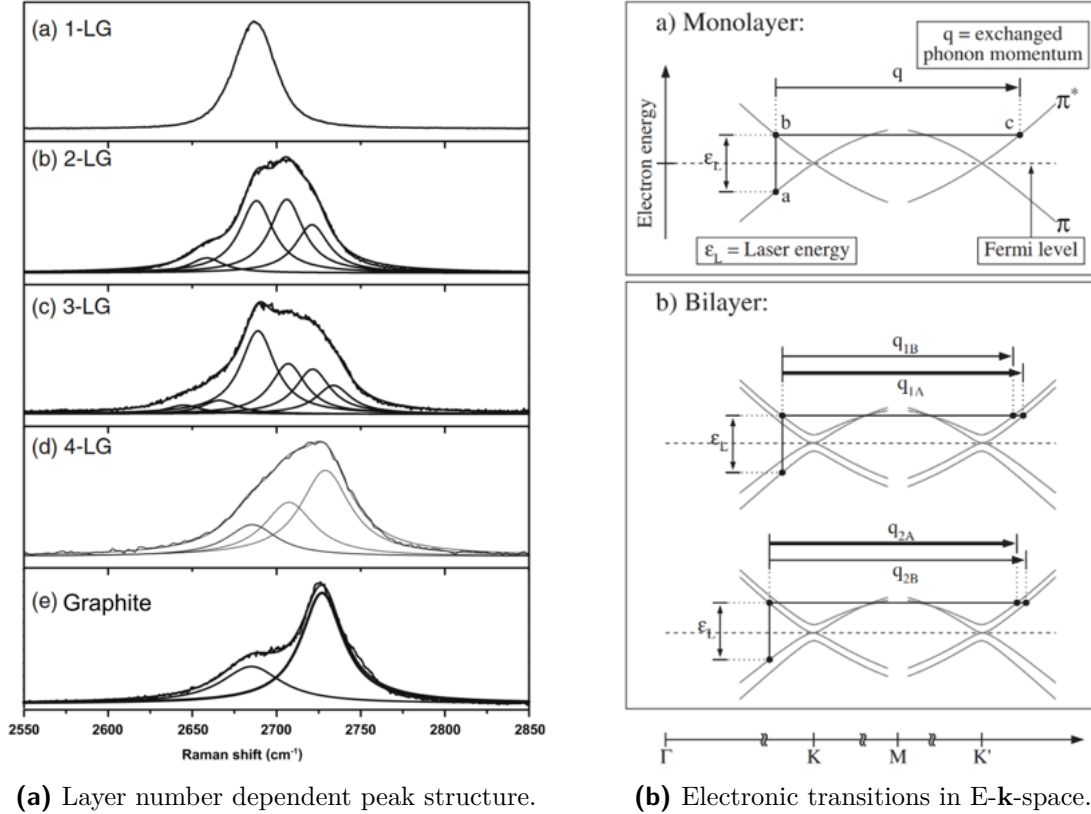
(b) Raman spectrum of graphene and graphite.

Figure 3.4 Working principles of Raman spectroscopy. Adapted from [59] [60]

Figure 3.4b presents typical Raman spectra for graphene and graphite, consisting of distinct peaks within the spectral region of $1500\text{--}3400\text{cm}^{-1}$. Notably, the shape of the 2D band ($\approx 2700\text{cm}^{-1}$) differs markedly between these two materials. Figure 3.5a further illustrates the evolution of the 2D peak as a function of the number of

layers.

In the transition from MLG to BLG, the 2D peak in MLG is observed as a sharp feature, which can be accurately fitted with a single Lorentzian line centered at 2687cm^{-1} . In contrast, the 2D peak in BLG is broader and is best described by four Lorentzian peaks around a shifted central frequency.



(a) Layer number dependent peak structure.

(b) Electronic transitions in E-k-space.

Figure 3.5 The 2D peak in FLG systems. Adapted from [61] [60].

The alterations in the 2D peak's shape are closely associated with changes in the electronic band structure as the number of layers increases, providing a reliable method for determining the layer count in FLG systems. The 2D peak in graphene arises from a two-phonon process involving phonons with opposite momentum. This fourth-order process entails four virtual transitions: (i) laser-induced excitation of an electron-hole pair (transition from state a to b in Fig. 3.5b(a)); (ii) electron-phonon scattering with exchanged momentum \mathbf{q} near the \mathbf{K} point (b to c); (iii) electron-phonon scattering with exchanged momentum $-\mathbf{q}$ (c to b); and (iv) electron-hole recombination (b to a). For simplicity, Fig. 3.5b omits the phonon energy and does not depict the equivalent hole-phonon scattering processes [60].

In BLG, the single 2D peak observed in MLG splits into four distinct components, attributed to the splitting of electronic bands. BLG's interlayer interactions produces four bands with different splittings for electrons and holes, thereby enabling four possible optical transitions, with the incident light coupling most strongly to

the two transitions shown in Fig. 3.5b(b). Electron-phonon scattering then couples all electron bands, involving phonons with momenta \mathbf{q}_{1B} , \mathbf{q}_{1A} , \mathbf{q}_{2A} , and \mathbf{q}_{2B} (Fig. 3.5b(b)). Along with the corresponding processes for holes, these interactions give rise to the four distinct peaks in the Raman spectrum of BLG [60].

As the number of layers increases, the number of possible optical interband transitions also rises. This leads to a broadening of the Raman spectrum due to the convolution of an increasing number of peaks until the spectrum reaches the limit of bulk graphite.

In summary, the electronic structure of graphene is distinctly captured in its Raman spectrum, which evolves significantly with the number of layers. The Raman fingerprints for single-, bilayer-, and few-layer graphene reflect changes in electronic structure and electron-phonon interactions, enabling unambiguous, high-throughput, and nondestructive identification of graphene layers.

3.4 Tip Device

The majority of the QTM has been assembled using commercially available components. However, it is necessary to replace the standard sharp tip of an atomic force microscope (AFM) with a flat plateau. To ensure a steady supply and adaptability for future experiments, a procedure to efficiently manufacture tips with any desired geometry is required. For this purpose, we employ electron-beam induced deposition.

3.4.1 Scanning Electron Microscope

The Scanning Electron Microscope (SEM) is a powerful characterization tool that offers far higher resolution than typical optical methods. It produces images of a sample by scanning its surface with a focused beam of electrons. The scattered electrons contain information about the sample's surface topography and composition.

A typical SEM setup is depicted in Fig. 3.6a. Free electrons are generated in an electron gun and accelerated by the accelerating voltage U . Magnetic fields generated by ring coils collimate and guide the electrons onto the surface of the sample as a focused beam. The scanning coils deflect the beam spot in the X and Y axes, allowing it to scan in a raster pattern over the surface. The scattered electrons are collected to generate a signal.

The nature of electron-sample interaction will be discussed in greater detail in the following section. For now, it is important to note that the reaction products include

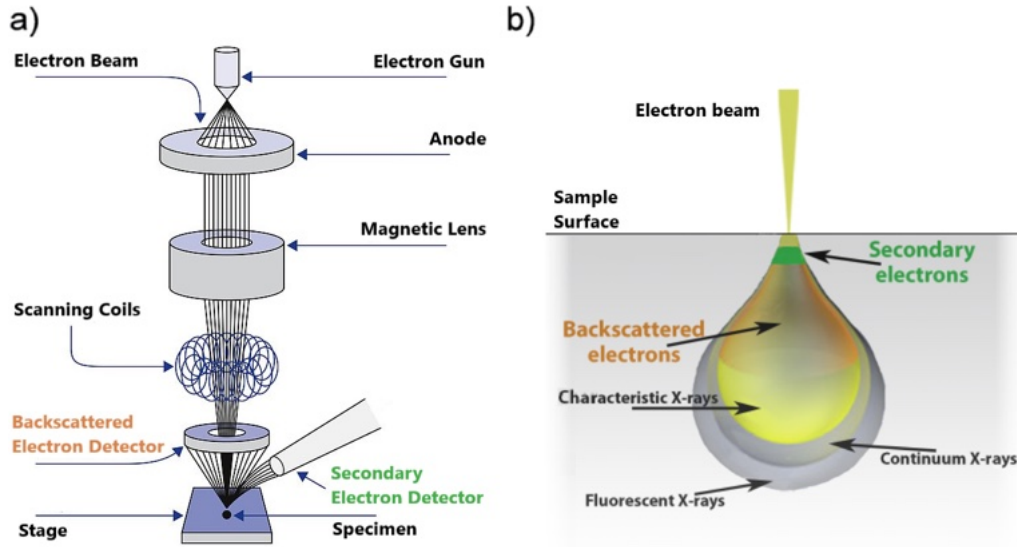


Figure 3.6 a) SEM setup. b) Schematic of electron beam interaction. Adapted from [62] [63].

back-scattered electrons and secondary electrons, which originate from different areas within the interaction volume (Fig. 3.6b) and differ in both the information they carry and their kinetic energy. The SEM is equipped with a detector for backscattered electrons and an additional detector at the side of the sample for secondary electrons.

The image pixels are formed step by step by the incremental displacement of the electron beam in the object plane in both the X and Y directions. For every particular beam position, the scattering and the detected signal intensity depend on the local morphology and composition of the sample [64]. The resulting SEM image is then a 2D intensity map, where each point located at coordinates x and y contains a numerical value related to a digitized signal I , and the resulting image can be described by a matrix $I[x, y]$.

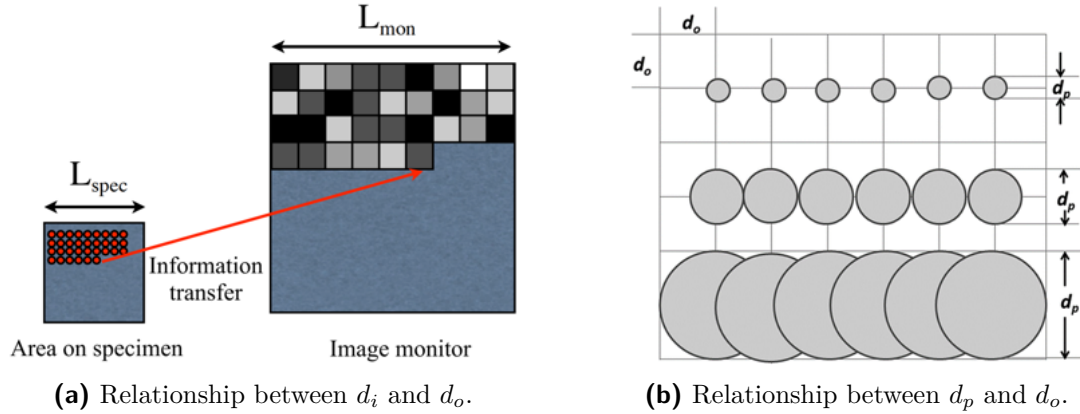
A pixel in object space has dimensions of $d_o \times d_o$ where d_o is the step size. Similarly, a pixel in image space has dimensions of $d_i \times d_i$ where d_i is the step size on the display. Magnification is therefore given by:

$$M = \frac{d_i}{d_o}, \quad (3.1)$$

where for our setup $d_i \approx 53.5 \mu m$

Magnification is achieved by scanning an area on the specimen that is smaller than the display. Since the monitor length is fixed, increasing or decreasing magnification is achieved by respectively reducing or increasing the length of the scan area on

the specimen. By controlling the magnification, we can adjust the fineness of the intensity grid (Fig. 3.7).



(a) Relationship between d_i and d_o .

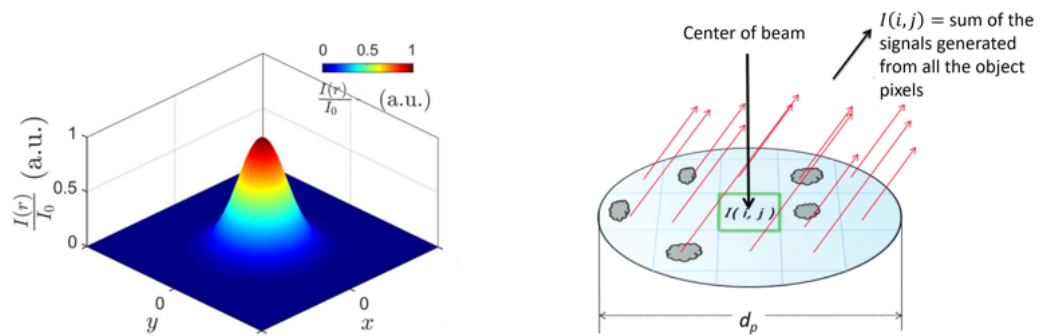
(b) Relationship between d_p and d_o .

Figure 3.7 Controlling and limitation of the Magnification. Adapted from [65] [64].

As d_o decreases, M increases. However, a practical limit is reached arising from the finite beam spot size. The actual radial distribution of the incident electron flux can be described by a Gaussian distribution (Fig. 3.8a) [66]:

$$f(r) = \frac{I/e}{2\pi\sigma^2} \exp\left(-\frac{r^2}{2\sigma^2}\right), \quad (3.2)$$

where $f(r)$ is the number of electrons per unit area and time, σ is the standard deviation, I is the beam current, and e is the elementary charge. The beam extent (probe size d_p) can be estimated by the full width at half maximum (FWHM), which is $d_p \approx 2\sigma\sqrt{2\ln 2}$.



(a) Gaussian distribution of the impinging electron flux with $\text{FWHM}=d_p$.

(b) For $d_p > d_o$ only sum of signals from multiple object pixels detectable.

Figure 3.8 Finite probe size. Adapted from [67] [64]

Adjacent pixels in the display contain mainly new information but also some information from previous pixels due to the finite exponential decay of the beam (Fig. 3.8b). Each image pixel remains relatively unique as long as $d_o > d_p$. However, if $d_o < d_p$, further decreasing the step size to increase magnification causes overlap-

ping exposure spots, resulting in a progressively blurred image. Thus, the resolution limit, or the finest detail that can be resolved, is determined by d_p .

The upper limit for the resolution d_p of the SEM can be determined using Abbe's equation [69]:

$$d_p = \frac{0.612\lambda}{n \sin \alpha}, \quad (3.3)$$

where n is the refractive index of the medium between the specimen and the column, and α is the half-angle of the cone of electrons converging onto the specimen. Using the aperture diameter D and the working distance Z , the semi-angle α can be given by:

$$\alpha = \tan^{-1} \left(\frac{D}{2Z} \right). \quad (3.4)$$

Using the de Broglie wavelength and the kinetic energy of electrons:

$$\lambda = \frac{h}{\sqrt{2em_e U}}, \quad (3.5)$$

where m_e is the mass of the electron and U the accelerating voltage, the resolution d_p becomes [69]:

$$d_p = \frac{0.753}{\alpha \sqrt{U}}. \quad (3.6)$$

For $U = 15keV$ and an typical α of around 0.01, the theoretical limit of resolution is $1.74nm$. However, this implies that continuously increasing the probe convergence angle would continuously improve precision, which is not feasible for electron optics. Besides lens errors and aberrations, the repulsive electron interaction causes the significant spreading of the beam. Therefore, the best resolutions are generally achieved in systems with small apertures. However, since it filters out electrons coming from large angles, this reduces the probe current and consequently the general signal intensity.

3.4.2 Electron-Substrate Interaction

When high-energy primary electrons (PE) strike a solid surface, they penetrate and interact with the atomic nucleus or shell electrons through electrostatic Coulomb forces. The resulting random collisions scatter the electrons into a teardrop-shaped interaction volume. These interactions continue until the primary electron loses energy or is ejected from the material. This scattering process produces specific

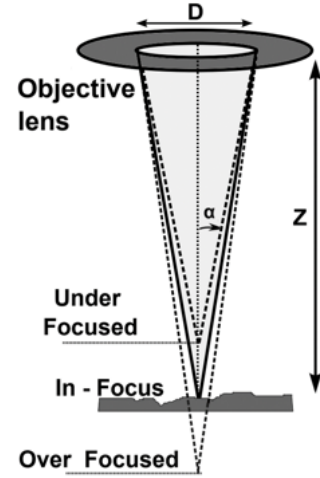


Figure 3.9 Beam geometry. Adapted from [68].

signals known as secondary electrons (SE) and backscattered electrons (BSE).

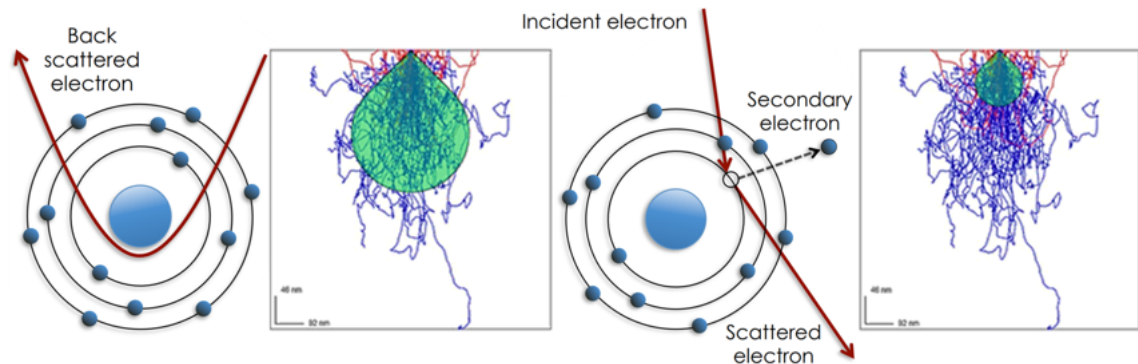


Figure 3.10 Electron-trajectory simulations. Blue (red) trajectories mark BSEs (SEs). Green area defines the interaction volume and origin of BSEs (left) and SEs (right). Adapted from [70][71].

BSEs result from elastic interactions, where the primary electron is deflected but energy is conserved (Fig. 3.10). Originating from a deeper interaction volume, BSEs have lower resolution and do not reveal surface features but provide composition-dependent contrast, with higher atomic number atoms generating more BSEs. The detector for backscattered electrons shows high sensitivity to atomic number differences, making higher atomic number materials appear brighter.

SEs, by contrast, arise from inelastic interactions where energy from the primary electron ejects a bound electron (Fig. 3.10). A part of the excitation energy is consumed during the extraction process, resulting in SEs possessing relatively low kinetic energy. Due to this limited energy, SEs can only escape from the outermost few nanometers of the sample surface. Consequently, they are particularly well-suited for revealing detailed surface topography [72].

3.4.3 Electron-Precursor Interaction

The basic principle of Electron-Beam Induced Deposition (EBID) is straightforward. The vacuum chamber is contaminated with precursor gas molecules, which adsorb onto a substrate. The solid deposition occurs when the electron beam "cracks" this thin layer of adsorbed precursors and dissociate them by converting the molecules into electronically excited states that subsequently decay into volatile and non-volatile moieties. The non-volatile components adhere to the substrate, forming a deposit (Fig. 3.11). This beam-induced reaction occurs locally at the irradiated area, and the lateral dimensions of the deposited structures are controlled by moving the electron beam [73].

The probability of dissociation depends on the electron energy and is generally expressed as a cross-section. A higher cross-section indicates a greater probability

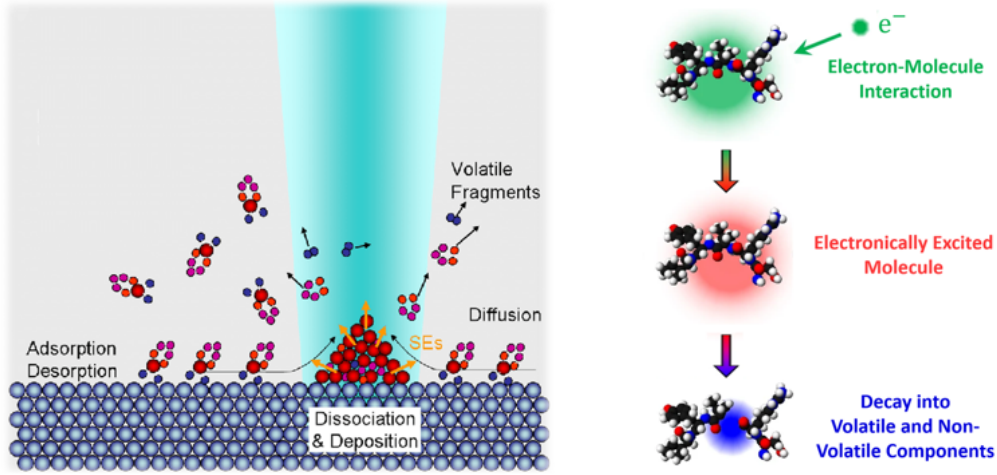
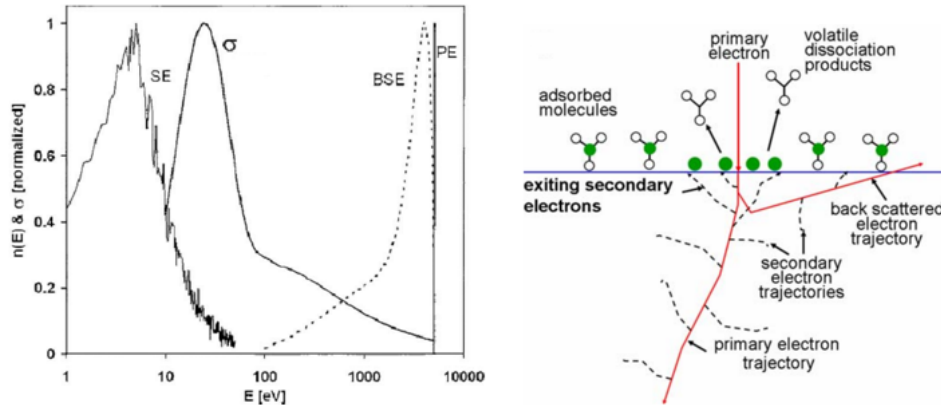


Figure 3.11 Electron-beam induced dissociation and deposition. Adapted from [66].

of bond dissociation in the molecule. A typical energy distribution of electrons and the cross-section as a function of energy are depicted in Fig. 3.12a [73].

The dissociation efficiency increases with the electron energy up to a maximum at around 70eV , which is due to the increased excess energy and access to further dissociation channels. Above this energy, the cross section declines again as the interaction time with a target molecule decreases due to the rising electron velocity. Thus, dissociation is most efficient in the low energy range characteristic of SEs. The PEs mainly serves as a source for SEs, which dominate the deposition process.



(a) Energy distribution of SEs and BSEs and the cross section for the dissociation as a function of electron energy.

(b) Interactions of PEs generating an emitted flux of SEs and BSEs, which dissociate adsorbed molecules.

Figure 3.12 Electron-Precursor interaction. Adapted from [73] [66].

The deposition rate $R(r)$ as a function of distance r from the center of the primary electron beam with energy E_0 is given by [66]:

$$R(r) = Vn(r) \int_0^{E_0} \sigma(E) f(r, E) dE, \quad (3.7)$$

where $n(r)$ is the local surface density of adsorbed precursor molecules, V is the volume occupied by a dissociated molecule, and $f(r, E)$ is the electron distribution at the surface as a function of position and energy. Both $f(r, E)$ and $n(r)$ have strong time dependencies, as the deposit changes the surface, influencing the distribution of secondary electrons and the adsorption dynamics of precursor molecules.

In our experiments, the precursor used was diesel oil, consisting of various hydrocarbons such as paraffins and aromatic compounds. The average chemical formula for common diesel oil is $C_{12}H_{23}$, ranging approximately from $C_{10}H_{20}$ to $C_{15}H_{28}$ [74].

3.4.4 Electron-beam Induced Deposition

The following study systematically investigates key experimental parameters, such as acceleration voltage U , aperture diameter D , dwell time per pixel τ , total exposure time t and magnification M , to elucidate their roles in the EBID process and to determine optimal conditions for fabricating tips with flat plateaus (EBID-tips). To this end, we produced several EBID-tips with varying geometries on cantilevers, as illustrated in fig.3.13.

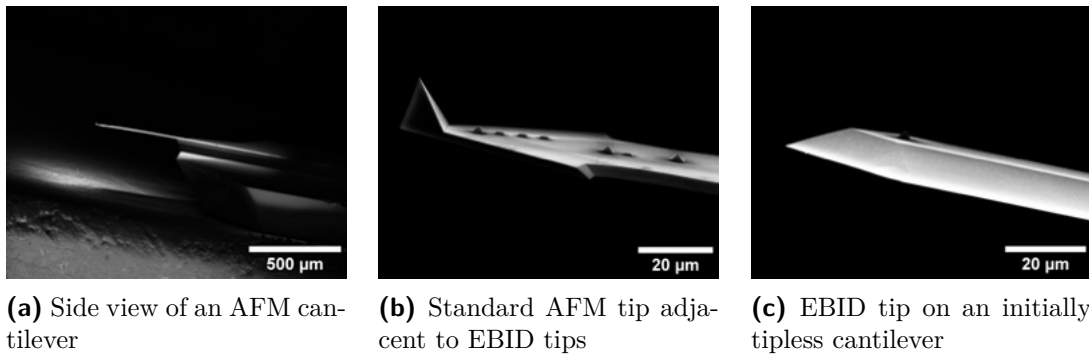


Figure 3.13 Tips fabricated by EBID on AFM cantilevers.

Sample Preparation

To fabricate the tips, we commenced with commercial tipless AFM cantilevers (Fig.3.14a). We coated the bottom side of the cantilevers with titanium/gold using an e-beam evaporator to ensure a good electrical connection, thus maintaining the vdW layers on the tip at the same electrical potential as the body of the cantilever. The cantilevers were then affixed with conductive tape to the SEM stage (Fig.3.14b) to minimize displacement and charging of the sample. In order to contaminate the vacuum chamber with hydrocarbons, a droplet of oil was placed on a screw thread of the stage, allowing it to evaporate continuously within the chamber.

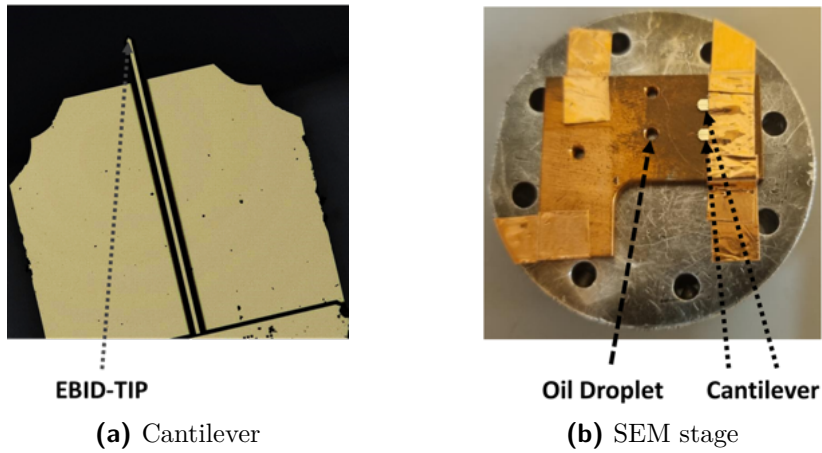


Figure 3.14 Sample preparation process.

Shape Control

The first step in our process involves defining the precise geometry we aim to achieve. It is critical to ensure that only the apex of the tip interacts with the sample, minimizing the influence of the surrounding folded regions. To achieve this, the plateau corners must exhibit sharp edges. However, a too steep a drop in height can induce significant folding of the flake, potentially causing strain in the apex region. A pyramidal structure offers a solution, providing a sharp plateau while reducing the intensity of folding. Additionally, the plateau's dimensions should be smaller than typical graphene flake sizes. Therefore, we aim for a length of approximately $0.5\mu\text{m}$. To construct such a geometry, we deposit successive layers with decreasing size on top of one another.

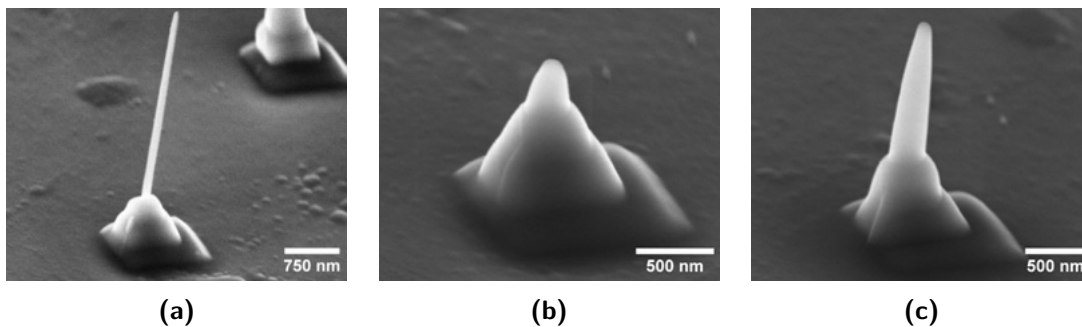


Figure 3.15 EBID-Pillars. The parameters are altered in accordance to Tab. [3.1](#).

Our initial attempts to create layered structures resulted in the pillar-like formations shown in Fig. [3.15](#), with the corresponding parameters listed in Tab. [3.1](#).

The pillars consist of four distinct layers, with the uppermost layer resembling a sharp tip. We observe that the subsequent pyramid levels narrow and grow more rapidly than the underlying ones. For example, in Fig. [3.15b](#), the layer sizes of the first three levels are $1\mu\text{m}$, 800nm , and 500nm , while their corresponding heights are

Fig. 3.15	Parameter	1st Layer	2nd Layer	3rd Layer	4th Layer
(a)	$U(kV)$	5	5	5	5
	$M(\times 10^3)$	30	60	100	100
	$l(px)$	256	256	256	1
	$D(\mu m)$	30	30	30	30
	$\tau(\frac{\mu s}{px})$	2.9	2.9	2.9	30
	$t(s)$	240	180	60	30
(b)	$U(kV)$	5	5	5	5
	$M(\times 10^3)$	30	60	100	100
	$l(px)$	256	256	256	1
	$D(\mu m)$	30	30	30	30
	$\tau(\frac{\mu s}{px})$	2.9	2.9	2.9	10
	$t(s)$	240	180	60	10
(c)	$U(kV)$	10	10	10	10
	$M(\times 10^3)$	30	60	100	100
	$l(px)$	256	256	256	1
	$D(\mu m)$	30	30	30	30
	$\tau(\frac{\mu s}{px})$	2.9	2.9	2.9	60
	$t(s)$	300	180	120	60

Table 3.1 Parameters used for Fig. 3.15.

200nm, 450nm, and 250nm. The horizontal dimensions of the layers were controlled by increasing the magnification for each subsequent layer. This magnification increment reduces the total irradiated area, enhancing current density and consequently increasing the growth rate. As a result, despite the reduced total exposure time t for each successive layer, we do not observe a continuous decrease in height.

Rather than increasing M , we can also reduce the total number of exposure points. The uppermost layer in Fig. 3.15 was created with the same M as the preceding layer, but the beam was allowed to dwell for $t = \tau$ on a single pixel. Focusing the total current on this one spot results in the formation of the large, thin pillar.

Comparing Fig. 3.15a and Fig. 3.15b, we observe a reduction in the height of the top layer from 2.5 μm to 300nm, which is attributed to a threefold reduction in dwell time.

The structure depicted in Fig. 3.15c was created in a similar manner but with the acceleration voltage doubled from 5kV to 10kV. Although the uppermost layer was exposed for double the time compared to that in Fig. 3.15a, the tip reaches a height of only 1.1 μm . To understand this correlation, it is necessary to consider the role of SEs in the deposition process (fig. 3.12). As beam energy increases, the electron trajectories near the surface straighten, and electrons penetrate deeper into the specimen before multiple elastic scattering events cause some to propagate back toward the surface. As the PEs energy increases, the number of SEs decreases, as

they are generated at greater depths from which they cannot reach the surface due to their low energy.

It is noteworthy that the image resolution is significantly higher than the deposition resolution (dimensions of the $1px$ -pillar). This discrepancy arises due to changes in the substrate surface, as illustrated in Fig. 3.16.

Initially, the deposit width is influenced by the SEs generated from the target surface, limiting the deposition to the probe size. However, as the deposit begins to grow, PEs interact with the newly formed structure and generate SEs that emerge through the inhomogeneous surface walls. Additionally, forward-scattered electrons can reach the surface and produce SEs along the sides of the structure. All these SE emissions from the pillar surface contribute to lateral growth along the sides of the deposits, in addition to the Gaussian beam shape, thereby limiting the achievable spatial resolution of the EBID process [66].

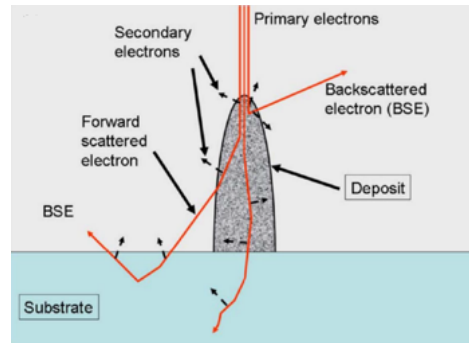


Figure 3.16 Deposition events on the surface of the deposit. Adapted from [75].

Small Aperture

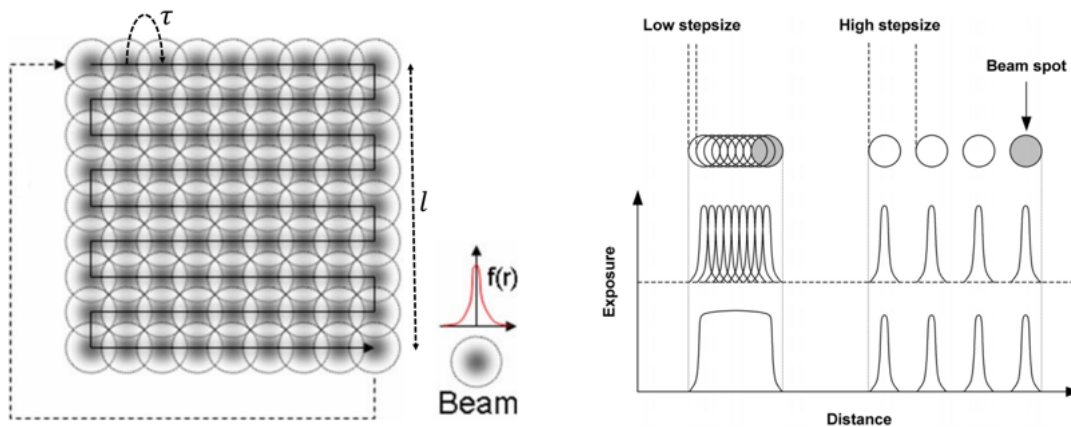


Figure 3.17 Digital serpentine raster scan scheme with overlap (left) and corresponding energy deposition (right). The Gaussian beam dwells for a time τ and is then moved by one object pixel (px) to the next exposure spot. After completing one raster scan ($frame$), the beam repeats the pattern. Adapted from [66].

We conducted the following experiments using a relatively small aperture with a diameter of $D = 30\mu m$ to achieve high resolution. The objective was to create flat plateaus that require consistent energy deposition across all pixels. To obtain a

smooth line exposure, Gaussian beam overlaps are necessary to ensure uniform energy deposition. Consequently, the ratio of step size to spot size must be minimized, which corresponds to a high magnification (Fig. 3.17).

However, increasing magnification reduces the depth of focus, which defines the allowable range of the image plane's position relative to the lens while still maintaining sharp images. In the context of the deposition process, its reduction implies increased broadening and non-uniform deposition when the tip grows too far out of the focal plane. As depicted in Fig. 3.18, the depth of focus is influenced by the rate at which the beam diverges from the focal plane. If the resolution on the sample is denoted by δ_{sample} , the corresponding resolution on the screen is $\left(\frac{\delta_{\text{sample}}}{M}\right)$, and the depth of focus can be estimated by [68]:

$$\frac{\delta_{\text{sample}}}{\alpha} = \frac{2\delta_{\text{screen}}Z}{DM}. \quad (3.8)$$

Here, a magnification of up to 50000 has proven to produce good results. According to eq. 3.1, this corresponds to object pixel size $d_0 \approx 1.07nm$.

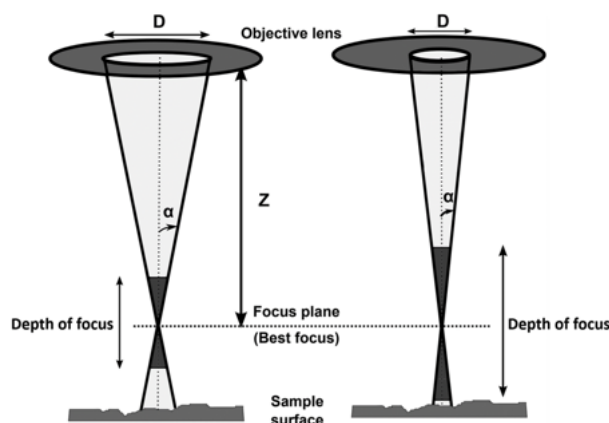


Figure 3.18 Relationship between the aperture diameter and depth of focus. Adapted from [68].

In previous experiments, the deposit dimensions were altered by adjusting either M or l . However, changing M significantly affects beam geometry, necessitating refocusing and astigmatism correction. Therefore, it is more practical to maintain a constant M throughout the entire process.

To create larger structures, we increased τ by an order of magnitude. This adjustment, however, places the dwell time τ in the same order as the total exposure time t . To ensure that each pixel is exposed to the same accumulated current, we counted the number of times the SEM completes one raster scan (*frame*).

In summary, during the deposition process, the horizontal dimension is controlled by l , while the vertical dimension is regulated by τ , the number of layers, and the number of frames per layer.

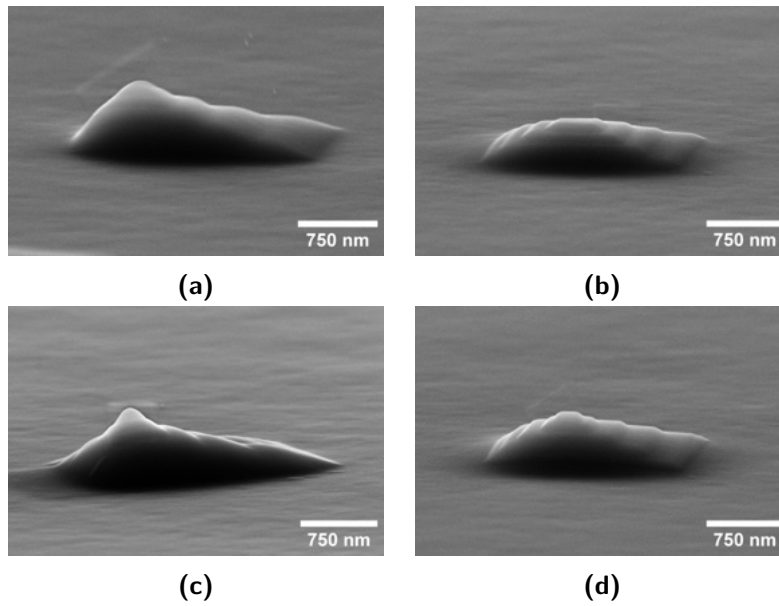


Figure 3.19 EBID-pyramids. The parameters are altered in accordance to Tab.3.2.

The parameters for the deposits shown in Fig.3.19 are listed in Tab.3.2. Overall, our modifications led to pyramids with more homogeneous surfaces and sharper edges.

Fig.3.19	Parameter	1st Layer	2nd Layer	3rd Layer	4th Layer	5th Layer
(a)	$U(kV)$	5	5	5	5	5
	$M(\times 10^3)$	50	50	50	50	50
	$l(px)$	800	600	400	200	100
	$D(\mu m)$	30	30	30	30	30
	$\tau(\frac{\mu s}{px})$	92.2	92.2	92.2	92.2	92.2
	frames	10	10	10	10	10
(b)	$U(kV)$	10	10	10	10	10
	$M(\times 10^3)$	50	50	50	50	50
	$l(px)$	800	600	400	200	100
	$D(\mu m)$	30	30	30	30	30
	$\tau(\frac{\mu s}{px})$	92.2	92.2	92.2	92.2	92.2
	frames	10	10	10	10	10
(c)	$U(kV)$	5	5	5	5	5
	$M(\times 10^3)$	50	50	50	50	50
	$l(px)$	800	600	400	200	100
	$D(\mu m)$	30	30	30	30	30
	$\tau(\frac{\mu s}{px})$	184.4	184.4	184.4	184.4	184.4
	frames	5	5	5	5	5
(d)	$U(kV)$	10	10	10	10	10
	$M(\times 10^3)$	50	50	50	50	50
	$l(px)$	800	600	400	200	100
	$D(\mu m)$	30	30	30	30	30
	$\tau(\frac{\mu s}{px})$	184.4	184.4	184.4	184.4	184.4
	frames	5	5	5	5	5

Table 3.2 Parameters used for Fig.3.19.

Figure 3.19a and Fig.3.19b were produced using identical parameters, except for a change in acceleration voltage. While the structure in Fig.3.19a has an approximate height of $\sim 780\text{nm}$, the one in Fig.3.19b is significantly smaller, measuring $\sim 480\text{nm}$. Additionally, Fig.3.19b displays a sharply defined apex, whereas the outlines in Fig.3.19a are completely broadened. A similar trade-off between height and sharpness is observed between Fig.3.19c and Fig.3.19d, where the dwell time was doubled while the number of frames was halved. This modification slightly increased the heights to 830nm (Fig.3.19c) and 580nm (fig.3.19d).

These trends are consistent with expectations, as a higher acceleration voltage enhances resolution but reduces the generation of SEs.

Charge Accumulation

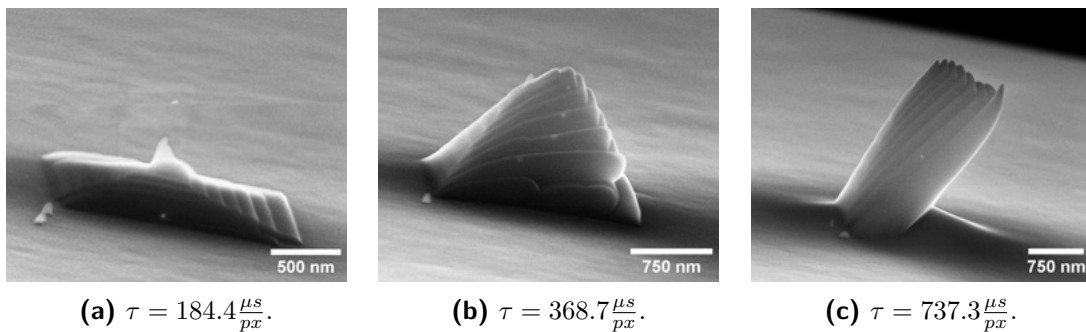


Figure 3.20 Influence of dwell time τ on charge induced growth effects.

Up to this point, we have successfully deposited pyramids with well-defined plateaus; however, these structures are generally too small for practical applications. To achieve the desired dimensions, it is necessary to increase the number of layers, frames, or dwell time. However, this approach is not feasible as we typically observe that larger structures exhibit undesired curvature and inhomogeneities. Figure 3.20 illustrates how this deformation becomes more pronounced with increasing dwell time.

This issue arises due to insufficient electrical conductivity, which causes charge accumulation within the deposit when exposed to the electron beam. The resulting electrostatic forces deflect the incident electron beam, leading to the observed distortions. It appears that the contact between the copper spacer and the sample stage (Fig.3.14b) does not provide adequate grounding. By switching from carbon tape to copper tape and applying conductive paste ("Electra 92" or "AR-PC 5090") to the surrounding area, electrostatic charging was minimized. Additionally, increasing the acceleration voltage to 15kV reduced the electron beam's sensitivity to deflection, significantly decreasing the observed shifts.

The improvement is evident in Fig.3.21, which shows a top view of typical deposited

pyramids before and after the modifications. The subsequent layers remain more centered and homogeneous after the modifications to the preparation process.

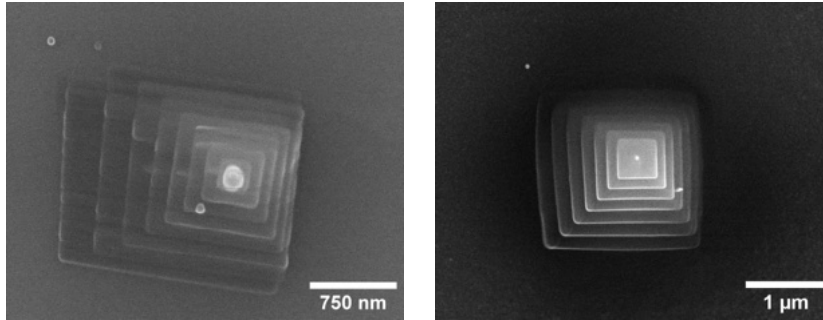


Figure 3.21 Typical observed spatial shift of deposited layers before(left) and after(right) modification of the preparation process.

Precursor-Substrate Interaction

In addition to the charge-induced shift, it is also noticeable that the first layer typically grows more inhomogeneously than subsequent layers. This phenomenon is particularly pronounced at the beginning of the deposition process, where the reaction occurs directly on the substrate. It is likely that the first layer forms more rapidly due to two factors: the greater availability of precursors and the fact that their dissociation occurs on a metallic surface, which may act as a catalyst [76]. Once the first layer is established, subsequent reactions take place on the chemically inert carbon deposit rather than on the bare metal.

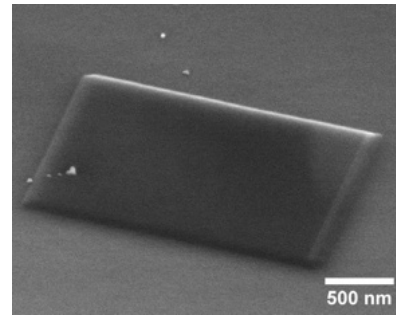


Figure 3.22 Seed layer.

To maintain a constant deposition rate, we create an initial substrate layer with a low dwell time of $\tau = 5.8 \frac{\mu\text{s}}{\text{px}}$ to avoid localized inhomogeneous catalytically accelerated growth on the pure metal substrate. On this seed layer, we then deposit the pyramid with longer dwell times.

Large Aperture

Till now, it has been challenging to create pyramids that reach a height of $1\mu\text{m}$. A substantial increase in exposure time primarily results in greater horizontal growth, which broadens and diminishes the sharp features of the structure. The decline in vertical deposition rates with increasing height can be attributed to at least two factors: increased molecule desorption due to beam heating and reduced diffusion. As surface diffusion transitions from the two-dimensional planar substrate during

the initial stages of deposition to the one-dimensional pillar surface, the amount of molecule diffusion to the tip apex decreases [66].

To enhance the vertical-to-horizontal growth ratio, we can increase the total probe current by using a larger aperture diameter of $60\mu m$.

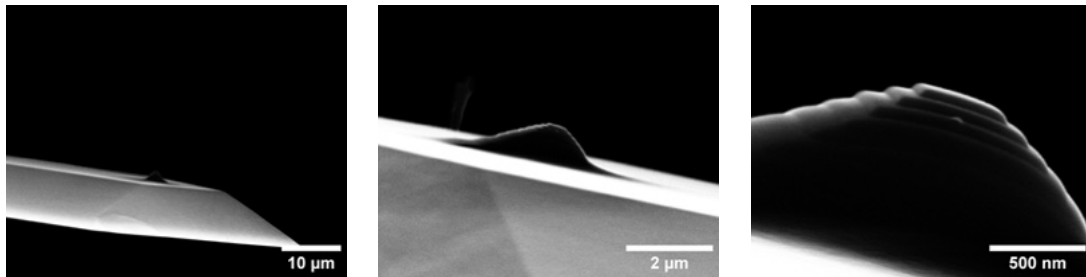


Figure 3.23 EBID-tip on cantilever, showcasing substantial improvement upon increasing the aperture size.

Figure 3.23 depicts a pyramid created using the parameters listed in Tab. 3.3, featuring a height of $1\mu m$ and a flat plateau with a diameter of $450nm$. To ensure a smooth slope, we increased the number of layers to nine, with each subsequent layer reduced in length by $100px$, culminating in a top layer length of $200px$ (Fig. 3.24).

Parameter	Seed Layer	Nth Layer
$U(kV)$	15	15
$M(\times 10^3)$	50	50
$l(px)$	1000	$N \times (10 - 1)$
$D(\mu m)$	60	60
$\tau(\frac{\mu s}{px})$	5.8	368.7
frames	100	3

Table 3.3 Parameters used for Fig. 3.23.

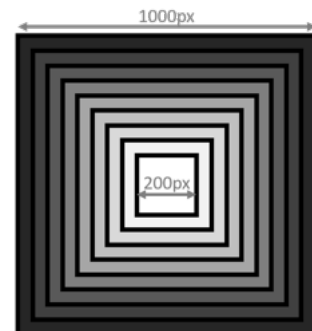


Figure 3.24 New layer sizes

Dwell Time and Frame Number

In the following section, we maintain the layer size structure as depicted in Fig. 3.24. Our objective is to determine the optimal configuration of the remaining parameters, specifically the dwell time and the number of frames, to produce pyramids of the highest quality with a target height of approximately $2\mu m$. The results of these experiments are presented in matrix form in Fig. 3.25.

To maintain a height of approximately $2\mu m$, an increase in dwell time necessitates a corresponding reduction in the number of frames, and vice versa. Consequently, pyramids that achieve the desired height are located along the anti-diagonal of the matrix. Regarding the quality of the plateau, an optimal region is identified, corresponding to a dwell time of approximately $180\mu s$ to $370\mu s$ and a frame number

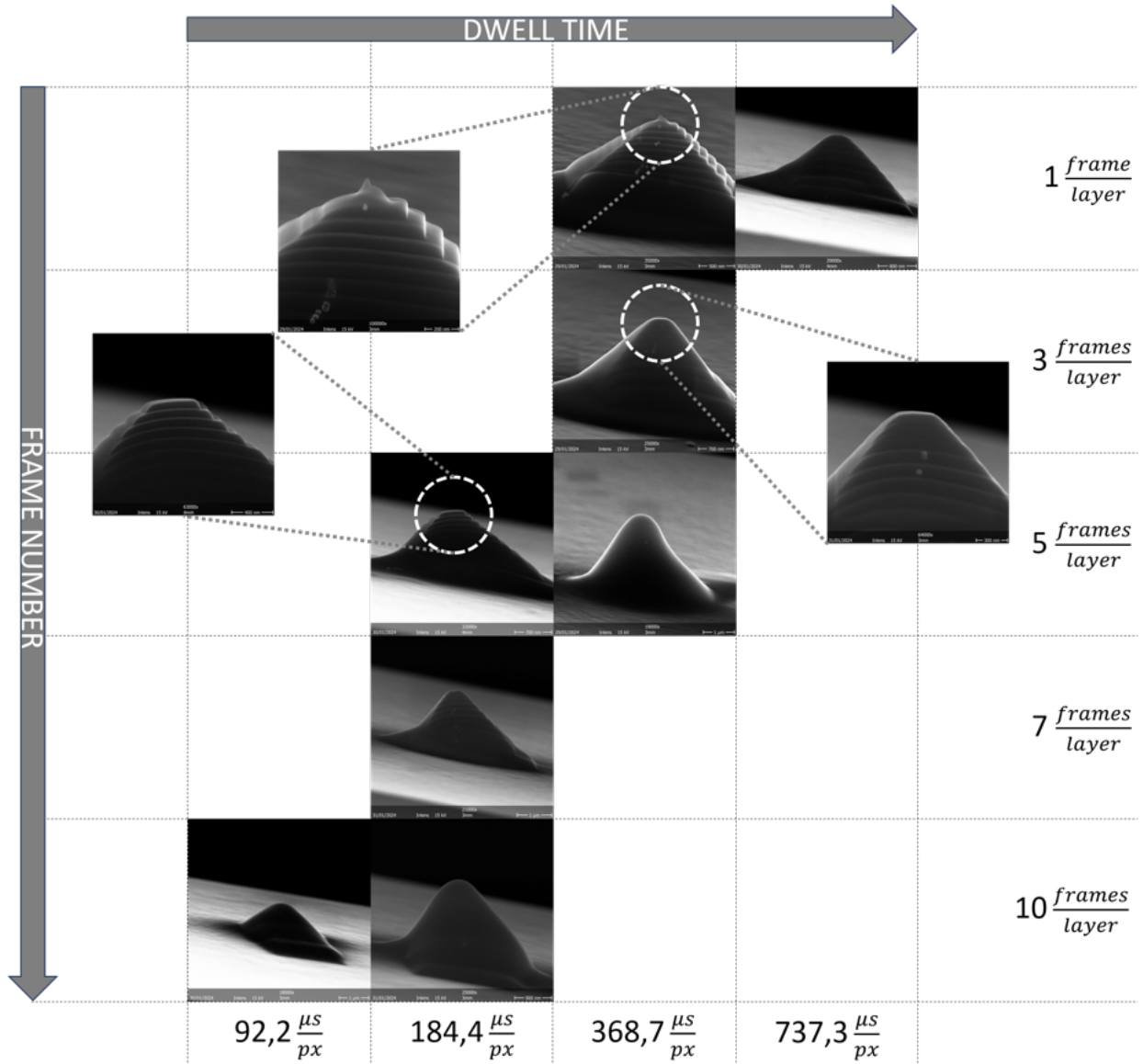


Figure 3.25 Dependence of pyramid growth on dwell time and frame number for the EBID process at $U = 15kV$, $D = 60\mu m$, $M = 50000$, with the layer structure as shown in Fig. 3.24.

of 3 to 5. Reducing the dwell time and increasing the number of frames results in homogeneous but less well-defined structures. There is a tendency for drift, likely due to charge accumulation, which causes minor shifts between subsequently deposited frames. With a higher number of frames, these accumulated shifts become significant, leading to an overall curved form. For frame numbers reaching 10, the shifts between frames cause a loss of sharp features, and the pyramids take on a globally smooth surface.

Importantly, in this case, local growth is distributed over many iterations, allowing the entire 2D surface of the layer to grow more homogeneously. Subsequent frames can smooth out previous fluctuations.

Conversely, when increasing the dwell time and reducing the number of frames,

the resulting pyramids exhibit sharper features but less homogeneity. The reduced number of frames makes the accumulated shifts between frames less significant. This produces straight pyramids with well-defined steps but also sharp peaks at the apex, rather than a flat plateau (e.g. $\tau = 368.7\mu s$ & $1\frac{\text{frame}}{\text{layer}}$). The larger dwell times likely cause strong localized growth of high pillar-like structures, which are deposited next to each other with each pixel increment of the beam. These pronounced surface changes at the beam spot strongly alter the secondary electron distribution, leading to inhomogeneous growth at the surface. This issue becomes especially problematic at the apex, where the surface-to-probe-size ratio is smallest. For dwell times exceeding $500\mu s$, the inhomogeneity spreads across the entire apex, resulting in a smoothly curved geometry, similar to the case of large frame numbers.

In conclusion, to ensure homogeneous growth, a large number of frames and short dwell times represent the most effective strategy. However, excessive frame numbers may lead to charge-induced shifts that dominate the growth process. Based on our experience, the parameters listed in Tab. 3.3 have proven to be optimal, typically producing pyramids with a height of approximately $1.7 - 2.1\mu m$ and a plateau length of approximately $0.3 - 0.5\mu m$.

Acceleration Voltage and Magnification

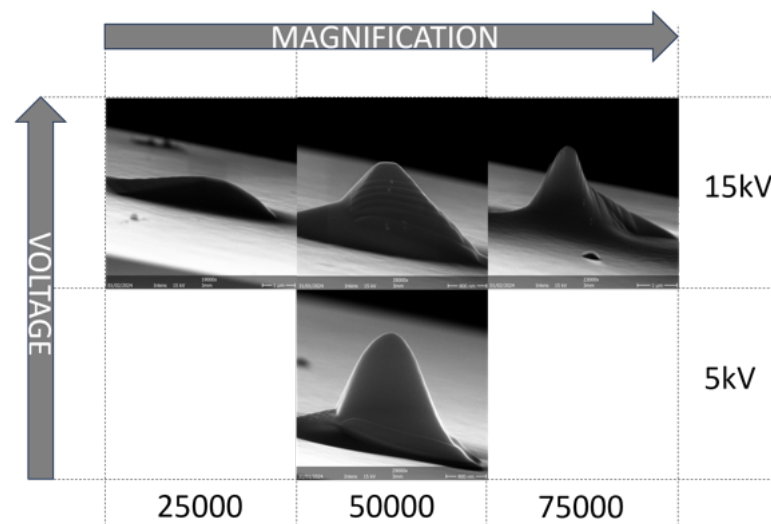


Figure 3.26 Dependence of pyramid growth on magnification and acceleration voltage for the EBID process at $D = 60\mu m$, $\tau = 368.7\frac{\mu s}{px}$, with the layer structure as in Fig. 3.24, and 3 frames per layer.

For completeness, we briefly examine the effects of parameters that were fixed earlier in the process, namely magnification and acceleration voltage. We set the dwell time and frame number as specified in Tab. 3.3 and investigate the impact of varying U and M on the growth dynamics.

As observed with $D = 30\mu m$, decreasing the acceleration voltage U results in an increased height from $1.9\mu m$ to $2.5\mu m$, but with less sharp features. This is due to the increased number of secondary electrons and the reduced resolution caused by the larger de Broglie wavelength.

When analyzing the influence of magnification M , we find that reducing it produces smaller and smoother structures, while increasing it results in larger, more inhomogeneous, and drifted structures. This outcome is expected, as M defines the deposition area and current density. Smaller magnification values lead to a larger growth area with a smoother current distribution, corresponding to the observed smooth large-scale deposition. Conversely, higher magnification causes localized and enhanced current densities, leading to higher and more inhomogeneous structures.

Raman Analysis

Fig. 3.27 presents the Raman spectrum of the pyramids, highlighting the prominent G-peak and the D-peak, the latter situated at approximately 1355cm^{-1} . Both peaks exhibit significant broadening and overlap, which is characteristic for amorphous carbon. This material consists of various clusters exhibiting differing orders, chemical bonding, and dimensions.

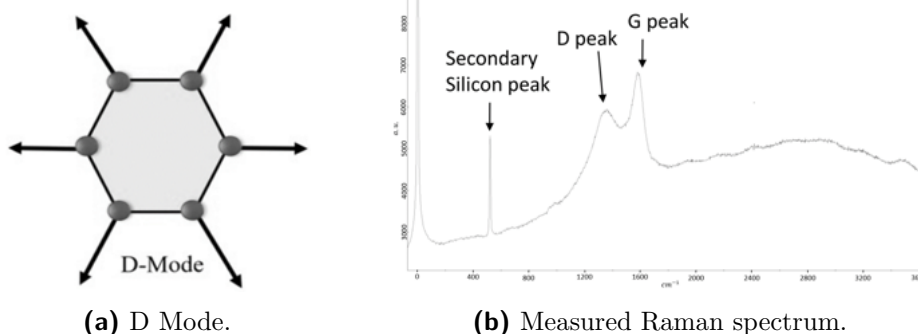


Figure 3.27 D(disorder)-peak in amorphous carbon. Adapted from [77].

Broadly, the intensity of the D-peak increases with the degree of disorder, transitioning from graphitic carbon to amorphous carbon. The D-peak corresponds to the breathing vibrations of the sixfold rings, which only occur where the graphite rings have space to stretch, thus being absent in monocrystalline graphite [78].

3.4.5 Polymer Membrane Transfer Technique

To transfer vdW-materials onto the tip, we employ Polymer Membrane Transfer Technique [79]. This method relies on a polymer layer carrying the flake from the exfoliation substrate onto the tip.

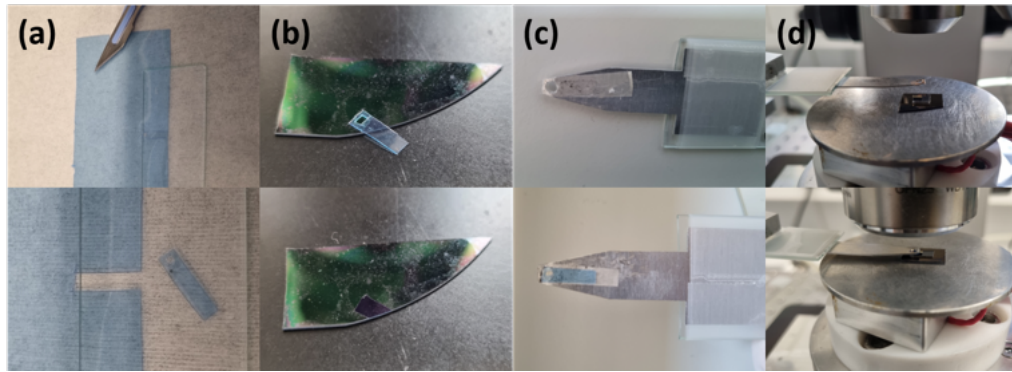


Figure 3.28 Preparation of the transfer slide: (a) A window is cut into a piece of adhesive tape. (b) Polymer layer with flake centered in the window is peeled of the substrate. (c) Flake is aligned with the hole on the transfer slide. (d) Transfer slide is mounted on the transfer stage and brought into contact with the cantilever.

To create a sacrificial polymer layer, which will carry the flake, we spin-coat polypropylene carbonate (PPC) onto the Si/SiO₂ substrate (PPC/polyvinyl pyrrolidone for MLG) before exfoliating graphene/hBN crystals onto it (Sec. 3.1). A window is cut into a piece of adhesive tape (Fig. 3.28a), which is used to pick up the polymer film with the target crystal centered within the window (Fig. 3.28b). The tape is then attached to a transfer slide (Fig. 3.28c) clamped to the micromanipulator and positioned under an optical microscope (Fig. 3.28d). The cantilever is placed on the sample stage which is heated up to 50°C. Using the microscope and micromanipulator, the flake can be located and precisely aligned with the target (Fig. 3.30(2)). The flake and the top of the carbon pyramid are then brought into contact (Fig. 3.30(3)). Heating up the sample to 120°C causes the melting of the polymer film, which allows the gentle detachment of the flake from the transfer slide (Fig. 3.30(4)). The transfer slide is then slowly raised, and any remaining residues are washed off using acetone and isopropanol (Fig. 3.30(5)).

The vdW heterostructure is assembled by successive transfers and cleanings after each layer. We fabricated two types of tips for our experiments. In one case, we only transferred a single graphite flake onto the pyramid. In the other case, this step was followed by the transfer of an insulating hBN flake and an MLG flake, as shown in Fig. 3.31. In this case, the number of layers of the graphene flake is determined by Raman analysis. For instance, the sharp single 2D peak with lorentzian shape in the Raman spectrum in Fig. 3.29 confirms the single layer thickness (Sec. 3.3).

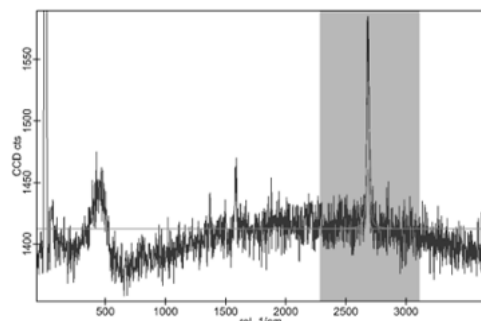


Figure 3.29 Raman spectrum of MLG with 2D-peak situated in grey area

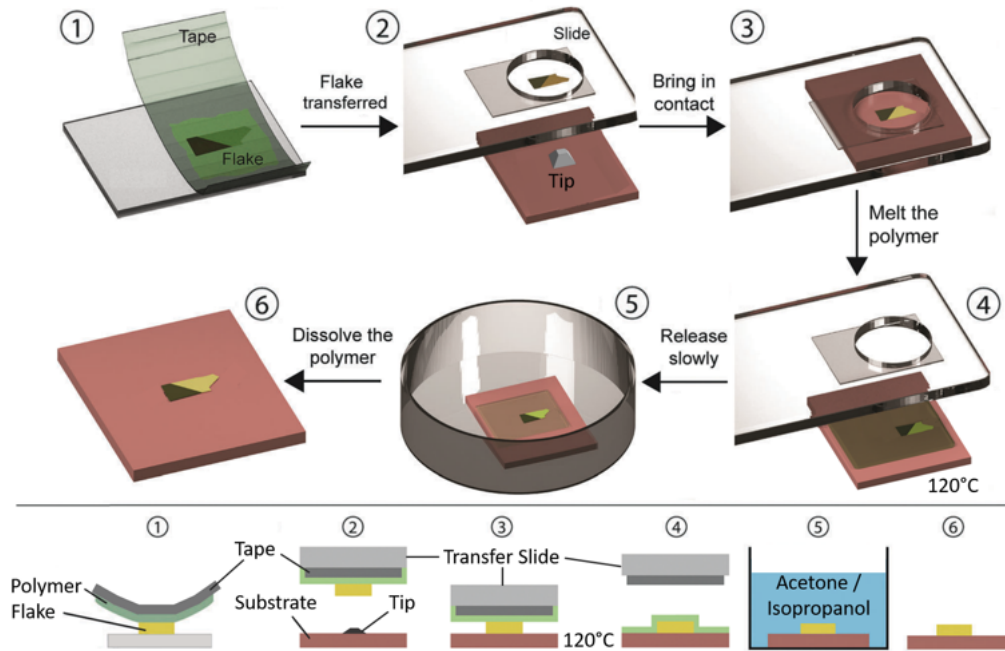


Figure 3.30 Polymer membrane transfer technique: The target flake is exfoliated onto a layer of PPC, which is used to pick up the flake with an adhesive tape (1). The tape is attached to a transfer slide and the flake aligned with the tip on the substrate (2). The flake is brought into contact with the substrate (3). The substrate is heated to 120°C, melting the polymer layer (4). The remaining polymer residues are then dissolved in acetone and isopropanol (5), leaving the flake transferred onto the tip (6). Adapted from [79]

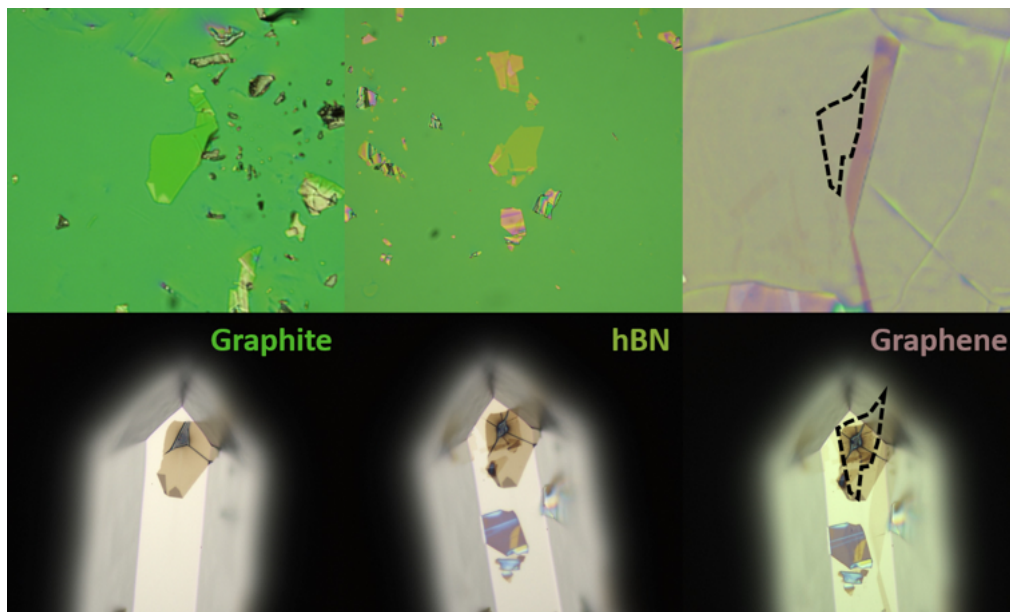


Figure 3.31 Successive transfer of graphite, hBN and graphene: Exfoliated flakes on coated Si/SiO₂ substrate (top). Flakes after transfer on cantilever (bottom).

Figure 3.32 depicts the deposition process of an hBN flake (yellow) initially situated on the membrane onto the EBID-tip covered by graphite (blue). Once the membrane

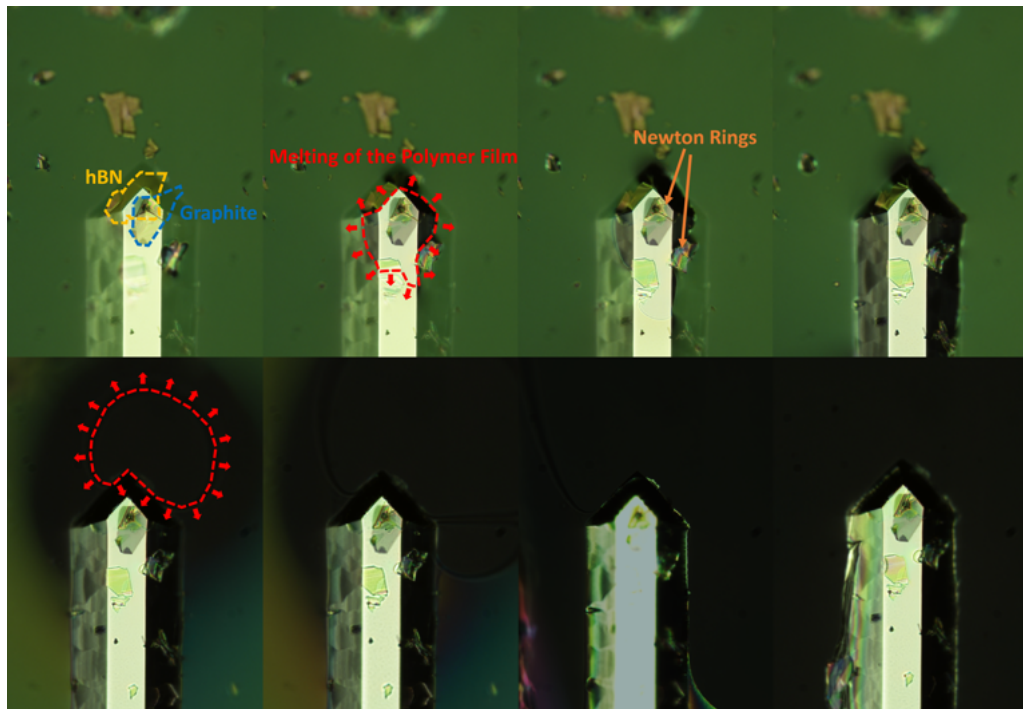


Figure 3.32 Top Row: Polymer film adheres on the heated cantilever (50°C) and melts. Bottom Row: After further heating (120°) film crumbles, leaving the cantilever detached from the transfer slide

touches, it adheres to the hot surface (50°C) and starts to melt pushing all flakes not in direct contact away from the cantilever. The emergence of the interference pattern (Newton rings) on the tip indicate a successful deposit. Subsequently, the sample is heated to 120°C , melting the remaining polymer film, which sticks to the body of the cantilever as illustrated in the lower row of Fig. 3.32 and Fig. 3.33.

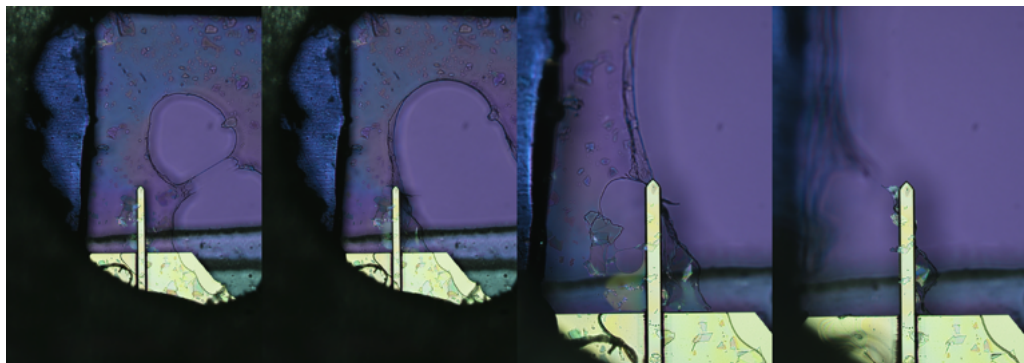
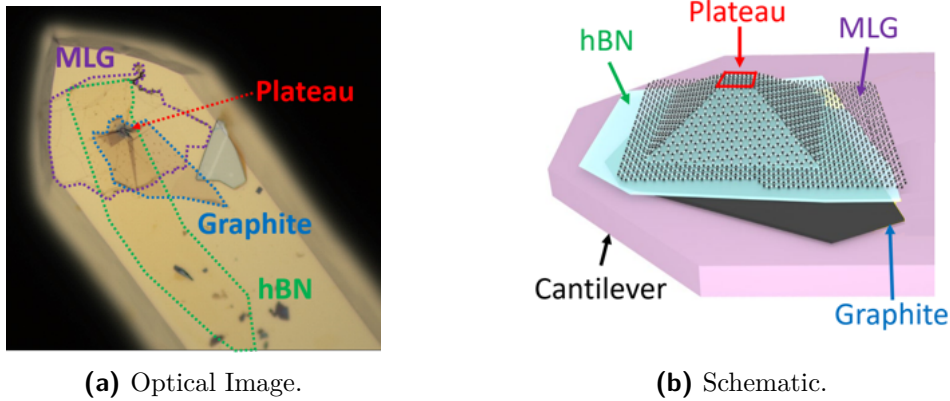


Figure 3.33 Heating causes the film to crumble which spreads over the whole window.

Figure 3.34 shows the schematic and an optical image of a fabricated tip. The graphite flake acts as an atomically flat mechanical support and contact material. The hBN layer is deposited to electronically decouple MLG from graphite on the apex of the tip. The MLG flake is then transferred in a way that it still touches the graphite flake away from the tip. This way the apex region is defined by the MLG flake, lying on the same electrical potential as the graphite flake.



(a) Optical Image.

(b) Schematic.

Figure 3.34 Tip device. Adapted from [14].

3.5 Sample Device

In this section, we briefly introduce the dry van der Waals pick-up transfer technique used for the assembly of our sample devices [79].

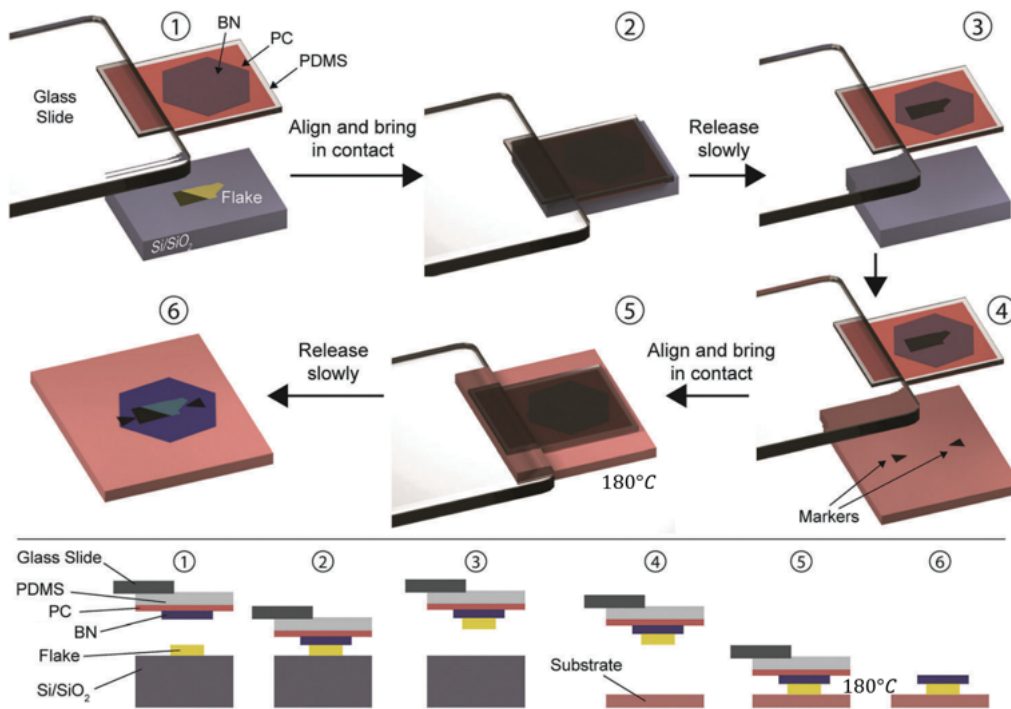


Figure 3.35 Van der Waals pick-up transfer method: The flake to be transferred is exfoliated onto a Si/SiO₂ substrate (1). A stack composed of PDMS with a layer of PC and a hBN flake is attached to a glass slide. The hBN is brought into contact with the target flake (2), and by releasing the contact slowly, the target flake can be picked up, remaining attached to the hBN flake (3). The stack is then positioned on top of the target substrate (4) and brought into contact (5). After melting the PC-film at 180°C, the target flake capped by the hBN flake can be transferred by slowly releasing the contact (6). Adapted from [79]

Unlike the previously described deterministic transfer method that relies on sacri-

ficial polymer membranes, the following concept exploits the van der Waals interaction between different 2D materials to transfer flakes without contacting the 2D materials with any polymer throughout the process.

The target flake to be transferred is exfoliated onto a SiO₂ surface (Sec. 3.1). To pick up the flake and transfer it to the desired position, a stamp composed of a polydimethylsiloxane (PDMS) film coated with a layer of polycarbonate (PC) and a thin hBN flake is used, as depicted in Fig. 3.35. The stamp, mounted on the micromanipulator for control and alignment (1), is lowered until the hBN flake contacts the target flake (2). The atomically flat and clean surfaces of both flakes result in a large contact area and adhesion force. By slowly lifting the stamp, the flake is picked up from the substrate (3), which is done subsequently for the FLG-flake, a large graphite flake (only partially covering the FLG) and another hBN flake. The stacked flakes are then precisely aligned with the target substrate (borosilicate glass) (4) and brought into contact, so that the large flake of graphite bridges between the pre-patterned electrical contacts on the substrate and the FLG flake (5). After melting the PC film at 180°C, the stack can be transferred by gently releasing the contact (6). After assembly, the heterostructure is cleaned by DCM or chloroform to remove bulk of the PC residues before annealing the sample at 450°C for 5min.

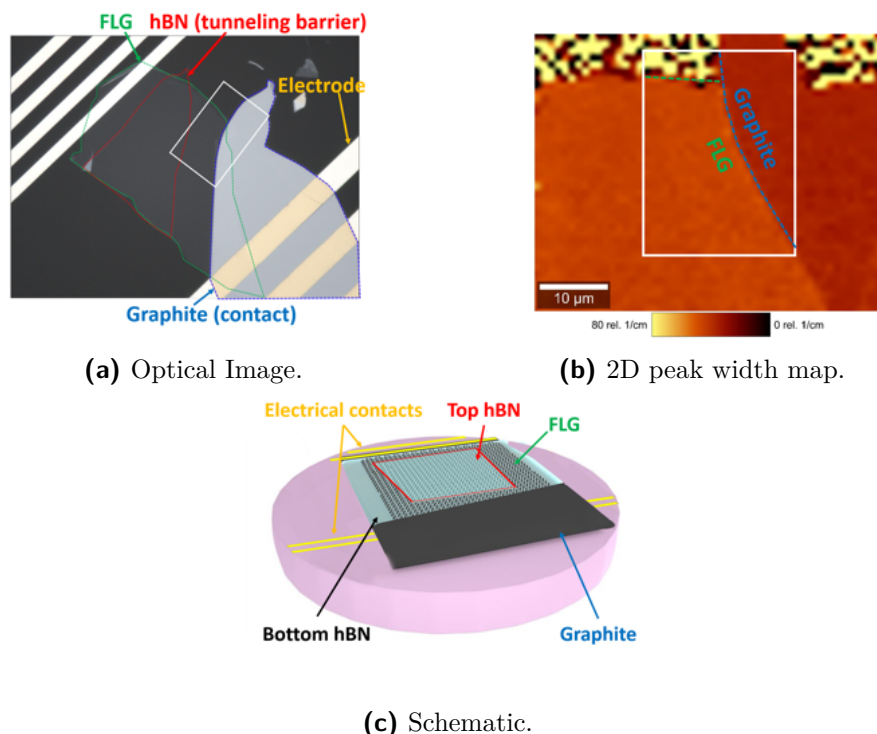


Figure 3.36 Sample device: (a)&(c) The stack consists of hBN (spacer towards substrate), graphite (contact for FLG), FLG (system to probe), thin hBN (insulating barrier). (b) Raman map of the white rectangle in (a): Boundary between the area where graphite lies below the FLG flake, causing the broadening of the 2D-peak. Adapted from [14].

The sample device is depicted in Fig. 3.36c. The large graphite flake is in direct contact with the electrodes as well as the FLG-flake, ensuring their both are at the same potential. Contact with the tip is made in the area covered by the thin hBN film.

3.6 Quantum Twisting Microscope

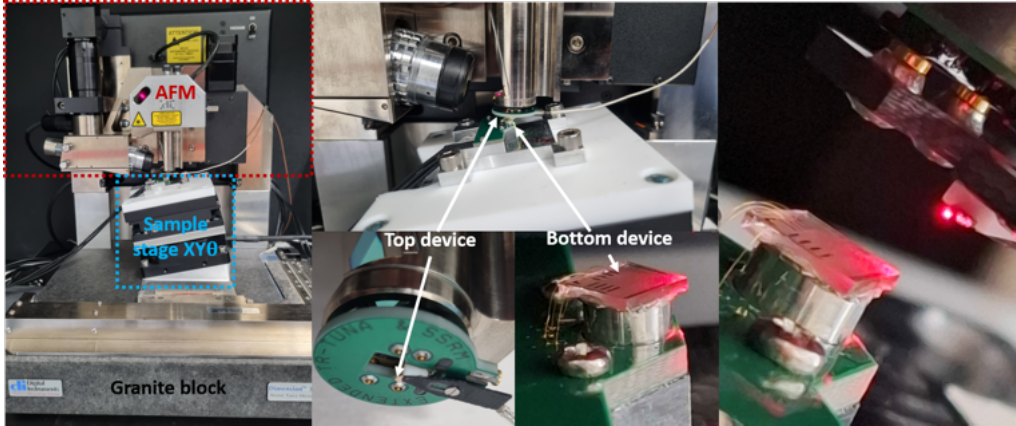


Figure 3.37 Images of the QTM setup.

Our QTM setup (Fig. 3.37) comprises of two parts: Firstly a custom-built rotating stage housing the bottom devices and secondly a commercial atomic force microscope (Veeco Dimension 3100) for performing the AFM operations (Force feedback and lateral positioning). In order to fit the rotation and translation stages beneath the scan head, an aluminium block is used as a spacer between the scanhead and the granite body. A conventional AFM has a large inclination angle, $\sim 12^\circ$, which is problematic for the QTM experiments, since our QTM tips have much shorter pyramids ($\sim 1 - 2\mu\text{m}$) than conventional AFM tip pyramids ($\sim 20\mu\text{m}$) (Fig. 3.13). In addition, for the QTM tip to work, the cantilever should have a few tens of μm of flat cantilever surface in all directions around the pyramid, such that the vdW heterostructure can adhere well to the cantilever all around the pyramid [14]. With conventional 12° inclination, such a tip will not reach the sample surface because the front of the cantilever will touch it instead. The QTM experiments are therefore designed such that the inclination of the tip with respect to the sample is small, $\sim 1^\circ$. In a commercial AFM we cannot change the inclination angle of the tip since the laser illumination and detector are designed to work at this angle. Instead, we mounted the rotator (DDR100 brushless rotator) on a wedge of $\sim 11^\circ$ such that the relative inclination between sample and tip is reduced to about 1° . XY stages (M30XY from Thorlabs) mounted on top of the rotator, position the device's point-of-interest in the center of rotation and assure that the rotation axis is perpendicular to the sample plane, and the sample surface rotates parallel to itself. DTRCH-AM

cantilever holder with a modified electrical connection is used to clamp down the cantilever while electrically connecting it to the measurement circuit. The AFM enables us to bring the two vdW surfaces (on the tip and the sample) into contact. Additionally, we use the active force feedback to maintain a constant force during rotation and measurement with a submicro-Newton precision.

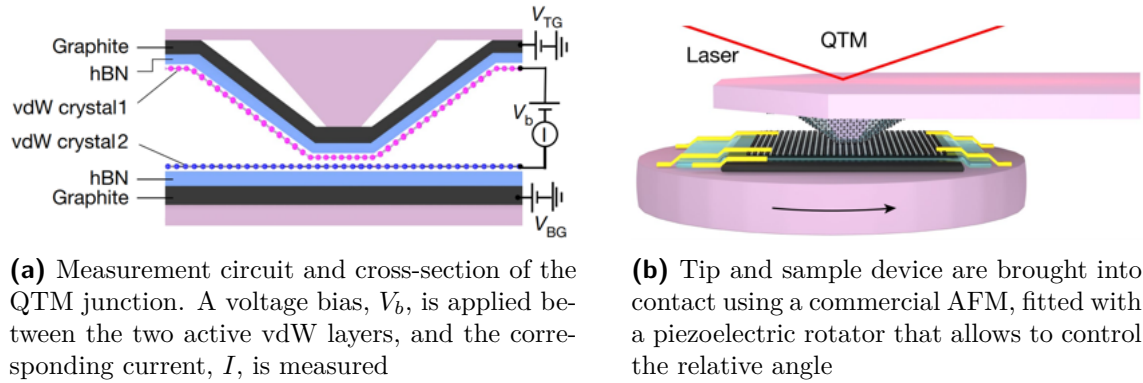


Figure 3.38 Schematic of the QTM setup. Adapted from [14].

The measurement circuit is depicted in Fig. 4.22b. Measurement is conducted such that the bias V_b is applied to the sample and the current is collected at the tip. The applied signal consists of a D.C. voltage (for biasing) from a source measure unit (SMU, Keithley 2450) and an A.C. voltage (for differential conductance) from a lock in amplifier (SR860) added through a summing amplifier (SIM 980). The measured tunneling current from the tip is converted to voltage and amplified using an op-amp (DLPCA-200). The signal is split such that the D.C. value is measured with a multimeter (DMM7510) and the A.C. value is measured back in the lock in amplifier. The buried top and bottom graphite gates (Fig. 4.22b) with gate voltages, V_{BG} and V_{TG} , allow modification of electric field in the junction, however within this thesis, the top gate and bottom gate stay physically shorted to the graphene layers on top of the sample and tip.

Chapter 4

Tunneling Spectroscopy

In this chapter, we explore the twist-angle dependent transport characteristics in various graphene systems. We begin with a brief review of QTM's working principle and establish the necessary theoretical framework. Following this, we present both theoretical simulations and experimental measurements of the interlayer current in twisted graphene layers in direct contact.

Subsequently, we introduce a tunneling barrier between the tip and the sample to examine the twist-dependent tunneling current in few-layer graphene samples. Again, this investigation is conducted through both theoretical analysis and experimental validation.

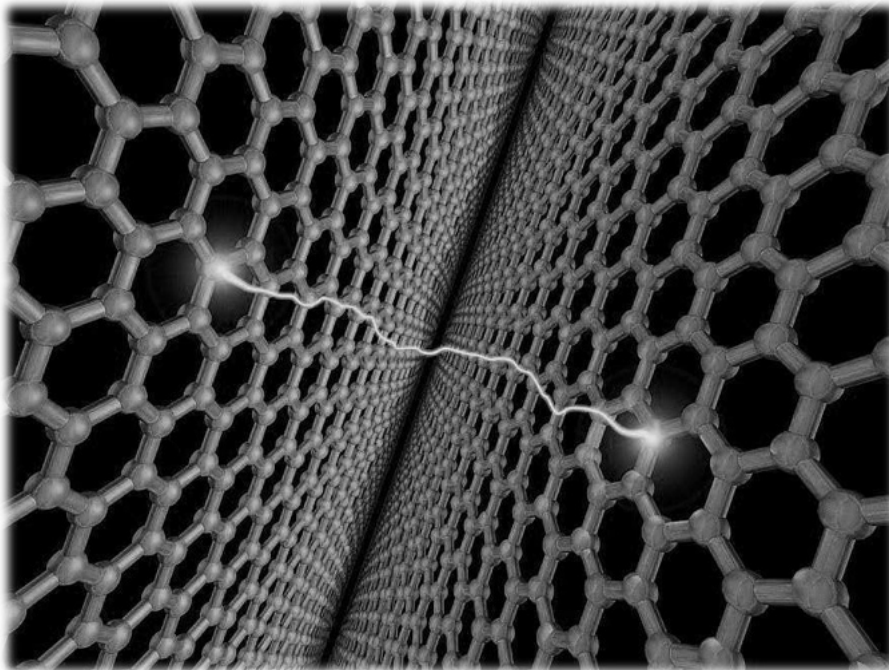


Figure 4.1 Adapted from [\[80\]](#).

4.1 QTM's Working Principle - STM and AFM

The development of the scanning tunneling microscope (STM) revolutionized the field of meso- and nanoscale physics, enabling unprecedented visualization of electron behavior in real space [81]. This groundbreaking technology, for which Binnig and Rohrer were awarded the Nobel Prize in 1986, paved the way for a variety of other scanning probe techniques that allow for localized measurements of electronic properties.

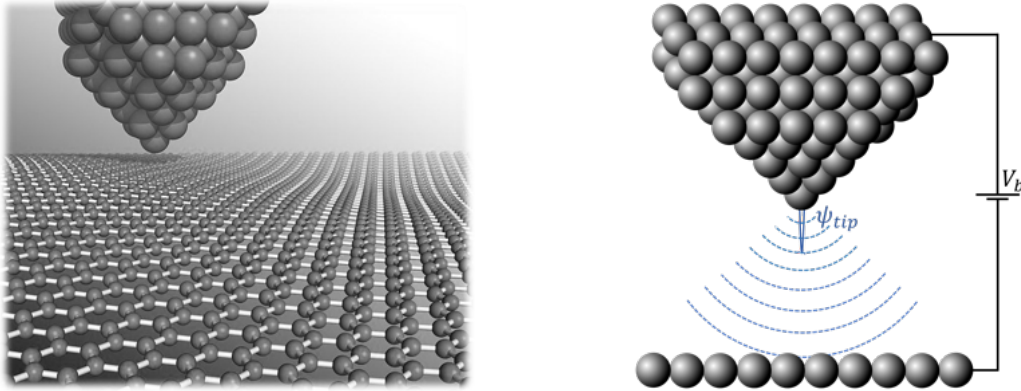


Figure 4.2 STM Working Principle. Adapted from [82].

Consider the STM measurement concept as illustrated in Fig. 4.2. The core component is a thin tip that serves as the source of electrons. The electron wavefunction in the tip overlaps with those in the sample surface, generating a finite tunneling conductance. When a bias voltage is applied between the tip and the sample, electrons tunnel into the sample surface, producing a current.

According to Fermi's Golden Rule, the tunneling current I for small bias voltages V_b (linear regime) can be calculated as [83]:

$$I = \frac{2\pi e^2}{\hbar} V_b \sum_{\mu, \nu} |M_{\mu, \nu}|^2 \delta(E_\mu - E_F) \delta(E_\nu - E_F) \quad (4.1)$$

where $M_{\mu, \nu}$ is the tunneling matrix element between the states ψ_μ of the probe and ψ_ν of the surface, and E_μ and E_ν are the corresponding eigenenergies in the absence of tunneling. For simplicity, we consider the limit where the tip is replaced with a point probe. If the tip wavefunctions are arbitrarily localized, the matrix element is proportional to the amplitude of ψ_ν at the position \mathbf{r}_0 of the probe, reducing eq. 4.1 to [83]:

$$I \propto \sum_{\nu} |\psi_\nu|^2 \delta(E_\nu - E_F) \quad (4.2)$$

Thus, the tunneling current is proportional to the surface local density of states

(LDOS) at E_F , i.e., the charge density from states at E_F at the position of the point probe. In this simplified model, the microscope image represents a contour map of constant surface LDOS. Figure 4.3 depicts such an STM image of graphite, reflecting the spatial charge density over the xy -plane, measured at a fixed tip-sample distance.

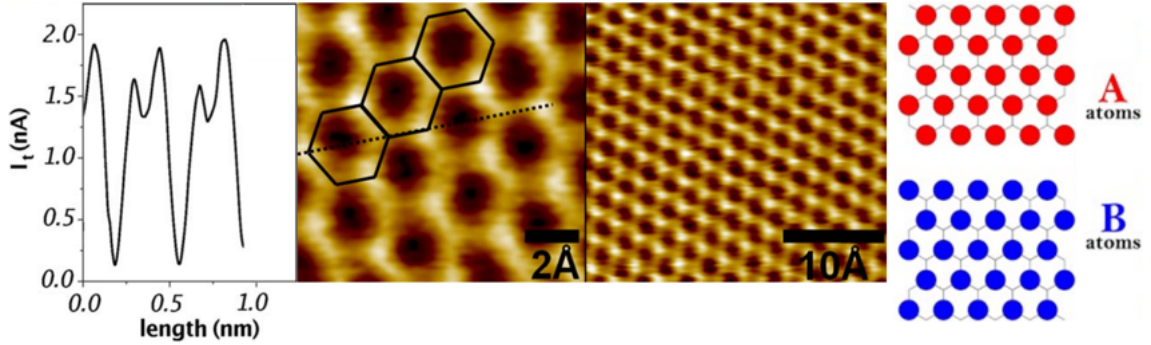


Figure 4.3 STM image (middle), line profile along the dashed lines (left) of Graphite at constant-height and $V_b = -300mV$. Illustration of monomer (A) and non-monomer (B) sites (right). Adapted from [84].

The images reveal the hexagonal atomic structure of the lattice, showing current maxima on three of the six carbon atoms of the hexagonal ring. This is most visible in the line profile measured along the dashed line, confirming that one kind of atom presents a higher current density, revealing a difference in the LDOS. This asymmetry between monomer and non-monomer sites (Sec. 2.5) is because the low energy bands are mainly composed of monomer sites, which feature a higher LDOS near the Fermi level compared to non-monomer sites. Therefore, we observe the superposition of two triangular lattices with distinct tunneling current amplitudes [84].

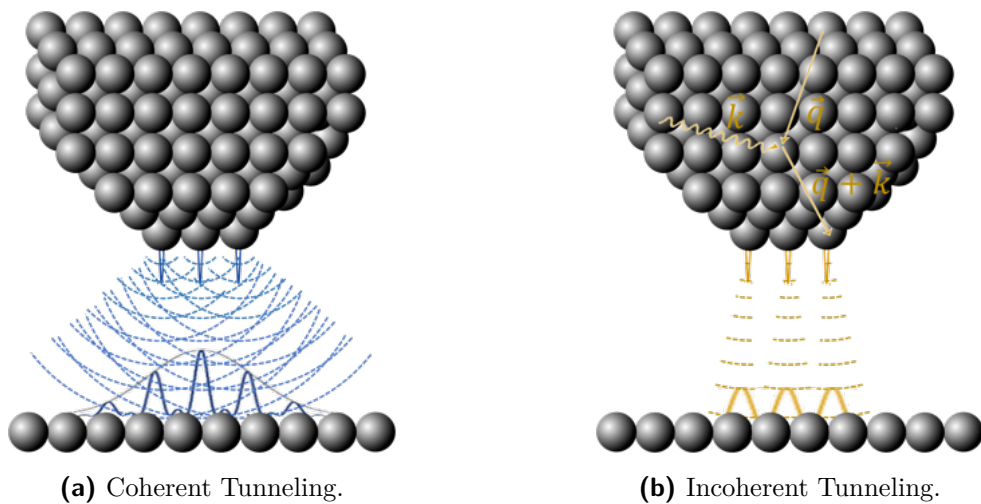


Figure 4.4 Phase (in-)coherent Tips.

In cases where tips have more than one atom at the apex, as depicted in Fig. 4.4a, STM images can be rather different, since the wave function coming through different

atoms interfere, yielding a current that is sensitive also to the local phases of the wavefunctions.

Let's model the electronic state of the tip with states $\{|1\rangle, |2\rangle, |3\rangle\}$ and sample states as the set of Bloch states $\{|\mathbf{k}\rangle\}$. If all three tip states are quantum coherent and equivalent in their contribution, the tip wavefunction can be written as $|\psi\rangle = \frac{1}{\sqrt{3}}(|1\rangle + e^{i\phi}|2\rangle + e^{i\theta}|3\rangle)$ with defined phase relations. The transition amplitude is then given by:

$$|\langle \mathbf{k} | H_{int} | \psi \rangle|^2 = \frac{1}{3} \left(|M_{\mathbf{k},1}|^2 + |M_{\mathbf{k},2}|^2 + |M_{\mathbf{k},3}|^2 \right) + \frac{1}{3} \left(\text{Re}(M_{2,\mathbf{k}} M_{\mathbf{k},1}) \cos(\phi) + \text{Re}(M_{3,\mathbf{k}} M_{\mathbf{k},2}) \cos(\phi - \theta) + \text{Re}(M_{1,\mathbf{k}} M_{\mathbf{k},3}) \cos(\theta) \right)$$

The first term represents the classical contribution obtained by summing probabilities, while the second term is the interference term dependent on the phase differences between different sites on the tip.

Loss of coherence (decoherence) refers to the diminishing of the interference term, due to interactions with environmental degrees of freedom, such as lattice vibrations or electromagnetic fields. This process is illustrated in Fig. 4.4b, where electron-phonon scattering destroys coherence. Consequently, tunneling events become independent, and summing them classically yields the total current. STM images, therefore, represent a superposition of images from single-tip atoms shifted by their relative positions.

The quantum twisting microscope (QTM) is a powerful new instrument complementing previously existing local probes. Rather than measuring the local tunneling current at the atomic scale, it relies on coherent tunneling across a twistable finite-area junction formed at the interface between van-der-Waals systems placed on a scanning tip with a flat plateau on top and on a substrate (Fig. 3.38b) [14]. By replacing the sharp tip with a plateau covered by a 2D material, the electrons delocalize over many equivalent unit cells. The tip Hamiltonian can be expressed as $H_{\text{tip}} = H_{\text{TB}} + V_{\text{edge}}$, where H_{TB} is the periodic crystal field Hamiltonian of the 2D material and V_{edge} accounts for the finite tip size. As $\frac{L_{\text{unitcell}}}{L_{\text{tip}}} \rightarrow 0$, H_{tip} approaches H_{TB} , and the eigenbasis of H_{tip} starts resembling delocalized Bloch states. In this limit, tunneling occurs between Bloch states, conserving both energy and crystal momentum. This E- \mathbf{k} selectivity allows QTM to directly access the energy-momentum dispersion of electronic systems [14].

Momentum- and energy-resolved tunneling rely on quantum coherence. The very existence of a Bloch state $|\mathbf{k}\rangle$ on the tip requires defined phase differences between lattice sites, while coupling between Bloch states relies on the interference of the

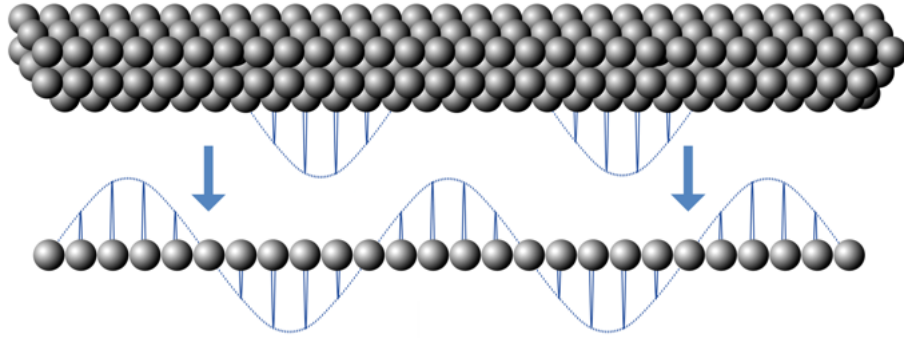


Figure 4.5 Interlayer Coupling of Bloch States.

respective wavefunction on both sides of the junction (Fig. 4.5). Loss of coherence results in independent tunneling events across the tip. At higher temperatures, when inelastic processes such as electron-phonon and electron-electron scattering become considerable, we can expect the QTM to lose its momentum-resolved nature.

Besides decoherence, momentum-resolved tunneling can be suppressed by elastic scattering, which provides momentum kicks, breaking momentum conservation during tunneling [14]. This typically happens at tip boundaries V_{edge} and from disorder, such as vacancies or dislocations (Fig. 4.6). This static disorder is represented by the potential V_{dis} . Especially at low temperature electrons near the Fermi surface predominantly scatter off elastically of V_{dis} and V_{edge} .

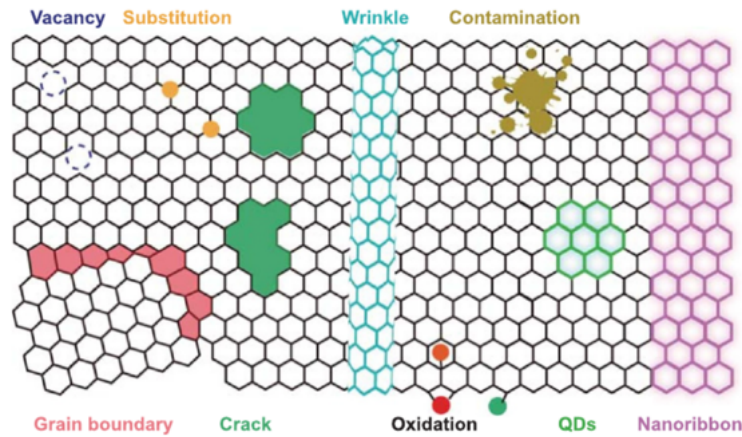


Figure 4.6 Schematic of Structural Disorder in Graphene. Adapted from [85].

It follows that the previously calculated eigenstates $\{|\mathbf{k}\rangle\}$ with well defined momentum and energy relation $E(\mathbf{k})$ from the undisturbed Hamiltonian no longer describe stable states of the complete system. Strictly speaking \mathbf{k} loses its meaning as a good quantum number. However assuming a weak disorder potential and relatively large tip plateaus on the atomic scale, so that V_{dis} and V_{edge} can be treated perturbatively, we can introduce the disorder averaged lifetime τ , a characteristic time interval in which the new eigenstates can be temporary approximated by the states $|\mathbf{k}\rangle$ of the unperturbed Hamiltonian H_{TB} . The effect of V_{dis} and V_{edge} can then be modeled

by scattering an initial state $|\mathbf{k}_i\rangle$ into $|\mathbf{k}'\rangle$ with a coupling rate τ^{-1} proportional to $\overline{\langle \mathbf{k}_i | V_{\text{dis}} | \mathbf{k}' \rangle}$ (Fig. 4.7) [86].

If disorder is negligible, our perturbative picture reduces to scattering events occurring after the time τ required for an electron to traverse the tip. Using graphene's Fermi velocity ($v_F \approx 10^6 \frac{m}{s}$), we derive $\tau = \frac{L_{\text{tip}}}{v_F}$ [14]. Thus, even for clean samples and low temperatures, the lifetime is limited by the tip size L_{tip} . Unlike STM, where $L_{\text{tip}} \rightarrow 0$ maximizes resolution, QTM favors tips extending over many unit cells.

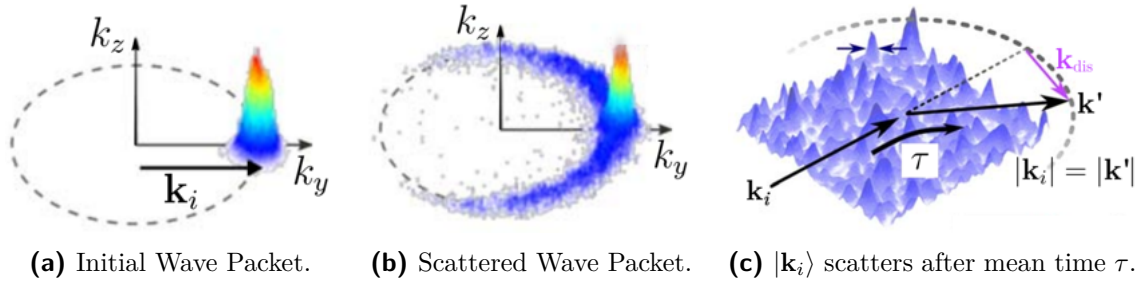
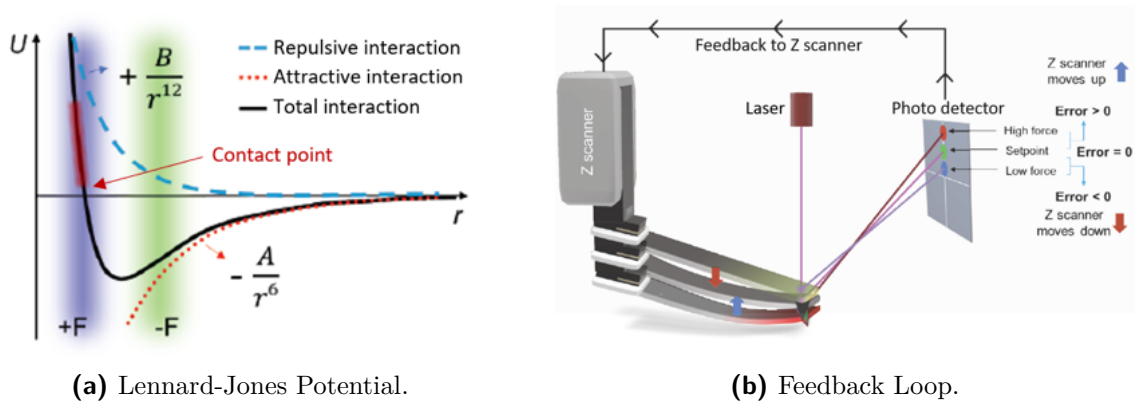


Figure 4.7 Elastic scattering process of a Bloch wave centered at $|\mathbf{k}_i\rangle$ into the spectrum of states $\{|\mathbf{k}'\rangle\}$ with the same energy. Adapted from [86].

Since tunneling relies on wavefunction overlap, tip-sample distance fluctuations are very problematic. To maintain constant height, the AFM force sensor is used. The interaction between the tip and sample generates a force field (Fig. 4.8a), deflecting the tip, which is registered by the position-dependent photodetector (Fig. 4.8b). The AFM fixes the deflection distance, by ensuring that a constant force is applied to the surface while twisting [87].



(a) Lennard-Jones Potential.

(b) Feedback Loop.

Figure 4.8 AFM Working Principle: Potential energy U of the tip versus tip deflection distance r (b) features two basic regions of interaction. First the long-ranged attractive region created van der Waals Forces (green). Those arise from dipole-dipole interactions which result from charge fluctuations in the electron clouds of atoms residing on adjacent layers. Secondly, the short-ranged repulsive region (blue), originating mainly from Pauli repulsion between overlapping electron clouds. The AFM (a) fixes the tip deflection distance, by ensuring that a constant force is applied to the surface. Adapted from [88] [89].

In summary, the QTM merges STM and AFM technologies. The AFM ensures

constant tip-sample distance and the STM measures current $I(\theta, V_b)$ by applying a voltage across them, while adjusting the angular alignment.

4.2 Transport Between Two-Dimensional Materials with Finite Disorder

In this section, we derive an expression for the tunneling current between parallel two-dimensional electron systems. The theory is based on impurity-averaged perturbation theory, where the second-order contribution defines the tunneling current as follows [90]:

$$I(V_b) = -\frac{4eg}{2\pi} \int dE \left(f_1(E - \phi(V_b)/2) - f_2(E + \phi(V_b)/2) \right) \times \sum T_{\mathbf{k}_0\mathbf{p}_0}^{\alpha\beta} T_{\mathbf{k}_1\mathbf{p}_1}^{\gamma\delta*} \overline{\text{Im}[G_{1\gamma\alpha}(\mathbf{k}_1, \mathbf{k}_0, E - \phi(V_b)/2)] \text{Im}[G_{2\beta\delta}(\mathbf{p}_0, \mathbf{p}_1, E + \phi(V_b)/2)]}, \quad (4.3)$$

where f_j denotes the Fermi distribution in layer j , G_j is the retarded Green's function in layer j corresponding to the propagation of a charge carrier from band α to band γ , $T_{\mathbf{k},\mathbf{p}}^{\alpha,\beta}$ are the interlayer coupling matrix elements, and ϕ is the electrostatic potential energy difference between the layers, typically a function of the applied bias voltage V_b . The overline denotes disorder averaging.

Assuming negligible interlayer disorder-potential correlations, we can independently perform the averaging in eq. 4.3 for each layer. Therefore, our interest lies in MLG's disorder-averaged Green's function $\overline{G}(\mathbf{k}, \mathbf{k}', E)$. Generally, disorder breaks translational invariance, causing the Green's functions to be non-diagonal in the momentum representation. However, it is reasonable to assume that averaging over many realizations of disorder restores translational invariance, making $\overline{G}(\mathbf{k}, E)$ diagonal in momentum space [40]. This can be expressed as [91]:

$$\overline{G}(\mathbf{k}, E) = \left(E - E(\mathbf{k}) \pm \frac{i}{2\tau} \right)^{-1}, \quad (4.4)$$

where τ represents the electron lifetime. Following typical conventions, we introduce the spectral function defined as:

$$A(\mathbf{k}, E) = -2 \text{Im}[\overline{G}(\mathbf{k}, E)]. \quad (4.5)$$

The spectral function represents the probability density for excitations with wavevector \mathbf{k} to have energy E . When disorder corrections are finite but small, $A(\mathbf{k}, E)$ as a function of E at fixed \mathbf{k} is strongly peaked around the real dispersion relation energy

$E(\mathbf{k})$. Evaluating eq. 4.5 transforms the spectral function into Lorentzian form:

$$A(\mathbf{k}, E) = \frac{2\tau^{-1}}{(E - E(\mathbf{k}))^2 + \tau^{-2}}, \quad (4.6)$$

indicating a broadening of energy levels with a full width at half maximum (FWHM) proportional to the inverse lifetime τ^{-1} .

Since the spectral function is diagonal, eq. 4.3 becomes 40:

$$I = \frac{eg}{2\pi} \int dE [f_1(E - \phi/2) - f_2(E + \phi/2)] \sum_{\mathbf{p}, \mathbf{k}} |T_{\mathbf{p}, \mathbf{k}}^{\alpha, \beta}|^2 A_{1\alpha}(E - \phi/2, \mathbf{k}) A_{2\beta}(E + \phi/2, \mathbf{p}), \quad (4.7)$$

where $A_{i\alpha}(\mathbf{k}_i, E)$ denotes the spectral function for band α and layer i .

4.3 Simulation of Interlayer Conductance

Equation 4.7 defines an expression for the interlayer current as a function of bias voltage and lifetime, illustrating that tunneling occurs only between wavefunctions with matching energy and momentum. In the following, we consider the interaction between two twisted graphene layers with a relative twist angle, θ . We fix the \mathbf{k} -space basis of the sample layer (bottom 'B'-layer with basis $\{|\mathbf{k}_B\rangle\}$) and rotate the basis of the tip (top 'T'-layer with basis $\{|\mathbf{k}_T\rangle\}$) by the relative angle θ . To elucidate the resulting physics, we first focus on the linear conductance at $T = 0$. From eq. 4.7, we obtain the following expression 40:

$$\begin{aligned} G &= \partial_{V_b} \lim_{T \rightarrow 0} I(V_b) \Big|_{V_b=0} + \mathcal{O}(V_b) \\ &= \frac{e^2 g}{2\pi} \sum_{\mathbf{k}_T, \mathbf{k}_B} |T_{\mathbf{k}_T, \mathbf{k}_B}^{\alpha, \beta}|^2 A_{B\alpha}(E_F, \mathbf{k}_B) A_{T\beta}(E_F, \mathbf{k}_T) + \mathcal{O}(V_b), \end{aligned}$$

where $T_{\mathbf{k}_T, \mathbf{k}_B}^{\alpha, \beta}$ are the matrix elements defined in 2.123.

Due to the low DOS in a single graphene layer, significant charge accumulation requires a substantial shift in chemical potential. Therefore, a small bias voltage applied between the tip and the sample primarily modifies the chemical potentials, accompanied by a smaller relative shift in the energy of the Dirac points of the tip and sample due to the electrostatic potential differ-

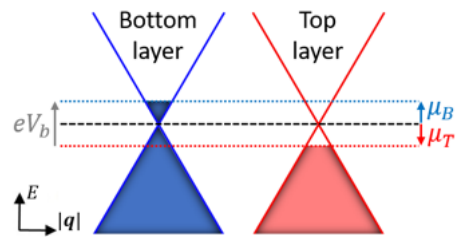


Figure 4.9 Energetics.

ence, ϕ . The magnitude of this shift depends on the geometric capacitance C_g of the system, which is inversely proportional to d_g , the distance between the tip and sample layers (see Sec. 4.26c for more details). In our analytical calculations, we focus on the limit of small d_g , where C_g becomes very large, implying $\phi \ll \mu$, and the electrostatic shift ϕ can be neglected. Consequently, the chemical potential difference is entirely determined by the electrical energy, $eV_b = \mu_B - \mu_T$. Assuming overall charge neutrality, the chemical potentials of the tip and sample feature equal magnitude and opposite sign, $\pm\mu$, leading to $eV_b = 2\mu$ (Fig. 4.9).

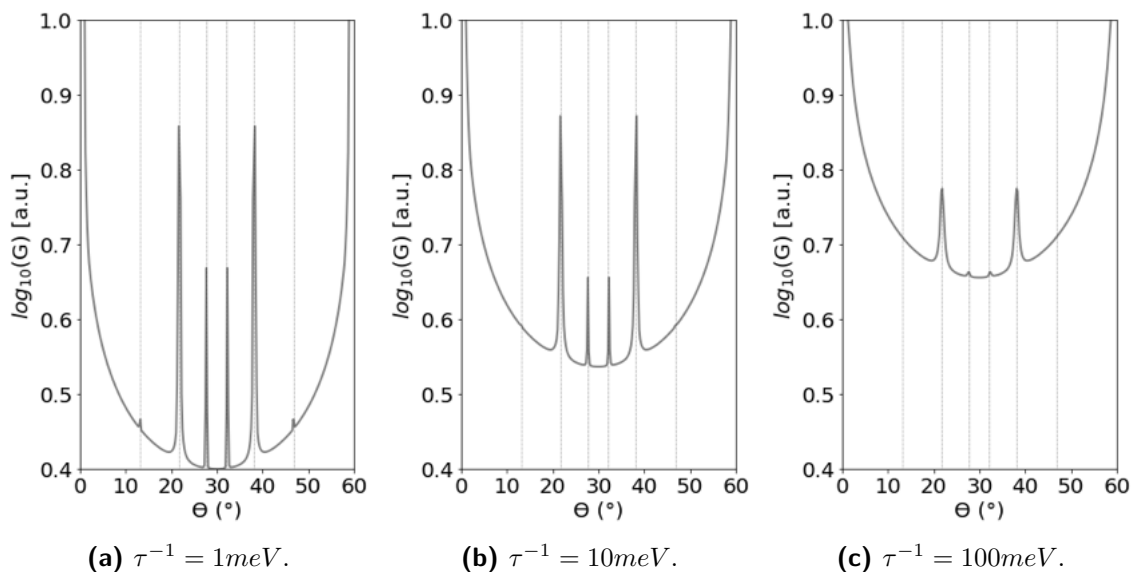


Figure 4.10 Simulated interlayer conductance G as a function of twist angle θ and $E_F = 0.1eV$. The eight conductance peaks correspond to the commensurate angles near 0° , 13.2° , 21.8° , 27.8° , 32.2° , 38.2° , 46.8° , and 60° .

The simulated linear conductance G for $V_b = 0.2V$ and τ^{-1} values of $1meV$, $10meV$, and $100meV$ is plotted in Fig. 4.10. The conductance increases sharply near the commensurate angles, with peak heights scaling with $E_F\tau$, and the peaks narrowing as τ increases [40]. When τ is reduced, some peaks become buried beneath the conduction tails of neighboring peaks.

To understand the relationship between interlayer current and commensurability, it is helpful to plot the Fermi surfaces of both layers, periodically extended in momentum space by adding reciprocal lattice vectors to the crystal momenta of the electrons. For typical carrier densities, the Fermi surface is well approximated by a circle centered on the Brillouin-zone corners. Since $\phi \approx 0$, the Dirac points of the tip and sample are aligned in energy but offset in momentum due to the rotation. The left panels in Fig. 4.11 correspond to the incommensurate rotation angles $\theta = 17^\circ, 26^\circ$, whereas the right panels correspond to the commensurate angles near $\theta = 21.8^\circ, 27.8^\circ$. Different Fermi surface sizes are used for clarity.

Near commensurate rotation angles, some Fermi spheres begin to overlap. Specifi-

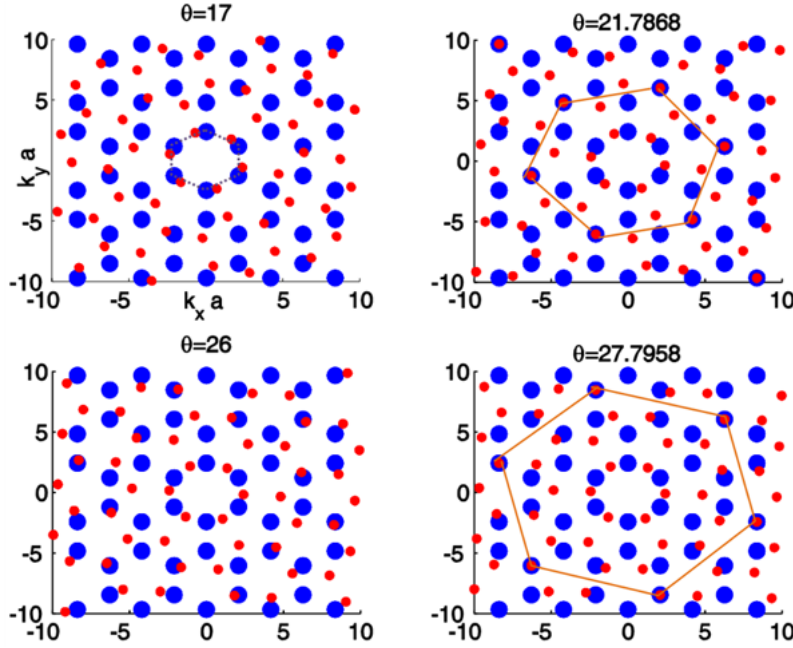


Figure 4.11 Fermi circles in an extended-zone scheme. The blue (large) and red (small) circles correspond to the Fermi circles in the unrotated and rotated layers, respectively. The Brillouin-zone boundary connects the centers of the inner shell of blue circles, as indicated by the dashed lines in the $\theta = 17^\circ$ panel. For commensurate angles, the matching Dirac points mark the corners of a supercell, as indicated by the orange lines. Adapted from [40].

cally, at $\theta = 0^\circ$, the Dirac cones of the two layers overlap at the corners of the first Brillouin zone, and at $\theta = 21.8^\circ$, they overlap at the corners of the third Brillouin zone [40].

At low energy, the Fermi surfaces are nesting when the Dirac points match perfectly (Fig 4.12). As a result, tunneling occurs between identical states, sharing the same energy and momentum, leading to the prominent peaks in Fig 4.10. Away from commensurate angles, the energy difference between states with the same extended momentum is typically much larger than the Fermi energy and the spectral function width τ^{-1} . Consequently, the conductance is very small away from the commensurate-angle peaks.

We can visualize the contributions in \mathbf{k} -space in Fig 4.13 by plotting the following expression:

$$G_B(\mathbf{k}_B) = \frac{e^2 g}{2\pi} \sum_{\mathbf{k}_T} |T_{\mathbf{k}_T, \mathbf{k}_B}^{\alpha, \beta}|^2 A_{B\alpha}(E_F, \mathbf{k}_B) A_{T\beta}(E_F, \mathbf{k}_T) \quad (4.8)$$

This approach allows us to map the contribution of each \mathbf{k}_B -state in the bottom layer. As anticipated, unlike incommensurate layers, commensurate layers exhibit pronounced peaks in the outer Brillouin zones, corresponding to the matching of

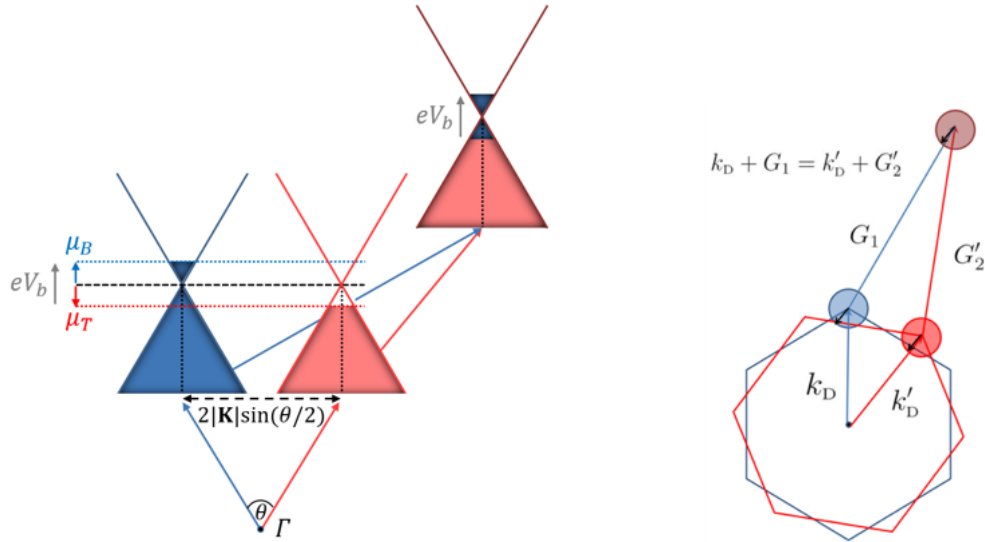


Figure 4.12 Nesting of Dirac cones at commensurability. For commensurate rotation angles, every momentum state on the rotated Fermi circle is mapped onto a momentum state of an unrotated Fermi circle. [40]

Dirac cones. Again, the sketched hexagons indicate the new super cell.

A decreasing peak conductance with increasing extended momentum $|\mathbf{k}|$ can be observed, which results from the exponential decay of the interlayer tunneling amplitude $t_{\mathbf{k}}$ (Fig. 2.47b). Consequently, for the 21.8° peak, where the Dirac cones align at the corner of the third Brillouin zone instead of the first, the corresponding $|t_{\mathbf{k}}|^2$ is predicted to be two orders of magnitude smaller than $|t_{\mathbf{K}}|^2$. For the subsequent commensurate angles at 27.8° and 32.2° , $|t_{\mathbf{k}}|^2$ is expected to decrease by an additional two orders of magnitude. Conversely, $|t_{\mathbf{k}}|^2$ at 13.2° and 46.8° is predicted to be four orders of magnitude smaller than the 21.8° peak. This explains the varying peak intensities observed in Fig. 4.10 and why the current characteristics of other commensurate angles with matching at even higher extended momentum are buried under the tails of adjacent commensurate peaks, even when considering large lifetimes.

This strong decay across the series of commensurate angles can be illustrated by decomposing the extended \mathbf{k} -space map into shells (Fig. 4.14b) and plotting their individual contributions (Fig. 4.14a). Dirac points lying on these shell lines share the same extended $|\mathbf{k}|$, meaning that the interlayer coupling $|t_{\mathbf{k}}|^2$ for states close to them contributes within the same order of magnitude. Figure 4.14a enables us then to localize the regions in \mathbf{k} -space from which the commensurate peaks arise.

Finally, a few remarks on the validity of the perturbative theory employed are warranted. Equation 4.7 is valid in the weak tunneling regime, where $|T|$ is smaller than the lifetime broadening τ^{-1} , so that the phase of the electron wave function is destroyed between two tunneling events. Consequently, the system can be described as

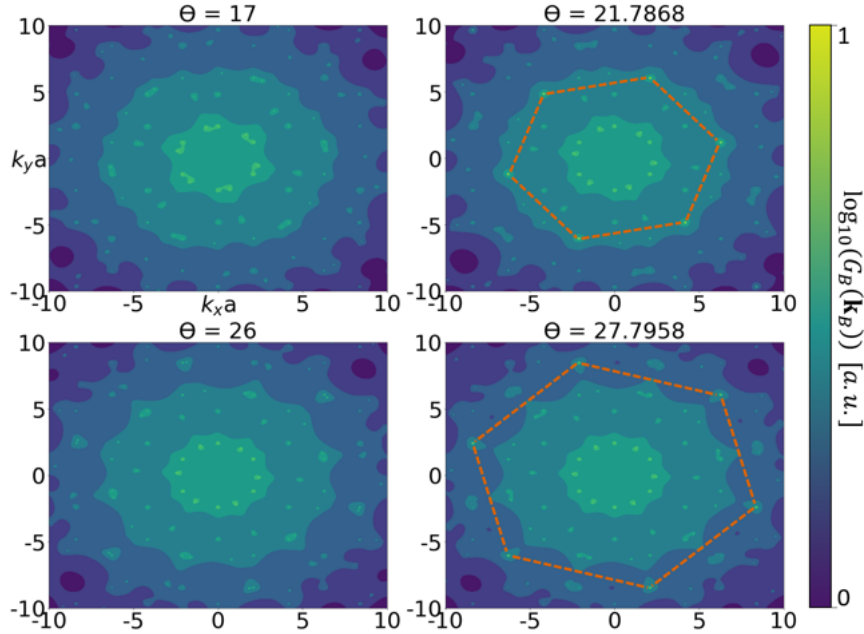


Figure 4.13 Mapping of conductance contribution $\log_{10}(G_B(\mathbf{k}_B))$ (eq. 4.8) in an extended-zone scheme. Contribution strength is proportional to the brightness. Conductance contributions occur where the Fermi circles intersect and are significantly larger when the intersection occurs closer to the origin of momentum space. At commensurate angles, peaks arise in higher Brillouin zones.

two nearly decoupled layers, and the electron dynamics between transition processes is primarily governed by the single-layer Hamiltonian.

Conversely, in the limit of large $|T|$ relative to the inverse lifetime, we encounter a strongly coherently coupled junction, where the resulting eigenstates cannot be reasonably approximated in the Bloch basis of a single layer. The divergence of G in Fig. 4.10 indicates the breakdown of this perturbative framework [40]. At commensurate angles, electrons rapidly delocalize across the two layers, and the crystal wave functions near the Dirac point represent coherent equal-weight contributions from both layers. Here, our perturbative approach fails. To determine the electronic properties of this hybridized interface at commensurate angles, a tight-binding method (Sec. 2.2.2) could be employed, now involving 14, 26, or 38-component eigenvectors that reflect the contributions of all atoms within the moiré supercells at 21.8° , 27.8° , and 13.2° , respectively. However, even near commensurate angles, strong coupling can significantly alter the electronic properties compared to the monolayers. Particularly in the small-angle regime ($\theta < 10^\circ$), the interaction causes band flattening (Sec. 2.7.6). The substantial enhancement of the DOS at E_F is entirely neglected in our perturbative model, which, as a result, generally underestimates the expected current. While these limitations of the perturbative approach preclude accurate predictions of current density, they nonetheless provide qualitative insights into the twist angle dependence observed in our measurements.

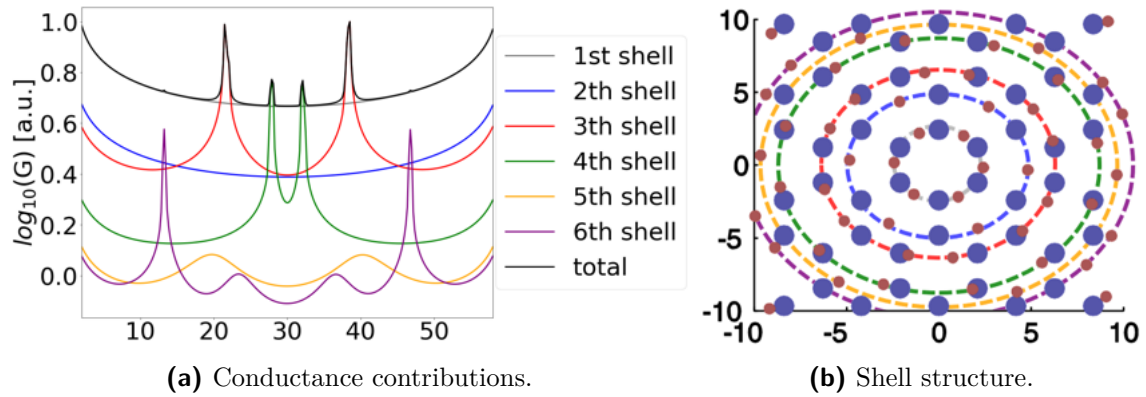


Figure 4.14 Shell numbering of the momentum lattice and the calculation of respective contributions from each shell.

4.4 Measurement of the Interlayer Conductance

The experiments commence with the formation of a twisted interface between two graphite layers, each several tens of nanometers thick. A bias voltage of $V_b = -0.1V$ is applied across the interface, and the conductance, $G = \frac{dI}{dV}$, is measured at room temperature ($T = 300K$).

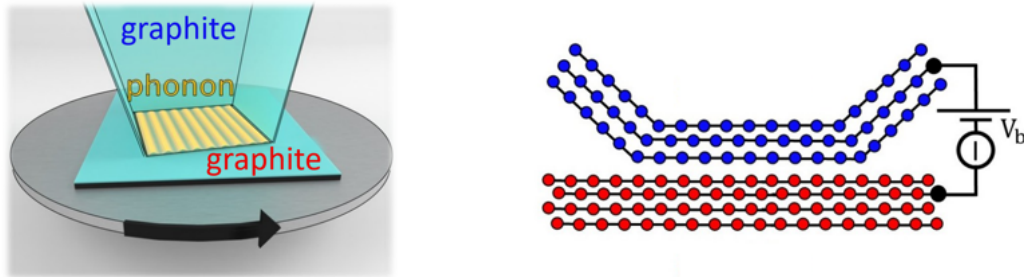


Figure 4.15 Schematics of the QTM junction (left), illustrating the formation of a continuously twistable interface between two graphite flakes. A bias voltage V_b is applied across the junction, and the conductance G is measured (right). A significant tunneling contribution arises from inelastic phonon scattering processes at the interface. Adapted from [92].

Figure 4.16 presents the conductance G , measured versus twist angle θ . The graph exhibits mirror symmetry around $\theta = 30^\circ$ ($\theta \rightarrow 60^\circ - \theta$), where the conductance reaches its minimum. As the angle decreases towards $\theta = 0^\circ$, the conductance rises continuously, but plateaus at small angles ($|\theta| < 3^\circ$) due to the contact resistance. Additionally, G exhibits pronounced peaks at commensurate angles of $\theta = 0^\circ$, 21.8° , and 38.2° .

It is surprising that the conductivity decreases only gradually, even at large incommensurate rotation angles, contrary to theoretical predictions which suggested that current transport in this regime should be substantially suppressed by a few orders of magnitude (Fig. 4.10). Furthermore, the expected commensurate peaks at 13.2° , 27.8° , 32.2° , and 46.8° are absent.

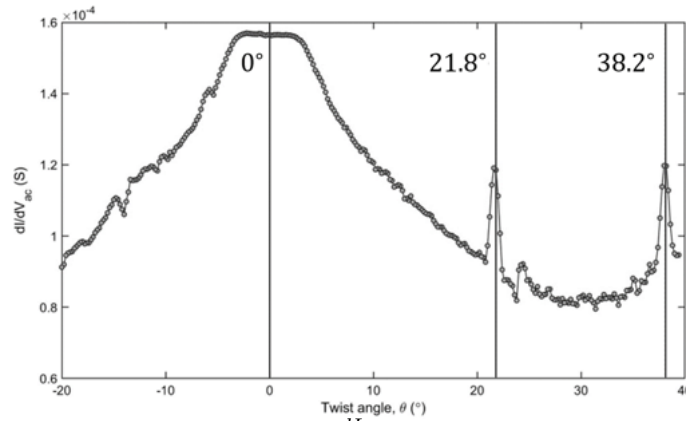


Figure 4.16 Measured conductance, $\frac{dI}{dV}$, versus rotation angle θ between two graphite flakes in direct contact ($V_b = 0.1V$, $T = 300K$). The sample and tip remain in continuous contact throughout the measurement. Commensurate angles 0° , 21.8° , and 38.2° are indicated by vertical lines.

To interpret these observations, it is instructive to consider the system in momentum space (Fig. 4.17). Although the band structure of graphite is more complex than that of MLG, it is evident that if the graphite flakes are twisted relative to each other by more than a few degrees, the momentum mismatch between their respective bands also becomes too large to permit elastic, momentum-conserving tunneling. The relatively smooth conductance, as opposed to a sharp decay, indicates access to other inelastic tunneling channels. Given the much shallower dispersion of phonons, phonon emission or absorption may suffice to supply the missing momentum, $q_{ph} \approx 2|\mathbf{K}|\sin(\theta/2)$, enabling inelastic tunneling across the interface [92]. Consequently, smaller peaks corresponding to other commensurate angles may be completely buried within this gradually decreasing background.

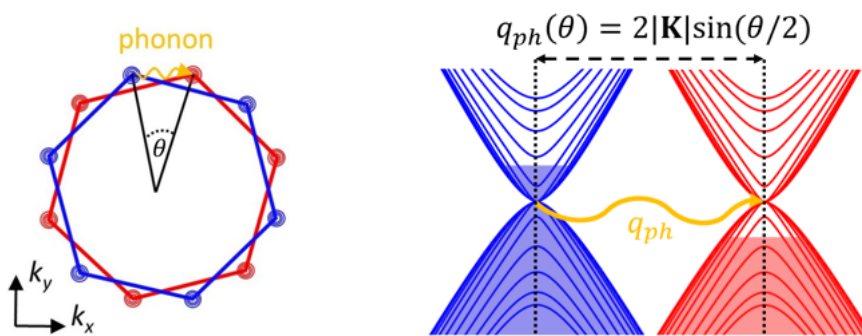


Figure 4.17 Fermi surfaces in k -space of the top and bottom graphite layers (left) and the corresponding energy bands (right). At a finite twist angle, there is a momentum mismatch between these energy bands, and momentum-conserving electronic tunneling between the layers can occur only via the emission or absorption of a phonon that provides the missing momentum $q_{ph}(\theta)$. Adapted from [92].

The observed mirror symmetry around $\theta = 30^\circ$ can be explained by recognizing that for each electron tunneling from the \mathbf{K} -point in the top layer and emitting a phonon

corresponding to θ , there is an equivalent process involving an electron tunneling from the \mathbf{K}' point and emitting a phonon corresponding to $(60^\circ - \theta)$ [92].

The remaining asymmetric features in the spectrum likely reflect additional momentum-non-conserving processes, potentially arising from scattering due to atomic defects or the edges of the tip.

4.5 Hexagonal Boron Nitride Tunneling Barrier

Since the the hybridization of the tip with the sample can substantially alter the system's properties, it does not allow to probe the sample's unperturbed characteristics. To achieve non-invasive measurements, we introduce layers of hexagonal boron nitride (hBN) as a tunneling barrier between the sample and the tip to suppress unwanted hybridization at the interface. This barrier significantly increases the tunnel junction resistance, ensuring that an applied bias predominantly falls across this junction, thereby preventing contact resistance from influencing measurements, even near $\theta = 0^\circ$. Furthermore, the weakened interlayer coupling makes the perturbative treatments valid across all twist angles.

hBN also crystallizes in a hexagonal lattice, where the carbon sublattices (Fig. 2.17) are replaced by nitrogen and boron sublattices, with distance between nearest sites $a = 1.44\text{\AA}$. In our tight-binding model, the distinction between boron and nitrogen atoms is accounted for by introducing different on-site energies, E_B and E_N , for the respective sublattices. This results in the following Hamiltonian:

$$H = \begin{bmatrix} E_B & -\gamma_{\text{BN}} \sum_i e^{i\mathbf{k}\cdot\delta_i} \\ -\gamma_{\text{BN}} \sum_i e^{-i\mathbf{k}\cdot\delta_i} & E_N \end{bmatrix}, \quad (4.9)$$

where $E_B = 6.0eV$, $E_N = -1.9eV$, and the nearest-neighbor hopping amplitude $\gamma_{\text{BN}} = 1.6eV$ [93].

The resulting band structure is shown in Fig. 4.18. We observe similarities in the global dispersion behavior of both graphene and hBN, characterized by the band gap extrema at the Γ and \mathbf{K} points, a consequence of their shared lattice structure. However, we note the degeneracy at the Dirac points are lifted and replaced by large band gaps. This significant gap opening is a direct consequence of the inequality between the two sublattices, which breaks the I -symmetry. Consequently, the IT -symmetry that protects the band crossing in graphene is absent, allowing the gap to open. As a result, the DOS exhibits a sharp onset at the band edge energy, approximately following $\sim \frac{m^*}{\pi\hbar^2}$ (eq. 2.31).

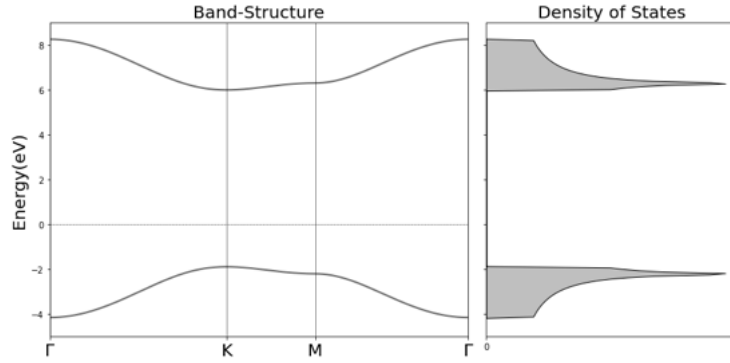
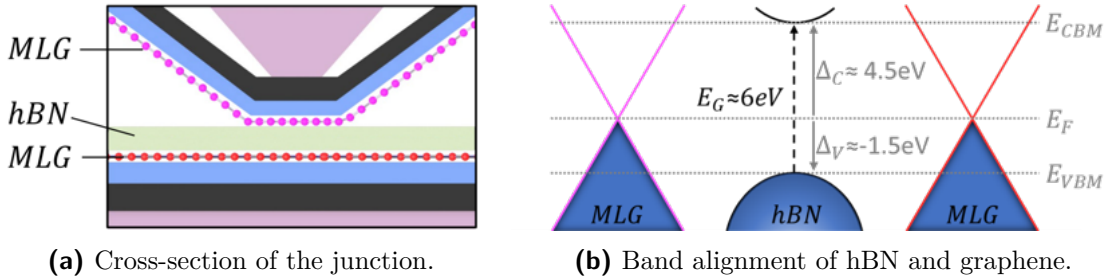


Figure 4.18 Band structure and DOS calculated using the tight-binding method.

The band gap of hBN is experimentally determined to be approximately $E_G \approx 6eV$ [94]. Consequently, hBN acts as an insulator, making it a suitable barrier material for our tunnel junctions (Fig 4.19a). A crucial aspect for our purposes is the band alignment between hBN and graphene. Tunneling experiments suggest that the effective barrier height is approximately $\Delta_V = -1.5eV$, representing the difference between the valence band edge of hBN and the Dirac point energy of graphene (Fig 4.19b) [95].



(a) Cross-section of the junction.

(b) Band alignment of hBN and graphene.

Figure 4.19 hBN as a tunneling barrier. Adapted from [14].

When a bias voltage is applied between the sample and the tip, electron accumulation occurs on one layer, while electron depletion (hole accumulation) occurs on the opposite layer (Fig 4.20a). This is described by the respective rise and lowering of the chemical potentials in both layers. In contrast to measurements taken with direct contact, we consider the relative shift in the energy of the Dirac points of the tip and sample due to the electrostatic potential difference ϕ and the resulting static electric field E_g within the hBN barrier:

$$\phi = eE_g d_g, \quad (4.10)$$

where d_g is the thickness of the barrier, and we assume a homogeneous field within it. Consequently, the bias potential energy eV_b can be expressed as:

$$eV_b = \phi + \mu_B - \mu_T, \quad (4.11)$$

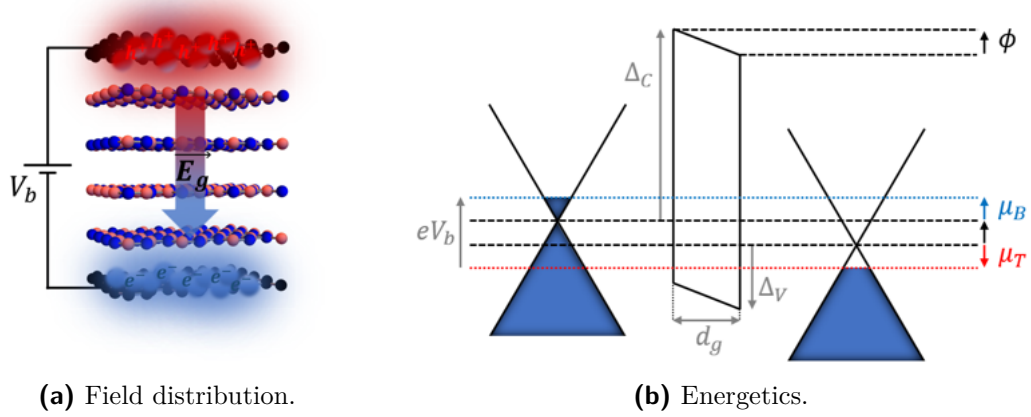


Figure 4.20 Tunneling junction.

As illustrated in Fig. 4.20b, ϕ causes an energy mismatch between the Dirac points, and the field linearly bends the barrier. Tunneling can only occur between occupied and unoccupied states; hence, the relevant energy interval for tunneling is defined by the two chemical potentials (bias window). Additionally, since $\Delta_V \ll \Delta_C$, holes encounter a smaller barrier than electrons. Therefore, at low voltages, hole tunneling is expected to be the dominant current contribution.

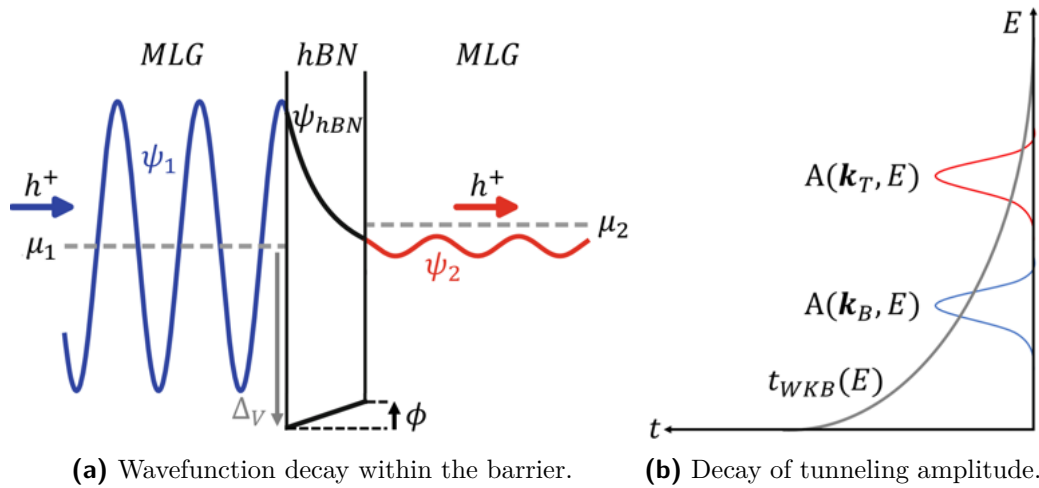


Figure 4.21 Implications of the WKB approximation.

To model the decay of the wavefunction within the barrier, we apply the WKB approximation. The tunneling barrier potential is influenced by the electric field, taking the form:

$$V(z) = \Delta_V - \frac{|\phi|}{2} + \frac{|\phi|}{d_g}z, \quad (4.12)$$

resulting in the tunneling amplitude:

$$t_{WKB}(E) = \exp \left[-\frac{1}{\hbar} \int_0^{d_g} \sqrt{2m^*(E - V(z))} dz \right] \quad (4.13)$$

$$= \exp \left[-\frac{2d_g\sqrt{2m^*}}{3\hbar|\phi|} \left((E - \Delta_V + \frac{|\phi|}{2})^{\frac{3}{2}} - (E - \Delta_V - \frac{|\phi|}{2})^{\frac{3}{2}} \right) \right], \quad (4.14)$$

where the effective hole mass in hBN is given by $m^* \approx 0.5m_e$ [95]. Consequently, the tunneling amplitude exhibits an exponential decay, suppressing contributions from large positive energies (Fig. 4.21b).

4.6 Electrostatics of the Tunnel Junction

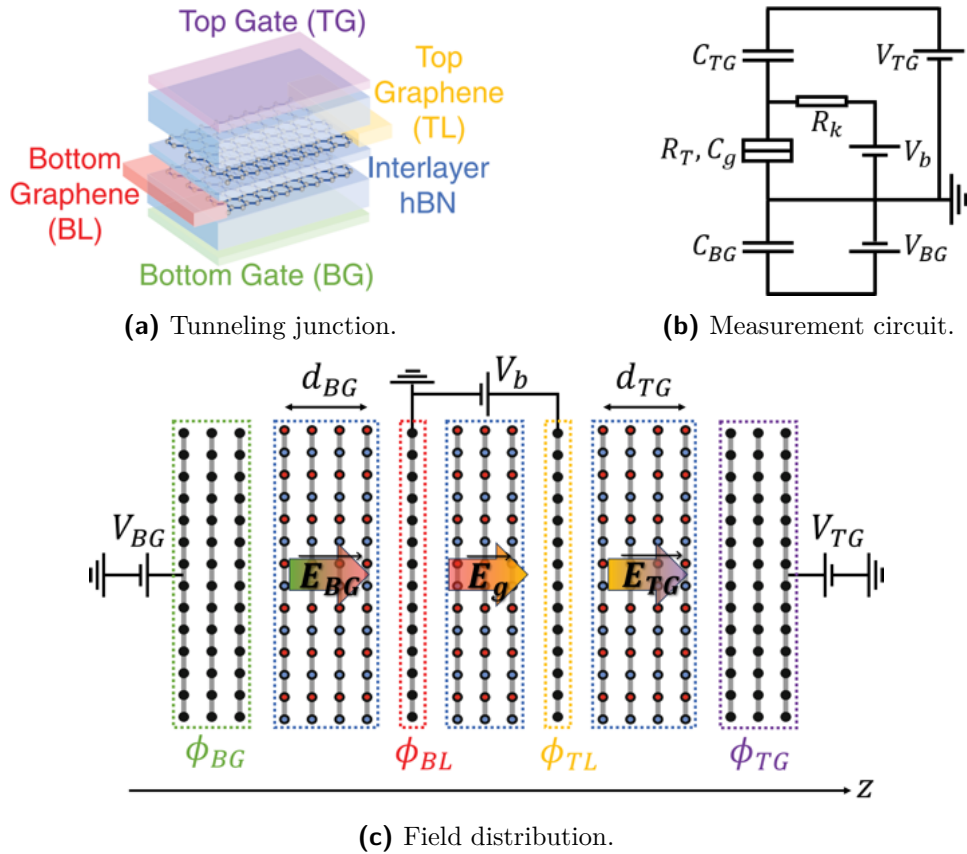


Figure 4.22 Electrostatics of the tunnel junction. Adapted from [96].

In the following, we develop a quantitative description of the electrostatics within the tunnel junction. The tunnel segment is characterized by its tunneling resistance R_T and capacitance C_T , where the latter can be derived by differentiating eq. 4.11 with respect to the charge density σ , yielding the following expression:

$$\frac{1}{C_T} = \frac{1}{C_g} + \left(\frac{1}{C_q^B} + \frac{1}{C_q^T} \right) = \frac{1}{C_g} + \frac{1}{C_q}, \quad (4.15)$$

Therefore, C_T is composed of the geometric capacitance $C_g = \frac{\partial n}{\partial \phi}$ and the quantum capacitance $C_q = \frac{\partial n}{\partial \mu}$.

The C_g refers to the "classical" capability of a material to accumulate charges in response to a difference in electrostatic potential. For a area-normalized parallel plate capacitor, it is defined as:

$$C_g = \frac{\epsilon_{\text{hBN}}\epsilon_0}{d_g}, \quad (4.16)$$

where ϵ_0 denotes the vacuum permittivity, and $\epsilon_{\text{hBN}} = 3.2$ is the dielectric constant of hBN [14]. In contrast, C_q arises from the Pauli exclusion principle and accounts for the energy required to shift the chemical potential. Since the tip and sample systems can differ, C_q is defined as the in-series sum of the quantum capacitances of the two systems, such that $\frac{1}{C_q} = \frac{1}{C_q^B} + \frac{1}{C_q^T}$.

The complete tunnel junction is schematically depicted in Fig. 4.22a. The system includes a top gate and a bottom gate, each separated from the sample and tip by additional hBN spacers. This configuration can be modeled by the measurement circuit shown in Fig. 4.22b. The top and bottom gates are represented by two capacitors with geometrical capacitances C_{TG} and C_{BG} , respectively, defined as:

$$C_{BG} = \frac{\epsilon_{\text{hBN}}\epsilon_0}{d_{BG}}, \quad C_{TG} = \frac{\epsilon_{\text{hBN}}\epsilon_0}{d_{TG}}, \quad (4.17)$$

where d_{BG} and d_{TG} denote the respective hBN spacer thicknesses. The gate voltages V_{TG} and V_{BG} control these gates, while V_b denotes the bias voltage between the sample and the tip. The contact resistance, denoted by R_k , is assumed to be much smaller than the tunneling resistance R_T ($R_k \ll R_T$), ensuring that the applied bias primarily falls across the tunneling resistance R_T , even when $\theta = 0^\circ$.

The objective of the subsequent derivation is to determine μ_B , μ_T , and ϕ in response to the externally controllable parameters V_b , V_{BG} , and V_{TG} .

The charge accumulation on the layers and the resulting field distribution (Fig. 4.22c) are governed by the first Maxwell equation in one dimension:

$$\partial_z E = \frac{\sigma}{\epsilon_r \epsilon_0}, \quad (4.18)$$

where the carrier occupation is defined as:

$$\sigma(\mu) = en(\mu) = e \int dE f_D(E) \text{DOS}(E), \quad (4.19)$$

where f_D is the Fermi-Dirac distribution, which accounts for the finite temperature. However, since the temperature T is typically much lower than the Fermi temperature T_F in electronic systems, we approximate $\mu \approx E_F$ and $f_D(E) \approx \theta(E - E_F)$, valid in the limit $T/T_F \rightarrow 0$. In this limit, C_q is directly proportional to the DOS. Figure 4.23 illustrates $\sigma(\mu)$ for different FLG systems, showing an increase in charge density with the number of layers, leading to an increase in the junction's quantum capacitance.

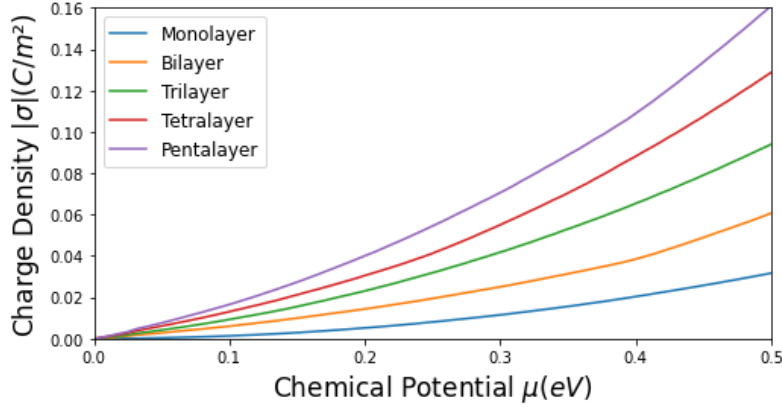


Figure 4.23 Charge density in FLG systems.

According to eq. 4.18, the charging of the top and bottom layers causes a corresponding change in the electric field:

$$E_{TG} - E_g = \text{sign}(\mu_T) \frac{en(\mu_T)}{\epsilon_{\text{hBN}}\epsilon_0}, \quad E_g - E_{BG} = \text{sign}(\mu_B) \frac{en(\mu_B)}{\epsilon_{\text{hBN}}\epsilon_0}. \quad (4.20)$$

Rewriting these equations in terms of the corresponding potential energy (eq. 4.10), we obtain:

$$E_{TG} - E_g = \frac{\phi_{TG} - \phi_{TL}}{ed_{TG}} - \frac{\phi_{TL} - \phi_{BL}}{ed_g} = \text{sign}(\mu_T) \frac{en(\mu_T)}{\epsilon_{\text{hBN}}\epsilon_0}, \quad (4.21)$$

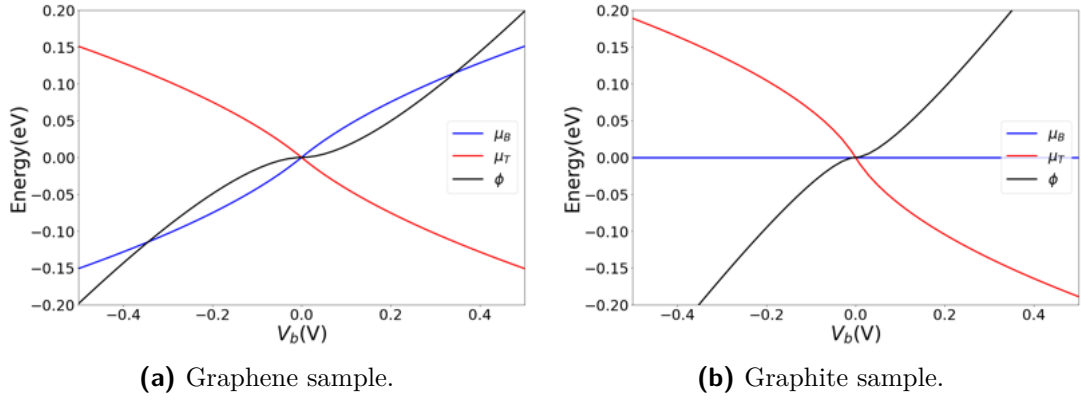
$$E_g - E_{BT} = \frac{\phi_{TL} - \phi_{BL}}{ed_g} - \frac{\phi_{BL} - \phi_{BG}}{ed_{BG}} = \text{sign}(\mu_B) \frac{en(\mu_B)}{\epsilon_{\text{hBN}}\epsilon_0}. \quad (4.22)$$

Since the sample is grounded ($\phi_B = 0$), and the large quantum capacitance of three-dimensional graphite leads to a negligible shift in μ_{Gate} ($\mu_{TG} \approx \mu_{BG} \approx 0$), we redefine the remaining quantities as $\phi_T = \phi$, $\phi_{TG} = eV_{TG}$, and $\phi_{BG} = eV_{BG}$. The electrostatics of the tunneling junction is then fully described by the following three equations:

$$\begin{aligned}
C_{TG}(eV_{TG} - \phi) - C_g\phi &= \text{sign}(\mu_T)en(\mu_T), \\
C_g\phi + C_{BGe}V_{BG} &= \text{sign}(\mu_B)en(\mu_B), \\
eV_b - \phi &= \mu_B - \mu_T,
\end{aligned} \tag{4.23}$$

In the classical limit, the quantum capacitance $C_q \rightarrow \infty$, rendering any shift in μ negligible. However, given the low carrier density of graphene, the quantum capacitance of the junction is generally of the same order of magnitude as its geometric capacitance [14].

To explore how these results vary with different sample systems, we consider two extreme cases: a MLG sample and a graphite sample (with the tip covered by MLG in both cases).



(a) Graphene sample. (b) Graphite sample.
Figure 4.24 Effect of finite bias on the electrostatic quantities.

Starting with an MLG sample under zero gating and assuming overall charge neutrality, symmetry enforces $\mu_B = -\mu_T$. The low-energy DOS of MLG can be approximated by $DOS_{\text{MLG}}(E) = \frac{2|E|}{\pi\hbar^2v_F^2}$ (eq. 2.30), leading to a carrier density of $n_{\text{MLG}}(\mu) = \text{sign}(\mu)\frac{\mu^2}{\pi\hbar^2v_F^2}$. Solving the set of equations provides the following relations:

$$\begin{aligned}
\mu_{B/T} &= \mp \frac{C_g\pi\hbar^2v_F^2}{e^2} \left[1 - \sqrt{1 + \frac{e^3V_b}{C_g\pi\hbar^2v_F^2}} \right], \quad \text{for } V_b > 0, \\
\mu_{B/T} &= \pm \frac{C_g\pi\hbar^2v_F^2}{e^2} \left[1 - \sqrt{1 - \frac{e^3V_b}{C_g\pi\hbar^2v_F^2}} \right], \quad \text{for } V_b < 0, \\
\phi &= eV_b \mp 2\mu_{B/T}.
\end{aligned} \tag{4.24}$$

In contrast, for a graphite sample, we expect a negligible energy shift ($\mu_B \rightarrow 0$), resulting in:

$$\begin{aligned}
\mu_T &= +\frac{C_g\pi\hbar^2v_F^2}{2e^2} \left[1 - \sqrt{1 + \frac{4e^3V_b}{C_g\pi\hbar^2v_F^2}} \right], \quad \text{for } V_b > 0, \\
\mu_T &= -\frac{C_g\pi\hbar^2v_F^2}{2e^2} \left[1 - \sqrt{1 - \frac{4e^3V_b}{C_g\pi\hbar^2v_F^2}} \right], \quad \text{for } V_b < 0, \\
\phi &= eV_b + \mu_T.
\end{aligned} \tag{4.25}$$

Figure 4.24 depicts the dependence of μ_B , μ_T , and ϕ on V_b for both systems, assuming an hBN barrier with $d_g = 2nm$. The symmetry $\mu_B = -\mu_T$ observed for MLG is absent in the graphite system.

In conclusion, as the number of layers increases, the response in μ_B decreases due to the larger DOS. In the limit of graphite ($C_q^B \gg C_q^T$), the quantum capacitance of the junction is dominated by the MLG tip.

4.7 Fowler–Nordheim Tunneling

Thus far, hBN has been treated as a \mathbf{k} -independent potential barrier, with its intrinsic structure accounted for only by modifying the effective mass. This approximation is valid at low bias voltages. However, under high bias conditions, the bending of the hBN bands becomes significant enough to allow charge carriers to directly tunnel between graphene and the band states of hBN.

This is referred to as the Fowler–Nordheim field emission regime [97]. As illustrated in Fig. 4.25, the reduced barrier width d_0 caused by the valence band bending can be expressed as:

$$d_0 = (E - \Delta_V) \frac{d}{|\phi|}, \tag{4.26}$$

This results in the tunneling amplitude:

$$t_{hBN}(E) = \exp \left[-\frac{1}{\hbar} \int_0^{d_0} \sqrt{2m^*(E - V(z))} dz \right] = \exp \left[-\frac{2d_g\sqrt{2m^*}}{3\hbar|\phi|} (E - \Delta_V)^{\frac{3}{2}} \right],$$

Applying Fermi's Golden Rule, the tunneling current can be approximated as follows

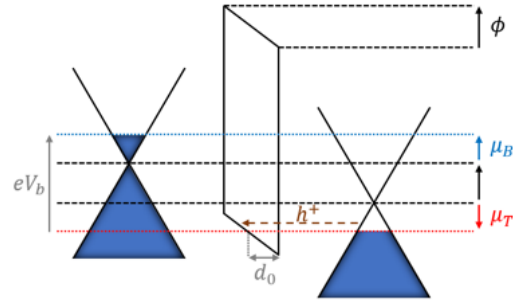


Figure 4.25 Tunneling between hBN and graphene.

[95]:

$$I_{\text{hBN}} = \frac{2\pi e}{\hbar} \int_{-\infty}^{\Delta_V + |\phi|} dE |t_{\text{hBN}}|^2 (1 - f_D(E)) \text{DOS}_{\text{MLG}} \text{DOS}_{\text{hBN}}, \quad (4.27)$$

The breakdown of the barrier imposes an upper limit on the applied bias to ensure that contributions from I_{hBN} remain negligible. In the extreme case, where the quantum capacitance C_q approaches infinity (i.e., the classical limit where all energy is contained in the field), the expected breakdown voltage is given by $V_b \approx \frac{|\Delta E_V|}{e}$. For finite values of C_q , this breakdown voltage shifts to higher values.

4.8 Monolayer Graphene

In this section, we examine tunneling experiments involving a MLG tip and an MLG sample, separated by a thin hBN barrier. The tunneling current, as a function of bias voltage and twist angle, provides direct signatures of momentum-resolved dispersions. Our focus is on elastic tunneling processes, which predominate as long as the Fermi circles of the tip and sample intersect in the first Brillouin zone. Consequently, we restrict our analysis to small twist angles (i.e., $\theta < 5^\circ$). Additionally, we limit our bias range to $\pm 1.5V$ to ensure that the Fowler-Nordheim tunneling contribution remains negligible. We begin with a theoretical investigation of the expected tunneling spectrum, analyzing the emerging characteristic features and their response to altered initial conditions. Subsequently, we present our experimental results and compare them to theoretical predictions.

4.8.1 Theory

In this subsection, we simulate the tunneling current as a function of bias and twist angle and extract the functional dependence of the characteristic features. We visualize the dynamics in momentum space and illustrate the effect of varying temperature, lifetime, geometric capacitance, and gate voltage.

Tunneling Spectrum

Figure [4.26] shows the simulated tunneling current, I , as well as the differential conductance, $G = \frac{dI}{dV}$, versus the interlayer bias, V_b , and twist angle, θ , for $\tau^{-1} = 5meV$, $C_g = 189 \frac{nF}{cm^2}$, $d_g = 1.5nm$, $\epsilon_{\text{hBN}} = 3.2$ at $T = 300K$. Figure [4.26c] illustrates the electrostatics of the junction.

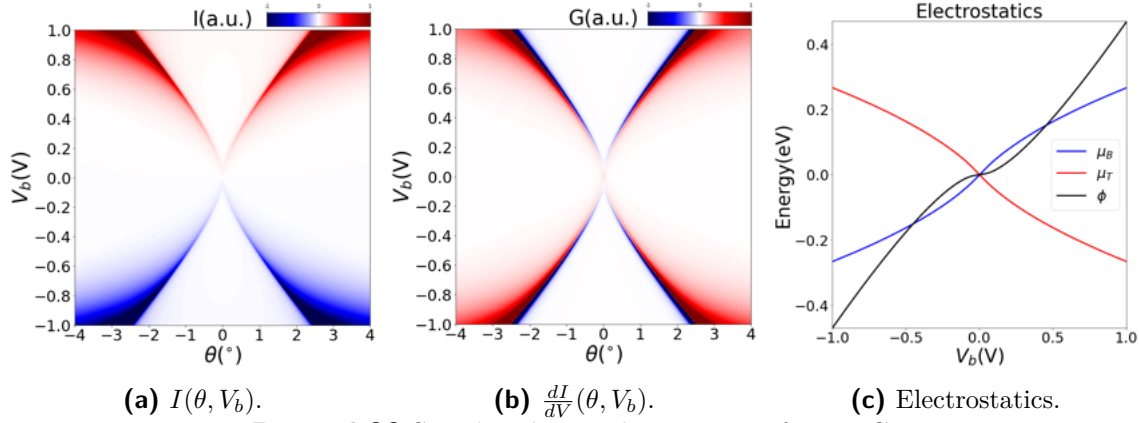


Figure 4.26 Simulated tunneling spectra for MLG.

Around $\theta = 0^\circ$, the tunneling current I increases slowly with V_b at low bias, followed by a sharp increase along a curved X feature, $V^{**}(\theta)$, in the θ - V_b plane. This is followed by a sharp drop at slightly higher V_b . In the conductance, this sharp drop in I manifests as a strong negative differential resistance. In addition to the strong curved X feature, we observe a straight X feature, $V^*(\theta)$, along with broad edges. This motivates the decomposition of the spectrum into three regions: the small bias regime $V_b < V^*(\theta)$, delimited by the straight X feature; the intermediate regime $V^*(\theta) < V_b < V^{**}(\theta)$, situated between the straight and curved X features; and the high bias regime $V_b > V^{**}(\theta)$, situated above the curved X feature.

Geometrical Analysis

To elucidate the origin of the two main features observed, we begin with a purely geometrical consideration of the E- \mathbf{k} -space. At a given twist angle θ , the Dirac cone of one MLG is shifted in momentum by $\approx |\mathbf{K}|\theta$ relative to the other, while the parameter ϕ induces a relative energy shift.

The conservation of energy and momentum restricts tunneling to states possessing the same energy and momentum. This restriction corresponds to the intersections of the dispersion lines, which are defined by the following conic equations:

$$q_x^2 + \left(q_y - \frac{|\mathbf{K}|\theta}{2}\right)^2 = \left(\frac{E + \phi/2}{\hbar v_F}\right)^2 \quad (4.28)$$

$$q_x^2 + \left(q_y + \frac{|\mathbf{K}|\theta}{2}\right)^2 = \left(\frac{E - \phi/2}{\hbar v_F}\right)^2 \quad (4.29)$$

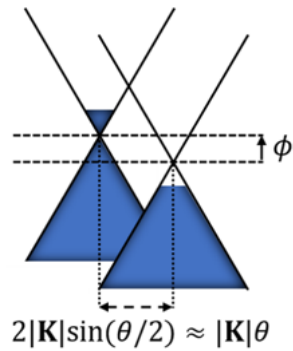


Figure 4.27 E- \mathbf{k} -space geometry.

By subtracting eq.4.28 from eq.4.29, we obtain:

$$E = (\hbar v_F)^2 \frac{|\mathbf{K}|\theta}{\phi} q_y \quad (4.30)$$

Substituting E from eq.4.30 into eq.4.28, we derive:

$$q_x = \pm \frac{\sqrt{((\hbar v_F |\mathbf{K}|\theta)^2 - \phi^2)((2\hbar v_F q_y)^2 - \phi^2)}}{\hbar v_F \phi} \quad (4.31)$$

Therefore, the parametric expression for the intersection curve in E- \mathbf{k} -space is:

$$\left(\pm \frac{\sqrt{((\hbar v_F |\mathbf{K}|\theta)^2 - \phi^2)((2\hbar v_F q_y)^2 - \phi^2)}}{\hbar v_F \phi}, q_y, (\hbar v_F)^2 \frac{|\mathbf{K}|\theta}{\phi} q_y \right) \quad (4.32)$$

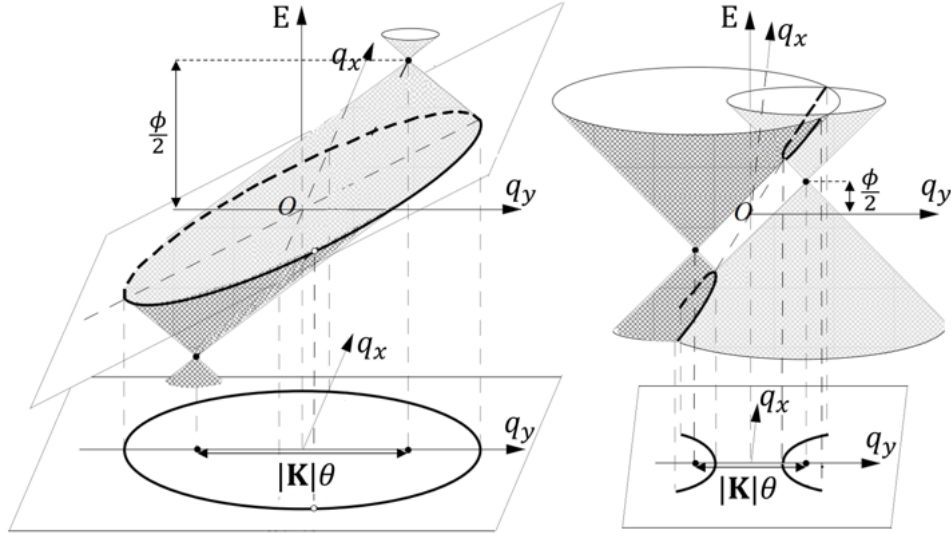
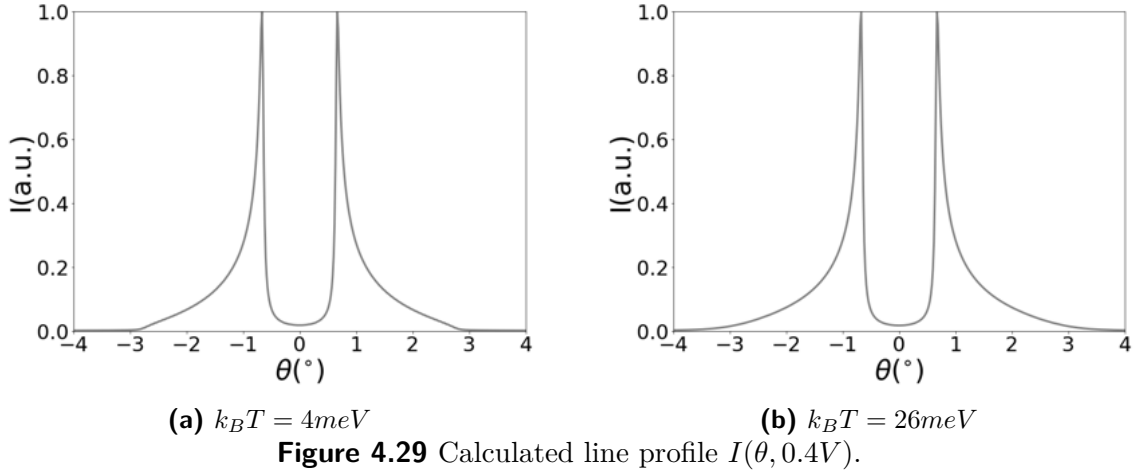


Figure 4.28 Intersections of two Dirac cones. Adapted from [98].

It follows that the intersection curve lies on a plane containing the q_x -axis (Fig.4.28). This planar curve, referred to as a conic section, takes the form of an ellipse when $\phi > \hbar v_F |\mathbf{K}|\theta$, and a hyperbola when $\phi < \hbar v_F |\mathbf{K}|\theta$. In the degenerate case where $\phi = \hbar v_F |\mathbf{K}|\theta$, the intersection curve reduces to a simple line segment. Projecting these curves onto the q_x - q_y plane traces a path through \mathbf{k} -space, encompassing all states with matching energy and momentum. In this simplified geometrical model, the functional dependence of the current results directly from the bias and twist-angle dependent intersection path.

Momentum Space Analysis



Examining the line profile $I(\theta)$ at $0.4V$ for $T = 45K$ (Fig. 4.29a) and $T = 300K$ (Fig. 4.29b) is illustrative. To fully recover the functional dependence of the spectrum, we must consider that only segments of the intersection path situated within the bias window contribute. For this purpose, we analyze the momentary \mathbf{k} -space contribution map, introduced in Sec. 4.3, for a range of specific angle configurations as shown in Fig. 4.31 and Fig. 4.32. The \mathbf{k} -space map is now centered at the Dirac point \mathbf{K}_D in the unrotated BZ and includes the intersection lines of the cones (white), the contours of constant energy of the top (red) and bottom (blue) layer at energy μ_T , rotated relatively by $\pm\theta/2$. For illustration purposes, we set the tunneling matrix element for the simulation of Fig. 4.31 and Fig. 4.32 to be a momentum-independent constant. The background brightness is proportional to the current contribution.

Next, we smoothly decrease the twisting angle from 4° to 0° and analyze how the current evolves. From our geometrical consideration, we know that for $\phi \ll \hbar v_F |\mathbf{K}| \theta$, tunneling states lie on a hyperbolic curve and both cones are strongly misaligned. Consequently, the paths lie completely outside the bias window, suppressing any considerable contribution besides a very small but finite current predominantly from thermal smearing.

At a given bias voltage, we can expect momentum-conserving tunneling to sharply onset when the Fermi surface of one layer touches the empty bands of the other layer [14]. However, as illustrated in Fig. 4.30, thermal broadening of the order of $k_B T$ relaxes the onset condition. Therefore, room temperature smearing has almost eliminated all the detailed structure related to the onset feature in Fig. 4.29b at $V^*(\theta)$. In particular, since the onset is entirely determined by the band characteristics at the edges

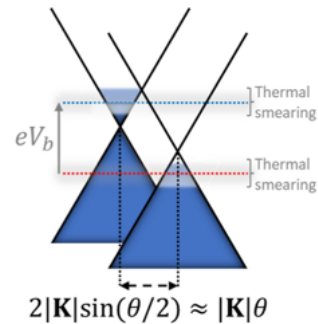


Figure 4.30 Smearing.

of the bias window, thermal smearing exhibits its strongest effects here. Accordingly, comparing Fig.4.29a and Fig.4.29b, the only observable differences lie around $V^*(\theta)$.

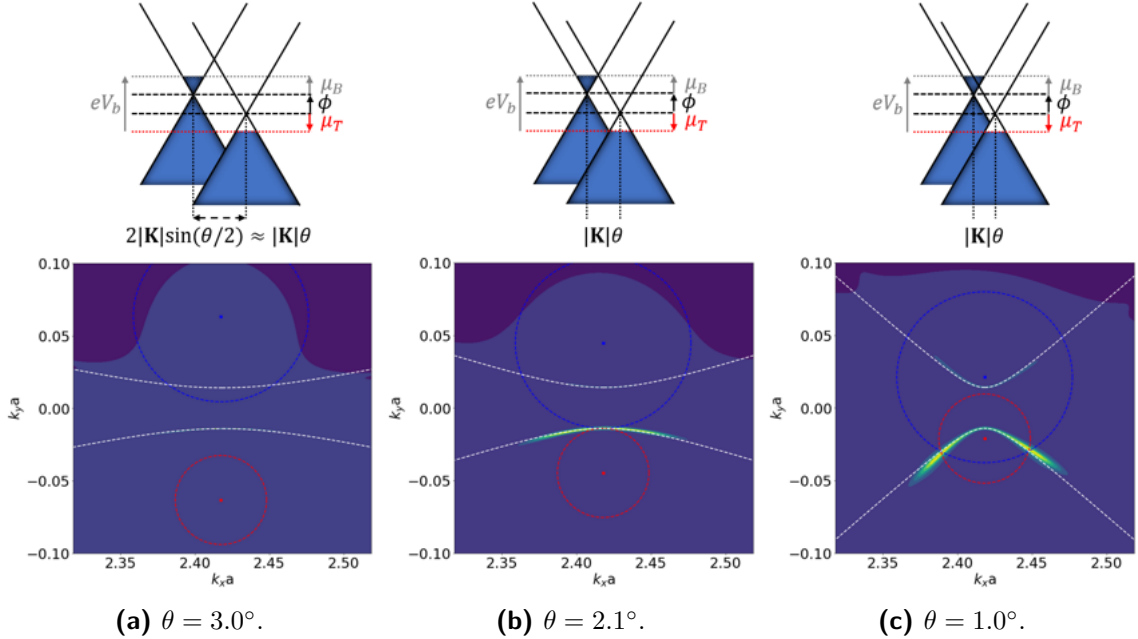


Figure 4.31 Energetics (above) and $I(\mathbf{k})$ -map (below) centered at \mathbf{K}_D (unrotated) for $V_b = 0.4\text{ V}$. White lines correspond to intersection lines, blue and red lines represent energy contours of band states at μ_T (rotated by $\pm\theta/2$ respectively). Background brightness is proportional to current strength.

In the $I(\mathbf{k}_B)$ -map for $V_b = V^*$ (Fig.4.31b), we observe the blue and red contour lines touching, while a white interaction line traces through the intersection point. For the charge-neutral case $\mu = \mu_B = -\mu_T$, this condition happens simultaneously for the Fermi surfaces of the top and bottom layers when:

$$\phi + \mu_B - \mu_T = eV_b = \pm\hbar v_F |\mathbf{K}|\theta \quad (4.33)$$

Effectively, this relation is the Dirac equation of graphene, but with energy E and momentum \mathbf{q} replaced by V_b and $|\mathbf{K}|\theta$, respectively.

Since in $E(\mathbf{k})$ space this happens at $E = \mu_B + \phi/2$ as well as $E = \mu_T - \phi/2$, we could expect both hyperbolic branches (white lines) to show the same contribution. However, we note that the contribution from the intersection line sitting above the Dirac point energy is completely suppressed. This asymmetry results from the asymmetric band alignment of hBN with MLG. Since electrons in the positive energy regime have to overcome a larger barrier, their contribution is strongly suppressed (eq.4.14).

As we further decrease the angle (Fig.4.31c), we continuously increase the overlap of the energy contours, thereby increasing the fraction of the intersection path lying

inside the bias window. Consequently, the current continuously increases until we arrive at the 'nesting' condition, roughly at $\approx 0.7^\circ$ (Fig. 4.32a). This marks the transition from a hyperbolic intersection to an elliptical intersection curve, where states along a line match in momentum and energy. According to eq. 4.32, shifting the Dirac bands in energy by

$$\phi = \pm \hbar v_F |\mathbf{K}| \theta \quad (4.34)$$

will bring the two MLG Dirac dispersions into nesting.

The large number of available energy-momentum conserving states causes the strong peak in the diagram, which corresponds to the curved X-feature in Fig. 4.26. Due to the exponential decay with increasing energy, we observe that the strongest contribution in the $I(\mathbf{k})$ -map comes from states close to the lower edge of the bias window.

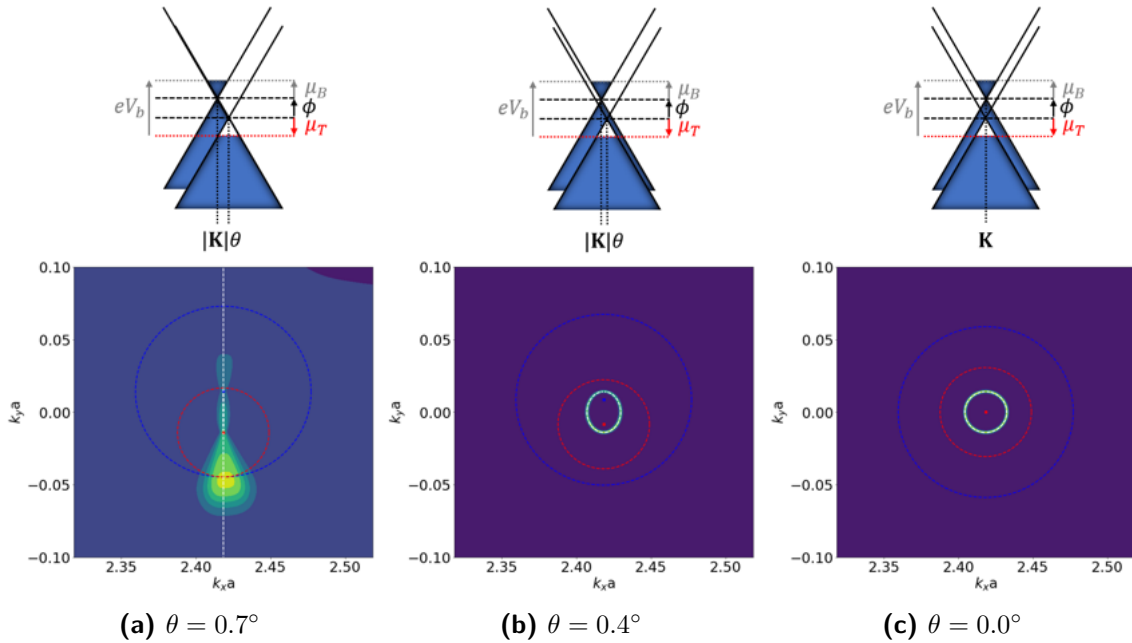


Figure 4.32 Energetics (above) and $I(\mathbf{k})$ -map (below) centered at \mathbf{K}_D (unrotated) for $V_b = 0.4$ V. White lines correspond to intersection lines, blue and red lines represent energy contours of band states at μ_T (rotated by $\pm\theta/2$ respectively). Background brightness is proportional to current strength.

Further decreasing the angle is accompanied by a strong drop in I . Since the tunneling states now sit on a limited elliptical path (Fig. 4.32b), the drop is concomitant with a substantial loss of energy-momentum-matched eigenstates in the two layers. We also observe that the current becomes relatively insensitive to further changes afterward. Because the ellipse lies deep inside the bias window, the path is not limited by the bias window edges and thus shows a weaker response to changes in bias or angle. Finally, at 0° , the atoms of the two layers are completely registered in real space, and the intersection curve forms a circle with radius $\frac{|\phi|/2}{\hbar v_F}$ lying in a horizontal plane between the two vertically shifted Dirac points (Fig. 4.32c).

Reduced Zone Scheme

Note that, up to this point, the \mathbf{k} -space maps were calculated in the extended zone scheme, as illustrated in Fig. 4.34b and limited to the environment of \mathbf{K}_D . Allowed interlayer tunneling processes are diagonal in the generalized extended momentum. Alternatively, we can project the relevant contributions of the \mathbf{K} -point counterparts at the edges of the Brillouin zone into the vicinity of \mathbf{K}_D . According to eq. 2.118 in the reduced zone scheme, besides $\langle \mathbf{k}, 1|V|\mathbf{k}, 2\rangle$, we must also consider the terms $\langle \mathbf{k}, 1|V|\mathbf{k} + \mathbf{b}_2^M, 2\rangle$ and $\langle \mathbf{k}, 1|V|\mathbf{k} - \mathbf{b}_1^M, 2\rangle$, which result from contributions from the other two equivalent \mathbf{K} -points.

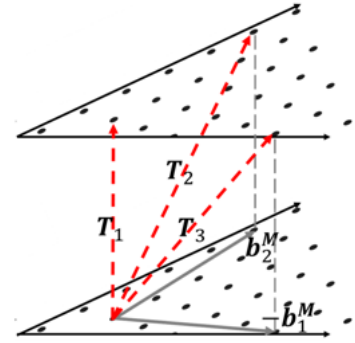
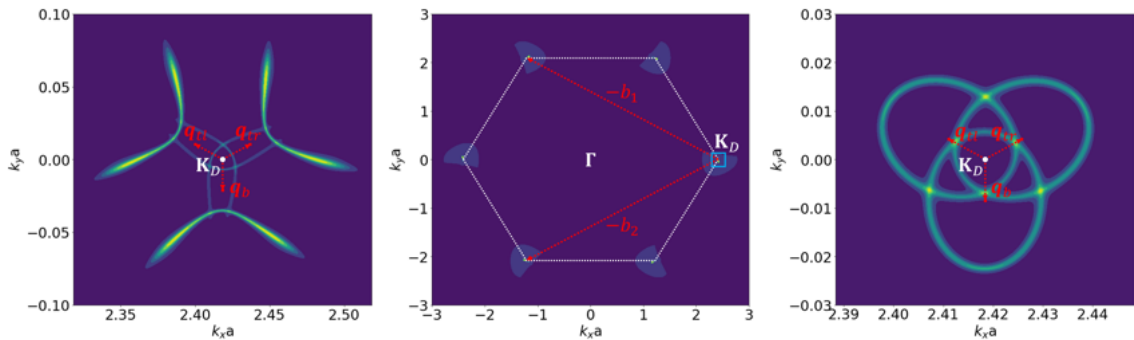


Figure 4.33 Tunneling in the Reduced Zone Scheme.

The resulting $I(\mathbf{k})$ -maps are depicted in Fig. 4.34a for hyperbolic intersection paths and Fig. 4.34c for elliptical intersection paths. We can now observe three representative current patterns, rotated relative to each other, reflecting the trigonal symmetry of the system.

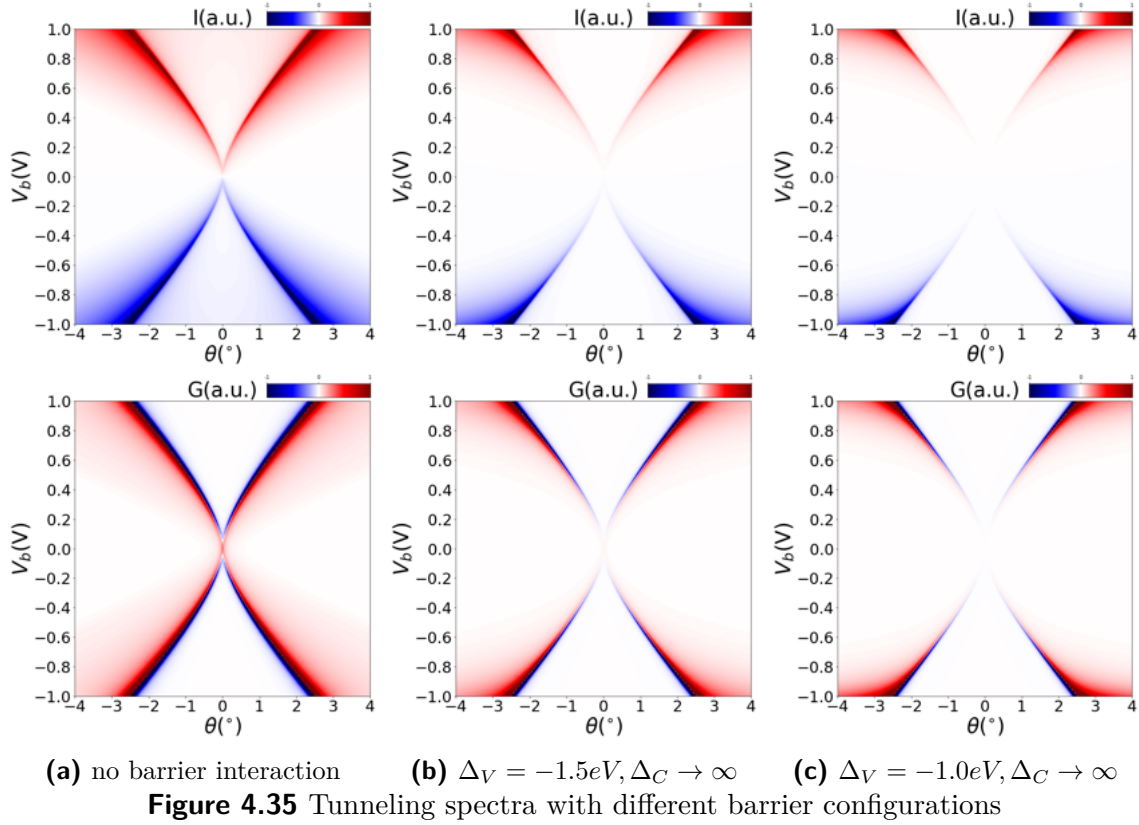


(a) Reduced Zone Scheme at $\theta = 3.0^\circ$ **(b)** Extended Zone Scheme at $\theta = 0.7^\circ$ **(c)** Reduced Zone Scheme at $\theta = 0.4^\circ$

Figure 4.34 Reduced vs Extended Zone Scheme. The bottom layer remains unrotated while the top layer is rotated by θ .

Tunnel Barrier

In Fig. 4.35, the spectra for various barrier configurations are presented. When $|\Delta_V| \gg |V_b|$, the variations in the tunneling amplitude t_{WK_B} (eq. 4.14) within the bias window become negligible. Consequently, all energies within the bias window contribute similarly, as would be the case without any barrier interaction. As the barrier height decreases, the absolute current increases. However, this reduction in barrier height also leads to a greater relative suppression of contributions away from the lower edge of the bias window. This phenomenon can be observed as an



increased steepness in the rise of the total current with a larger bias, as the lower edge of the bias window shifts to lower energies.

Analytical Expression

We can express the functional dependence of the onset condition (eq.4.33) as follows:

$$eV_b^*(\theta) = \pm \hbar v_F |\mathbf{K}| \theta \quad (4.35)$$

Similarly, the nesting condition (eq.4.34) can be expressed as:

$$\begin{aligned} eV_b^{**}(\theta) &= \phi + 2\mu = \phi + 2 \operatorname{sign}(\phi) \sqrt{\frac{\pi \hbar^2 v_F^2 C_g |\phi|}{e^2}} \\ &= \pm \hbar v_F |\mathbf{K}| \theta \pm \operatorname{sign}(\theta) \sqrt{\frac{4\pi \hbar^3 v_F^3 C_g |\mathbf{K}| |\theta|}{e^2}} \end{aligned} \quad (4.36)$$

Equation 4.35 and eq.4.36 are plotted in Fig.4.36, reproducing the characteristic features observed in Fig.4.26.

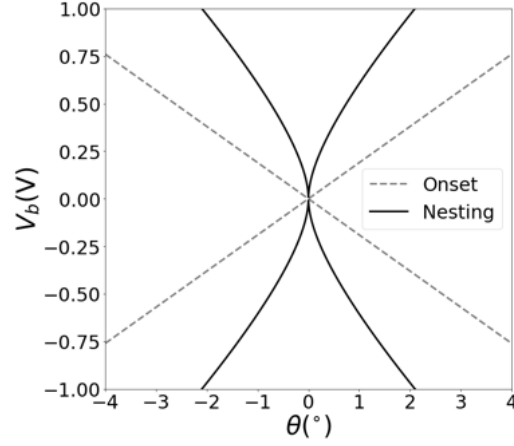
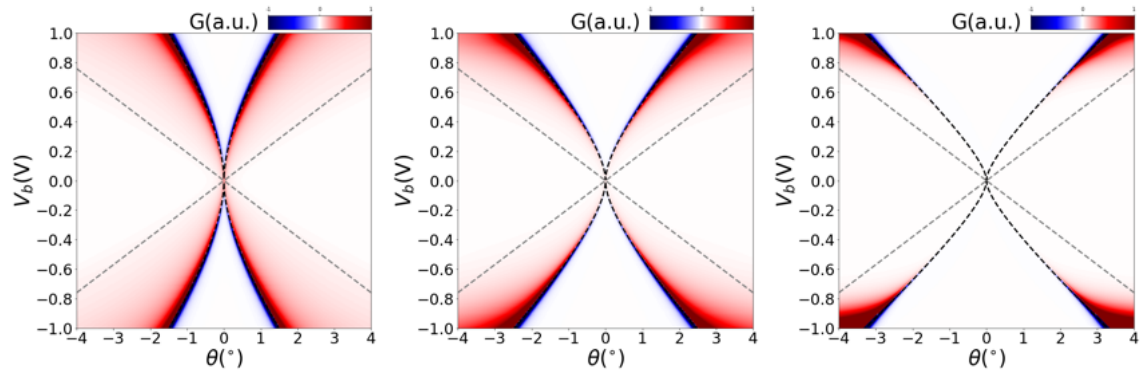


Figure 4.36 Schematic of the charge-neutral MLG-MLG tunneling experiment, showing the analytically derived lines in the θ - V_b plane, which correspond to the momentum-resolved 'onset' and 'nesting' conditions.

Geometric Capacitance

Figure 4.37 depicts the spectra for different d_g values and the corresponding C_g , along with the analytically predicted curves. The onset line maintains its shape irrespective of C_g , since eq. 4.35 depends only on the total bias energy eV_b .

In contrast the slope of the nesting line approaches the onset line for decreasing geometric capacitance. Since the nesting condition is determined by ϕ , the nesting lines are sensitive to the energy distribution between chemical and electrostatic potentials.



(a) $d_g = 0.5\text{nm}$, ($C_g = 566 \frac{\text{nF}}{\text{cm}^2}$). **(b)** $d_g = 1.5\text{nm}$, ($C_g = 189 \frac{\text{nF}}{\text{cm}^2}$). **(c)** $d_g = 4.0\text{nm}$, ($C_g = 71 \frac{\text{nF}}{\text{cm}^2}$).

Figure 4.37 Dependence on hBN thickness (Capacitance). The gray (black) line corresponds to the onset (nesting).

According to eq. 4.23, we can express the relationship between μ and ϕ as:

$$\phi = \frac{e^2 d_g}{\epsilon_0 \epsilon_{hBN}} n(\mu) = \left(\frac{e^2}{2\epsilon_0 \epsilon_{hBN}} \frac{2\mu}{\pi v_F^2 \hbar^2} d_g \right) \mu = (q_{TF} d_g) \mu, \quad (4.37)$$

where $q_{TF} = \frac{e^2}{2\epsilon_0 \epsilon_{hBN}} \text{DOS}(\mu)$ is the Thomas-Fermi screening wavevector. Accord-

ingly, the ratio of shifts in electrostatic and chemical potentials is of the order of $q_{TF}d_g$.

At small bias voltages, in the limit of $q_{TF}d_g \ll 1$, where the geometric capacitance is large (corresponding to a thin barrier), $\Delta\phi \ll \Delta\mu$. Therefore the bias hardly shifts the energy bands but mostly changes their occupation and we can approximate $e|V_b| \approx 2|\mu|$. According to eq. 4.36 nesting lines move further apart due to the decreasing contribution from the square root term.

In the opposite limit, where $q_{TF}d_g \gg 1$, which corresponds to the case of a thick tunneling barrier, most of the applied bias goes into shifting the bands, and only a small fraction of it goes to increasing the chemical potentials. We enter the classical regime where $\phi \approx eV_b$. Accordingly, with increasing d_g , the onset and nesting lines converge.

Finite Lifetime

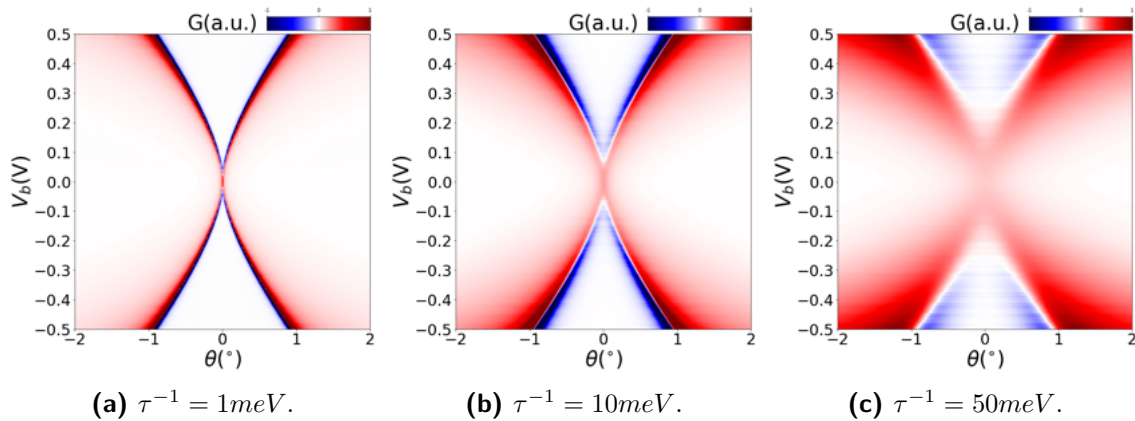


Figure 4.38 Lifetime dependence.

Finite temperature introduced thermal smearing $\sim k_B T$ of the bias window entering via the Fermi-Dirac functions. An additional source of broadening arises due to the finite electron lifetime τ , which results in a Lorentzian broadening of the spectral functions. This broadening directly affects the linewidth in E- \mathbf{k} -space, influencing features irrespective of their position, whether near the edge or deep within the bias window. This effect is particularly critical for the linewidth of the nesting lines, where the tunneling states are distributed across the entire bias window. Figure 4.38 illustrates the differential conductance for varying electron lifetimes τ . Decreasing τ not only causes smearing of the curved X feature but also leads to the emergence of a gap-like feature in the center of the spectrum.

To further analyze the width of the curved X feature, we consider the line profile $I(\theta)$ at a small bias of $V_b = 4\text{mV}$, as shown in Fig. 4.39. The profile exhibits a roughly Lorentzian shape with a linewidth Δ_θ of approximately described by the

relation:

$$\tau^{-1} = \hbar v_F |\mathbf{K}| \frac{\Delta_\theta}{2} \quad (4.38)$$

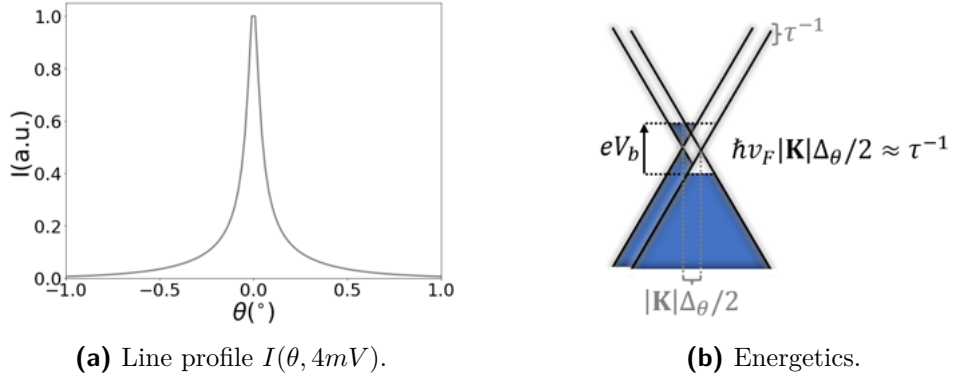


Figure 4.39 Lorentzian current broadening near charge neutrality.

Alternatively, we can examine a line profile $G(V_b)$ at $\theta = 0^\circ$ (Fig. 4.40). While small bias misaligns the Dirac points, substantial tunneling remains possible as long as $\phi < \tau^{-1}$ due to the overlap of the spectral function. Consequently, the significant drop in conductance is shifted to a finite bias, producing the gap-like feature in Fig. 4.38. In the small bias regime, the bias gap Δ_b can be estimated by assuming $\mu \gg \phi$:

$$\tau^{-1} \approx \phi = \frac{e^2}{\pi \hbar^2 v_F^2 C_g} \mu^2 \approx \frac{e^2}{\pi \hbar^2 v_F^2 C_g} \left(\frac{e \Delta_b}{4} \right)^2 = \frac{e^4 \Delta_b^2}{16 \pi \hbar^2 v_F^2 C_g} \quad (4.39)$$

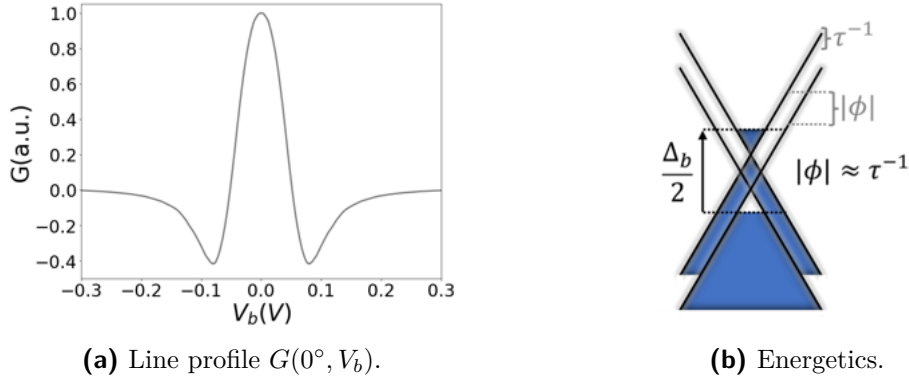
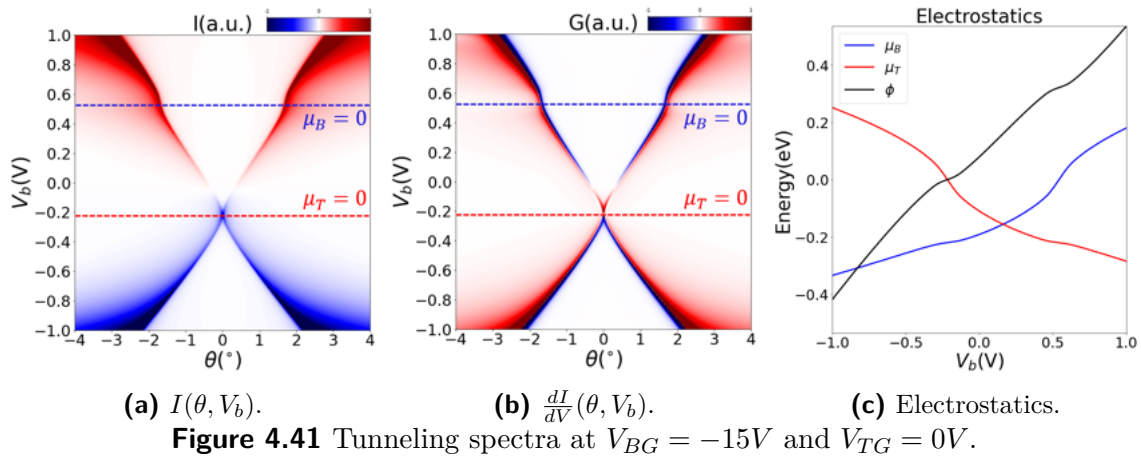


Figure 4.40 Broadening in the Conductance near charge neutrality.

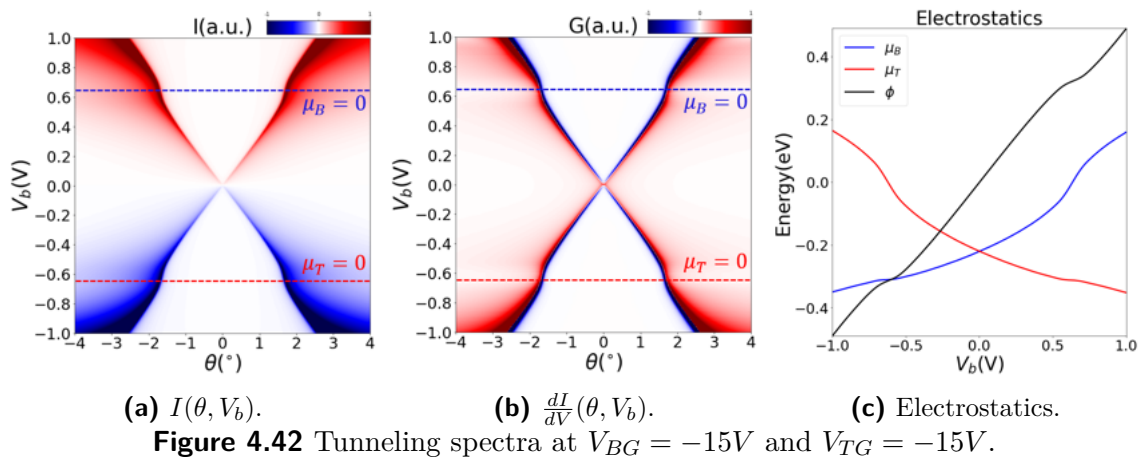
Gating

The setup presented in Fig. 4.22b, includes additional top and bottom gate. In the following we investigate how the spectra evolve with finite gate voltage. Figure 4.41 depicts the electrostatics for $V_{BG} = -15V$ and $V_{TG} = 0V$.

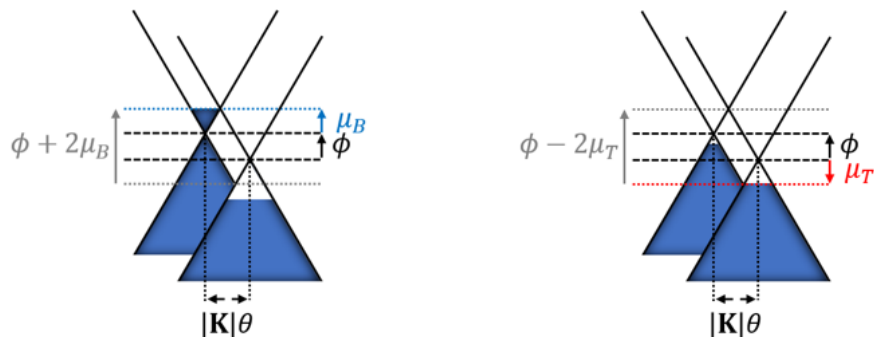
In contrast to the charge neutral case before finite V_{BG} now breaks the mirror symmetry along the z axis, causing the chemical potentials of the two layers to be



different in their absolute values. The resulting tunneling spectrum resembles this asymmetry. The crossing point of the curved-X formally at zero bias, shifts to finite bias. In addition, the symmetric X shape evolves into a “bell-shape” that is asymmetric with respect to bias.



Applying the topgate voltage $V_{TG} = -15V$ restores the symmetry of the junction, which is also evident in the again symmetrical spectrum in Fig. 4.42.



From geometrical consideration (fig. 4.43), we get the generalized condition for the onset:

$$\phi + 2\mu_B = \pm \hbar v_F |\mathbf{K}| \theta \quad (4.40)$$

$$\phi - 2\mu_T = \pm \hbar v_F |\mathbf{K}| \theta \quad (4.41)$$

which are plotted together with nesting line eq. 4.34 in Fig. 4.44. We see the bell-shaped 'nesting' lines and that now each 'onset' line splits in two, since the Fermi surfaces in both layers have a different size and they touch the empty bands in the other layer at different twist angles. Another feature that is visible are the horizontal (dashed) lines along which the $\frac{d^2 I}{dV^2}$ flips sign. Each such line corresponds to one of the MLG layers going across charge neutrality, namely either $\mu_B = 0$ or $\mu_T = 0$ [14].

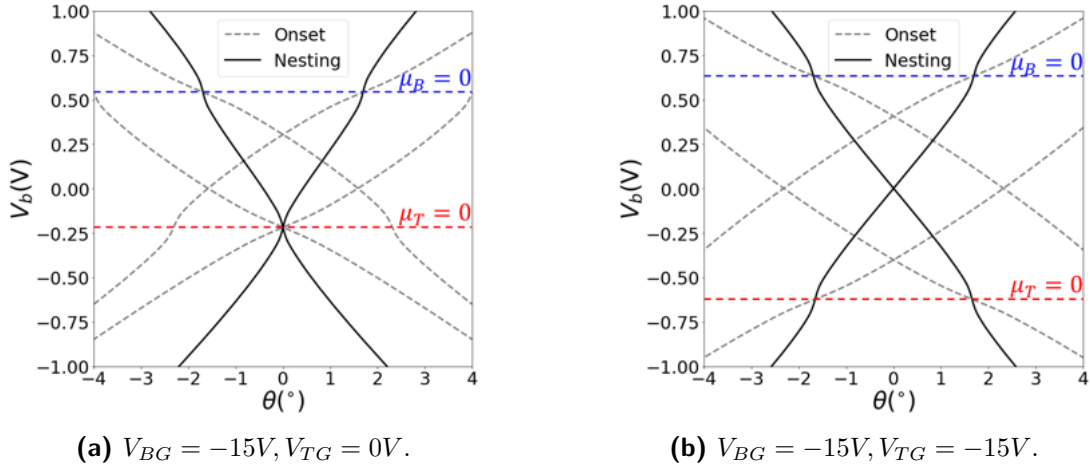


Figure 4.44 Gate dependence.

Concluding, gating allows to shift the bias window to different energies, allowing us to probe different band energy regimes with the QTM.

4.8.2 Measurement

In this section, we compare our experimental measurements with theoretical predictions by identifying the characteristic features associated with the momentum-resolved onset condition, the nesting condition, and finite lifetime. According to our theoretical framework, the spectrum should be governed by the parameters γ_0 , C_g , and τ . We aim to extract these parameters from the experimental data.

Tunneling Spectrum

Figure 4.45 presents the measured tunneling spectra and the corresponding theoretical calculations. We can clearly identify both the curved and straight X-shaped

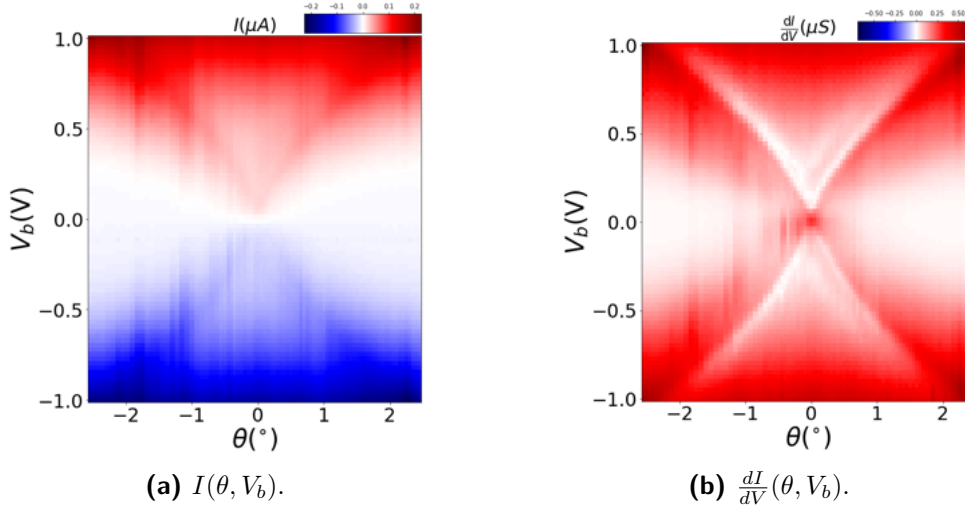


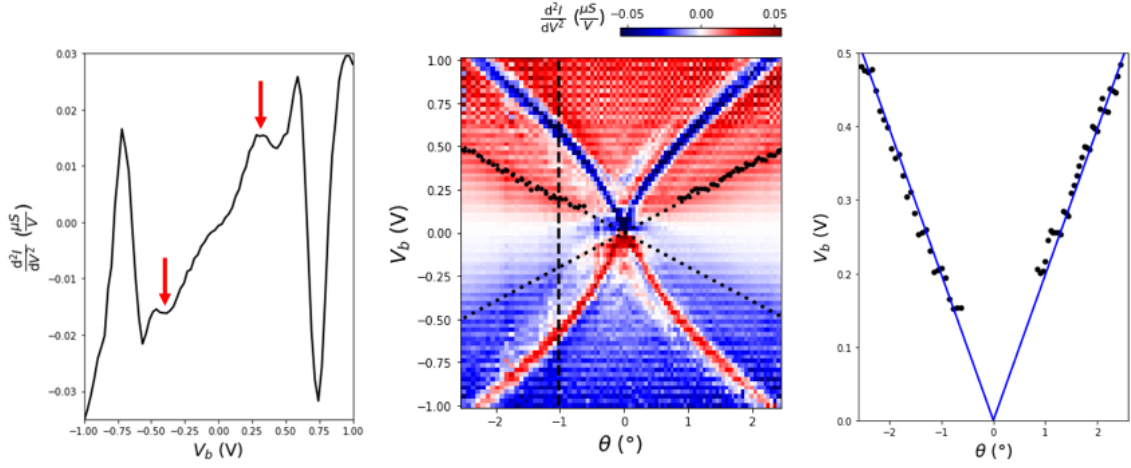
Figure 4.45 Measured tunneling spectra.

features. However, Fig. 4.45b does not exhibit pronounced negative conductance dips along the nesting line. This discrepancy is likely due to scattering processes induced by disorder, which relax the strict momentum conservation and introduce a homogeneous contribution atop the momentum-resolved spectrum, thereby smoothing out sharp features. Similarly, tunnelling through defect states within the hBN band gap could contribute to a homogeneous, twist angle independent current that increases continuously with increasing bias voltage. Additionally, a faint asymmetry is observable when comparing the spectra for $\pm\theta$. This asymmetry could arise because the rotation of the tip is invariably accompanied by a finite translation, leading to transitions into regions with higher disorder or the accumulation of debris on the tip, thereby disrupting the expected $I(\theta) = I(-\theta)$ symmetry.

To smooth out the strong fluctuation in the measurement data, we use the Savitzky-Golay filter for the following analysis.

Momentum-Resolved Onset Condition

The features associated with the onset condition have been significantly broadened, yet they remain discernible as peaks in $\frac{d^2I}{dV^2}$. Figure 4.46b presents $\frac{d^2I}{dV^2}$, while Fig. 4.46a illustrates the corresponding line profile along the vertical dashed line. The onset points are determined by tracking the peaks (dips) at positive (negative) bias. A linear Dirac dispersion, fitted with a Fermi velocity of $v_F = (1.01 \pm 0.03) \times 10^6 \frac{m}{s}$ ($\gamma_0 = (3.13 \pm 0.09)eV$), provides a good agreement with the data, as shown in Fig. 4.46c, which is consistent with previous measurements in graphene [99]. The error estimate is based on the asymmetry observed in the spectrum.

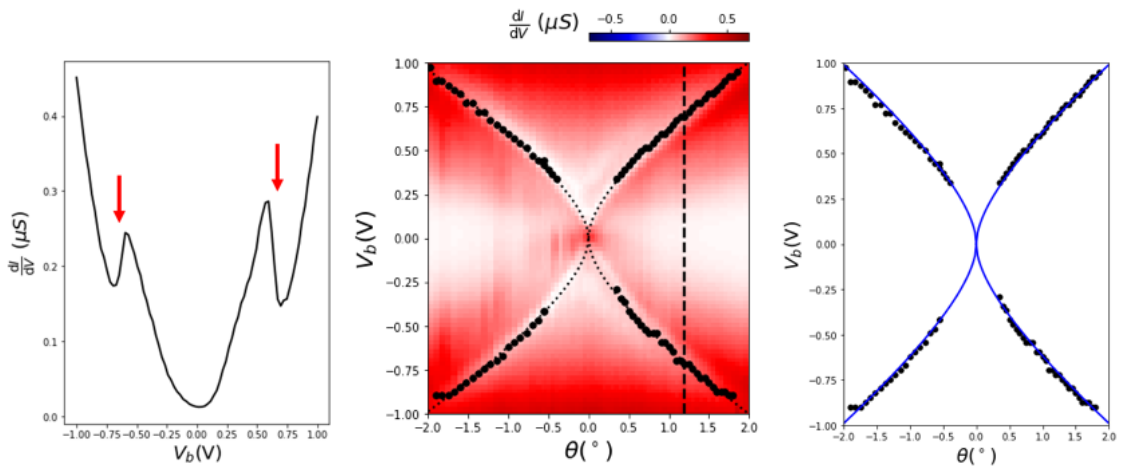


(a) Onset features. (b) $\frac{d^2I}{dV^2}$ and onset features. (c) Fit of eq. 4.35

Figure 4.46 (a) Line profile along dashed path revealing onset features as local maxima (minima) at positive (negative) bias. (b) Measured $\frac{d^2I}{dV^2}$ and onset features (black dots). (c) Fitted Dirac dispersion (blue lines) with $v_F = 1.01 \cdot 10^6 \frac{m}{s}$.

Nesting Condition

Nesting manifests as pronounced peaks in the current, and correspondingly, as dipoles in the differential conductance. Figure 4.77b shows the measured $\frac{dI}{dV}$ along with the extracted dipole positions. With the v_F obtained from the onset condition, we proceed to extract the geometric capacitance C_g . Fitting eq. 4.36 to the extracted data points, as depicted in Fig. 4.77c, yields $C_g = (2.6 \pm 0.3) \frac{\mu F}{cm^2}$. The error is primarily due to the uncertainty in v_F . This result suggests that the barrier consists of four layers of hBN with $\epsilon_r = 3.58$ [100].



(a) Nesting features (b) $\frac{dI}{dV}$ and nesting features (c) Fit of eq. 4.36

Figure 4.47 (a) Line profile along dashed path revealing nesting features as dipoles. (b) Measured $\frac{dI}{dV}$ and nesting features (black dots). (c) Fitted nesting relation (blue lines) with $v_F = 1.01 \cdot 10^6 \frac{m}{s}$ and $C_g = 2.6 \frac{\mu F}{cm^2}$.

Finite Lifetime

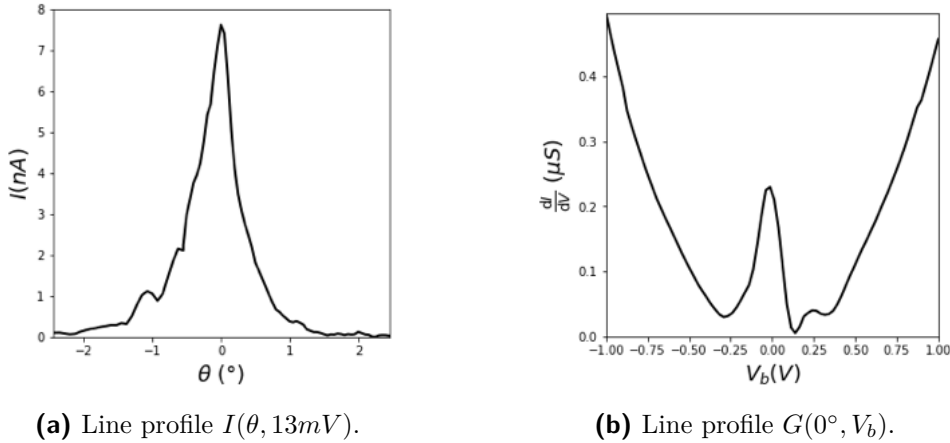


Figure 4.48 Measured line profiles.

The lifetime τ can be inferred by analyzing the linewidth Δ_θ of the Lorentzian line profile in Fig. 4.48a or the width Δ_b of the gap-like feature in Fig. 4.48b. Given the asymmetric shape of Fig. 4.48b, the former method is preferable. By inserting the extracted parameters v_F and C_g , along with the observed FWHM of approximately 0.51° , into eq. 4.38, we estimate an inverse lifetime $\tau^{-1} \approx 50meV$.

4.9 Bilayer Graphene

In this section, we examine tunneling spectroscopy involving a BLG sample. Again, we begin with a theoretical analysis, followed by a comparison with the experimental results.

4.9.1 Theory

In contrast to MLG, the band structure of BLG is characterized by three additional interlayer coupling parameters, denoted as γ_1, γ_3 , and γ_4 . We derive the functional dependence of characteristic features within the spectrum and analyze how these features, along with the intersection curves in \mathbf{k} -space, evolve as the parameters are varied.

Tunneling Spectrum

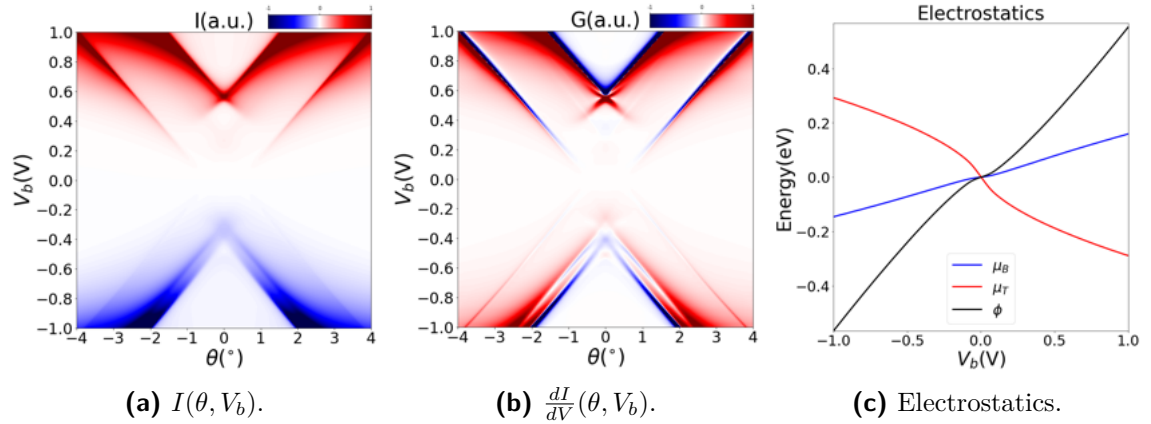


Figure 4.49 Simulated tunneling spectra for BLG.

Figure 4.49 presents the simulated tunneling spectra for $\tau^{-1} = 5meV$, $C_g = 189 \frac{nF}{cm^2}$, $d_g = 1.5nm$, $\epsilon_{hBN} = 3.2$ at $T = 300K$, using the hopping parameters defined in Sec. 2.5. In contrast to MLG, the BLG spectrum exhibits asymmetry with respect to the $V_b = 0V$ line. Notably, a straight X-shaped feature is observed, which crosses the charge neutrality point and is more pronounced for positive V_b . Furthermore, the spectrum reveals cones in the high-bias regime, along with a line splitting of the cone under negative bias conditions.

The electrostatic behavior markedly differs from that in MLG. In the low-bias regime, where the effective mass approximation for BLG is valid, the carrier density can be expressed as $n(\mu) = \frac{2m^*}{\pi\hbar^2}|\mu|$, where the effective mass is given by $m^* = \frac{\gamma_1}{2v_F}$. The following relationship between the electrostatic quantities is derived from eq. 4.23:

$$\mu_B = \frac{\pi\hbar^2 v_F^2 C_g}{\gamma_1 e^2} \phi, \quad |\mu_T|^2 = \gamma_1 |\mu_B| \quad (4.42)$$

$$eV_b = \phi + \frac{\pi\hbar^2 v_F^2 C_g}{\gamma_1 e^2} \phi + \text{sign}(\phi) \sqrt{\frac{\pi\hbar^2 v_F^2 C_g}{e^2} |\phi|}. \quad (4.43)$$

Consequently, the ratio of the shifts in electrostatic and chemical potentials in BLG remains constant, while the respective chemical potentials are connected by a quadratic relationship. This quantifies the inherent asymmetry between μ_B and μ_T .

Nesting and Matching Condition

Analogous to MLG, onset features are expected when the Fermi surface of one material touches the empty bands of the other material. However, due to the generally larger number of features in the spectrum, resolving these faint onsets is not feasible at room temperature. Consequently, our focus is on the pronounced lines similar

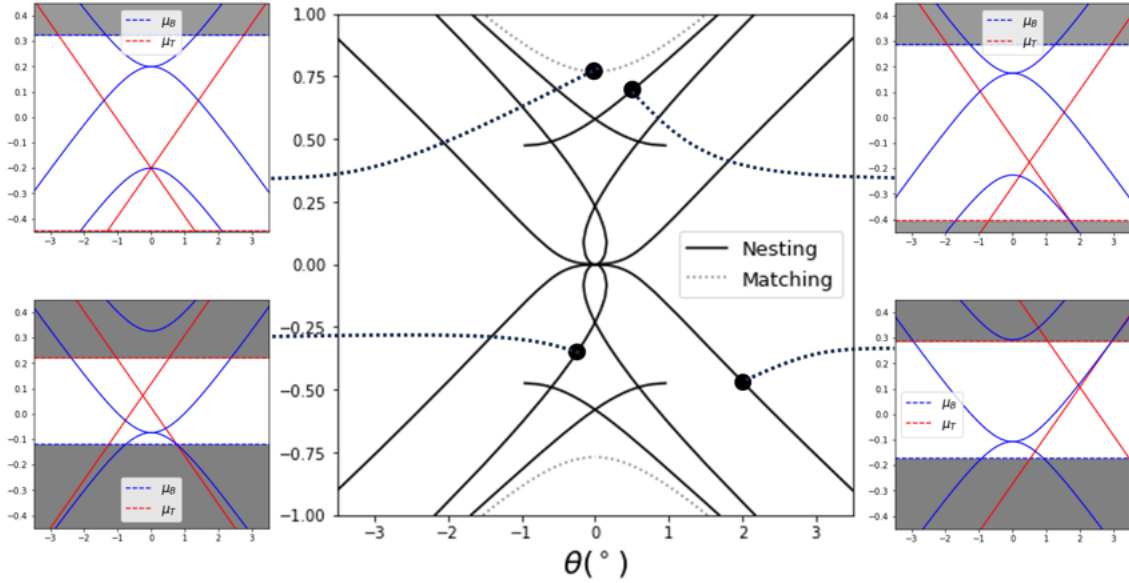


Figure 4.50 Nesting and matching lines in BLG (probed with MLG on tip).

to the nesting lines observed in MLG. Unlike in MLG, the band velocity in BLG, $v_{BLG} \approx \hbar|\mathbf{q}|/m^*$, is momentum-dependent, and thus complete nesting is not possible. Although v_{BLG} is generally lower than v_F , it closes up as \mathbf{q} increases. The prominence of features related to intersection points in E - \mathbf{k} space is governed by the difference in band velocity of the probe v_F and the system v_{BLG} at these points. Due to the finite lifetime τ , states separated by less than τ^{-1} are expected to be available for tunneling. When $v_{BLG} \ll v_F$, this condition is only met in a very small region of \mathbf{k} -space, and tunneling states are well-localized at the band intersection points.

As $v_{BLG} \rightarrow v_F$, a larger region in \mathbf{k} -space emerges where states from different bands are separated by less than τ^{-1} in energy, making them available for tunneling. These local nestings produce the strong features observed in the spectrum. For simplicity, we will continue to refer to them as nesting lines. Notably, for every V_b , the current is dominated by the intersection point at the edge of the bias window, where v_{BLG} is largest.

The condition that the bands intersect at the edge of the bias window allows us to derive an expression for the path in the θ - V_b plane. Initially, we consider only the strongest coupling terms, γ_0 and γ_1 , so that the two bands can be approximated by:

$$E_{BLG} \approx \pm \frac{\gamma_1}{2} \left(\sqrt{1 + \frac{4\hbar^2 v_F^2 |\mathbf{q}|^2}{\gamma_1^2}} \pm 1 \right), \quad E_{MLG} \approx \pm \hbar v_F |\mathbf{q}|. \quad (4.44)$$

Since these expressions are isotropic in momentum, we only need to consider the momentum dispersion along the q_y -axis. As depicted in Fig. 4.28, twisting causes a

relative shift of the \mathbf{K} -points by $|\mathbf{K}|\theta$ along the q_y -axis, allowing us to focus on band touching in the q_y - E plane. Intersections occurring at μ_B are defined by:

$$E_{BLG}(q) = |\mu_B|, \quad E_{MLG}(q - |\mathbf{K}|\theta) = |\mu_B| + |\phi|, \quad (4.45)$$

For μ_T , the relations are:

$$E_{BLG}(q) = |\mu_T| + |\phi|, \quad E_{MLG}(q - |\mathbf{K}|\theta) = |\mu_T|, \quad (4.46)$$

where $q = q_y$ and the tip has been rotated relative to the sample \mathbf{k} -space by θ .

The six observed nesting lines follow these relations:

$$\hbar v_F |\mathbf{K}|\theta = \pm \left[\sqrt{|\mu_B|^2 + \gamma_1 |\mu_B|} - |\mu_B| - |\phi| \right], \quad (4.47)$$

$$\hbar v_F |\mathbf{K}|\theta = \pm \left[\sqrt{(|\mu_T| + |\phi|)^2 - \gamma_1 (|\mu_T| + |\phi|)} - |\mu_T| \right], \quad (4.48)$$

$$\hbar v_F |\mathbf{K}|\theta = \pm \left[\sqrt{(|\mu_T| + |\phi|)^2 + \gamma_1 (|\mu_T| + |\phi|)} - |\mu_T| \right], \quad (4.49)$$

where expressions related to momentum-resolved onsets have been omitted.

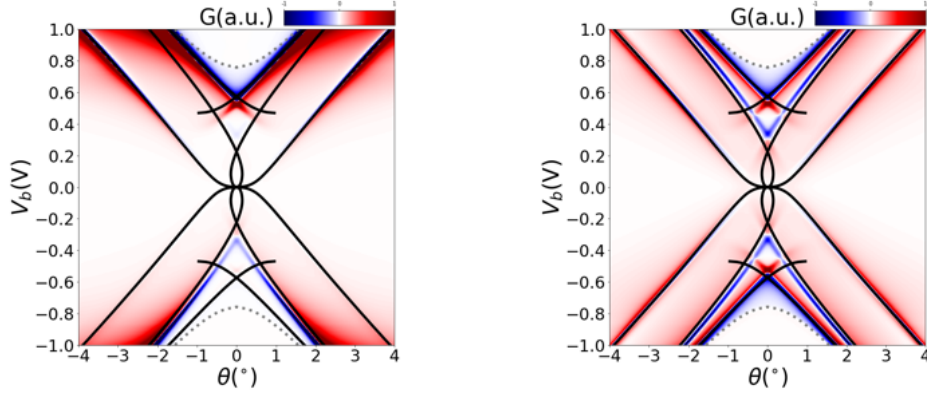
Additionally, a step-like behavior in conductance is observed at large bias (Fig 4.49b). Since the DOS for parabolic bands is constant and that for Dirac bands features a linear relationship, a minimum in the current is expected when the Dirac point aligns with a parabolic band. This matching condition with a high-energy band of BLG is defined by:

$$E_{BLG}(|\mathbf{K}|\theta) = |\phi|, \quad (4.50)$$

leading to:

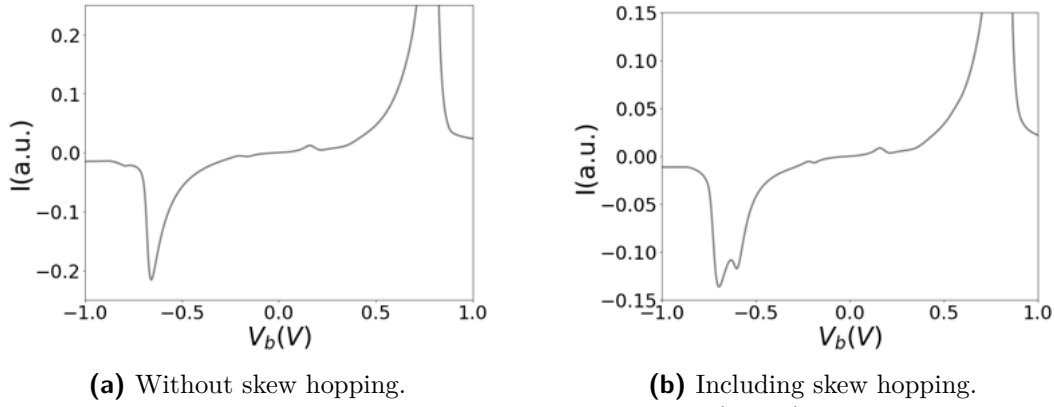
$$\hbar v_F |\mathbf{K}|\theta = \pm \left[\sqrt{|\phi|^2 - \gamma_1 |\phi|} \right]. \quad (4.51)$$

In Fig 4.50, we plot all the nesting and matching lines, and in Fig 4.51, we overlay these on the tunneling spectrum for $\gamma_3 = \gamma_4 = 0$. The lines show a good match, especially at large bias when $v_{BLG} \approx v_F$ at the bias window edge.



(a) With barrier interaction (b) Without barrier interaction
Figure 4.51 Tunneling spectra with nesting (solid black) and matching (dashed gray) lines.

Momentum Space Analysis



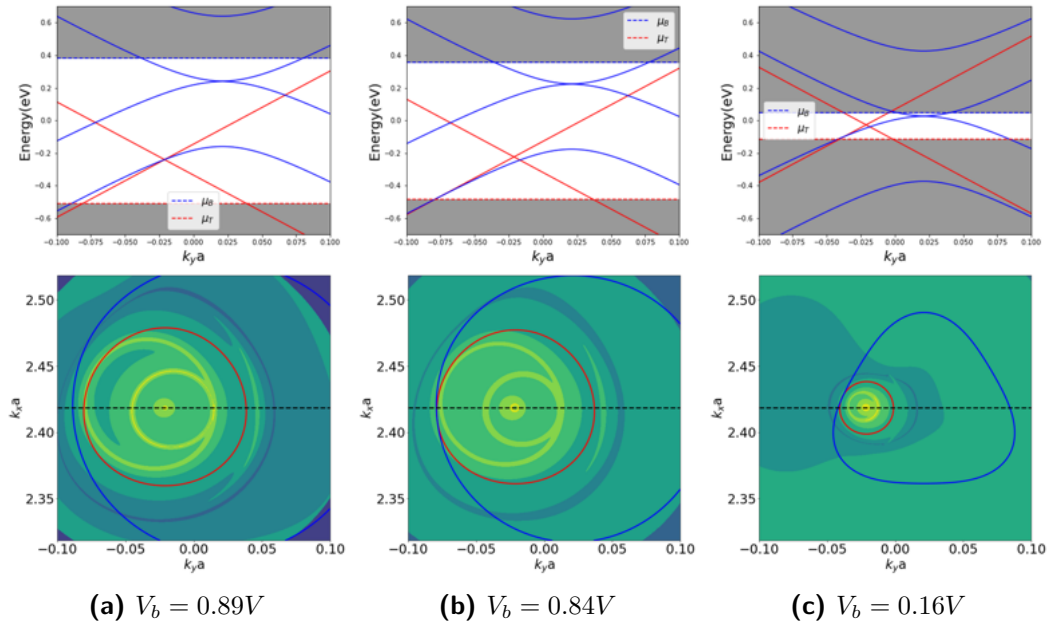
(a) Without skew hopping. (b) Including skew hopping.
Figure 4.52 Calculated line profile $I(1^\circ, V_b)$.

We can examine the origin of the characteristic features in the $I(\mathbf{k})$ -map. To this end, we now consider the line profile $I(V_b)$ along the vertical line at $\theta = 1^\circ$. Figure 4.52a and Fig. 4.52b depict the spectra without and with skew hopping terms, respectively. The subsequent calculations of $I(\mathbf{k})$ incorporate these terms.

For each (θ, V_b) configuration, we plot the $I(\mathbf{k})$ -map and mark the contours of BLG with blue lines and those of MLG with red lines.

We begin with a bias of $1.0V$ and progressively reduce the current. Despite the high bias, a very low current is observed until approximately $0.89V$ is reached. As shown in Fig. 4.53a, the intersection of the high-energy valence band of BLG occurs near the Dirac point of MLG, where the DOS is low, resulting in a small contribution. The $I(\mathbf{k})$ -map reveals circular contribution lines, originating from the intersection of MLG's conduction band with the low-energy valence band of BLG. However, the opposite signs of the band velocities confine the tunneling states to a very small region, as indicated by the thin lines along the intersection paths. Moreover, these lines lie in the upper half of the bias window and are thus strongly suppressed by

the barrier.



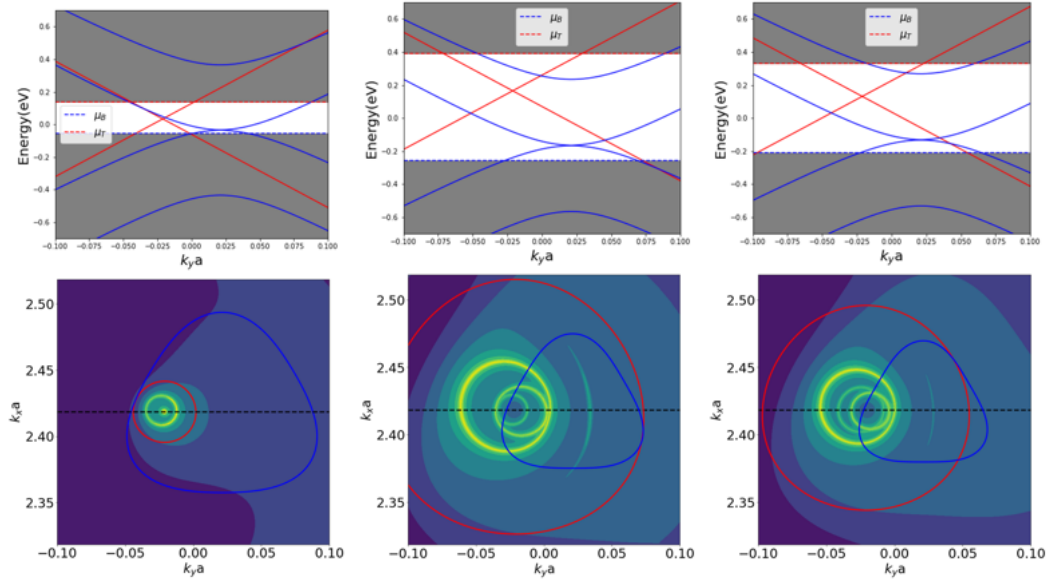
(a) $V_b = 0.89V$ (b) $V_b = 0.84V$ (c) $V_b = 0.16V$
Figure 4.53 Energy bands (top) along \mathbf{k} -path (dashed black), $I(\mathbf{k})$ map (bottom) centered at \mathbf{K}_D (unrotated), showing the energy contours of MLG (red) and BLG (blue) at μ_T . Background brightness is proportional to the logarithmic current.

As the bias voltage is further reduced, a sharp increase in the current is observed, with a maximum at $V_b = 0.84V$, corresponding to the nesting of MLG's valence band with BLG's high-energy valence band (Fig. 4.53b).

Further reduction in bias voltage leads to a continuous decrease in current, until a small peak is observed at $V_b = 0.16V$, corresponding to the nesting of MLG's valence band with BLG's low-energy valence band. Due to the narrow bias window, current contributions become increasingly confined to band states with low momenta as clearly observable in the $I(\mathbf{k})$ -map (Fig. 4.53c).

The current then changes sign as the bias transitions through $V_b = 0$, and continuously decreases until a dip is reached at $V_b = -0.19V$ (Fig. 4.54a). This dip is the symmetric counterpart to the small peak at $V_b = 0.16V$, where the nesting occurs between MLG's conduction band and BLG's low-energy conduction band at the upper edge of the bias window. Since both of these nestings occur close to charge neutrality, the exponential suppression is not as severe, and the peak and dip are of similar magnitude. The difference in absolute bias voltage is related to electron-hole asymmetry induced by γ_4 .

A double peak structure is then observed at $V_b = -0.54V$ and $V_b = -0.65V$, which is absent in the spectrum without skew hopping. As illustrated in Fig. 4.54b and Fig. 4.54c, trigonal warping causes the splitting of the nesting lines arising from MLG's valence band and BLG's low-energy valence band.



(a) $V_b = -0.19V$ (b) $V_b = -0.54V$ (c) $V_b = -0.65V$
Figure 4.54 Energy bands (top) along \mathbf{k} -path (dashed black), $I(\mathbf{k})$ map (bottom) centered at \mathbf{K}_D (unrotated), showing the energy contours of MLG (red) and BLG (blue) at μ_T (left) and μ_B (middle and right). Background brightness is proportional to the logarithmic current.

This higher bias regime also reveals the strong asymmetry in the spectrum. While at positive bias, the current is here dominated by the nesting with BLG's high-energy valence band at the lower edge of the bias window, the nesting with BLG's high-energy conduction band at the upper edge is now strongly suppressed due to the barrier interaction. This suppression also applies to the double peak structure, which was not observable at positive bias.

Tunnel Barrier

An asymmetric alignment of the barrier creates the asymmetric spectrum by suppressing either electron or hole tunneling. Figure 4.55 illustrates the cases of $\Delta_V = -1.5eV$ & $\Delta_C \rightarrow \infty$, $\Delta_V \rightarrow -\infty$ & $\Delta_C = 1.5eV$ and for no barrier interaction at all. We can see how the first two cases are related by switching the orientation of the V_b -axis. For the last case $t_{WKB}(E) = 1$ so that tunneling across all energy slices contribute in the same order of magnitude. Besides material-intrinsic electron-hole asymmetry related features, the spectrum is then symmetric.

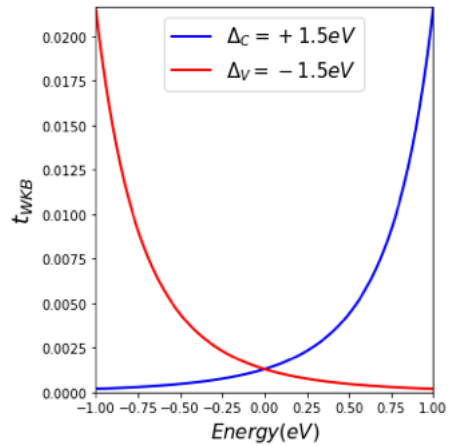
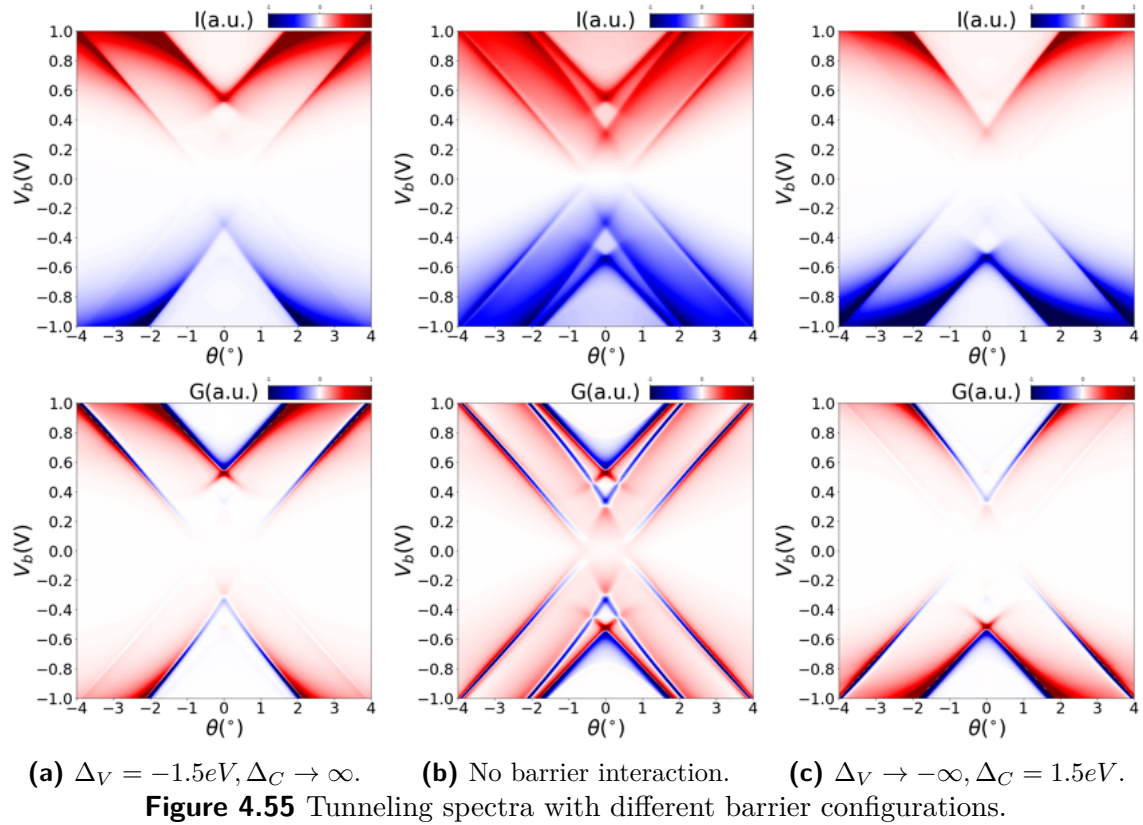
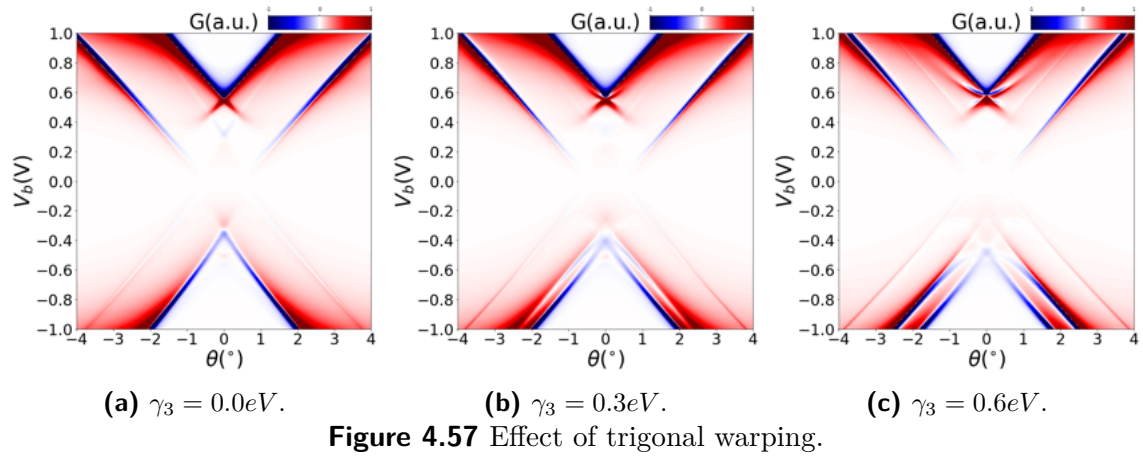


Figure 4.56 WKB amplitudes for different barrier configurations.



Trigonal Warping



The parameter γ_3 represents the skew interlayer coupling between non-dimer sites, leading to a trigonal distortion of the otherwise circular iso-energetic contours. To elucidate the effect of this coupling on the electronic spectrum, we examine the variations in the spectrum as γ_3 is varied, as shown in Fig. 4.57. It is evident that increasing γ_3 results in the splitting of nesting lines, a phenomenon particularly pronounced at the nesting of the MLG valence band with the low-energy valence band of BLG.

Figure 4.58 presents the energy bands alongside the corresponding energy contours

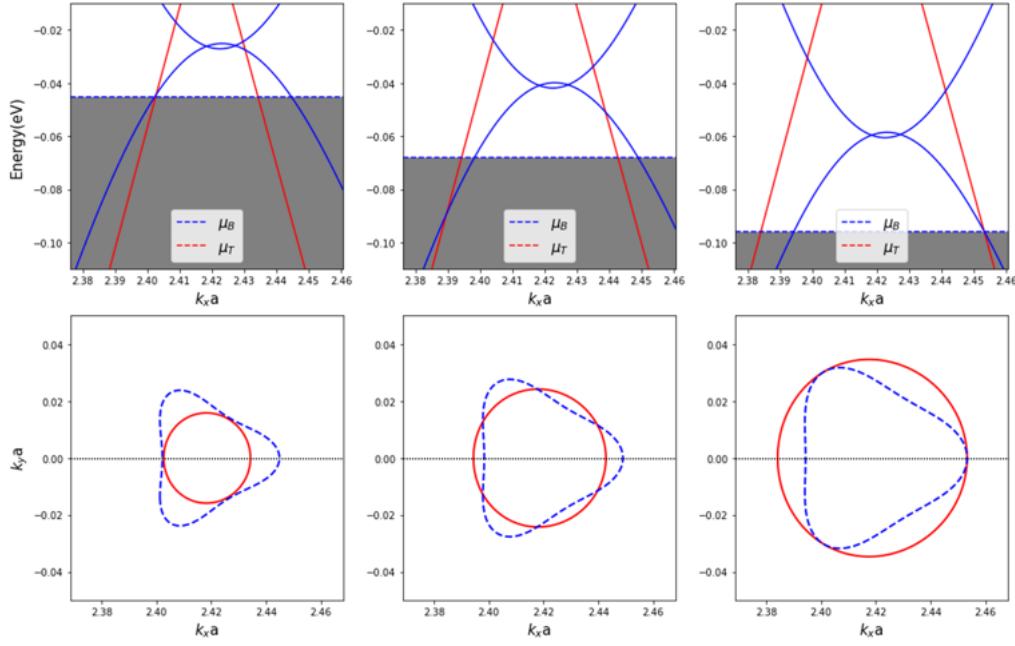


Figure 4.58 Energy bands (top) and Fermi surface of MLG (solid red) and empty band states (dashed blue) of BLG in \mathbf{k} -space at μ_B . The Fermi surface is depicted for bias voltages of $V_b = -0.17V$ (left), $V_b = -0.23V$ (middle), and $V_b = -0.29V$ (right).

in \mathbf{k} -space for $\theta = 0^\circ$. At a bias voltage of $V_b = -0.17V$, the Fermi surface of MLG (solid red) just touches the empty valence band of BLG (dashed blue). However, due to the trigonal distortion, this intersection occurs only at three distinct points. By $V_b = -0.29V$, the entire energy contour of BLG lies within the Fermi circle of MLG.

An analytical expression can be derived for the difference in ϕ between these separated nesting conditions for $\theta = 0^\circ$. The energy contour for MLG is given by:

$$\hbar v_F |\mathbf{q}| = |\phi| + |\mu_B| = \left(1 + \frac{\pi \hbar^2 v_F^2 C_g}{e^2 \gamma_1}\right) |\phi| = A |\phi|, \quad (4.52)$$

where eq. 4.42 has been used, and $A = 1 + \frac{\pi \hbar^2 v_F^2 C_g}{e^2 \gamma_1}$ is a dimensionless constant. Given that this phenomenon occurs near the Dirac point of BLG, we can apply the low-energy expression from eq. 2.87. The corresponding energy contour at μ_B with extremal $|\mathbf{q}|$ is expressed as:

$$|\mu_B|^2 = (\hbar v_3 |\mathbf{q}|)^2 \pm \frac{v_3 \hbar^3 |\mathbf{q}|^3}{m^*} + \left(\frac{\hbar^2 |\mathbf{q}|^2}{2m^*}\right)^2 \quad (4.53)$$

Substituting eq. 4.52 into eq. 4.53, we obtain:

$$(1 - A)^2 |\phi|^2 = \left(A \frac{v_3}{v_F} \right)^2 |\phi|^2 \pm \frac{2A^3 v_3}{\gamma_1 v_F} |\phi|^3 + \left(\frac{A^2}{\gamma_1} \right)^2 |\phi|^4, \quad (4.54)$$

$$0 = |\phi|^2 \left[\left(A \frac{v_3}{v_F} \right)^2 - (1 - A)^2 \pm \frac{2A^3 v_3}{\gamma_1 v_F} |\phi| + \left(\frac{A^2}{\gamma_1} \right)^2 |\phi|^2 \right]. \quad (4.55)$$

The difference between the roots, Δ_ϕ , of the polynomial in the brackets is given by:

$$\Delta_\phi = 2 \frac{\gamma_1}{A} \left(\frac{v_3}{v_F} \right) = \frac{2\gamma_1^2 e^2}{\gamma_1 e^2 + \pi C_g \hbar^2 v_F^2} \left(\frac{v_3}{v_F} \right). \quad (4.56)$$

Assuming the ratio of $\frac{v_3}{v_F} = 0.1$, we find that $\Delta_\phi = 0.06eV$, which aligns with the numerical analysis (Fig. 4.58), where $\phi(-0.17V) - \phi(-0.29V) \approx (-0.06eV) - (-0.12eV) = 0.06eV$. Here, $\phi(V_b)$ is defined by eq. 4.43.

For finite values of θ , a more complex functional dependence is expected. However, we can generally assume that the observed splitting of the nesting lines arises from the distorted energy contours due to the presence of γ_3 .

Electron-Hole Asymmetry

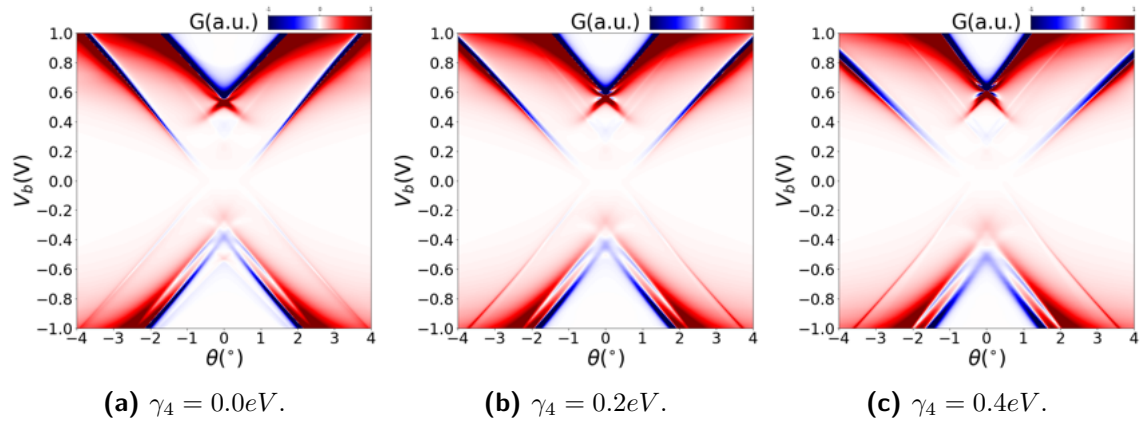


Figure 4.59 Effect of electron-hole asymmetry.

The skew interlayer coupling parameter, γ_4 , which couples a non-dimer site to a dimer site, induces electron-hole asymmetry within the band structure. As γ_4 increases, this asymmetry becomes more pronounced, particularly in the nesting lines for $V_b > 0$ when compared to $V_b < 0$, as illustrated in Fig. 4.59. This effect is most evident when comparing the nesting lines at the lowest bias voltages, corresponding to the nesting of the low-energy conduction (valence) band of BLG with the conduction (valence) band of MLG, denoted as $\theta^-(V_b)$ and $\theta^+(V_b)$. For $\gamma_4 > 0$, we observe that $|\theta^+| \geq |\theta^-|$.

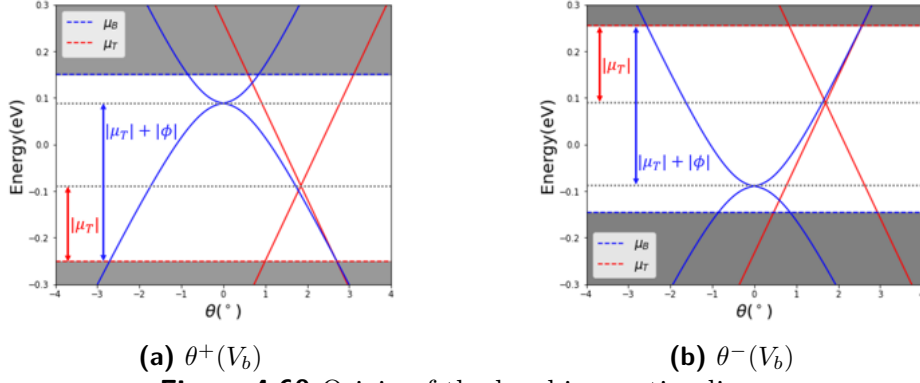


Figure 4.60 Origin of the low-bias nesting lines.

Next, we derive the functional dependence of $\Delta_\theta = |\theta^+| - |\theta^-|$ on γ_4 . Using eq. [2.88](#) and noting that the intersection occurs at μ_T , the following relations for momentum and twist angle can be established:

$$\hbar v_F(|\mathbf{q}| - |\mathbf{K}|\theta) = |\mu_T|, \quad (1 \pm 2 \frac{v_4}{v_F}) \frac{\hbar^2 (|\mathbf{q}|)^2}{2m^*} = |\mu_T| + |\phi| \quad (4.57)$$

$$\hbar v_F |\mathbf{K}|\theta = \hbar v_F |\mathbf{q}| - |\mu_T|, \quad \hbar v_F |\mathbf{q}| = \sqrt{\frac{\gamma_1 (|\mu_T| + |\phi|)}{1 \pm 2 \frac{v_4}{v_F}}} \quad (4.58)$$

We then obtain:

$$\hbar v_F |\mathbf{K}|\theta^\pm = \sqrt{\frac{\gamma_1 (|\mu_T| + |\phi|)}{1 \pm 2 \frac{v_4}{v_F}}} - |\mu_T| \quad (4.59)$$

$$= \sqrt{\frac{1 \mp 2 \frac{v_4}{v_F}}{1 - 4 (\frac{v_4}{v_F})^2}} \sqrt{\gamma_1 (|\mu_T| + |\phi|)} - |\mu_T| \quad (4.60)$$

$$= \frac{1 \mp \frac{v_4}{v_F} + \mathcal{O}\left(\left[\frac{v_4}{v_F}\right]^2\right)}{1 + \mathcal{O}\left(\left[\frac{v_4}{v_F}\right]^2\right)} \sqrt{\gamma_1 (|\mu_T| + |\phi|)} - |\mu_T| \quad (4.61)$$

$$\approx \left[1 \mp \frac{v_4}{v_F}\right] \sqrt{\gamma_1 (e|V_b| - |\mu_B|)} - |\mu_T| \quad (4.62)$$

Thus, when comparing the nesting lines at $\pm V_b$, we anticipate a shift in θ at the lowest order, given by:

$$\Delta_\theta \approx 2 \frac{\sqrt{\gamma_1 e |V_b|}}{\hbar v_F |\mathbf{K}|} \left(\frac{v_4}{v_F}\right) \sqrt{1 - \left|\frac{\mu_B}{eV_b}\right|} = 2 \frac{\sqrt{\gamma_1 e |V_b|}}{\hbar v_F |\mathbf{K}|} \left(\frac{v_4}{v_F}\right) \sqrt{1 + \mathcal{O}\left(\left[\frac{\mu_B}{eV_b}\right]\right)} \quad (4.63)$$

Considering that the shift in μ_B is negligible for small V_b due to the large onset of the DOS relative to MLG, we approximate the relation:

$$\Delta_\theta \approx 2 \frac{\sqrt{\gamma_1 e |V_b|}}{\hbar v_F |\mathbf{K}|} \left(\frac{v_4}{v_F} \right) \quad \text{for} \quad \frac{\mu_B}{eV_b} \ll 1 \quad (4.64)$$

Eq. 4.64 is plotted in Fig. 4.61b, alongside the corresponding numerical calculations.

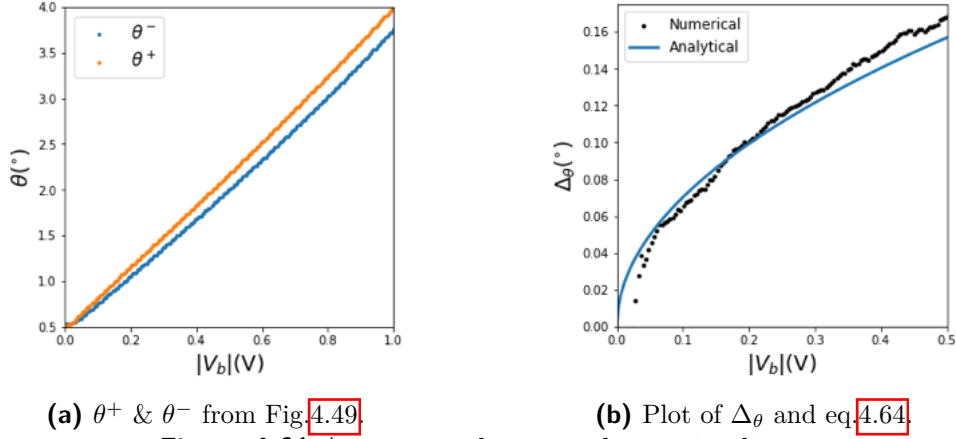


Figure 4.61 Asymmetry between the nesting lines.

4.9.2 Measurement

In the following sections, we present and interpret our measurement data. Notably, the measured spectrum exhibits significant deviations from theoretical predictions. Our primary focus is to understand the discrepancies between the theoretical simulations and the experimental data.

Tunneling Spectrum

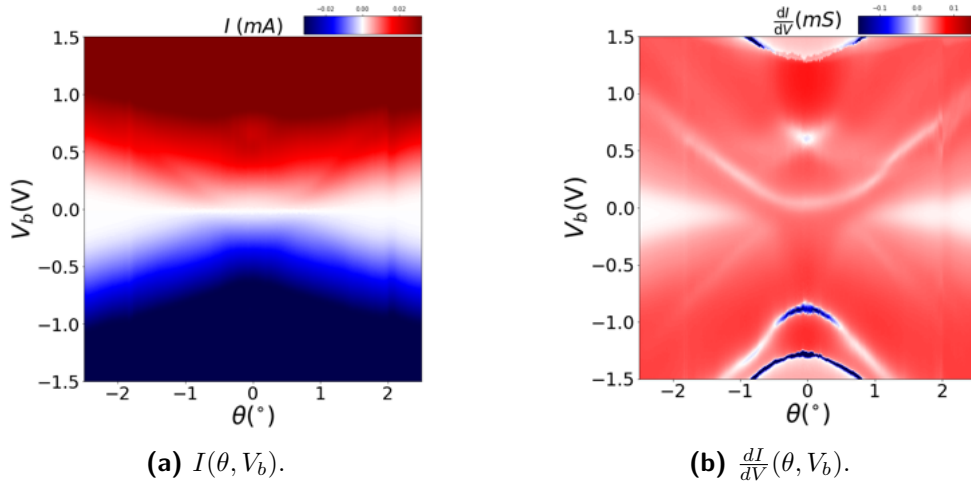


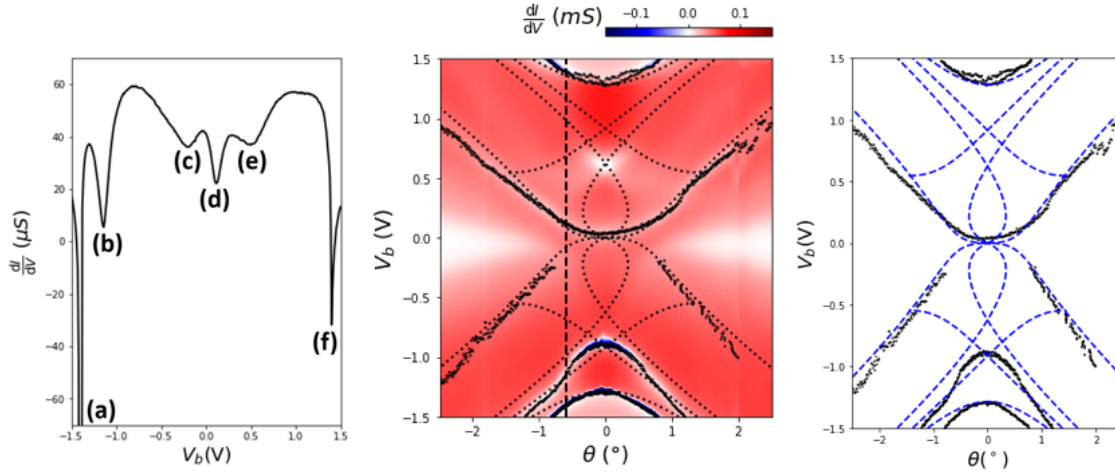
Figure 4.62 Measured tunneling spectra.

Figure 4.62 displays the measured tunneling spectra. Several parabolic-shaped curves, identifiable as local minima, can be observed in Fig. 4.76b, alongside a pronounced asymmetry between the positive and negative bias regimes.

Nesting and Matching Features

Figure 4.63a presents a line profile along a vertical line at $\theta = -0.6^\circ$, revealing six distinct dipole-like features. In Fig. 4.63c, we extract their positions and fit the nesting conditions from eq. 4.45 and eq. 4.46, as well as the matching condition from eq. 4.50. The fitting parameters used include v_F , γ_1 , and C_g . Knowing v_F and C_g , allows to extract the value of γ_1 . An AFM scan of the surface topography suggests a hBN thickness of approximately 1.6nm , corresponding to five layers of hBN, with a relative permittivity $\epsilon_r = 3.62$ [100]. However, using the resulting $C_g \approx 2 \frac{\mu F}{\text{cm}^2}$ does not yield a satisfactory fit.

The observed discrepancy is likely attributable to inaccuracies in modeling the junction as a parallel-plate capacitor. This model does not fully account for the field distribution extending beyond the contact area, leading to interactions in the surrounding region. Consequently, this effect can result in an increased effective thickness, d_g . Additionally, the relative permittivity, ϵ_r , is expected to differ due to the increased proportion of air within the volume, coupled with the finite in-plane field component experiencing an enhanced screening effect.



(a) $\frac{dI}{dV}(-0.6^\circ, V_b)$ (b) $\frac{dI}{dV}$ and nesting/matching points (c) Fitting

Figure 4.63 (a) Line profile along dashed path. (b) Measured $\frac{dI}{dV}$ and nesting/matching features (black dots). (c) Fitted nesting relation (blue lines) with $v_F = 1.01 \cdot 10^6 \frac{\text{m}}{\text{s}}$ and $C_g = 7.9 \frac{\mu F}{\text{cm}^2}$.

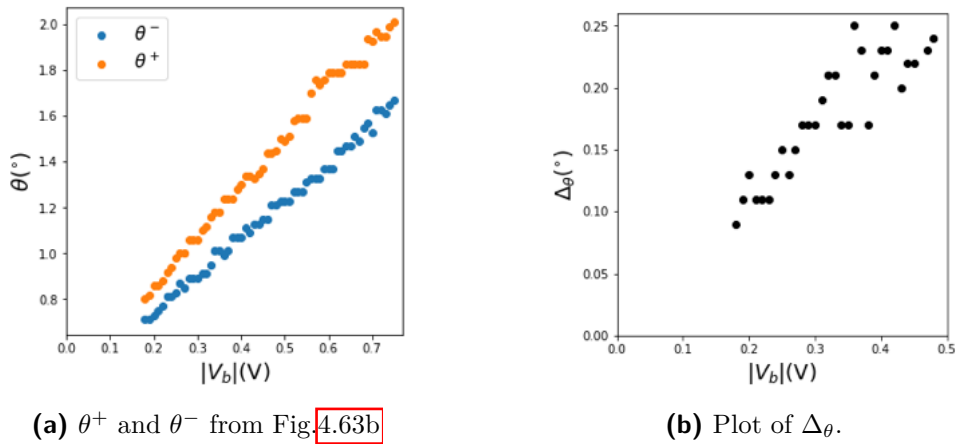
Using $\gamma_1 \approx 0.4 \text{ eV}$ [37], we obtain the fit shown in Fig. 4.63c with $C_g \approx 7.9 \frac{\mu F}{\text{cm}^2}$. While some features can be matched, the overall spectrum diverges from theoretical predictions. Beginning with the low bias regime in Fig. 4.63a, the dip (c) is significantly

more pronounced than its symmetric counterpart (d). The hBN barrier should only induce this effect at higher biases, where nesting is localized at higher energy.

Another notable discrepancy with the theoretical model is the presence of strong circular features in the high bias regime. Based on their shape, these features align only with the matching condition, as shown in Fig. 4.63c. According to this interpretation, the nestings at higher biases result in the dipoles at (b) and (e). This contrasts with theoretical predictions, where the strong dips at (a) and (f) correspond more closely to nesting with high-energy bands of BLG.

Skew Hopping

The impact of the skew hopping term γ_3 , would result in line splitting; however, the resolution limit of our measurements does not allow for the identification of these features. The parameter γ_4 , on the other hand, introduces asymmetry between the nesting lines as predicted by eq. 4.64. In Fig. 4.64, we trace the corresponding nesting lines θ^+ and θ^- and plot the difference Δ_θ . Although the expected asymmetry is confirmed, strong fluctuations hinder the precise extraction of nesting points, particularly in the low bias regime $|V_b| < 0.2V$. Consequently, it is not possible to identify a clear functional dependence and extract γ_4 .



(a) θ^+ and θ^- from Fig. 4.63b

(b) Plot of Δ_θ .

Figure 4.64 Asymmetry between the nesting lines.

Doping and Strain Effects

Additional sources of asymmetry may arise from unintentional doping and strain.

Given that the polymer transfer method (Sec. 3.4.5) involves interactions between graphene and other chemical species, it is plausible to assume charge transfer occurs between graphene and surface adsorbates, leading to a shift in the chemical potential (Fig. 4.65) [101].

A shift in the initial Fermi level leads to a corresponding displacement of the entire bias window. Given that the nesting lines arise from the intersections at the edges of the bias window and that the DOS in MLG increases as one moves away from the Dirac point energy, a significant asymmetry is expected to emerge due to doping. Depending on the polarity of the applied bias, the chemical potential of graphene can either be tuned back to the Dirac point energy or shifted to higher absolute energy values.

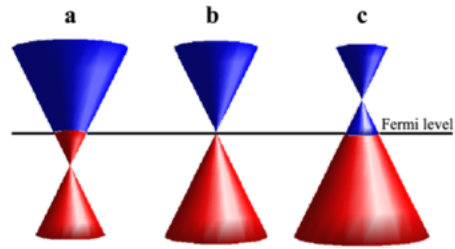


Figure 4.65 Fermi-level for n-type (a), neutral (b) and p-type (c) doping. Adapted from [101].

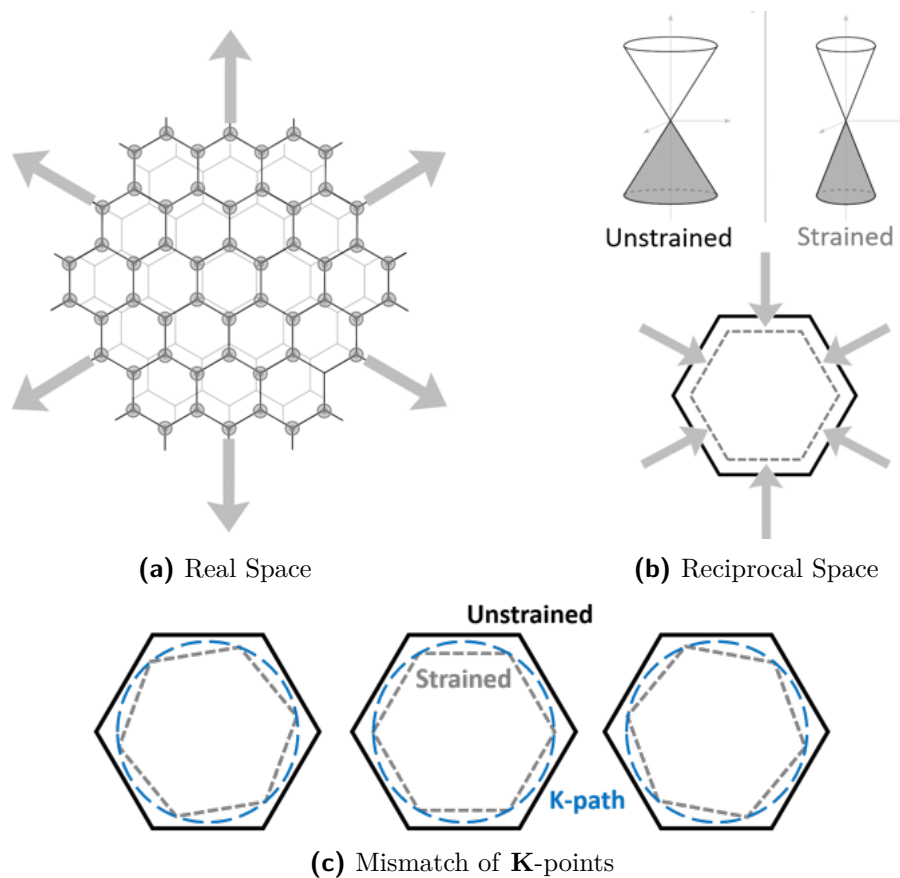


Figure 4.66 Effect of isotropic strain. Adapted from [102].

In addition to the asymmetry near charge neutrality, we also want to identify the origin of the differing shapes of features in the high bias regime. A likely cause is strain, which may originate from lattice mismatch between hBN and graphene or due to the tip geometry. As illustrated in Fig. 4.66, isotropic strain preserves the original crystal symmetry but increases (or reduces) the lattice constant, thereby reducing (or increasing) the size of the first Brillouin zone. Consequently, the Dirac points of both systems are shifted and cannot align for any twist angle.

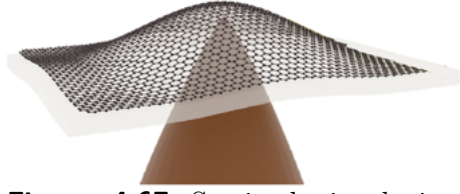


Figure 4.67 Strained tip device. Adapted from [103]

In Fig. 4.68, we depict the measured and simulated $\frac{d^2I}{dV^2}$, where the latter includes a shifted chemical potential by $\Delta\mu_T = +0.15eV$ and an increased lattice constant of MLG by 0.8% (1.6% corresponds to the lattice constant of hBN). This adjustment allows us to approximately reproduce the characteristics observed in the low bias

regime. Similar to the simulations conducted with a finite gate voltage, we observe a horizontal line in the spectrum, indicating that the Fermi level is traversing through the Dirac point.

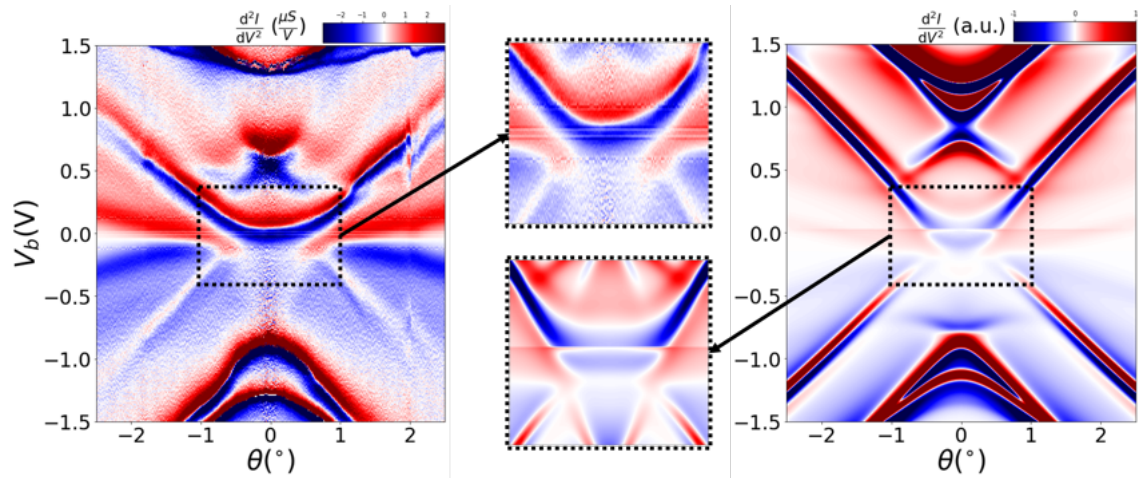


Figure 4.68 Measurement (left) and numerical calculation (right), with $C_g = 5.66 \frac{\mu F}{cm^2}$, including MLG strained by 0.8% and doped by $\Delta\mu_T = +0.15eV$.

4.10 Few-Layer Graphene

We now focus on few-layer graphene systems, extending the concepts of nesting and matching lines to an arbitrary number of layers. Following this theoretical discussion, we present and analyze the measured spectra for trilayer and pentalayer graphene samples.

4.10.1 Theory

Figure 4.69 and Fig. 4.70 depict the simulated tunneling current and conductance for trilayer, tetralayer, and pentalayer graphene, both with and without hBN barrier interaction.

With each additional layer, a characteristic feature emerges, attributable to either an additional parabolic or linear band. In the case of trilayer graphene, the system

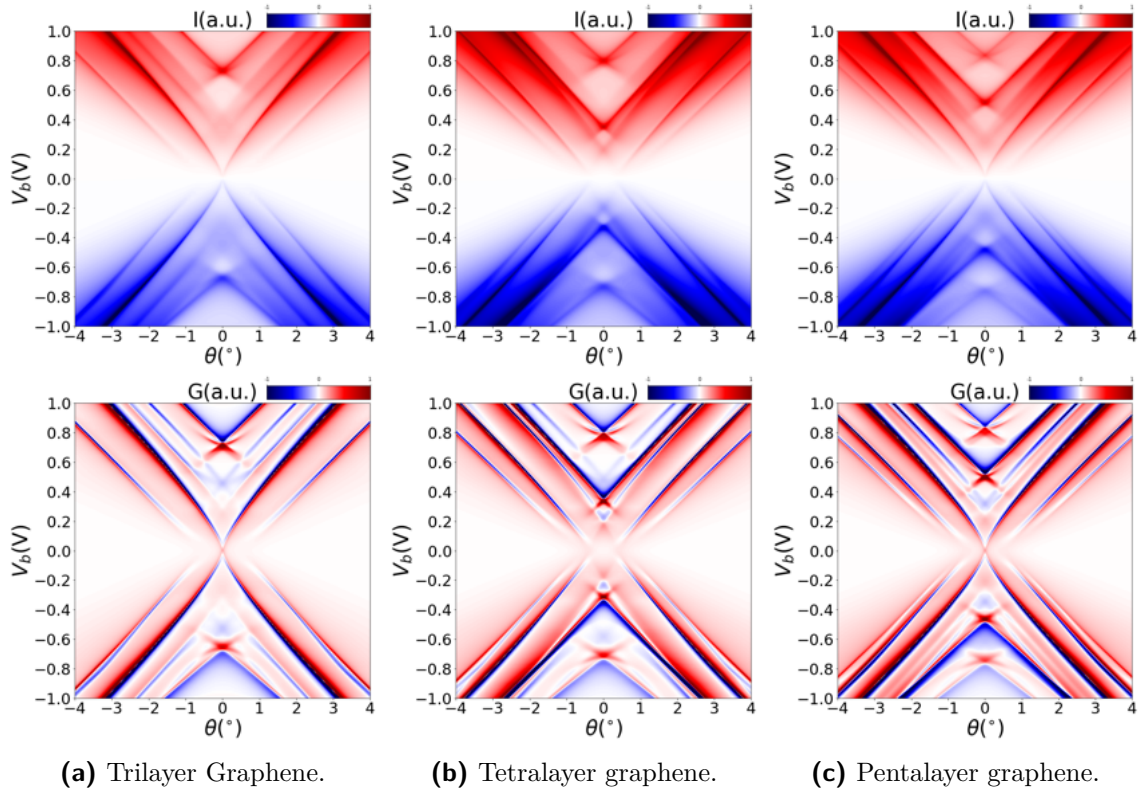


Figure 4.69 Tunneling spectra without barrier interaction.

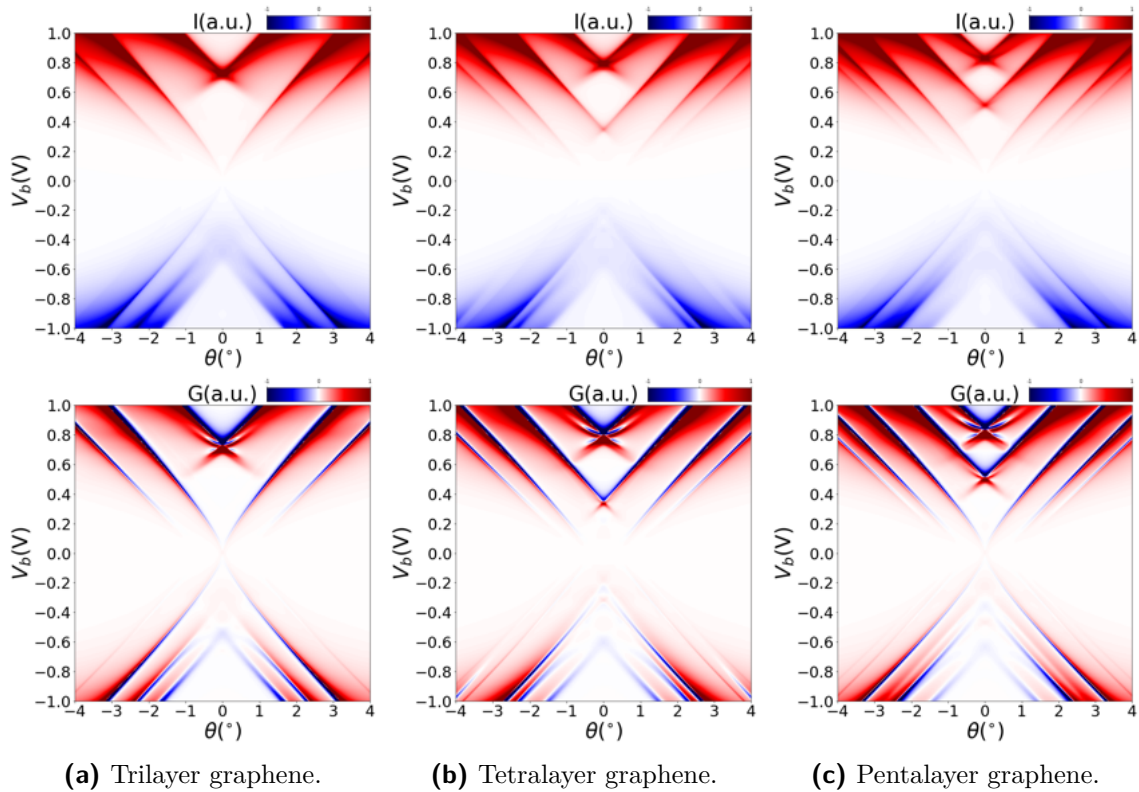


Figure 4.70 Tunneling spectra including barrier interaction.

exhibits four parabolic bands and two linear bands. The transition from BLG to trilayer graphene can be roughly described by superimposing the curved X feature from MLG onto the BLG spectrum. Compared to BLG, Tetralayer graphene, on

the other hand, introduces two additional pairs of parabolic bands. Accordingly, we observe additional BLG nesting lines with different curvature and shifted in energy. The transition from tetralayer to pentalayer graphene simply involves adding the curved X feature. Consequently, the spectra clearly reflect the even-odd layer number effect characteristic of FLG systems (Sec. 2.6.3).

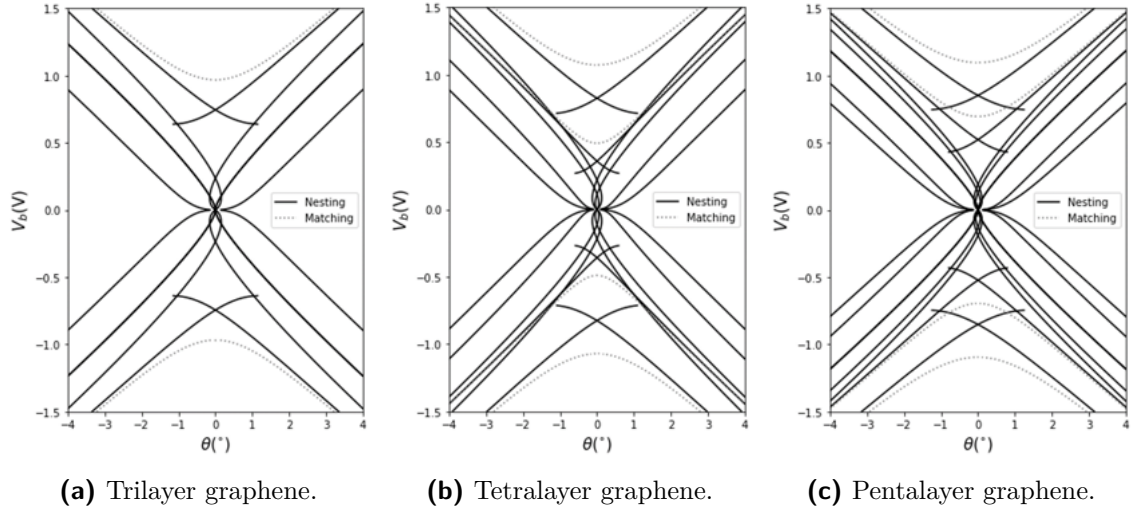


Figure 4.71 Nesting and matching lines.

By considering only the strongest coupling terms, γ_0 and γ_1 , we can generalize the expressions for nesting and matching lines in BLG to N-layer graphene systems. Applying the conditions outlined in Sec. 4.9.1 and utilizing the Bloch band functions from eq. 2.89, we derive the nesting lines:

$$\hbar v_F |\mathbf{K}| \theta_r = \pm \left[\sqrt{|\mu_B|^2 - 2\gamma_1 \cos\left(\frac{r\pi}{N+1}\right) |\mu_B|} - |\mu_B| - |\phi| \right], \quad (4.65)$$

$$\hbar v_F |\mathbf{K}| \theta_r = \pm \left[\sqrt{(|\mu_T| + |\phi|)^2 - 2\gamma_1 \cos\left(\frac{r\pi}{N+1}\right) (|\mu_T| + |\phi|)} - |\mu_T| \right], \quad (4.66)$$

while the matching condition leads to:

$$\hbar v_F |\mathbf{K}| \theta_r = \pm \left[\sqrt{|\phi|^2 - 2\gamma_1 \cos\left(\frac{r\pi}{N+1}\right) |\phi|} \right], \quad (4.67)$$

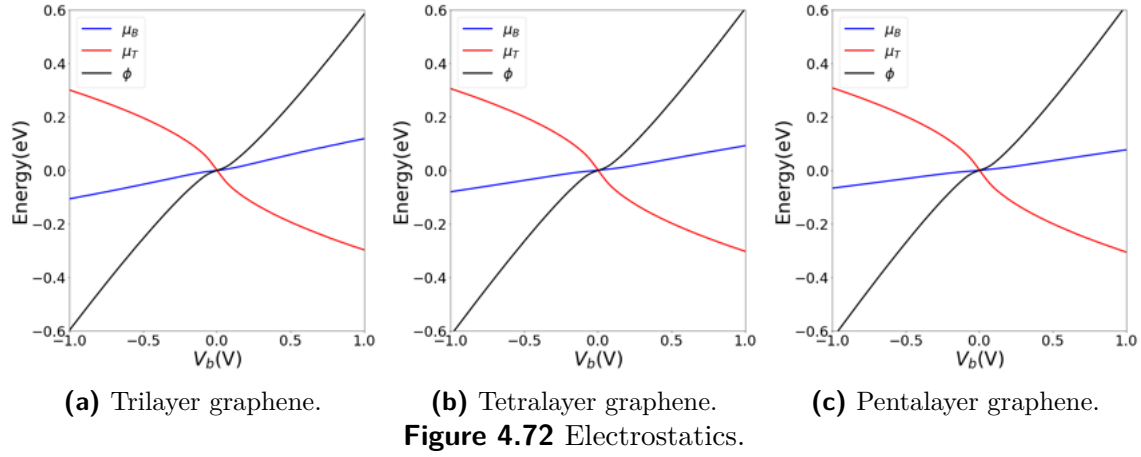
where $r \in \{1, 2, \dots, N\}$.

Figure 4.71 illustrates these lines for $N = 3, 4, 5$. Within this approximation, the charge densities of the tip and sample are given by:

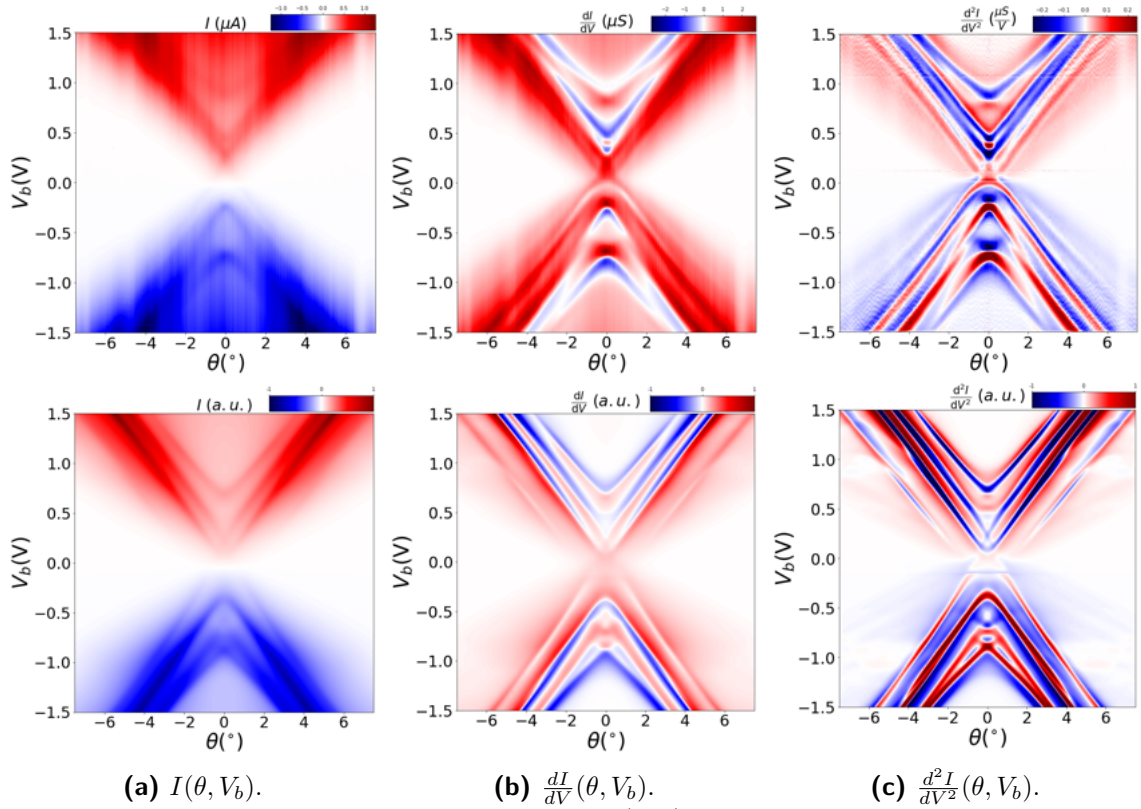
$$n_B(\mu) = \text{sign}(\mu) \sum_r \left[\frac{|\mu|^2}{\pi \hbar^2 v_F^2} + \frac{2\gamma_1 |\mu|}{\pi \hbar^2 v_F^2} \cos\left(\frac{r\pi}{N+1}\right) \right], \quad (4.68)$$

$$n_T(\mu) = \text{sign}(\mu) \frac{|\mu|^2}{\pi \hbar^2 v_F^2}. \quad (4.69)$$

The corresponding electrostatics are plotted in Fig 4.72.



4.10.2 Trilayer Graphene



The measurements obtained from the trilayer graphene sample are presented in Fig 4.73. However, the nesting lines in the higher bias regime do not exhibit the expected sharp edges, appearing more parabolic in shape. According to the theoretical model, we would also expect to observe the curved X feature traversing the

charge neutrality point, corresponding to the nesting of linear bands. Instead, we observe a gap-like feature in the spectrum.

Previous analyses suggest that strain can smooth out sharp edges. Additionally, due to strain-induced misalignment of the K-points between the tip and the sample, tunneling between linear bands onsets only at finite bias (Fig. 4.74), effectively "gapping out" the curved X feature.

Further insights can be gained by focusing on the small bias regime (Fig. 4.75). Here, we observe characteristics similar to those in the BLG measurements, particularly the shifted sign change of $\frac{d^2I}{dV^2}$. In the BLG measurement, this shift was towards negative bias, indicating electron doping of the tip. In the trilayer measurement, the shift is towards positive bias, suggesting hole doping. The numerical calculations plotted alongside the measurement data were performed assuming MLG strained by 0.08% and doped by $\Delta\mu_T = -0.15eV$.

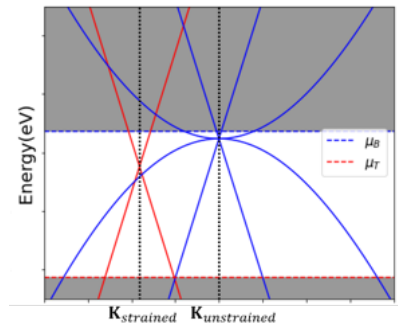


Figure 4.74 Tunneling between linear band onsets at finite bias.

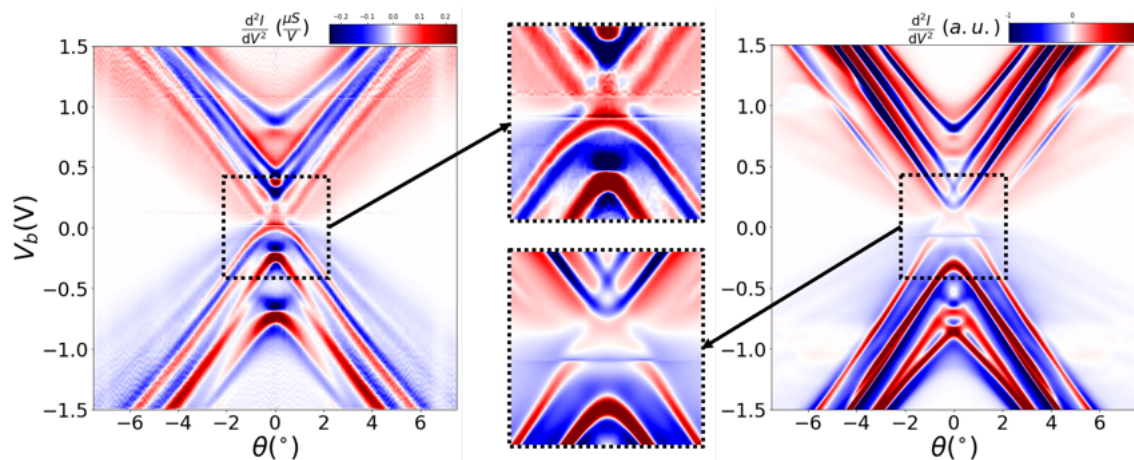


Figure 4.75 Measurement (left) and numerical calculation (right), with $C_g = 1.89 \frac{\mu F}{cm^2}$, including MLG strained by 0.8% and doped by $\Delta\mu_T = -0.15eV$.

4.10.3 Pentlayer Graphene

Figure 4.76 shows the tunneling measurements conducted on the pentalayer graphene sample. In contrast to the trilayer measurement, the curved X feature corresponding to the nesting of the linear bands is clearly observed, indicating that strain plays a less significant role in this case. In Fig. 4.77, we extract the nesting positions by tracing the peaks and dips in $\frac{d^2I}{dV^2}$. Our analysis focuses on the curved X feature, whose position is indicated by the red arrows in Fig. 4.77a.

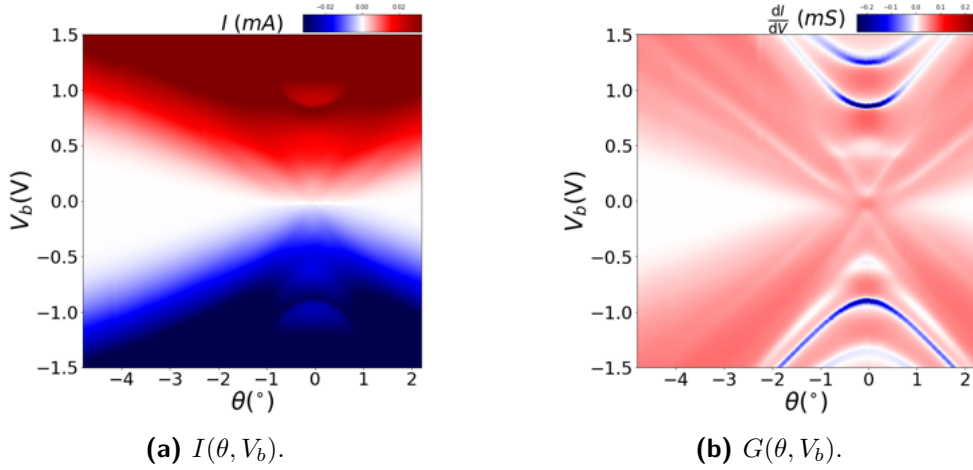
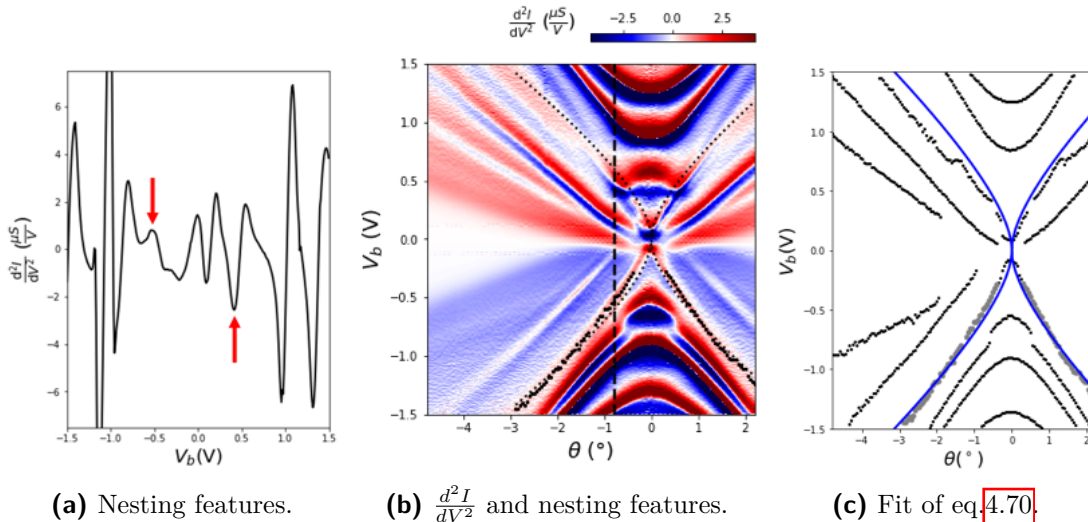


Figure 4.76 Measured tunneling spectra.

Given the relatively large DOS of pentalayer graphene, we approximate the electrostatics of this junction with $\mu_B \approx 0$ (graphite-like) in the low bias regime. Similar to eq. 4.39, we derive the following expression:

$$e|V_b| \approx |\phi| + |\mu_T| = \phi + \sqrt{\frac{\pi C_g \hbar^2 v_F^2 |\phi|}{e^2}} = \hbar v_F |\mathbf{K}| \theta + \sqrt{\frac{\pi C_g \hbar^3 v_F^3 |\mathbf{K}| \theta}{e^2}}, \quad (4.70)$$

where we have incorporated the nesting condition from eq. 4.34



(a) Nesting features. **(b)** $\frac{d^2I}{dV^2}$ and nesting features. **(c)** Fit of eq. 4.70.

Figure 4.77 (a) Line profile along dashed path revealing nesting features as local maxima (minima) at negative (positive) bias. (b) Measured $\frac{d^2I}{dV^2}$ and nesting features (black dots). (c) Fitted Dirac dispersion (blue lines) with $v_F = 1.01 \cdot 10^6 \frac{\text{m}}{\text{s}}$ and $C_g = 14.3 \mu\text{F}$.

By fitting eq. 4.70 using v_F extracted from MLG, we estimate an upper limit for the geometric capacitance of $C_g \approx 14.3 \frac{\mu\text{F}}{\text{cm}^2}$. Note that we used data points only in the lower bias regime (gray dots), due to discontinuities observed in the positive bias regime.

Similar to Sec. 4.8.1, we extract an lower limit for the carrier lifetime as follows:

$$\tau^{-1} \approx \phi = \frac{e^2}{\pi \hbar^2 v_F^2 C_g} \mu^2 \approx \frac{e^2}{\pi \hbar^2 v_F^2 C_g} \left(\frac{e \Delta_b}{2} \right)^2 = \frac{e^4 \Delta_b^2}{4 \pi \hbar^2 v_F^2 C_g} \quad (4.71)$$

From Fig. 4.78, we extract a linewidth of approximately $0.2V$, which, according to eq. 4.71, corresponds to an inverse lifetime $\tau^{-1} \approx 4meV$.

We note that these results include strong approximations and more accurate results require precise knowledge of parameters like capacitance, strain, and doping. The small discontinuities in the upper bias regime, as well as the curved shape of the higher nesting lines, suggest their relevance in this measurement.

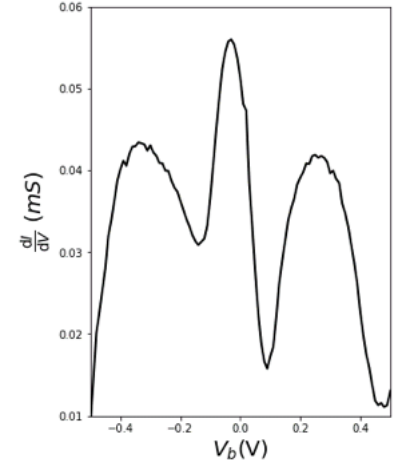


Figure 4.78 Measured line profile $\frac{dI}{dV}(0^\circ, V_b)$.

Chapter 5

Conclusion

The twist angle between graphene layers has emerged as a critical parameter that grants access to a wide array of exotic phases, with the QTM offering precise control over this variable. The primary challenge in leveraging the QTM for these systems lies in ensuring coherent coupling between the tip and the sample, such that external contributions from the setup exert minimal influence on the dynamics at the interface.

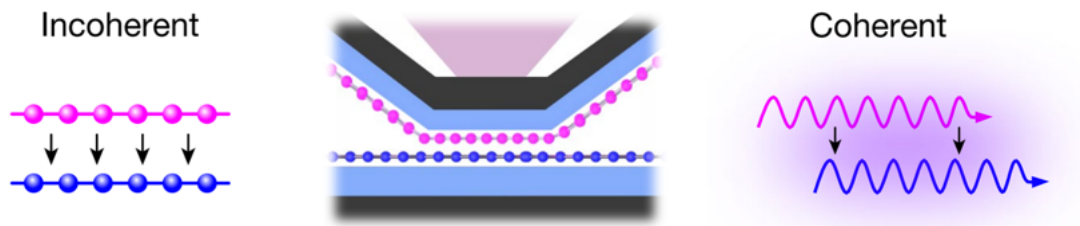


Figure 5.1 Illustrations of incoherent and coherent tunneling across the 2D junction. In incoherent tunneling, electrons tunnel at various locations independently, with the tunneling rate being proportional only to the local wavefunction squared. In coherent tunneling, however, trajectories interfere, making the tunneling sensitive to the phase variations of the wavefunctions in both the top and bottom layers across the junction. Adapted from [14].

We first established the overall coherence of our junction by examining the coupling strength between the graphite layers as a function of twist angle. The observation of two commensurate peaks, alongside the absence of others, is consistent with the predicted exponential decay of peak conductance.

In a fully incoherent junction, potentially due to continuous environmental interactions, states would localize on both the tip and the sample. In such a scenario, the measured conductance peaks would manifest purely as real-space phenomena, merely reflecting the enhanced real-space overlap of atoms between the two layers. For example, the moiré unit cells at 0° , 13.2° , 21.8° , and 27.8° comprise 2,

38, 14, and 26 atoms, respectively. This would lead to a weak algebraic decay of peak amplitude, proportional to the fraction of overlapping atoms between the two layers, i.e., $\frac{1}{2}$, $\frac{1}{14}$, $\frac{1}{26}$, $\frac{1}{38}$. This stands in sharp contrast to the exponential decay predicted by the BM-Model, where delocalized Bloch waves are involved in coupling (Fig. 5.1) [14]. Consequently, the pronounced peaks observed at 21.8° and 38.2° underscores the QTM's capability to create coherently coupled twisted 2D materials with arbitrary twist angles.

By enabling the creation of highly controllable interfaces between vdW materials, the QTM paves the way for a new class of experiments on quantum materials. Measurements can now be performed under high magnetic fields, with variable carrier densities and electrical displacement fields controlled by local gates, with continuously tunable pressure and twist angle. This capability allows for the exploration of even richer phase diagrams in novel materials.

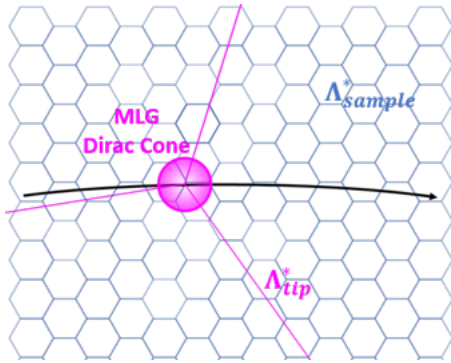


Figure 5.2 When the MLG probe layer is rotated relative to the sample system with $a_{tip} \ll a_{sample}$, its Dirac cone (pink circle) traces the energy bands along an arc (black) in momentum space.

The QTM's ability to interact directly with momentum space also introduces a novel approach to analyzing electronic structures. We demonstrated that measuring the tunneling current as a function of bias voltage and twist angle provides direct signatures of momentum-resolved dispersions. Here, the tip serves as a momentum-resolved probe for the unperturbed energy bands of a sample by tracing an arc in momentum space using the MLG Dirac cone as a "local" probe. This is illustrated in Fig. 5.2, where we consider a hexagonal sample system with $a_{tip} \ll a_{sample}$, such as TBG. Similar to how a STM probes local tunneling in real space, the QTM exploits

tunneling, which is local in reciprocal space.

Despite these promising initial results, it is important to emphasize that this project is still in its early stages. The tip and sample preparation processes, in particular, have shown susceptibility to the creation of strong disorder as well as strain and doping, which can reduce resolution and complicate the interpretation of measurement data. Extracting unperturbed band parameters with high accuracy will require improvements in these preparation processes. Moreover, it is crucial to determine the geometric capacitance in advance, since the measurement data suggest that modeling the junction as a parallel capacitor is inaccurate. Even for very clean samples, uncertainties in C_g significantly limit the accuracy with which band parameters can be extracted.

Once these challenges are overcome, the QTM has the potential to serve as a powerful alternative to ARPES, as this technique should be applicable to a wide range of layered conductors, semiconductors, and superconductors. The ability to control the geometry and dimensions of the tip allows for perfect adjustment to any flake size, and the resulting high spatial resolution of the QTM suggests significant advantages. Furthermore, the high surface sensitivity of ARPES necessitates the absence of an hBN flake encapsulating the structure, which poses challenges for device fabrication, as the electronic properties of open devices are more susceptible to the degrading effects of polymer residues and hydrocarbon contamination on the surface.

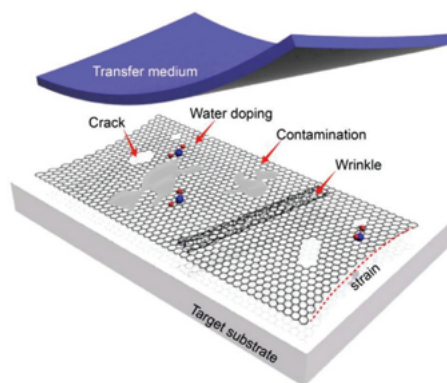


Figure 5.3 Schematic illustration of the as-transferred graphene film on target substrates with the assistance of transfer medium, highlighting the issues of cracks, unintentional doping, contamination, wrinkles, and strains. Adapted from [104]

Lastly, achieving high resolution in the meV range requires very low temperatures. Given the relatively simple steps needed to transition from an AFM to a QTM setup, it is possible to build on the already well-established foundation of low-temperature AFM systems. In comparison, low-temperature ARPES measurements remain challenging, as the typical geometrical design of these systems disrupts thermal conduction between the sample and cryostat, making it difficult to achieve sample temperatures below 10–30K [11].

In conclusion, the QTM holds the potential to become a powerful new tool in the arsenal of experimental condensed matter physics. While this thesis represents an initial step, it will take time to fully harness the capabilities of this new measurement concept. Nonetheless, it has the potential to join the ranks of state-of-the-art machinery for material characterization. Since the first exfoliation of graphene in 2004, the 2D materials field has presented numerous mysteries waiting to be unraveled. Introducing a little twist may reshape our understanding of exotic phenomena in condensed matter in ways that are yet unpredictable.

List of Figures

1.1 Mechanical exfoliation from graphite	1
1.2 vdW heterostructures	2
1.3 Twisted graphene layers	3
1.4 ARPES working principle	4
1.5 ARPES spectrum	5
1.6 QTM working principle	6
2.1 Dirac Cones	9
2.2 Sets of lattice basis vectors	10
2.3 Unit cells	10
2.4 Inner structure of a unit cell	11
2.5 Brillouin zone of a square lattice	12
2.6 Bloch wave	13
2.7 Tight binding 1D-chain	15
2.8 Typical dispersion relations	17
2.9 Electronic Structure of Solids	19
2.10 Carbon in the periodic table	20
2.11 Atomic Potential	20
2.12 Orbital Shapes of the Second Shell	21
2.13 Crystal potential	22
2.14 sp^2 -hybrid orbitals	23
2.15 Orbital Configuration	23
2.16 Mechanical strength	23
2.17 Real-space lattice and reciprocal lattice of MLG	24
2.18 π -bonding network	27
2.19 Band structure and DOS of MLG	29
2.20 Bonding orbital configuration	29
2.21 Antibonding orbital configuration	30
2.22 Bonding and antibonding orbital networks at the Γ -point	30
2.23 Bonding and antibonding orbital networks at the M -point	31
2.24 Bonding and antibonding orbital networks at the K -point	31
2.25 Band structure and DOS of MLG including next nearest neighbours	33

2.26 Low Energy Band structure and DOS of MLG	35
2.27 Low energy surface plot and contour plot of MLG	36
2.28 BLG lattice structure	36
2.29 Band structure and DOS of BLG	38
2.30 Energy surface plot and contour plot of BLG	39
2.31 Energy bands at the K -point	39
2.32 High-energy band orbital configurations at the K -point	40
2.33 Low-energy band orbital configurations at the K -point	40
2.34 Low-energy band structure and DOS of BLG	41
2.35 Contour plots showing the effects of varying γ_3	41
2.36 Band structure plots showing the effects of varying γ_4	42
2.37 Crystal structure of FLG	43
2.38 Band structures and DOS of FLG systems.	44
2.39 Low-energy band structures of FLG systems.	45
2.40 Moiré pattern	46
2.41 Moiré periodicity	47
2.42 Commensurate and incommensurate angles	48
2.43 Moiré reciprocal lattice	49
2.44 Moiré potential	51
2.45 Orbital arrangement at the interface of twisted layers	51
2.46 Illustration of the overlap integral calculation in TBG	52
2.47 Functional form of the interlayer coupling amplitude	53
2.48 Momentum space delocalization	54
2.49 k -space geometry.	56
2.50 Moiré BZ in the extended zone scheme	58
2.51 Shell numbering of the momentum lattice	58
2.52 Eigenvalue equation for 8-band model	59
2.53 8-band TBG Hamiltonian	59
2.54 20-band TBG Hamiltonian	59
2.55 TBG Band structure for different truncations and angles	60
2.56 Effects of lattice relaxation on the crystal structure.	61
2.57 Effect of lattice relaxation on the band structure	62
2.58 Band structure of TBG	63
2.59 Renormalized Dirac-point band velocity	63
2.60 Band structure of magic angle TBG.	64
2.61 DOS of TBG.	64
3.1 Close-up diagram of the quantum twisting microscope in action	65
3.2 Mechanical exfoliation	66

3.3	Transfer setup	67
3.4	Working principles of Raman spectroscopy	67
3.5	The 2D peak in FLG systems	68
3.6	SEM-Setup and electron beam interaction	70
3.7	Controlling and limitation of the Magnification	71
3.8	Finite probe size	71
3.9	Beam geometry	72
3.10	Electron-trajectory simulations	73
3.11	Electron-beam induced dissociation and deposition	74
3.12	Electron-Precursor interaction	74
3.13	EBID tips on AFM cantilevers	75
3.14	Sample preparation process.	76
3.15	EBID-Pillars	76
3.16	Deposition Events on the Surface of the Deposit	78
3.17	Raster Scan Scheme	78
3.18	Aperture diameter and depth of focus	79
3.19	EBID-pyramids	80
3.20	Charging effects	81
3.21	Spatial shift of deposited layers	82
3.22	Seed layer.	82
3.23	EBID-tip on cantilever	83
3.24	New layer sizes	83
3.25	Dwell time vs frame number	84
3.26	Magnification vs voltage	85
3.27	D-peak in amorphous carbon	86
3.28	Preparation of the transfer slide	87
3.29	Raman spectrum of MLG	87
3.30	Polymer membrane transfer technique	88
3.31	Successive transfer of 2D flakes	88
3.32	Melting of the polymer film (zoomed in)	89
3.33	Melting of the polymer film (zoomed out)	89
3.34	Tip device	90
3.35	Van der Waals pick-up transfer method	90
3.36	Sample device	91
3.37	Images of the QTM setup	92
3.38	Schematic of the QTM setup	93
4.1	Illustration interlayer transport	95
4.2	STM Working Principle	96

4.3 STM image	97
4.4 Phase (in-)coherent Tips	97
4.5 Interlayer Coupling of Bloch States	99
4.6 Structural Disorder in Graphene	99
4.7 Elastic Scattering	100
4.8 AFM Working Principle	100
4.9 Energetics for direct contact	102
4.10 Simulated interlayer conductance	103
4.11 Fermi circles in an extended-zone scheme	104
4.12 Nesting of Dirac cones at commensurability	105
4.13 Mapping conductance contribution in \mathbf{k} -space	106
4.14 Shell numbering and their contributions	107
4.15 Twisted junction between two graphite flakes	107
4.16 Measured conductance	108
4.17 Inelastic phonon scattering	108
4.18 Band structure and DOS of hBN	110
4.19 hBN as a tunneling barrier. Adapted from [14].	110
4.20 Tunneling junction	111
4.21 WKB-approximation	111
4.22 Electrostatics of the tunneling junction	112
4.23 Charge density in FLG systems	114
4.24 Effect of finite bias	115
4.25 Fowler–Nordheim Tunneling	116
4.26 MLG Simulated tunneling spectra	118
4.27 E- \mathbf{k} -space geometry	118
4.28 Intersections of two Dirac cones	119
4.29 MLG Line profile $I(\theta, 0.4V)$	120
4.30 Thermal Smearing	120
4.31 MLG $I(\mathbf{k})$ -map for onset	121
4.32 MLG $I(\mathbf{k})$ -map for nesting	122
4.33 Tunneling in the Reduced Zone Scheme	123
4.34 Reduced vs Extended Zone Scheme	123
4.35 Tunneling spectra with different barrier configurations	124
4.36 Schematic of the charge-neutral MLG-MLG tunneling experiment	125
4.37 Dependence on hBN thickness	125
4.38 Lifetime dependence.	126
4.39 Current broadening	127
4.40 Conductance Broadening	127
4.41 Tunneling spectra with finite V_{BG}	128

4.42 Tunneling spectra with finite V_{BG} and V_{TG}	128
4.43 Onset condition at finite gate voltage	128
4.44 Gate dependence	129
4.45 MLG Measured tunneling spectra	130
4.46 MLG Measured onset features	131
4.47 MLG Measured nesting features	131
4.48 MLG Measured line profiles	132
4.49 BLG Simulated tunneling spectra	133
4.50 BLG Nesting/matching lines	134
4.51 Tunneling spectra and nesting/matching lines	136
4.52 BLG Line profile $I(1^\circ, V_b)$	136
4.53 BLG $I(\mathbf{k})$ map for positive bias	137
4.54 BLG $I(\mathbf{k})$ map, negative bias	138
4.56 WKB amplitude	138
4.55 BLG Tunneling spectra with different barrier configurations	139
4.57 Effect of trigonal warping	139
4.58 Trigonal distortion of energy contours	140
4.59 Effect of electron-hole asymmetry	141
4.60 Origin of the low-bias nesting lines	142
4.61 Numerical asymmetry between the nesting lines	143
4.62 BLG Measured tunneling spectra	143
4.63 BLG Measured nesting/matching features	144
4.64 Asymmetry between the nesting lines	145
4.65 Doping of graphene	146
4.66 Effect of isotropic strain	146
4.67 Strained tip device	147
4.68 BLG Spectrum low bias regime	147
4.69 FLG Tunneling spectra without barrier interaction	148
4.70 FLG Tunneling spectra including barrier interaction	148
4.71 FLG nesting/matching lines	149
4.72 FLG Electrostatics	150
4.73 3LG Measured tunneling spectra	150
4.74 Strain induced K-point displacement	151
4.75 3LG Spectrum low bias regime	151
4.76 5LG Measured tunneling spectra	152
4.77 5LG Measured nesting features	152
4.78 5LG Line profile	153
5.1 (In-)coherent tunnelling	155

5.2 Tip tracing an arc in \mathbf{k} -space	156
5.3 Material-transfer issues	157

Bibliography

- [1] Richard Feynman. There's plenty of room at the bottom. *Resonance: Journal of Science Education*, 16(9), 2011.
- [2] Ossila. 2d materials: An introduction to two-dimensional materials. <https://www.ossila.com/pages/introduction-2d-materials>.
- [3] Kostya S Novoselov, Andre K Geim, Sergei V Morozov, De-eng Jiang, Yanshui Zhang, Sergey V Dubonos, Irina V Grigorieva, and Alexandr A Firsov. Electric field effect in atomically thin carbon films. *science*, 306(5696):666–669, 2004.
- [4] Andre K Geim and Irina V Grigorieva. Van der waals heterostructures. *Nature*, 499(7459):419–425, 2013.
- [5] B Andrei Bernevig and Dmitri K Efetov. Twisted bilayer graphene's gallery of phases. *Physics Today*, 77(4):38–44, 2024.
- [6] Rafi Bistritzer and Allan H MacDonald. Moiré bands in twisted double-layer graphene. *Proceedings of the National Academy of Sciences*, 108(30):12233–12237, 2011.
- [7] Yuan Cao, Valla Fatemi, Ahmet Demir, Shiang Fang, Spencer L Tomarken, Jason Y Luo, Javier D Sanchez-Yamagishi, Kenji Watanabe, Takashi Taniguchi, Efthimios Kaxiras, et al. Correlated insulator behaviour at half-filling in magic-angle graphene superlattices. *Nature*, 556(7699):80–84, 2018.
- [8] Yuan Cao, Valla Fatemi, Shiang Fang, Kenji Watanabe, Takashi Taniguchi, Efthimios Kaxiras, and Pablo Jarillo-Herrero. Unconventional superconductivity in magic-angle graphene superlattices. *Nature*, 556(7699):43–50, 2018.
- [9] Sung-Kwan Mo. Angle-resolved photoemission spectroscopy for the study of two-dimensional materials. *Nano Convergence*, 4(1):6, 2017.
- [10] Wikipedia. Angle-resolved photoemission spectroscopy. https://en.wikipedia.org/wiki/Angle-resolved_photoemission_spectroscopy.

- [11] Chan-young Lim, Sunghun Kim, Sung Won Jung, Jinwoong Hwang, and Yeongkwan Kim. Recent technical advancements in arpes: Unveiling quantum materials. *Current Applied Physics*, 2024.
- [12] M Iqbal Bakti Utama, Roland J Koch, Kyunghoon Lee, Nicolas Leconte, Hongyuan Li, Sihan Zhao, Lili Jiang, Jiayi Zhu, Kenji Watanabe, Takashi Taniguchi, et al. Visualization of the flat electronic band in twisted bilayer graphene near the magic angle twist. *Nature Physics*, 17(2):184–188, 2021.
- [13] Rebeca Ribeiro-Palau. A twist in the bid to probe electrons in solids, 2023.
- [14] Alon Inbar, John Birkbeck, Jiewen Xiao, Takashi Taniguchi, Kenji Watanabe, Binghai Yan, Yuval Oreg, Ady Stern, Erez Berg, and Shahal Ilani. The quantum twisting microscope. *Nature*, 614(7949):682–687, 2023.
- [15] Kostya Novoselov and Daniel Elias. Artistic impressions of the dirac cones. <http://www.condmat.physics.manchester.ac.uk/imagelibrary/>.
- [16] David Tong. *Lectures on Solid State Physics*. University of Cambridge Lecture, 2017.
- [17] Dmitri K. Efetov. *Advanced Solid State Physics*. LMU Munich University Lecture, 2023.
- [18] Chegg. Energy bands and brillouin zones. <https://www.chegg.com/homework-help/questions-and-answers/4-energy-bands-brillouin-zones-bz-consider-two-dimensional-square-lattice-associ>
- [19] Neil W. Ashcroft, N. David Mermin, and et al. *Solid State Physics*. Holt, Rinehart and Winston, New York London, 1976.
- [20] Wikipedia. Bloch’s theorem. https://en.wikipedia.org/wiki/Bloch%27s_theorem.
- [21] Keiichi Edagawa. Photonic crystals, amorphous materials, and quasicrystals. *Science and technology of advanced materials*, 15(3):034805, 2014.
- [22] Alexander B Watson, Tianyu Kong, Allan H MacDonald, and Mitchell Luskin. Bistritzer–macdonald dynamics in twisted bilayer graphene. *Journal of Mathematical Physics*, 64(3), 2023.
- [23] Mikhail I Katsnelson. *The physics of graphene*. Cambridge University Press, 2020.

- [24] Alexander Urban. *Einführung in die Festkörperphysik*. LMU Munich Lecture, 2020.
- [25] Andrew Breeson. *Control of Crystallinity in Photocatalytic Titanium Dioxide*. PhD thesis, UCL (University College London), 2017.
- [26] Adobe Stock. Carbon atom on white background. <https://stock.adobe.com/de/images/carbon-atom-on-white-background/59676535>.
- [27] LibreTexts Project. *CHEM 1201*. NICE CXone Expert, 2024.
- [28] John Proctor. Graphene is thin, but not infinitely so. *Physical Review Letters*, 2019.
- [29] Akanksha Urade. Why does graphene’s incredible tensile strength begin at 30 microns in lateral flake. . . .? *Avadain*, 2022.
- [30] Jia-Ming Liu and I-Tan Lin. *Graphene photonics*. Cambridge University Press, 2019.
- [31] Fenton John Doolan. An alternative explanation of the ‘spokes’ observed in saturn’s rings. *arXiv preprint arXiv:2303.07197*, 2023.
- [32] LM Zhang, ZQ Li, Dimitri N Basov, MM Fogler, Zhao Hao, and Michael C Martin. Determination of the electronic structure of bilayer graphene from infrared spectroscopy. *Physical Review B—Condensed Matter and Materials Physics*, 78(23):235408, 2008.
- [33] John P Lowe and Kirk Peterson. *Quantum chemistry*. Elsevier, 2011.
- [34] Gonçalo Filipe Santos Catarina. *Twisted bilayer graphene—electronic and optical properties*. PhD thesis, PhD thesis, 2017.
- [35] Ken-ichi Sasaki, Shuichi Murakami, and Riichiro Saito. Stabilization mechanism of edge states in graphene. *Applied Physics Letters*, 88(11), 2006.
- [36] Edward McCann and Mikito Koshino. The electronic properties of bilayer graphene. *Reports on Progress in physics*, 76(5):056503, 2013.
- [37] Edward McCann, David SL Abergel, and Vladimir I Fal’ko. The low energy electronic band structure of bilayer graphene. *The European Physical Journal Special Topics*, 148(1):91–103, 2007.
- [38] Mikito Koshino and Edward McCann. Landau level spectra and the quantum hall effect of multilayer graphene. *Physical Review B—Condensed Matter and Materials Physics*, 83(16):165443, 2011.

- [39] Hongki Min and Allan H MacDonald. Electronic structure of multilayer graphene. *Progress of Theoretical Physics Supplement*, 176:227–252, 2008.
- [40] Rafi Bistritzer and Allan H MacDonald. Transport between twisted graphene layers. *Physical Review B—Condensed Matter and Materials Physics*, 81(24):245412, 2010.
- [41] Deepanshu Aggarwal, Rohit Narula, and Sankalpa Ghosh. A primer on twistrionics: a massless dirac fermion’s journey to moiré patterns and flat bands in twisted bilayer graphene. *Journal of Physics: Condensed Matter*, 35(14):143001, 2023.
- [42] Tomasz Necio and Magdalena Birowska. Supercell-core software: a useful tool to generate an optimal supercell for vertically stacked nanomaterials. *AIP Advances*, 10(10), 2020.
- [43] DV Chalin, DI Levshov, AE Myasnikova, and SB Rochal. Tight-binding approximation for bilayer graphene and nanotube structures: From commensurability to incommensurability between the layers. *Physical Review B*, 105(4):045402, 2022.
- [44] Wei Yao, Eryin Wang, Changhua Bao, Yiou Zhang, Kenan Zhang, Kejie Bao, Chun Kai Chan, Chaoyu Chen, Jose Avila, Maria C Asensio, et al. Quasicrystalline 30 twisted bilayer graphene as an incommensurate superlattice with strong interlayer coupling. *Proceedings of the National Academy of Sciences*, 115(27):6928–6933, 2018.
- [45] Michael G Scheer, Kaiyuan Gu, and Biao Lian. Magic angles in twisted bilayer graphene near commensuration: Towards a hypermagic regime. *Physical Review B*, 106(11):115418, 2022.
- [46] Ron Cowen. Twisted science: Nist researchers find a new quantum ruler to explore exotic matter. *National Institute of Standards and Technology*, 2023.
- [47] Patrice EA Turchi, Antonios Gonis, Luciano Colombo, et al. Tight-binding approach to computational materials science. In *MRS Symp. Proc.*, volume 491, 1998.
- [48] G Trambly de Laissardière, Didier Mayou, and Laurence Magaud. Localization of dirac electrons in rotated graphene bilayers. *Nano letters*, 10(3):804–808, 2010.
- [49] Pekka Koskinen and Ville Mäkinen. Density-functional tight-binding for beginners. *Computational Materials Science*, 47(1):237–253, 2009.

- [50] Jan Attig, Jinhong Park, Michael M Scherer, Simon Trebst, Alexander Altland, and Achim Rosch. Universal principles of moiré band structures. *2D Materials*, 8(4):044007, 2021.
- [51] Yves Hon Kwan. *Topology and correlations in twisted bilayer graphene*. PhD thesis, University of Oxford, 2022.
- [52] B Andrei Bernevig, Zhi-Da Song, Nicolas Regnault, and Biao Lian. Twisted bilayer graphene. i. matrix elements, approximations, perturbation theory, and $ak \cdot p$ two-band model. *Physical Review B*, 103(20):205411, 2021.
- [53] Yuan Cao et al. *Study Of electronic correlation and superconductivity in twisted graphene superlattices*. PhD thesis, Massachusetts Institute of Technology, 2020.
- [54] Kazuyuki Uchida, Shinnosuke Furuya, Jun-Ichi Iwata, and Atsushi Oshiyama. Atomic corrugation and electron localization due to moiré patterns in twisted bilayer graphenes. *Physical Review B*, 90(15):155451, 2014.
- [55] Ilani Group. Close-up diagram of the quantum twisting microscope in action. *Weizmann Institute of Science*, 2023.
- [56] Yuan Huang, Eli Sutter, Norman N Shi, Jiabao Zheng, Tianzhong Yang, Dirk Englund, Hong-Jun Gao, and Peter Sutter. Reliable exfoliation of large-area high-quality flakes of graphene and other two-dimensional materials. *ACS nano*, 9(11):10612–10620, 2015.
- [57] Ipsita Das. *Study of Different Quantum Phases in Magic-angle Twisted Bilayer Graphene*. PhD thesis, Universitat Politècnica de Catalunya, 2023.
- [58] Rémi Gilliot. Introduction to magic-angle twisted bilayer graphene and its fabrication process. *Institut Polytechnique de Paris*, 2023.
- [59] Sara Mosca, Claudia Conti, Nick Stone, and Pavel Matousek. Spatially offset raman spectroscopy. *Nature Reviews Methods Primers*, 1(1):21, 2021.
- [60] Andrea C Ferrari, Jannik C Meyer, Vittorio Scardaci, Cinzia Casiraghi, Michele Lazzeri, Francesco Mauri, Stefano Piscanec, Dingde Jiang, Konstantin Sergeevich Novoselov, Siegmund Roth, et al. Raman spectrum of graphene and graphene layers. *Physical review letters*, 97(18):187401, 2006.
- [61] Leandro M Malard, Marcos Assunção Pimenta, Gene Dresselhaus, and Mildred Spiewak Dresselhaus. Raman spectroscopy in graphene. *Physics reports*, 473(5-6):51–87, 2009.

- [62] Physik Instrumente USA. *Electron Microscopy*. <https://www.pi-usa.us/en/tech-blog/electron-microscopy-nonmagnetic-drives-and-stages-for-vacuum/>.
- [63] Nanoscience Instruments. *Scanning Electron Microscopy*. <https://www.nanoscience.com/techniques/scanning-electron-microscopy/>.
- [64] Eric Lifshin, Yudhishtir P Kandel, and Richard L Moore. Improving scanning electron microscope resolution for near planar samples through the use of image restoration. *Microscopy and Microanalysis*, 20(1):78–89, 2014.
- [65] E Kim, E Iroaga, and B Murmann. Brief introduction to scanning electron microscopy (sem), 2004.
- [66] Ivo Utke, Patrik Hoffmann, and John Melngailis. Gas-assisted focused electron beam and ion beam processing and fabrication. *Journal of Vacuum Science & Technology B: Microelectronics and Nanometer Structures Processing, Measurement, and Phenomena*, 26(4):1197–1276, 2008.
- [67] G Di Battista, KC Fong, A Diez-Carlon, K Watanabe, T Taniguchi, and DK Efetov. Ultra-low carrier density superconducting bolometers with single photon sensitivity based on magic-angle twisted bilayer graphene. *arXiv preprint arXiv:2403.02049*, 2024.
- [68] Naresh Marturi, Sounkalo Dembélé, and Nadine Piat. Depth and shape estimation from focus in scanning electron microscope for micromanipulation. In *2013 International Conference on Control, Automation, Robotics and Embedded Systems (CARE)*, pages 1–6. IEEE, 2013.
- [69] Robyn McNeil Mia Au Valentin Schmid Daniel Korchinski, Johannes Duereth. A brief introduction to scanning electron microscopy. *University of British Columbia*, 2019.
- [70] Emad Oveisi. Scanning electron microscopy techniques. *École Polytechnique Fédérale de Lausanne*, 2019.
- [71] Wade Jensen. Interpreting images from scanning electron microscopy. *Deringer-Ney*, 2022.
- [72] Thomas Schmid. *Scanning electron microscopy*. <http://schmid.mygoodpage.org/wordpress/scanning-electron-microscopy-sem/>.
- [73] WF Van Dorp and Cornelis W Hagen. A critical literature review of focused electron beam induced deposition. *Journal of Applied Physics*, 104(8), 2008.
- [74] Anil Waman Date. *Analytic combustion*. Springer, 2011.

- [75] Rachel M Thorman, Ragesh Kumar TP, D Howard Fairbrother, and Oddur Ingólfsson. The role of low-energy electrons in focused electron beam induced deposition: four case studies of representative precursors. *Beilstein journal of nanotechnology*, 6(1):1904–1926, 2015.
- [76] I Utke, P Swiderek, K Höflich, K Madajska, J Jurczyk, P Martinović, and IB Szymańska. Coordination and organometallic precursors of group 10 and 11: Focused electron beam induced deposition of metals and insight gained from chemical vapour deposition, atomic layer deposition, and fundamental surface and gas phase studies. *Coordination Chemistry Reviews*, 458:213851, 2022.
- [77] Abgeena Shabir, Poonam Sehrawat, CM Julien, SS Islam, et al. Reversible synthesis of go: Role of differential bond structure transformation in fine-tuning photodetector response. *Nanotechnology*, 32(4):045601, 2020.
- [78] D Haddock, T Parker, C Spindloe, and M Tolley. Characterisation of diamond-like carbon (dlc) laser targets by raman spectroscopy. In *Journal of Physics: Conference Series*, volume 713, page 012007. IOP Publishing, 2016.
- [79] Riccardo Frisenda, Efrén Navarro-Moratalla, Patricia Gant, David Pérez De Lara, Pablo Jarillo-Herrero, Roman V Gorbachev, and Andres Castellanos-Gomez. Recent progress in the assembly of nanodevices and van der waals heterostructures by deterministic placement of 2d materials. *Chemical Society Reviews*, 47(1):53–68, 2018.
- [80] David Parker. Electrical charge conduction of graphene. *Fine Art America*, 2016.
- [81] Gerd Binnig, Heinrich Rohrer, Ch Gerber, and Eddie Weibel. Tunneling through a controllable vacuum gap. *Applied Physics Letters*, 40(2):178–180, 1982.
- [82] Henry Greenside. Scanning tunneling microscope. *Duke University*, 2015.
- [83] Jerry Tersoff and Donald R Hamann. Theory of the scanning tunneling microscope. *Physical Review B*, 31(2):805, 1985.
- [84] Eduardo Cisternas, F Stavale, M Flores, Carlos Alberto Achete, and Patricio Vargas. First-principles calculation and scanning tunneling microscopy study of highly oriented pyrolytic graphite (0001). *Physical Review B—Condensed Matter and Materials Physics*, 79(20):205431, 2009.

- [85] Kui Zhou, Ziqi Jia, Xin-Qi Ma, Wenbiao Niu, Yao Zhou, Ning Huang, Guanglong Ding, Yan Yan, Su-Ting Han, Vellaisamy AL Roy, et al. Manufacturing of graphene based synaptic devices for optoelectronic applications. *International Journal of Extreme Manufacturing*, 5(4):042006, 2023.
- [86] Adrien Signoles, Baptiste Lecoutre, Jérémie Richard, Lih-King Lim, Vincent Denechaud, Valentin V Volchkov, Vasiliki Angelopoulou, Fred Jendrzejewski, Alain Aspect, Laurent Sanchez-Palencia, et al. Ultracold atoms in disordered potentials: elastic scattering time in the strong scattering regime. *New Journal of Physics*, 21(10):105002, 2019.
- [87] Paul E West. *Introduction to atomic force microscopy theory, practice, applications*. PhD thesis, Universität Würzburg, 2007.
- [88] Park Systems. Schematic diagram of experimental setup for contact mode afm. <https://www.parksystems.com/en/products/research-afm/AFM-modes/imaging-modes/ContactMode>.
- [89] CS Shivananda. *Synthesis of Silver Nanoparticles Using Silk Fibroin Characterization and Potential Antibacterial Applications*. PhD thesis, Mangalore University, 2017.
- [90] Gerald D Mahan. *Many-particle physics*. Springer Science & Business Media, 2013.
- [91] Alexander Altland and Ben D Simons. *Condensed matter field theory*. Cambridge university press, 2010.
- [92] John Birkbeck, Jiewen Xiao, Alon Inbar, Takashi Taniguchi, Kenji Watanabe, Erez Berg, Leonid Glazman, Francisco Guinea, Felix von Oppen, and Shahal Ilani. Measuring phonon dispersion and electron-phason coupling in twisted bilayer graphene with a cryogenic quantum twisting microscope. *arXiv preprint arXiv:2407.13404*, 2024.
- [93] Sergio C de la Barrera. *Layered two-dimensional heterostructures and their tunneling characteristics*. Springer, 2017.
- [94] Yoichi Kubota, Kenji Watanabe, Osamu Tsuda, and Takashi Taniguchi. Deep ultraviolet light-emitting hexagonal boron nitride synthesized at atmospheric pressure. *Science*, 317(5840):932–934, 2007.
- [95] Liam Britnell, RV Gorbachev, Rashid Jalil, BD Belle, Fredrik Schedin, Artem Mishchenko, Thanasis Georgiou, MI Katsnelson, Laurence Eaves, SV Moro-

- zov, et al. Field-effect tunneling transistor based on vertical graphene heterostructures. *Science*, 335(6071):947–950, 2012.
- [96] Kenneth A Lin, Nitin Prasad, G William Burg, Bo Zou, Keiji Ueno, Kenji Watanabe, Takashi Taniguchi, Allan H MacDonald, and Emanuel Tutuc. Emergence of interlayer coherence in twist-controlled graphene double layers. *Physical Review Letters*, 129(18):187701, 2022.
- [97] Ralph Howard Fowler and Lothar Nordheim. Electron emission in intense electric fields. *Proceedings of the Royal Society of London. Series A, Containing Papers of a Mathematical and Physical Character*, 119(781):173–181, 1928.
- [98] Jia F Weng. An approach to conic sections. *mh*, 2(h2):m2x2–h2, 1998.
- [99] DC Elias, RV Gorbachev, AS Mayorov, SV Morozov, AA Zhukov, P Blake, LA Ponomarenko, IV Grigorieva, KS Novoselov, F Guinea, et al. Dirac cones reshaped by interaction effects in suspended graphene. *Nature Physics*, 7(9):701–704, 2011.
- [100] Akash Laturia, Maarten L Van de Put, and William G Vandenberghe. Dielectric properties of hexagonal boron nitride and transition metal dichalcogenides: from monolayer to bulk. *npj 2D Materials and Applications*, 2(1):6, 2018.
- [101] Isabella Gierz, Christian Riedl, Ulrich Starke, Christian R Ast, and Klaus Kern. Atomic hole doping of graphene. *Nano letters*, 8(12):4603–4607, 2008.
- [102] Ho-Kin Tang, E Laksono, JNB Rodrigues, Pinaki Sengupta, FF Assaad, and S Adam. Interaction-driven metal-insulator transition in strained graphene. *Physical review letters*, 115(18):186602, 2015.
- [103] Jz-Yuan Juo, Bong Gyu Shin, Wolfgang Stiepany, Marko Memmler, Klaus Kern, and Soon Jung Jung. In-situ atomic level observation of the strain response of graphene lattice. *Scientific Reports*, 13(1):2451, 2023.
- [104] Yuqing Song, Wentao Zou, Qi Lu, Li Lin, and Zhongfan Liu. Graphene transfer: Paving the road for applications of chemical vapor deposition graphene. *Small*, 17(48):2007600, 2021.

Acknowledgements

First and foremost, I would like to express my heartfelt gratitude to **Prof. Dr. Dmitri K. Efetov** for the invaluable opportunity to join his team and explore this fascinating field of research. From our very first interview, he took the time to understand my interests and helped align me with a project that was the perfect fit. By granting me the freedom to shape my work according to my passions, I was able to deeply engage with both theoretical and experimental physics, giving me a clear vision of my future in academia.

I extend my deepest appreciation to my supervisor, **Martin Lee**. As a team leader, his guidance and support have been instrumental in overcoming the many obstacles that arose throughout this journey. His calm and friendly demeanor fostered an incredibly pleasant working atmosphere, and over the past year, he has consistently provided me with the direction I needed. No question went unanswered, and no request was overlooked.

There were certainly challenging moments when things didn't go as planned—when I found myself staring helplessly at images of yet another broken QTM tip. In those times, I am especially grateful to **Janos Papp**. Sharing our frustrations and laughing together over failed attempts helped us maintain our humor and perseverance through the setbacks.

I would also like to extend my sincere thanks to **Philipp Altpeter** and **Ipsita Das** for their expert guidance in the cleanroom. Their mentorship in exfoliation, spin coating, and the EBID system laid the foundation for all the experimental work I conducted.

Lastly, I want to express my gratitude to my fellow group members: **Giorgio di Battista**, **Andres Díez-Carlón**, **Rafael Luque Merino**, **Jiazhuo Li**, **Jaime Díez-Merida**, **Christian Obermayer**, **Leon Schubert**, **Daniil Ivanov**, **Hajar Mouqadem**, and **Heribert Lorenz**. From day one, they welcomed me with open arms and made me feel like an integral part of the team. Their openness and support made this time both enjoyable and memorable. Thank you all, and I wish you the very best for the future!

Selbständigkeitserklärung

Hiermit erkläre ich, die vorliegende Arbeit mit dem Titel

**Theoretical and Experimental Study of the Electronic Structure of
Graphene-based Systems with the Quantum Twisting Microscope**

selbständig verfasst zu haben und keine anderen als die in der Arbeit angegebenen Quellen und Hilfsmittel benutzt zu haben.

München, den 12.09.2024

Marc Currle